

**Magnetic fluid bearings & seals
Methods, design & application**

Lampaert, S.G.E.

DOI

[10.4233/uuid:361ba18e-298a-483c-bfb9-0528a4ee6119](https://doi.org/10.4233/uuid:361ba18e-298a-483c-bfb9-0528a4ee6119)

Publication date

2020

Document Version

Final published version

Citation (APA)

Lampaert, S. G. E. (2020). *Magnetic fluid bearings & seals: Methods, design & application*. [Dissertation (TU Delft), Delft University of Technology]. <https://doi.org/10.4233/uuid:361ba18e-298a-483c-bfb9-0528a4ee6119>

Important note

To cite this publication, please use the final published version (if applicable).
Please check the document version above.

Copyright

Other than for strictly personal use, it is not permitted to download, forward or distribute the text or part of it, without the consent of the author(s) and/or copyright holder(s), unless the work is under an open content license such as Creative Commons.

Takedown policy

Please contact us and provide details if you believe this document breaches copyrights.
We will remove access to the work immediately and investigate your claim.



Magnetic Fluid Bearings & Seals: Methods, Design & Application

Stefan G.E. Lampaert

Part 2: Appendices

Load and stiffness of a planar ferrofluid pocket bearing

Proc IMechE Part J:

J Engineering Tribology

2018, Vol. 232(1) 14–25

© IMechE 2017

DOI: 10.1177/1350650117739200

journals.sagepub.com/home/pij



SGE Lampaert, JW Spronck and RAJ van Ostayen

Abstract

A ferrofluid pocket bearings is a type of hydrostatic bearing that uses a ferrofluid seal to encapsulate a pocket of air to carry a load. Their properties, combining a high stiffness with low (viscous) friction and absence of stick-slip, make them interesting for applications that require fast and high precision positioning. Knowledge on the exact performance of these types of bearings is up to now not available. This article presents a method to model the load carrying capacity and normal stiffness characteristics of this type of bearings. Required for this is the geometry of the bearing, the shape of the magnetic field and the magnetization strength of the fluid. This method is experimentally validated and is shown to be correct for describing the load and stiffness characteristics of any fixed shape of ferrofluid pocket bearing.

Keywords

Precision engineering, hydrostatic bearing, mathematical modelling, planar bearing, magnetics

Date received: 30 September 2016; accepted: 27 September 2017

Introduction

As man began to explore space, it became relevant to develop efficient techniques to use and store rocket engine propellants under zero gravity conditions. For this reason, the NASA Research Center developed in the 1960s a kerosene-based magnetic fluid that could be collected at a desired location by the use of a magnetic field.¹ This magnetic fluid consisted of a stable colloidal suspension of tiny magnetic particles (~10 nm) providing the fluid with paramagnetic properties.² Rosensweig continued the research into these so-called ferrofluids and showed in the early 1970s that these fluids might also be interesting for the usage in seals and bearings.^{3,4} Pressure builds up in the fluid because the magnetic particles are attracted by a magnetic field. This pressure can be used to develop a force to carry a load or to seal a volume. Compared to other bearing concepts, the ferrofluid bearings are an easy way to create a low friction movement that is free of stick-slip.^{5–9} The bearing is furthermore inherently stable due to the use of permanent magnets. The magnetic field of these magnets can additionally be used for Lorentz actuation.^{10–16} The overall specifications presented in literature show that the bearing is particularly interesting for low load applications that require fast and high precision positioning. Examples of possible applications are microscopy, wafer/chip inspection and pick and place machines. The low vapour pressure ferrofluids are suitable for vacuum conditions

and even application in a zero gravity environment is possible since the ferrofluid is kept in place by the magnetic field.

Two types of planar ferrofluid bearings can be distinguished. The first type is a ferrofluid pressure bearing that uses solely the magnetic pressure to carry a load.^{17–19} The second category is a ferrofluid pocket bearing that enhances the load carrying capacity of an air pocket (or any other non-magnetic fluid), which is encapsulated and pressurized by a surrounding ferrofluid seal.^{3,20,21} A simple example of this bearing concept is given in Figure 1. The planar ferrofluid bearing can be seen as a sort of hydrostatic bearing meaning that it does not need a relative movement between bearing faces to create a pressure field. Though the working principles are fundamentally different from the hydrostatic bearings of literature^{22–25} that uses the magnetorheological effect and a pressure source to create a pressure field.

The tribological performance of the planar ferrofluid bearing is, despite its potential, barely discussed in literature. This is completely opposite to the

Department of Precision and Microsystems Engineering, Delft University of Technology, Delft, The Netherlands

Corresponding author:

SGE Lampaert, Department of Precision and Microsystems Engineering, Delft University of Technology, Mekelweg 2, 2628CD Delft, The Netherlands.

Email: S.G.E.Lampaert@tudelft.nl

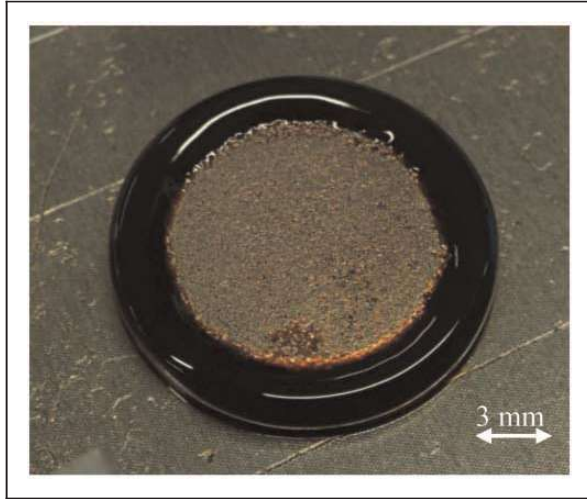


Figure 1. Ferrofluid is applied to a disc-shaped magnet with axial magnetization and placed on a ferromagnetic surface. The ferrofluid collects at the circumference of the magnet where the magnetic field strength is highest (Figure 2). A bearing is built by placing a surface on top of this configuration such that a pocket of air is encapsulated (Figure 3). The ring of ferrofluid functions as a seal that captures the air inside. The magnetic field of this magnet is shown in Figure 2.

performance of the hydrodynamic journal bearing lubricated with ferrofluid that has received significant attention recently.^{26–33}

A problem experienced in these types of bearings is that there are no mathematical models available yet that describe the load and stiffness characteristics; the designer interested in using these bearing has limited information available on how to dimension the bearing to achieve certain specifications. All literature describing these bearings lacks the link between the measured performance and a theoretical model.²⁰

Another problem seen in these bearings is the poor repeatability in fly height.^{13,14} The fly height is reduced during translation because of the trail formation that results in a smaller amount of fluid to be available for levitation. In the case of a pocket bearing, this might even cause air to escape from the encapsulated pocket of air resulting in a permanent change in fly height. In Café¹² and Lampaert et al.,¹⁵ the absence of a mathematical model to describe this effect accurately is mitigated in the presented positioning system by adding a control loop that controls the fly height of the bearing. This decision introduces extra actuators, sensors and therefore complexity in the system, which might take away the benefit of being low cost and simple. More knowledge on how the load and stiffness of this type of bearing is created might give more insight in how the trail formation affects the fly height of the bearing.

In this article, a method is presented to predict the load and stiffness characteristics of a ferrofluid pocket bearing. A model is derived using this method that is then validated with an experimental setup. The

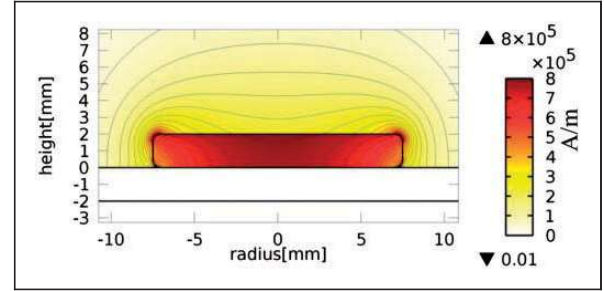


Figure 2. The magnetic field is highest at the corners of the magnet as shown here in a cross section of the configuration presented in Figure 1. The calculation is done with a remanent flux density of the magnet of $B_r = 17$ and a relative permeability of the iron base plate of $\mu_r = 4000$.

resulting knowledge can be used to understand how a ferrofluid bearing should be designed to meet the desired load and stiffness specifications.

Methods

In this section, the derivation of the mathematical model of the ferrofluid pocket bearing is explained and validated. The validation is divided into three parts. The maximum load carrying capacity, the load carrying capacity as a function of the fly height and the bearing stiffness are validated.

Mathematical model

In the following section, the method to calculate the load and stiffness specifications of a ferrofluid pocket bearing is derived. It provides the theoretical basis on how the different parameters contribute to the final specifications. This method is not limited to the examples given in Figures 3 and 4 but is valid for all possible shapes of magnets and magnetic fields. The derivation starts from the Navier–Stokes equations for incompressible, Newtonian magnetic fluids.³⁴ In this formula, the assumption of Newtonian fluids is reasonable for fluids that do not show any particle chain formation (i.e. fluids with a small dipolar interaction parameter³⁵).

$$\rho \left(\frac{\partial \vec{u}}{\partial t} + \vec{u} \cdot \nabla \vec{u} \right) = -\nabla p + \eta \nabla^2 \vec{u} + \vec{f} + \mu_0 M \nabla H$$

$$\nabla \cdot \vec{u} = 0$$
(1)

In this relation, the density is represented by ρ , the viscosity is represented by η and the magnetic permeability of vacuum is represented by μ_0 . Definitions of other symbols can be found in Figure 3 or in the text. Now it is assumed that the fluid velocity \vec{u} of the ferrofluid is small and therefore of negligible influence on the pressure distribution p in the liquid. There are no other body forces except those induced by the

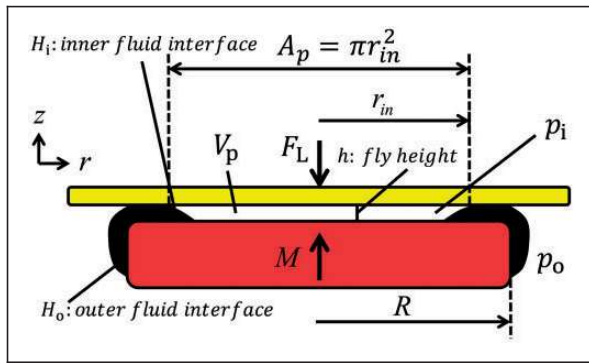


Figure 3. The figure presents a cross section of a disc-shaped magnet to define the parameters used in this article. The inner fluid interface defines H_i and the outer fluid interface defines H_o .

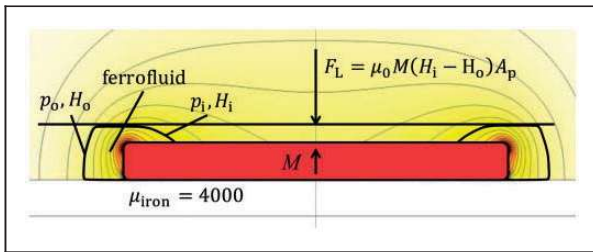


Figure 4. A graphical representation of the force development in a pocket bearing. A magnet with ferrofluid is placed on an iron plate with a nonmagnetic plate (black line) on top of the configuration. The contour plot on the background presents the magnetic field intensity. Ferrofluid is added and attracted to the corners due to highest field intensity there. The pressure difference across the ferrofluid seal is proportional to the difference in magnetic field intensity across the seal ($p_i - p_o \sim H_i - H_o$). This difference defines the load capacity of the bearing. The figure furthermore shows that the contour lines of the magnetic field intensity are identical to the contour lines of the pressure distribution.

magnetic field ($\vec{f} = 0$). These assumptions reduce relations (equation (1)) to the following form

$$\nabla p = \mu_0 M \nabla H \quad (2)$$

In general, the magnetization strength M of the ferrofluid is a function of the magnetic field, but can be assumed to be constant and equal to the saturation magnetization of the fluid when the fluid is subjected to a magnetic field larger than that saturation magnetization. Furthermore, when the magnetic field is much larger than the saturation magnetization of the fluid, it can be assumed that the magnetic field is unaffected by the presence of the ferrofluid. The low relative permeability of the fluid ensures furthermore that considering the magnetic behaviour, the fluid does not behave much differently than air. Typical magnetic fluids have a relative permeability μ_r of approximately 2 with a saturation magnetization of approximately $M = 32 \text{ kA/m}$ or 0.04 T .

For a ferrofluid pocket bearing primarily the pressure difference across the seal $p_i - p_o$ is of importance for calculating the total load. This pressure difference can be calculated with the assumptions mentioned above, the relation given in (2) and the fundamental theorem of calculus in the following way

$$p_i - p_o = \int_C \nabla p \cdot d\vec{r} = \mu_0 M_s \int_C \nabla H \cdot d\vec{r} = \mu_0 M_s (H_i - H_o) \quad (3)$$

The magnetic field at the inner fluid interface is equal to H_i and the magnetic field at the outer fluid interface is equal to H_o . From this relation follows that only the magnetic field strength at the fluid-air interfaces will determine the pressure increase in the pocket. The load capacity F_L can be approximated by integrating the pressure over the force carrying surface area of the pocket A_p . This is done with relation (equation (4)) in which it is furthermore assumed that the load carrying capacity of the ferrofluid ring itself is negligible (in the given example, its less than 10%). In a subsequent analysis, this effect is taken into account (see equation (11)). A graphical representation of the force relation is given in Figure 4. This only includes the load capacity caused by the ferrofluid seal.

$$F_L = \int_S (p_i - p_o) dA_p = \mu_0 M_s (H_i - H_o) A_p \quad (4)$$

The normal stiffness of the bearing k_{ff} is defined by the derivative of the load capacity (equation (4)) with the fly height h .

$$k_{ff} = -\frac{dF_L}{dh} = -A_p \frac{d(p_i - p_o)}{dh} - (p_i - p_o) \frac{dA_p}{dh} \quad (5)$$

Relation (equation (5)) implies that an increase in force, and the related increase of pressure, causes the ferrofluid interfaces to move outwards causing an increased counteracting pressure across the seal and an increased surface area for the force. The increase in surface area can be assumed to be negligible for a typical bearing design. Applying this assumption and combining relation (equation (5)) with (equation (3)) yields:

$$k_{ff} = -\mu_0 M_s A_p \frac{d(H_i - H_o)}{dh} \quad (6)$$

The change of magnetic field difference ($H_i - H_o$) over the displacement h is not directly known but can be found by relating that displacement with that of the inner fluid interface r_{in} .

$$k_{ff} = -\mu_0 M_s A_p \frac{d(H_i - H_o)}{dr_{in}} \frac{dr_{in}}{dh} \quad (7)$$

The relation dr_{in}/dh can be seen as a pneumatic leverage meaning that a small change of bearing fly height will result in a large displacement of the inner fluid interface (Figure 5). The two parameters are coupled via the geometry of the pocket, and the pressure, and therefore density of the air, inside the pocket. In this model, it is assumed that the pressure variation inside the pocket is small, and that therefore the air inside the pocket can be assumed to behave incompressible. This practically means that the stiffness of ferrofluid seals is much smaller than the stiffness of the pocket of air.

The pneumatic leverage can, in the case of a cylindrical shaped incompressible pocket, be described with relation (equation (8)). Figure 6 shows the magnitude of the pneumatic leverage for different initial fly heights and fixed bearing radii. The figure shows that the pneumatic leverage can in general be assumed to be constant for small compression ratios.

$$V_p = h\pi r_{in}^2$$

$$\frac{dr_{in}}{dh} = \frac{d}{dh} \sqrt{\frac{V_p}{\pi h}} = -\sqrt{\frac{V_p}{4\pi h^3}} = -\frac{r_{in}}{2h} \quad (8)$$

In the case of a ring-shaped pocket bearing, the air stiffness can be modelled as the stiffness of a

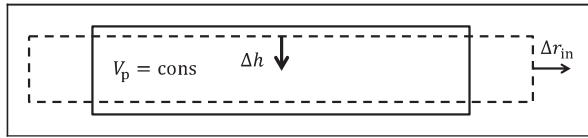


Figure 5. Graphical representation of the pneumatic leverage showing that a small displacement of h results in a large displacement in r_{in} . The relation dr_{in}/dh (equation (8)) can be calculated by assuming a constant air volume V_p of the pocket, which is reasonable for small displacements.

pneumatic cylinder. That is given with the following relation at which V_{ini} is the initial volume, V_h is the compressed volume and γ is the heat capacity ratio.

$$k_{air} = \left(\frac{V_{ini}}{V_h}\right)^\gamma p_{ini} \gamma \frac{A_p}{h} = \left(\frac{h_{ini}}{h}\right)^\gamma p_{ini} \gamma \frac{A_p}{h} \quad (9)$$

The stiffness of the encapsulated pocket of air can be seen as a stiffness that is in series with the stiffness of the ferrofluid seal. The total stiffness of the system can then be described to be

$$k_{total} = \frac{k_{ff} k_{air}}{k_{ff} + k_{air}} \quad (10)$$

The effect of the air stiffness can be assumed to be negligible when it is much larger than the seal stiffness.

$$k_{air} = \left(\frac{V_{ini}}{V_h}\right)^\gamma p_{ini} \gamma \frac{A_p}{h} = \left(\frac{h_{ini}}{h}\right)^\gamma p_{ini} \gamma \frac{A_p}{h} \quad (11)$$

The assumption of an incompressible (cylindrical) air pocket can be checked by making sure that the stiffness of bearing is much smaller than the stiffness of the pocket

$$\frac{k_{ff}}{k_{air}} = \frac{\mu_0 M_s A_p \frac{d(H_i - H_o)}{dr_{in}} \frac{r_{in}}{2h}}{\left(\frac{h_{ini}}{h}\right)^\gamma p_{ini} \gamma \frac{A_p}{h}} = \frac{\mu_0 M_s}{2p_{ini} \gamma} \frac{d(H_i - H_o)}{dr_{in}} \times \left(\frac{h}{h_{ini}}\right)^\gamma r_{in} \ll 1 \quad (12)$$

Figures 7 and 8 give some examples of the stiffness values for some different bearing sizes. From the graph, it can be seen that the stiffness increases for smaller gap heights. The figures also illustrate that the

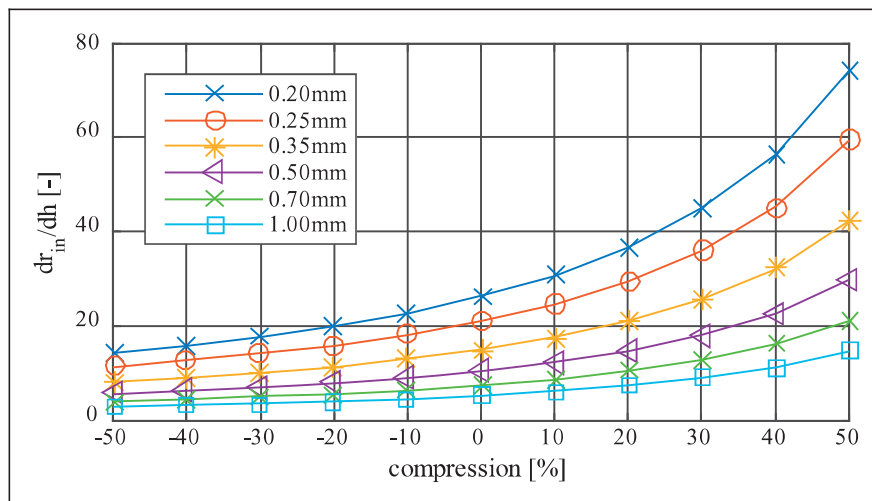


Figure 6. The figure presents the modelled pneumatic leverage for different initial gap heights and a fixed radius of $r_{in} = 10.5$ mm. The compression is a measure for how much the height is decreased for achieving the pneumatic leverage. A positive compression means a decrease in fly height.

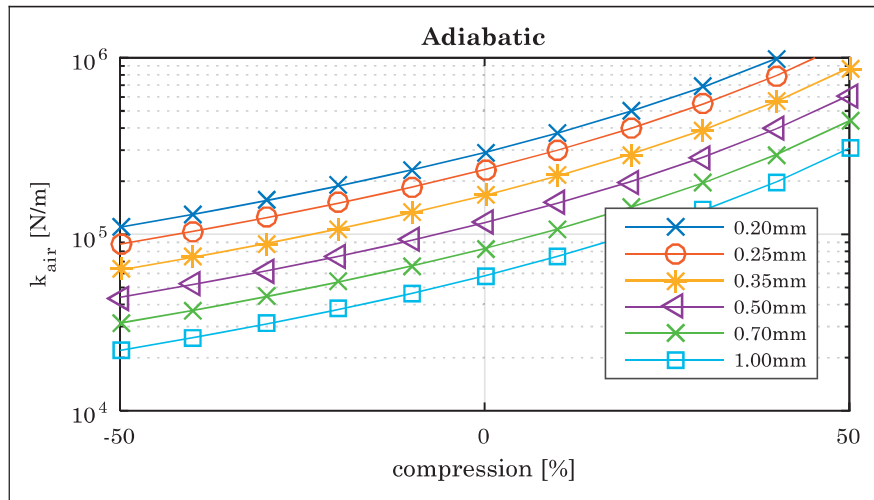


Figure 7. The modelled adiabatic stiffness of an air filled cylinder with different initial gap heights and a fixed radius of $r_{in} = 10.5$ mm. The graph shows that the air pocket is stiffer for decreasing fly height. At zero compression, the pressure condition is $p_i = p_o$.

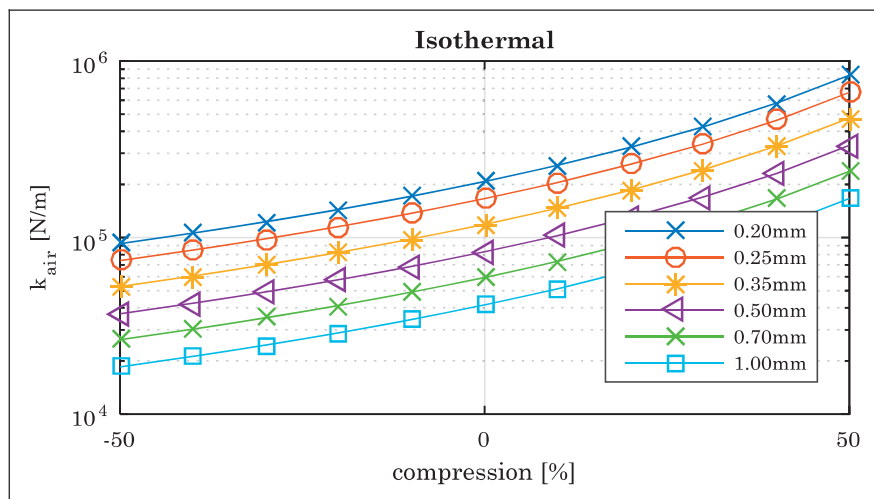


Figure 8. The modelled isothermal stiffness of an air filled cylinder with different initial gap heights and a fixed radius of $r_{in} = 10.5$ mm. The graph shows that the air pocket is stiffer for decreasing fly height. At zero compression, the pressure condition is $p_i = p_o$.

stiffness of the bearing is dependent on whether there is an adiabatic or isothermal situation. In general, the stiffness at low frequencies will behave isothermally and stiffness at high frequencies will behave adiabatically.

Experimental setup for validation

Experiments are performed to investigate whether the derived mathematical models describe the load and stiffness characteristics of this bearing correctly. The validation is realised by comparing the performances predicted by the theory with the results of experiments. The required input parameters are the geometrical dimensions of the setup and the shape and strength of the magnetic field.

The measurement data are obtained by pressing the bearing onto a surface using a tensile test bench that is able to measure the force over the displacement

(Figure 9). The setup has a relative force accuracy of 0.2 % and a relative force repeatability of 0.3%. The displacement is measured with a repeatability of 0.3 μm and an accuracy of 0.6 μm . The bearing consists of a ferrofluid pocket bearing constructed using a ring-shaped neodymium magnet with the magnetization in axial direction (see Figure 10 for more specifications). The ferrofluid that is used is the APG 513A from Ferrotec with a saturation magnetization of 32 kA/m. The magnetic field is derived using a FE analysis that is shown in Figures 10 and 11. It should be noted here that the ring magnet causes two radially distributed peaks in magnetic field intensity that potentially causes two seals in series. However, the two peaks act as one seal in this configuration due to capillary forces that connect the two seals together.

The process for validating the maximum load capacity of this bearing (equation (4)) is divided into four steps. The first step is to apply a specified amount of

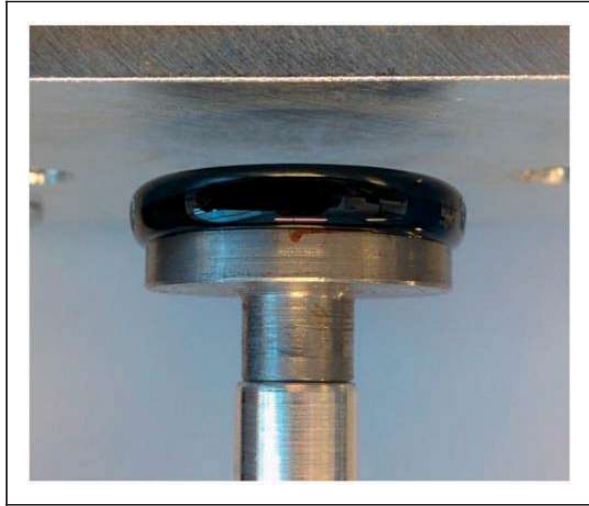


Figure 9. The ring magnet is placed on a steel adapter and magnetic fluid is added to the configuration. The core of the magnet is filled with an aluminium disc to reduce the volume of the air pocket and so create higher stiffness. A tensile testing machine is used to measure the force-displacement curves by pressing this configuration onto a surface. The stiffness of the setup is about $k_{setup} = 3 \times 10^6$ N/m.

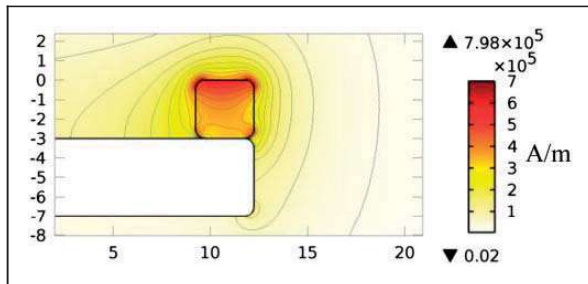


Figure 10. This figure presents the modelled magnetic field and the isolines of the bearing configuration used in the pocket bearing experiment. The ring magnet is placed on top of a steel body with a relative permeability of $\mu_{iron} = 4000$. The dimensions presented are in mm. The centre of the ring is filled with aluminium and is not presented in the figure since it has no influence on the magnetic field. The ring magnet used is the HKCM 9963-433 with an outer radius of $R = 12.25$ mm.

ferrofluid on the magnet after which the fluid will flow according to the magnetic field and form a uniform ring. The second step is to move the bearing to a point where it is just touching the opposing surface. A pocket of air is now encapsulated by a seal of ferrofluid. The magnetic field intensity at the inner fluid interface is the same as the magnetic field intensity at the outer fluid interface ($\Delta H = 0$) meaning that no pressure is build up across the seal yet ($\Delta p = 0$) and so the bearing has no load carrying capacity in this configuration (Figure 4). The initial outer magnetic field interface, when the bearing faces were not touching, is measured by comparing the position of the ferrofluid in the situation that the ferrofluid is not

touching the opposing surface (Figure 9) to the magnetic field given in Figure 10. The outer magnetic field interface in this situation is measured by comparing the position and shape of the ferrofluid in the real system (Figure 9) to the simulated shape (Figure 10). The outer contour of the ferrofluid in the real system should coincide with one of the contour lines of the magnetic field in the simulated system. The contour line where it coincides is the value of the outer field intensity.

The third step is to compress the bearing resulting air to leak out of the seal, since there is no ability to develop a counteracting pressure over the seal. The bearing is now at a lower fly height where the magnetic field intensity at the inner fluid interface now differs from the magnetic field intensity at the outer fluid interface ($\Delta H > 0$). The inner fluid interface has moved to a location with a higher magnetic field intensity while the magnetic field at the outer fluid interface remains approximately the same (this stays the same due to the geometry of the bearing, the shape of the magnetic field and the amount of fluid added to the bearing configuration). This causes pressure to build up across the seal that gives the bearing a load carrying capacity ($\Delta p > 0$). The inner fluid interface is furthermore at a peak in field intensity (Figure 11) since it is at the border of leaking air.

The fourth step is to decrease the fly height even more. This causes air to escape and causes the magnetic field intensity at the inner fluid interface to increase even further. Now an even larger difference in pressure across the seal has developed and results in an even higher load capacity.

Decreasing the fly height of the bearing in this way increases the magnetic field intensity at the inner fluid interface while the magnetic field intensity at the outer interface stays more or less the same. The inner fluid interface is located at a peak of field intensity (Figure 11) along the whole curve of maximum load capacity of this bearing.

The maximum load capacity of the bearing is calculated by determining the pressure build-up across the seal that is defined by the relevant magnetic field intensities at the inner and outer fluid interfaces of the seal. These values can be read from Figure 11 that presents the field intensity as a function of the radius for different fly heights. The field intensity at the outer fluid interface when there is no contact between the bearing faces is derived by comparing the location of the outer fluid interface with the isolines of Figure 10. When the load is increased further, the outer fluid interface will move outwards to a location with lower magnetic field intensity during the measurement. This is taken into account by the model, by a linear interpolation of these two values. The direct load contribution of the seal itself also has been taken into account in the model by averaging the magnetic field intensity over the surface area of

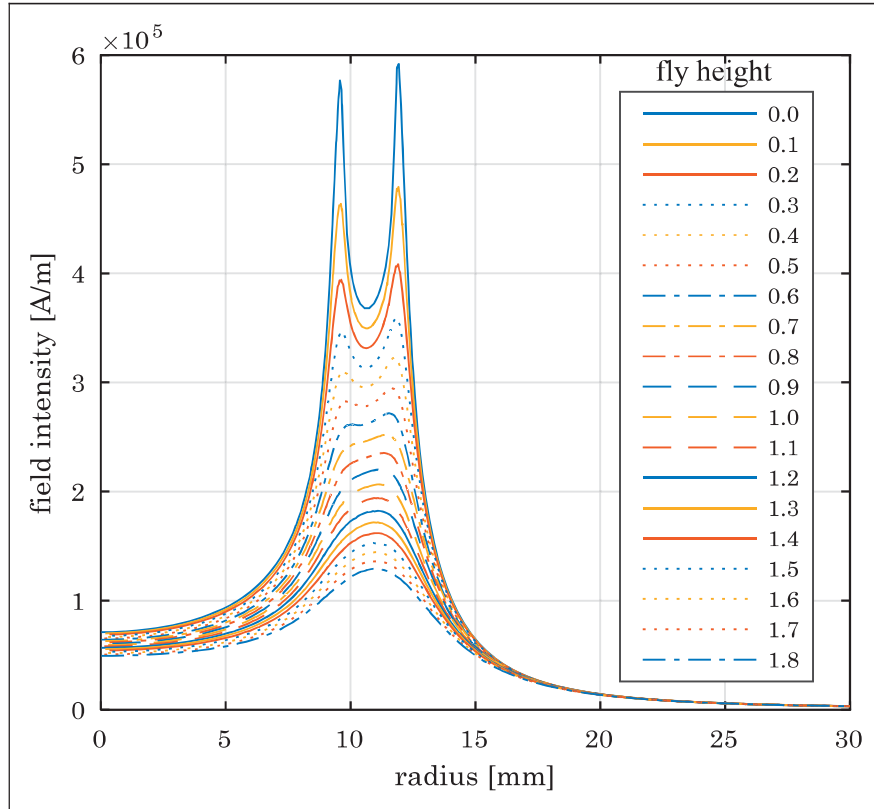


Figure 11. The modelled magnetic field intensity at different fly heights (in mm) as function of the radius for a ring-shaped magnet with the dimensions of (24.5 mm × 18.5 mm × 3 mm) and a remanent flux density of $B_r = 1.17$ T. The outer peak of the magnetic field is defining the relevant magnetic field for the load capacity since this has the highest magnitude. The relevant magnetic field intensities at the inner and outer fluid interfaces can be read from this figure.

the seal. Relation (equation (4)) is now extended to the following relation:

$$F_L = \mu_0 M_s (H_i - H_o) \left(A_p + \frac{A_s}{3} \right) \quad (13)$$

For the stiffness, two different expressions are mentioned in this article (relation (equation (6)) and (equation (7)) that are both validated individually. Relation (equation (6)) is validated by analysing the stiffness of the bearing between two points on the load curve generated by decompressing the bearing. To maintain a constant pocket volume, it is made sure that no air leaks across the ferrofluid seal during this decompression. One point that is easily distinguishable is the point of maximum load capacity given by relation (equation (13)). Another point that is easily distinguishable is the so-called ‘knee point’, which is a point on the force curve that shows a sudden change in slope. This ‘knee point’ is caused by a sudden change in the slope of the curve of the magnetic field intensity followed by the inner fluid interface. This occurs when the inner fluid interface is right in-between the two peaks of magnetic field intensity presented in Figure 11. The inner fluid interface moves inwards for a decreasing compression.

For the stiffness validation, it is required to know the difference in magnetic field intensity across the

seal for a certain fly height for the two points (the point of maximum load capacity and the knee point). This is no problem for the point of maximum load capacity since the location of the inner fluid interface is known. The fly height of the knee point can be derived from the point of maximum load capacity by analysing how the inner fluid interface moves inwards for increasing fly height. For small displacements and so small change in pressure, the air volume of the pocket can be assumed to be incompressible. The fly height for a corresponding knee point can then be calculated with

$$h_{knee} = h_{max} \frac{r_{max}^2}{r_{knee}^2} \quad (14)$$

Relation (equation (7)) is validated in a similar way by predicting the linear stiffness between the point of maximum load capacity and the knee point. This is done by using the pneumatic leverage value of exactly in-between the two points.

For the whole stiffness validation, it is assumed that the field intensity at the outer fluid interface stays constant since the displacements are only small. The measurements are performed by increasing the force up to a value of $F_L = 5$ N or $p_i = 0.13$ bar. Next the force is decreased to a negative value to demonstrate that the bearing also is capable to deliver

a tension force. This is done three times to show hysteresis present in the system.

Results and discussion

This chapter validates the theoretical predictions with experimental results and is divided into three parts: first the model of the load capacity is validated followed by the validation of the knee point that is then used to validate the stiffness model.

Maximum load capacity

The measured curve of maximum load capacity is presented in Figure 12. During the experiments, it is observed that the initial outer magnetic field interface, when the bearing faces were not touching, is measured to be $H_o = 1.3 \times 10^5 \text{ A/m}$. The outer magnetic field interface when the bearing faces are fully touching is measured to be $H_o = 1.0 \times 10^5 \text{ A/m}$. Air is escaping from the pocket of air through the seal along the whole path, this means that the inner fluid interface is at a peak in field intensity along the whole path. The location of this peak for the measured fly height is traced back by using Figure 11. These values are used to plot relation (equation (13)) in Figure 12. The small ripple visible in the curve is caused by air popping out of the seal and demonstrates that the inner fluid interface is at a maximum value of magnetic field intensity.

The data show that the theoretical model fits the measurements well. This furthermore shows that the load capacity is mainly defined by the pressure across the seal and only partly defined by the contribution of the pressure of the seal itself.

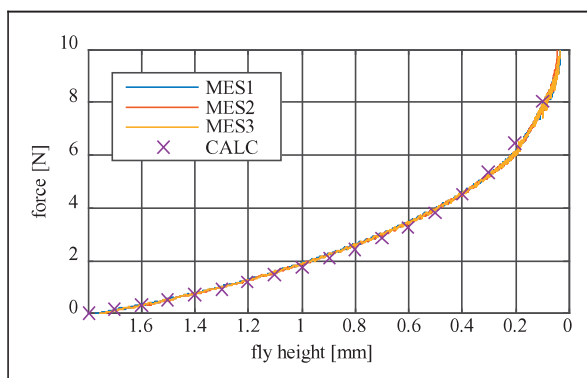


Figure 12. The force in the figure presents the maximum load of the in function of the fly height. Compressing the bearing will cause air to escape from the seal, because the pressure in the pocket of air becomes larger than the pressure that can be counteracted by the seal. The first three datasets in the figure are three different measurements that show that the maximum load curve of the bearing has a high repeatability. The fourth dataset is the result from the theoretical model of this process presented in relation (equation (12)). The figure shows that the model fits the measurements well.

Knee point

The force curve that is applied over time is presented in Figure 13. The force in function of the fly height is presented in Figure 14. The location of knee point in the load curve is presented in Figure 15. The knee point can be calculated by using formula (equation (14)) and the shape of the magnetic field presented in Figure 13. These graphs show that point of maximum load capacity is located at a radial position of $r_{max} = 11.8 \text{ mm}$ with a fly height of $h_{max} = 0.235 \text{ mm}$. Decompressing the bearing causes the inner fluid interface to move inwards towards the knee point. The air mass inside the pocket stays approximately constant during this process, which means that the location of the inner fluid interface can be calculated from the

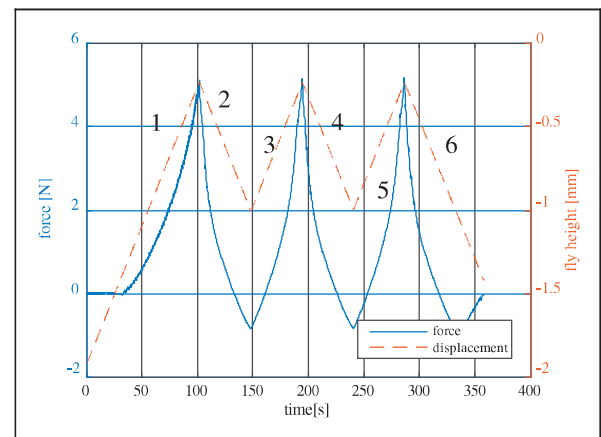


Figure 13. This figure presents the measured force and fly height of the bearing over time. The measurement starts with no contact between the bearing and the surface. The load-unload cycle is repeated three times and shows the hysteresis of the bearing. The numbers correspond with the numbers of Figure 14.

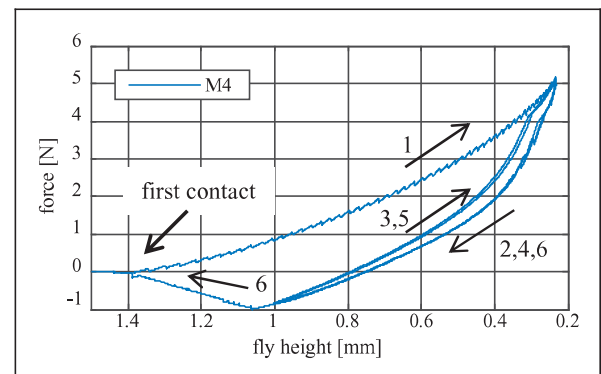


Figure 14. This figure presents the measured force of the bearing as function of its fly height. In the initial part, some force ripple can be observed that is caused by air escaping from the pocket. The repeated part of the graph shows two different stiffness values that are caused by the shape of the magnetic field. The hysteresis mainly is caused by the air transport across the inner ferrofluid seal. The numbers corresponds with the numbers of Figure 13.

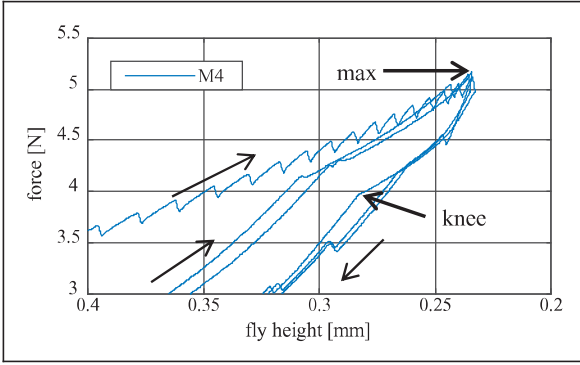


Figure 15. This figure presents a zoomed-in part of Figure 14. It can be seen that the curve shows some hysteresis. The two points of interest are the point of maximum load capacity and the knee point. The point of maximum load capacity (max) is at a force of $F_L = 5.2$ N and an fly height of $h = 0.235$ mm.

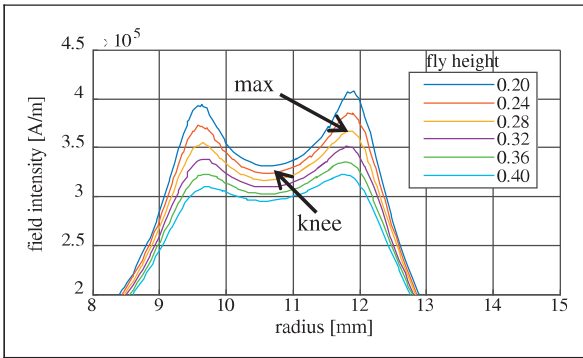


Figure 16. This figure presents the modelled magnetic field intensity as function of the radial position r for different fly heights. The point of maximum load capacity has a fly height of $h_{max} = 0.235$ mm and the knee point has a fly height of $h_{knee} = 0.28$ mm.

known fly height of the bearing and the known volume of the pocket. The fly height of the knee point can now be calculated to have the following value

$$h_{knee} = h_{max} \frac{r_{max}^2}{r_{knee}^2} = 0.235 \frac{11.8^2}{10.8^2} = 0.28 \text{ mm} \quad (15)$$

Decreasing the compression even more makes the inner fluid interface to jump over this peak to continue back down at the other side of the inner peak (Figure 16). The inner fluid interface is able to jump over this peak due to the fluid that sticks behind as can be seen from Figure 17. Fluid sticks behind due to the attracting force of the inner peak in magnetic field.

This inner peak also causes ripple in the load curve due to air escaping from the outer chamber into the inner chamber. This introduces a hysteresis like behaviour that is clearly visual in the shape of the curve presented in Figure 14. The hysteresis decreases for increasing fly height due to the



Figure 17. This figure presents the ferrofluid pocket bearing used for the experiment discussed in this section. With a glass plate, the two seals with capillary interconnection are made visible. The magnet used is the HKCM 9963-433.

decreasing contribution of the inner peak as can be seen in Figure 16.

Bearing stiffness

The stiffness of the bearing can now be validated by comparing the measured stiffness with the stiffness that is described with relation (equation (7)). The location of the knee point is now used to calculate the average measured stiffness between the two points of interest in Figure 15. This has the following value

$$k_{mes} = -\frac{F_2 - F_1}{h_2 - h_1} = \frac{5.1 - 4}{0.28 - 0.235} = 2.4 \times 10^4 \text{ N/m} \quad (16)$$

The theoretical stiffness can be calculated from the magnetic field presented in Figure 16.

$$\begin{aligned} k_{mod} &= -\mu_0 M_s A_p \frac{\Delta H_{r=11.8} - \Delta H_{r=10.8}}{h_2 - h_1} \\ &= -4\pi \times 10^{-7} \times 32 \times 10^3 \times \pi \times 0.0118^2 \frac{0.6 \times 10^5}{45 \times 10^{-6}} \\ &= 2.3 \times 10^4 \text{ N/m} \end{aligned} \quad (17)$$

The theoretical stiffness can also be calculated by using the pneumatic leverage.

$$\frac{dr_{in}}{dh} = -\sqrt{\frac{\pi \times 0.0118^2 \times 0.235 \times 10^{-3}}{4\pi(0.2575 \times 10^{-3})^3}} = -21.9 \quad (18)$$

$$\begin{aligned}
 k_{mod} &= -\mu_0 M_s A_p \frac{d(H_i - H_o)}{dr_{in}} \frac{dr_{in}}{dh} \\
 &= 4\pi \times 10^{-7} \times 32 \times 10^3 \times \pi \\
 &\quad \times 0.0118^2 \frac{0.6 \times 10^5}{1 \times 10^{-3}} 21.9 \\
 &= 2.3 \times 10^4 \text{ N/m}
 \end{aligned} \tag{19}$$

The three calculated stiffness's have a value of around 2.3×10^4 N/m, which shows that the theoretical model fits the experimental results well. This furthermore justifies the assumption of the air to be incompressible for small displacements. From Figure 7, it can be seen that the stiffness of the air is about 10 times higher than the stiffness of the seal itself. The contribution of the stiffness of the ferrofluid ring itself is low and not taken into account, so the theoretical model is actually slightly overestimating the real system.

Discussion

The experimental results of this research are in good accordance with the derived model. This shows that the proposed method provides a reasonable method to predict the load and stiffness characteristics of a ferrofluid pocket bearing. This furthermore shows that the load capacity of the bearing is mainly determined by, the magnitude of the magnetic field, the magnetization strength of the ferrofluid and the surface area of the pocket. This also shows that the stiffness of the bearing is mainly determined by the gradient of the magnetic field at the fluid interfaces, the magnetization strength of the fluid and the surface area of the pocket.

Maximizing the load and stiffness requires maximizing the different parameters they are related to or by placing multiple ferrofluid seals in series. The magnetic field strength at the fluid interfaces can be increased by using stronger magnets or by focusing the magnetic field with the use of example iron. Focusing the magnetic field has the additional effect that the gradient increases, which is beneficial for the stiffness. The compressibility of the pocket of air in the bearing is negligible for the bearing design, because the effective stiffness of the air is much larger than the stiffness of the seal. This might not be the case anymore for other designs that for example use a larger surface area of the pocket, the stiffness of bearing will in this case be predominantly determined by the stiffness of the air instead (see equation (11)).

Conclusions

The theoretical model for the maximum load capacity and the stiffness is in good accordance with the experimental results, which means that the proposed method is valid for describing the load capacity and the stiffness of a ferrofluid pocket bearing. This

method shows that the load characteristics can be directly calculated from the shape of the magnetic field and the geometry of the bearing. Comparing the theoretical model with the measurements also shows that the load and stiffness of the bearing are in general mainly determined by the sealing capacity of the seal and only partly determined by the pressure of the ferrofluid itself. The results furthermore show that having two radially distributed peaks in magnetic field intensity introduces some hysteresis in the system that might be undesirable. It has been shown that a bearing with a diameter of 24.5 mm is capable of carrying a load of approximately 8 N with a stiffness of approximately $\sim 2 \times 10^4$ N/m.

Declaration of Conflicting Interests

The author(s) declared no potential conflicts of interest with respect to the research, authorship, and/or publication of this article.

Funding

The author(s) disclosed receipt of the following financial support for the research, authorship, and/or publication of this article: Dutch TKI Maritime Funding Program.

References

1. Papell SS. Low viscosity magnetic fluids obtained by the colloidal suspension of magnetic particles. Patent 3,215,572, USA, 1965.
2. Rosensweig RE. Buoyancy and stable levitation of a magnetic body immersed in a magnetizable fluid. *Nature* 1966; 210: 613–614.
3. Rosensweig RE. Bearing arrangement with magnetic fluid defining bearing pads. Patent 3,612,630, USA, 1971.
4. Rosensweig RE. Magnetic fluid seals. Patent 3,620,584, USA, 1971.
5. Lampaert SGE, Spronck JW and van Ostayen RAJ. Friction and trail formation of a planar ferrofluid bearing. *Leeds-Lyon symposium 2016*. 6–9 September 2016.
6. Lampaert SGE. Modelling and design principles of planar ferrofluid bearings. In: *DSPE-conference 2016*, December, 2016, pp.157–158.
7. Alvarez-aguirre A, et al. Performance improvement of optical mouse sensors?: Application in a precision planar stage. *Adv Intell Mechatr* 2015; IEEE International Conference on Advanced Intelligent Mechatronic, 7–11 July 2015 in Busan, p.6.
8. Alvarez-Aguirre A, Mok G, Hosseinnia SH, et al. Performance improvement of optical mouse sensors for position measurement. In: *Euspen's international conference*, 2015, 1–5 June 2015.
9. Mok G. *The design of a planar precision stage using cost effective optical mouse sensors*. MSc Thesis, Delft University of Technology, 2015.
10. Assadsangabi B, Tee MH and Takahata K. Electromagnetic microactuator realized by ferrofluid-assisted levitation mechanism. *J Microelectromech Syst* 2014; 23: 1112–1120.

11. Assadsangabi B, Tee MH and Takahata K. Ferrofluid-assisted levitation mechanism for micromotor applications. In: *2013 Transducers eurosensors XXVII 17th international conference on solid-state sensors, actuators microsystems*, June 2013, pp.2720–2723.
12. Café M. *Nanometer precision six degrees of freedom planar motion stage with ferrofluid bearings*. MSc Thesis, Delft University of Technology, 2014.
13. van Veen S. *Planar ferrofluid bearings for precision stages*. MSc Thesis, Delft University of Technology, 2013.
14. Deng R, van Veen S, Café M, et al. Linear nano-positioning stage using ferrofluid bearings. In: *Euspen's international conference*, June 2014, p.4.
15. Lampaert SGE, Café M, van Ostayen RAJ, et al. (2+4) DOF precision motion stage with ferrofluid bearings. In: *2016 Spring meeting: Precision mechatronic system design and control*, 2016, pp.7–10.
16. Lampaert SGE, Habib H, Spronck JW, et al. XY360 planar positioning stage with ferrofluid bearings. In: *DSPE-conference 2016*, 2016, pp.57–61.
17. Ridler KD, Gosling AB and Edge GM. Linear bearing for parallel tracking arm. Patent 4,065,188, USA, 1977.
18. Huang W, Shen C and Wang X. Study on static supporting capacity and tribological performance of ferrofluids. *Tribol Trans* 2009; 52: 717–723.
19. Huang W, Shen C, Liao S, et al. Study on the ferrofluid lubrication with an external magnetic field. *Tribol Lett* 2011; 41: 145–151.
20. Lampaert SGE. *Planar ferrofluid bearings modelling and design principles*. MSc Thesis, Delft University of Technology, 2015.
21. Lampaert SGE, Spronck JW and van Ostayen RAJ. Load and stiffness of a ferrofluid pocket bearing. *17th Nordic Symposium on Tribology*. 2016, pp.1–11.
22. Hesselbach J and Abel-Keilhack C. Active hydrostatic bearing with magnetorheological fluid. In: *Proceedings of eighth international Conference on new actuators*, 2002, pp.343–346.
23. Hesselbach J and Abel-Keilhack C. Active hydrostatic bearing with magnetorheological fluid. *J Appl Phys* 2003; 93: 8441–8443.
24. Guldbakke JM and Hesselbach J. Development of bearings and a damper based on magnetically controllable fluids. *J Phys Condens Matter* 2006; 18: S2959–S2972.
25. Bayat N, et al. Technical applications. In: *Colloidal magnetic fluids SE-6*, vol. 763 (ed S Odenbach), 2009, pp.1–72. Berlin, Heidelberg: Springer.
26. Jianmei W, Jianfeng K, Yanjuan Z, et al. Viscosity monitoring and control on oil-film bearing lubrication with ferrofluids. *Tribol Int* 2014; 75: 61–68.
27. Ravaud R, Lemarquand G and Lemarquand V. Mechanical properties of ferrofluid applications: Centering effect and capacity of a seal. *Tribol Int* 2010; 43: 76–82.
28. Kuzhir P. Free boundary of lubricant film in ferrofluid journal bearings. *Tribol Int* 2008; 41: 256–268.
29. Osman TA, Nada GS and Safar ZS. Static and dynamic characteristics of magnetized journal bearings lubricated with ferrofluid. *Tribol Int* 2001; 34: 369–380.
30. Osman TA, Nada GS and Safar ZS. Effect of using current-carrying-wire models in the design of hydrodynamic journal bearings lubricated with ferrofluid. *Tribol Lett* 2001; 11: 61–70.
31. Shah RC and Bhat MV. Ferrofluid squeeze film in a long journal bearing. *Tribol Int* 2004; 37: 441–446.
32. Miwa M, Harita H, Nishigami T, et al. Frequency characteristics of stiffness and damping effect of a ferrofluid bearing. *Tribol Lett* 2003; 15: 97–105.
33. Urrreta H, Leicht Z, Sanchez A, et al. Hydrodynamic bearing lubricated with magnetic fluids. *J Intell Mater Syst Struct* 2010; 21: 1491–1499.
34. Neuringer JL and Rosensweig RE. Magnetic fluids. *Phys Fluids* 1964; 7: 1927–1937.
35. Shliomis MI. Magnetic fluids. *Uspekhi Fizicheskikh Nauk* 1974; 17(2): 153–169.

Appendix

Notation

A_p	Surface area pocket (m ²)
B_r	Remanent flux density (T)
F_L	Load capacity (N)
\vec{f}	Body force (N/m ³)
H	Magnetic field strength (A/m)
H_i	Magnetic field inner fluid interface (A/m)
H_0	Magnetic field outer fluid interface (A/m)
h	Fly height (m)
h_{knee}	Fly height at knee point (m)
h_{max}	Fly height at point of maximum load capacity (m)
k_{air}	Stiffness air (N/m)
k_{ff}	Stiffness ferrofluid bearing (N/m)
k_{mes}	Measured stiffness (N/m)
k_{mod}	Modelled stiffness (N/m)
k_{setup}	Stiffness of setup (N/m)
k_{total}	Combined stiffness (N/m)
M	Magnetization strength (A/m)
M_s	Saturation magnetization (A/m)
p	Pressure (Pa)
p_i	Pressure inside the pocket (Pa)
p_{ini}	Initial pressure (Pa)
p_0	Pressure outside the pocket (Pa)
R	Radius of magnet (m)
r	Radius/ Coordinate in-plane direction (m)
\vec{r}	Direction vector (m)
r_{in}	Radial distance of inner fluid interface (m)
r_{knee}	Radius at knee point (m)
r_{max}	Radius at point of maximum load capacity (m)
t	Time (s)
\vec{u}	Fluid velocity (m/s)
V_h	Volume of pocket for a certain fly height (m ³)
V_{ini}	Initial volume (m ³)
V_p	Volume of nonmagnetic fluid pocket (m ³)

z	Coordinate out-of-plane direction (m)	μ_{iron}	Relative permeability iron
β	Angle between magnetic field and vorticity (rad)	μ_0	Magnetic permeability of vacuum (N/A ²)
γ	Ratio of the specific heats	μ_r	Relative permeability
η	Viscosity (kg/ms)	ρ	Density (kg/m ³)



In-plane friction behaviour of a ferrofluid bearing[☆]

S.G.E. Lampaert^{*}, B.J. Fellingner, J.W. Spronck, R.A.J. van Ostayen

ARTICLE INFO

Keywords:

Precision engineering
Fluid dynamics
Magnetics
Viscous damping
Modelling

ABSTRACT

Ferrofluid bearings have been demonstrated to be very interesting for precision positioning systems. The friction of these bearings is free of stick-slip which results in an increase of precision. More knowledge on the friction behaviour of these bearings is important for their application in precision positioning systems. This paper demonstrates that the friction of a ferrofluid bearing can be modelled by a viscous damper model and provides a basic model to predict the friction behaviour of a bearing design. The model consists of a summation of a Couette flow with a Poiseuille flow such that there is no net fluid transport under the bearing pads. The model is experimentally validated on a six degrees of freedom stage using ferrofluid bearings. A stiffness in the form of a closed-loop control gain is introduced in the system to create a resonance peak at the desired frequency. The damping coefficient can be identified from the peak height of the resonance, since the peak height is the ratio of total energy to dissipated energy in the system. The results show that the newly derived model can be used to make an estimate of the damping coefficient for small (~ 1 mm) stroke translations. Furthermore, the model shows that the load capacity of a ferrofluid pocket bearing is affected during sliding.

1. Introduction

The repeatability of precision positioning systems can be improved by reducing the effects of stick-slip in system [1]. Stick-slip is the result of a spontaneous jerking motion which is introduced when overcoming the static friction coefficient between two sliding contacts. Bearing concepts like magnetic bearings, fluid bearings and flexures don't have this stick-slip effect but have other drawbacks like complexity, cost, or the storage of energy while moving.

Ferrofluid bearings, first proposed by Rosensweig et al. [2], provide a cost-effective alternative to these more conventional bearing systems. The bearing consists of a magnet and a ferrofluid that are attracted to each other forming a thin layer of ferrofluid in between the permanent magnet and the opposing bearing surface (Fig. 1).

The permanent magnet makes it a natural candidate for combination with Lorentz actuators, as demonstrated in various systems [3–15]. The result is a bearing that has distinct advantages for precision positioning systems, such as inherent stability, viscous friction, linear actuation, absence of external equipment, and no discernible stick slip effects. Furthermore, the carrier fluid can be chosen to suit the operating environment and the design allows for a compact, lightweight and cost effective solution.

Ferrofluid bearings have been successfully incorporated in precision positioning systems. Café [9,10] has built a six degrees of freedom (DoF) stage with nanometer accuracy, demonstrating that the bearing can be

used in high precision positioning systems. Mok [13], Habib [11] and van Moorsel [15] have successfully implemented ferrofluid bearings in combination with low-cost sensor solutions, to capitalize on the cost-effectiveness.

Ferrofluid bearings can be divided into pressure bearings and pocket bearings. The load capacity of a ferrofluid pressure bearing is solely developed by the pressure in the fluid developed by the magnetic body force [16]. The load capacity and stiffness behaviour of ferrofluid pocket bearings have recently been described in Refs. [17–19]. Though, this previous work does not yet include the effect of translating the bearing, nor does it describe the friction of the bearing. Due to this uncertainty that is introduced in the model, Café [9] and Habib [11] have put a large safety factor on the friction forces during the design of the system, resulting in a situation where the friction forces are dominating the disturbance forces.

This paper describes and experimentally validates a basic model of the in-plane friction behaviour of a ferrofluid bearing. It will do so by deriving a model describing the viscous damping forces of a ferrofluid bearing. The model will be experimentally validated on a demonstrator stage.

2. Theoretical bearing model

The forces that act on a ferrofluid bearing are found by deriving the flow field between two surfaces from the general Navier-Stokes

[☆] This paper was recommended by Associate Editor Gorka Aguirre.

^{*} Corresponding author.

E-mail address: s.g.e.lampaert@tudelft.nl (S.G.E. Lampaert).

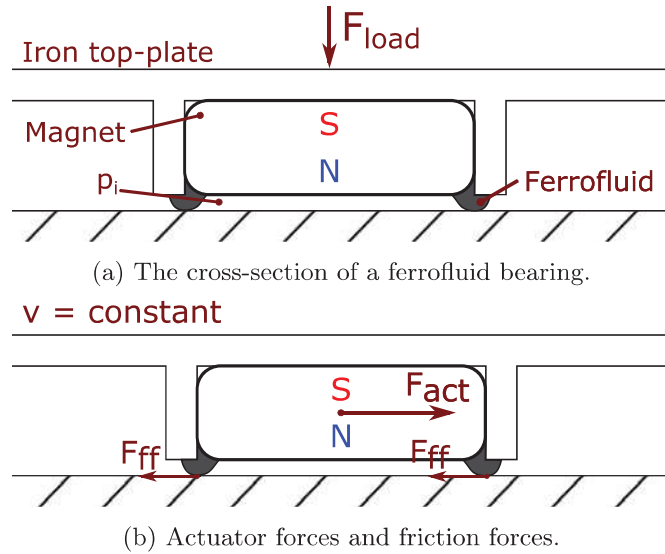


Fig. 1. a shows how a load bearing ring is created by the permanent magnet and ferrofluid, while the iron top-plate increases the magnetic field intensity at the underside. b shows the actuation force and counteracting friction forces for a constant speed.

equation. The flow field is then used to determine the shear stresses in the system which can be related to the friction forces. An analysis of the viscosity of ferrofluids is added to verify the used viscosity model.

2.1. Viscosity

The viscosity of a ferrofluid changes when subjected to a magnetic field [20]. This happens due to two different effects: rotational viscosity and particle chain formation. The following section discusses the impact of these effects on the rheology of the fluid.

2.1.1. Rotational viscosity

The effect of rotational viscosity is caused by the alignment of the particles to the magnetic field. This results in a larger effective viscosity when the vorticity is perpendicular to the magnetic field. The viscosity of the fluid using spherical particles can be modelled with the following relation that uses η_c for carrier viscosity, ϕ for volumetric concentration, β for the angle between magnetic field and vorticity, μ_0 for magnetic permeability of vacuum, m for magnetic moment of a ferrofluid particle, H for magnetic field intensity, k for Boltzmann constant and T for temperature [21].

$$\eta = \eta_c \left(1 + \frac{5}{2}\phi + \frac{3}{2}\phi \frac{\alpha - \tanh \alpha}{\alpha + \tanh \alpha} \sin^2 \beta \right)$$

$$\alpha = \frac{\mu_0 m H}{k T} \quad (1)$$

The first term of this equation presents the viscosity of the carrier fluid, the second term presents the increase in viscosity due to the suspension of particles and the third term presents the change in viscosity due to the magnetic field. For large values of α this relation has a maximum value of:

$$\eta_{max} = \eta_c \left(1 + \frac{5}{2}\phi + \frac{3}{2}\phi \right) = \eta_c (1 + 4\phi) \quad (2)$$

The viscosity of a ferrofluid is often given in the absence of a magnetic field, the relation for the viscosity then reduces to the Einstein formula [22]:

$$\eta_0 = \eta_c \left(1 + \frac{5}{2}\phi \right) \quad (3)$$

A typical value for the increase in viscosity caused by the effect of

rotational viscosity can be calculated by combining relation (2) and (3) and assuming a typical concentration of about $\phi = 8\%vol.$

$$\frac{\eta_{max}}{\eta_0} = \frac{1 + 4\phi}{1 + \frac{5}{2}\phi} = \frac{1 + 4 \times 0.08}{1 + \frac{5}{2} \times 0.08} = 1.1 \quad (4)$$

This relation shows that the increase in viscosity due to the magnetic attraction is in the order of 10%.

2.1.2. Particle chain formation

The particle chain formation, often referred to as the magneto-viscous effect [23], is the formation of chain like structures in the fluid due to the magnetic interaction between the particles. These structures are more difficult to rotate in the fluid resulting in a larger resistance to shear which results in an increase in effective viscosity [24]. Applying a magnetic field on the fluid increases the resistance to rotation even more resulting in an even further increase in viscosity. Shear forces in fluid might break the chains in the fluid resulting in a shear thinning effect. The formation of chains can be investigated by analysing the dipolar interaction parameter λ which is given with the following relation that uses M_0 for particle magnetization strength and V for particle volume.

$$\lambda = \frac{\mu_0 m^2}{4\pi k T d^3} = \frac{\mu_0 M_0^2 V}{24kT} \propto d^3 \quad (5)$$

Chain like structures will develop in the fluid when this parameter becomes larger than one. Increasing this parameter results in longer chains in the fluid [25]. The formula shows that λ increases with the diameter d of the particles resulting in only the larger particles contributing to the formation of chains. It has been shown that even a small concentration of large particles in the fluid can cause a high increase of viscosity [26]. For the models presented in this paper, it is key to choose a ferrofluid at which the dipolar interaction parameter is lower than one for all suspended magnetic particles.

2.2. Flow field

The geometry of the ferrofluid seal consists of a thin layer of fluid which is held fixed on the magnet against a moving counter surface (see Figs. 1 and 2). The derivation of the flow field starts with the general Navier-Stokes equations for incompressible Newtonian fluids, with an additional term ($\mu_0 M_s \nabla H$) describing the magnetic body forces. The assumption of a Newtonian fluid is reasonable for magnetic fluids with a small effect of rotational viscosity and a small dipolar interaction parameter λ . The relation uses \vec{u} for fluid velocity, p for pressure, η for viscosity and \vec{f} for body forces.

$$\rho \left(\frac{\partial \vec{u}}{\partial t} + \vec{u} \cdot \nabla \vec{u} \right) = -\nabla p + \eta \nabla^2 \vec{u} + \mu_0 M_s \nabla H + \vec{f}$$

$$\nabla \cdot \vec{u} = 0 \quad (6)$$

For a typical bearing application, the Reynolds number in the flow can be shown to be small as is done in the following relation that uses L for the length of the bearing, U for its speed and ρ is the density of the ferrofluid.

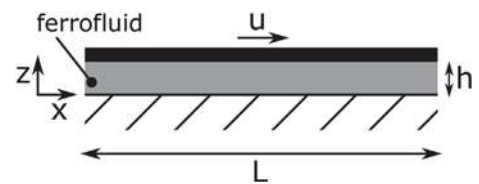


Fig. 2. Two large plates ($L \gg h$) moving with respect to each other with velocity u and separated with a ferrofluid film with height h .

$$\frac{\partial p}{\partial x} = \eta \frac{\partial^2 u_x}{\partial z^2} + \mu_0 M_s \frac{\partial H}{\partial x} \quad (9)$$

$$Re = \frac{\rho UL}{\eta} = \frac{1380 \times 10^{-3} \times 10^{-2}}{0.15} = 0.09 \ll 1 \quad (7)$$

This demonstrates that it is reasonable to neglect the inertial terms. This leads to the Stokes equation given in equation (8) where the magnetic body force is the only body force.

$$\begin{aligned} \nabla p &= \eta \nabla^2 \vec{u} + \mu_0 M_s \nabla H \\ \nabla \cdot \vec{u} &= 0 \end{aligned} \quad (8)$$

The flow field between the bearing pads is modelled as a fluid between two large parallel plates ($L \gg h$) that slide relative to each other, as shown in Fig. 2. Equation (8) can be further reduced to equation (9) by noting that the flow is parallel to the x-axis and by assuming that both the pressure and magnetic field are constant across the film height.

Equation (9) shows that the pressure is the result of the viscous forces and magnetic body forces.

$$\frac{\partial^2 u_x}{\partial z^2} = \frac{1}{\eta} \frac{\partial}{\partial x} (p - \mu_0 M H) \quad (10)$$

For the sake of simplicity, the magnetic body force and the pressure are replaced by the following substitution.

$$\frac{\partial^2 u_x}{\partial z^2} = \frac{1}{\eta} \frac{\partial p^*}{\partial x} \quad (11)$$

Integrating relation (11) twice over the height and introducing the no slip boundary conditions at $z = 0, u = 0$, and $z = h, u = U$ results in the following relation for the velocity profile:

$$u_x = \frac{1}{2\eta} \frac{\partial p^*}{\partial x} (z^2 - hz) + \frac{U}{h} z \quad (12)$$

Translating the bearing causes no net fluid transport under the bearing pads due to the magnetic body force that keeps the ferrofluid in place. This can be used to calculate a value for $\frac{\partial p^*}{\partial x}$ by setting the integral of the fluid velocity over the fly height h to zero.

$$\int_0^h u_x dz = -\frac{1}{12\eta} \frac{\partial p^*}{\partial x} h^3 + \frac{U}{h} z = 0 \quad (13)$$

and thus:

$$\frac{\partial p^*}{\partial x} = 6 \frac{\eta U}{h^2} \quad (14)$$

Which, after substituting in (12), results in the flow field:

$$u_x = 3U \frac{z}{h} \left(\frac{z}{h} - \frac{2}{3} \right) \quad (15)$$

The resulting flow field presented in equation (15) is plotted in Fig. 3. The flow field shows a summation of a Couette flow with a Poiseuille in such a way that there is no net fluid transport. The Couette flow is caused by the translational motion and the Poiseuille flow is the result of the magnetic body force.

2.3. Friction force

The friction force can be calculated by integrating the shear stress of the fluid on the bearing surface. The shear stress in the fluid is defined by the velocity gradient between the bearing surfaces and can be determined using the flow field given by relation (15).

$$\tau_{zx} = \eta \frac{\partial u_x}{\partial z} \quad (16)$$

$$= \eta \frac{\partial}{\partial z} \left[3 \frac{U}{h} \frac{z^2}{h} - \frac{2z}{3} \right] \quad (17)$$

$$= 6\eta \frac{U}{h} \left(\frac{z}{h} - \frac{1}{3} \right) \quad (18)$$

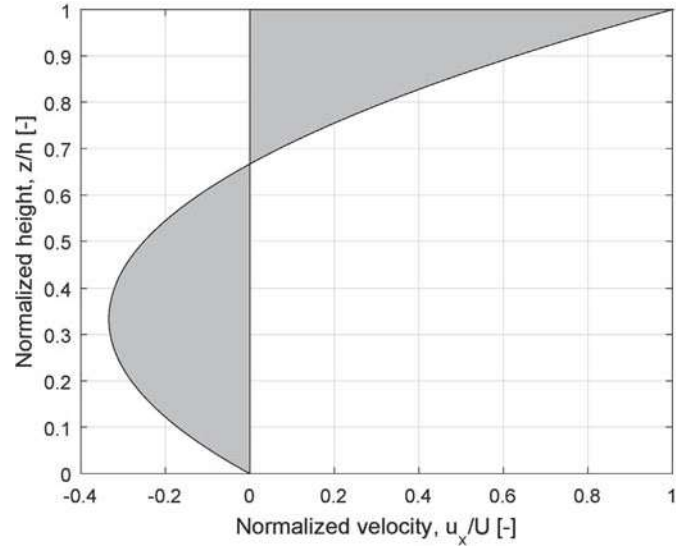


Fig. 3. This figure presents the modelled flow field of a ferrofluid bearing during a translational motion, as described in (15). A Couette flow is combined with a counteracting Poiseuille flow. The flow-field is normalized with respect to the velocity at $z = h$.

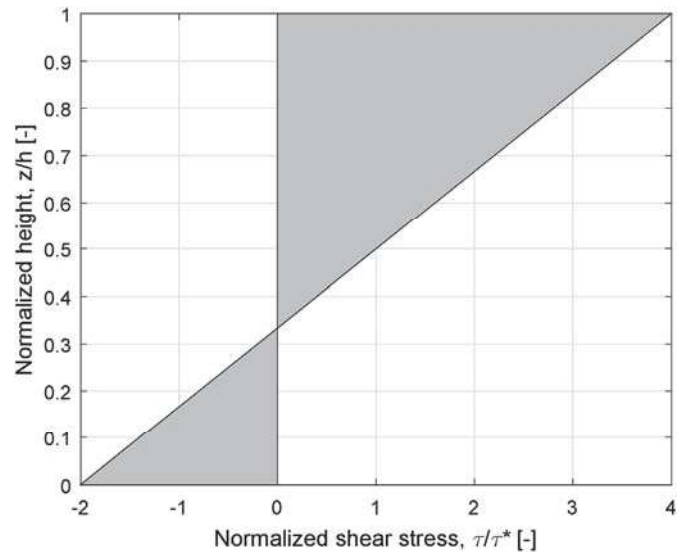


Fig. 4. This figure presents the normalized shear stress profile in-between the two bearing surfaces of a ferrofluid bearing, as described in (18). The shear stress is normalized for $\tau^* = \frac{\eta h}{U}$.

A graphical representation of the shear force in-between the two bearing pads is given by Fig. 4. The shear force at the surface of the moving bearing is defining the force on the moving surface. The value of this shear force can be calculated for a value of $z = h$.

$$\tau_{zx} = 4\eta \frac{U}{h} \quad (19)$$

The magnetic body force retaining the ferrofluid at the magnet is found in the factor four, describing the additional forces introduced. The friction at the moving surface can be calculated by integrating the shear stress over the area of the bearing surface.

$$F_{fric} = \int_s \tau_{zx} dA \quad (20)$$

$$= 4\eta \frac{UA}{h} \quad (21)$$

From equation (21) it is apparent that a ferrofluid bearing behaves like a linear viscous bearing. So the damping coefficient can be determined by dividing the friction force by the velocity.

$$c = \frac{F_{\text{fric}}}{U} = 4\eta \frac{A}{h} \quad (22)$$

2.4. Sealing capacity during translation

According to equation (11) the pressure distribution across a seal is influenced by the viscous effect during translation. A model of this effect can be developed by combining this relation with relation (14).

$$\frac{\partial}{\partial x}(p - \mu_0 M H) = 6 \frac{\eta U}{h^2} \quad (23)$$

Based on the work presented in Ref. [17], the pressure difference across a seal can now be calculated the following relation where l_{seal} is the width of the seal in the sliding direction.

$$\Delta p = \mu_0 M \Delta H - \int_0^{l_{\text{seal}}} 6 \frac{\eta U}{h^2} dx \quad (24)$$

$$= \mu_0 M \Delta H - 6 \frac{\eta U}{h^2} l_{\text{seal}} \quad (25)$$

In the case of a pocket bearing as introduced in Ref. [17], the maximum load capacity can be modelled with equation (26) where A_p stands for the surface area of the enclosed and pressurised pocket of air carrying the load. The relation shows that shows that the load capacity reduces during a translational motion.

$$F_L = \mu_0 M \Delta H A_p - 6 \frac{\eta U}{h^2} l_{\text{seal}} A_p \quad (26)$$

This relation for the load capacity of a ferrofluid pocket bearing is an extension of the relation presented in Ref. [17] for situations where the bearing is sliding with a velocity U .

3. Experimental method

The damping is both predicted based on the theory presented in the previous chapter and measured using an experimental set-up. Validation of the predicted damping coefficient with the experimental set-up is used to demonstrate that the proposed model is reasonable to predict the friction of a ferrofluid bearing or seal.

3.1. Damping coefficient prediction

Based on the theory presented in the previous chapter, the damping coefficient can be predicted by measuring the viscosity, contact surface area and fly height of the bearing. The fly height is measured by taking a foto of the air-gap with a scale next to it. The known scale length is used as a reference in the photograph and related to the length of a single pixel. Then by using a pixel counter the air-gap is measured at several points. The contact area is measured by resting the moving mass against two endstops on a white acrylic sheet. The mass is removed and the imprint left by the bearings is photographed next to a known scale. The length of a pixel is derived from the scale and the resulting surface area is measured using the software ImageJ.

3.2. Experimental set-up

The experimental validation will be performed on an improved version of the (2 + 4) degrees of freedom stage of Cafe et al. [9,10]. This is a system that can do large translational motions in x- and y-direction while having the other four degrees of freedom constrained through closed-loop control (Fig. 5). The system is chosen because the different parameters defining the dynamic behaviour (mass, damping and stiffness) are properly defined. The mass is solely defined by the

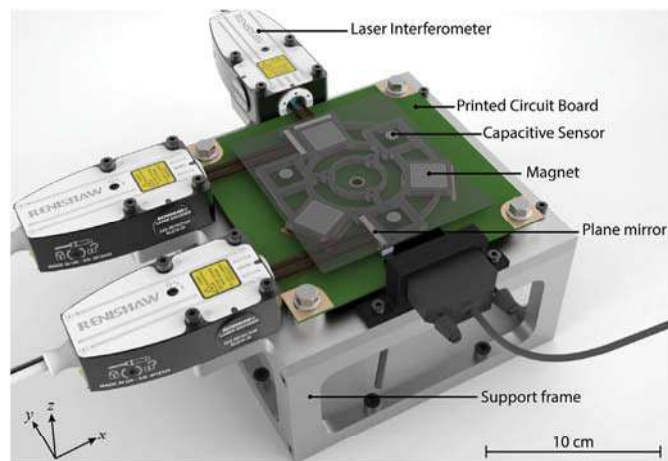


Fig. 5. An overview of the general layout of the demonstrator stage on which the experimental validation will be performed. In this figure the moving mass is opaque to better showcase the internal components. The magnets are mounted on the moving mass and are used as a ferrofluid bearing and magnetic field source for actuation. The PCB contains the force generating coils. The in-plane measurements are done with three laser interferometers and the out-of-plane measurements are done with three capacitive sensors underneath the moving mass. The plane mirrors are used as a reference for the laser interferometer and mounted on the moving mass. The support frame is mounted on a vibration isolation table.

moving mass of the system, the damping is solely defined by the friction of the ferrofluid bearings and the stiffness is solely defined by the applied control stiffness.

The moving mass is used as a reference for the sensors and contains three square magnets, as shown in Fig. 5. The magnets provide the magnetic field both for the ferrofluid bearing and Lorentz actuation. The stage has an in-plane movement range of 10mmx10 mm and the rotation is constrained through control action.

The system has six sensors to sense the principal degrees of freedom of a rigid body. The in-plane motions and rotation are measured by interferometers and the out-of-plane motion and tilts are measured by capacitive sensors. The in-plane position is limited by the sensor resolution of 10 nm. The position is controlled with a bandwidth of 200Hz, while the rotation is controlled with 100Hz. The out-of-plane motions and tilts are measured by three capacitive sensors limited by the noise level of 2.54 nm at a sampling frequency of 10 kHz. They are constrained through closed-loop control using three out-of-plane Lorentz actuators and with a bandwidth of 200 Hz.

The actuation is performed by two sets of three Lorentz actuators embedded in a multi-layered PCB. Fig. 6 shows how the coils are configured to create resultant in-plane and out-of-plane forces for a non-uniform magnetic field. The in-plane control actuation has a motor constant of 0.145 NA^{-1} . The motor-constant of the experimental set-up is determined with a load-cell test in the direction of the movement. The test is conducted by applying a current to the in-plane coils, such that the moving mass enacts a force in line with the load cell. The current is increased to map the data points, which are then fitted to find the motor constant.

The closed-loop system is identified by supplying a pseudo random white noise signal with an amplitude of 1 to 10 μm at the input. The input and output signals are measured for 300s and used to construct the FRF according to Welch's method [27].

The moving mass has a fly height of $0.18 \pm 0.05\text{mm}$ corresponding to a volume of 0.2 mm ferrofluid per bearing and a total weight of 0.185kg. It is supported by three square ferrofluid bearings using the magnet Q-20-20-05-N from Supermagnete.

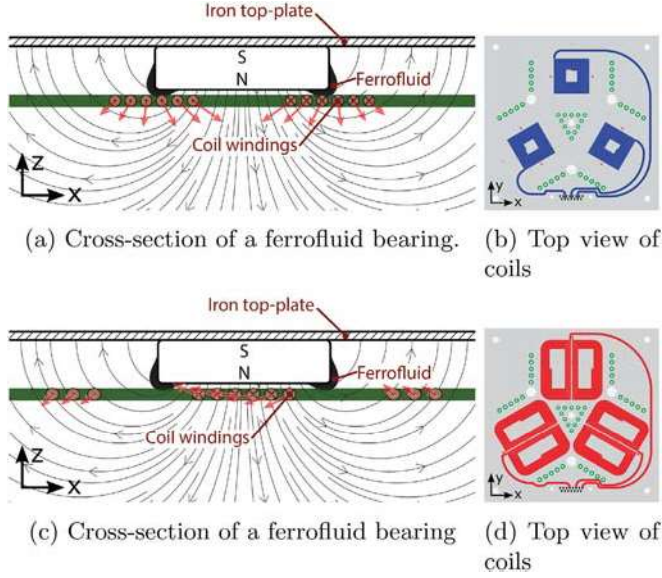


Fig. 6. The coils create a resultant out-of-plane(6a) and in-plane(6c) force as a result of the Lorentz forces and designed coil configuration. Fig. 6d and b shows the coil configuration from a top-view, with the three coil-sets corresponding to three ferrofluid bearings.

3.3. Damping coefficient by dynamic response

The system can be described as a mass-spring-damper system with transfer function (27), using the results from section 2.3 that a ferrofluid bearing behaves like a linear viscous damper. Where the mass is denoted as m , the damping coefficient as c and the stiffness value as k .

$$\frac{X_o(s)}{F(s)} = \frac{1}{ms^2 + cs + k} \quad (27)$$

Fig. 7 shows the response of the system described by equation (27) in the case of an over- and underdamped mass-damper-spring system. At low frequencies the stiffness of the system will determine the dynamic behaviour, while at high frequencies the inertia of the moving mass will dominate. The damper-line limits the resonance peak height, by dissipating energy as a result of the damping forces.

The value of system parameters can be determined by finding the pole locations in the frequency response function(FRF). According to equation (27), the pole location of the damping is described by equation (28).

$$\omega_{cm} = \frac{c}{m} \quad (28)$$

However, the ferrofluid bearing system is underdamped, with a pole expected at approximately 0.5Hz. The identification through a FRF suffers from limits in exposure time and assumptions made in the signal processing, leading to inaccurate measurements at low frequencies. Therefore a control stiffness k is added to the system expanding it to a mass-spring-damper system as presented in Fig. 7.

The damping coefficient can be expressed in system parameters according to (29). It is now expressed in one known parameter, mass; one chosen parameter, stiffness; and one unknown parameter, damping ratio.

$$c = 2\zeta\sqrt{km} \quad (29)$$

The damping ratio can be related to the Q-factor, which can be defined as the ratio of stored energy to dissipated energy.

$$\zeta = \frac{1}{2Q} \quad (30)$$

Combining (29) and (30) gives:

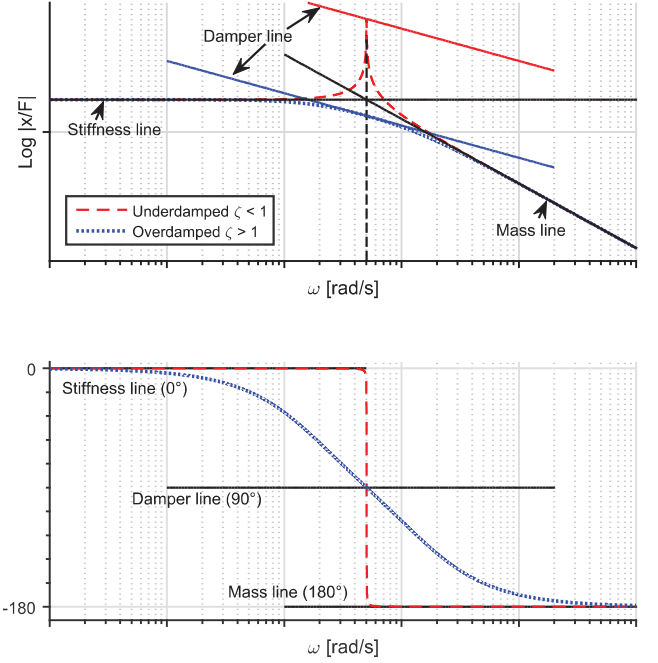


Fig. 7. This figure shows a typical response for an underdamped ($\zeta < 1$) and an overdamped ($\zeta > 1$) mass-spring-damper system. At low frequencies the stiffness of the system dominates, while at high frequencies the inertia dominates. The amplitude of the resonance is related to the dissipated energy of the system, a result of the damping forces.

$$c = \frac{\sqrt{km}}{Q} \quad (31)$$

For measurement purposes the Q-factor can be defined as the frequency-to-bandwidth ratio of the resonator, where f_r is the resonant frequency and Δf is the full width at half maximum(FWHM) bandwidth.

$$Q = \frac{f_r}{\Delta f} \quad (32)$$

In the system used for this research, stiffness is created by adding a control gain(K_p) in the closed-loop control scheme. Fig. 8 shows the block diagram of a typical closed-loop feedback controller, where $G(s)$ is the plant model and K_p the control stiffness. The transfer function describing the response of this system is shown in (33).

$$\frac{X_o(s)}{X_i(s)} = \frac{G(s)C(s)}{1 + G(s)C(s)} \quad (33)$$

The plant of a ferrofluid bearing can be modelled as a mass-damper system and the closed-loop transfer function becomes (34).

$$\frac{X_o(s)}{X_i(s)} = \frac{K_p}{ms^2 + cs + K_p} \quad (34)$$

Which can be rewritten in the form of (27), by noting that $F(s) = K_p X_i(s)$.

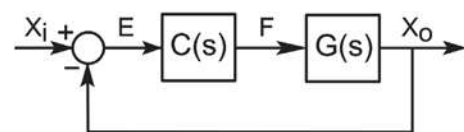


Fig. 8. The block diagram of closed-loop feedback control, with plant model $G(s)$ and controller gain K_p . $X_i(s)$ is the reference signal, $E(s)$ is the error signal, $F(s)$ is the plant input signal and $X_o(s)$ is the output signal.

Table 1

This table shows the measured parameters and modelled in-plane damping coefficient of a ferrofluid bearing. The damping coefficient is calculated according to (22).

	Quantity	Value
System:	η [kgm ⁻¹ s]	$150 \pm 15 \times 10^{-3}$
	A [m ²]	$220 \pm 10 \times 10^{-6}$
	h [m]	$0.18 \pm 0.05 \times 10^{-3}$
	c [Nsm ⁻¹]	2.2 ± 0.8

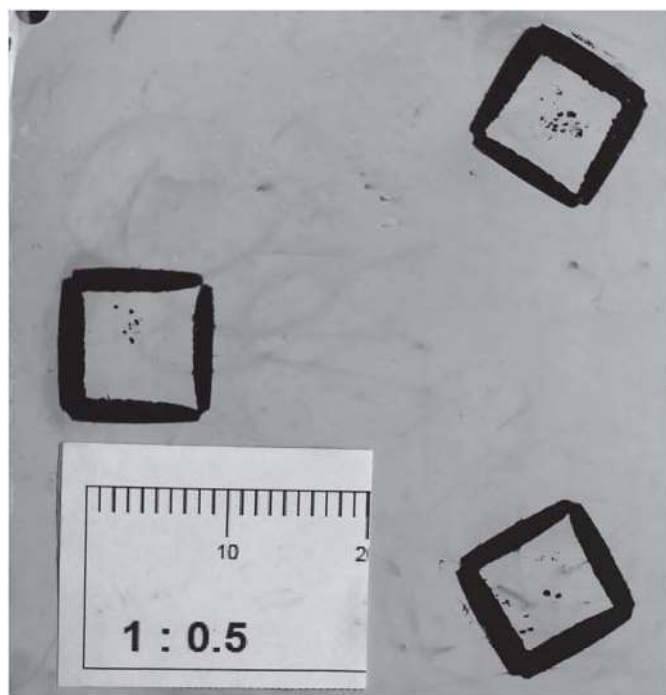


Fig. 9. The imprint left by the ferrofluid bearings on a smooth surface compared to a 1:0.5 mm scale. In this image the red and green has been filtered out to increase contrast between the ferrofluid and background.

$$\frac{X_o(s)}{F(s)} = \frac{X_o(s)}{K_p X_i(s)} = \frac{1}{ms^2 + cs + K_p} \quad (35)$$

The Q-factor can now be measured according to (32).

4. Results

The damping coefficient that is calculated using equation (22), is presented in Table 1 together with the different values that are used to calculate the coefficient (see Fig. 9 for surface area). The predicted damping coefficient for the three bearings in the system is $2.2 \pm 0.8 \text{ Nsm}^{-1}$.

Fig. 10 shows the frequency response for closed-loop control stiffness values, ranging from 5×10^3 up to $30 \times 10^3 \text{ Nm}^{-1}$. Fig. 11 shows the different damping coefficients corresponding to the different control stiffnesses shown in of Fig. 10. Fig. 12 shows the effect of different input amplitudes on the damping coefficient for a constant stiffness. The measured damping coefficient of the complete system based on the dynamic response is found to be $2.97 \pm 0.45 \text{ Nsm}^{-1}$.

5. Discussion

From the measured dynamic behaviour of the system presented in Fig. 10, it has been shown that the system can be considered to be a perfect mass-spring-damper system. At low frequencies the response

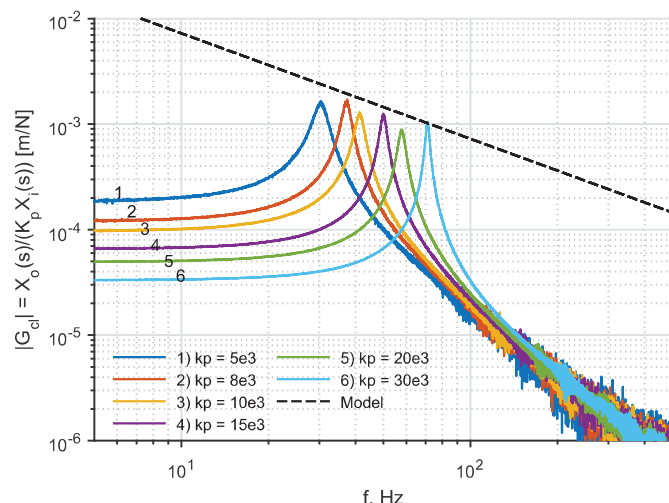


Fig. 10. The frequency response of the closed-loop system with added control stiffness K_p . The black dotted line resembles the modelled damping coefficient. The peaks being close to the black dotted lines demonstrates that the model is in line with the measurements.

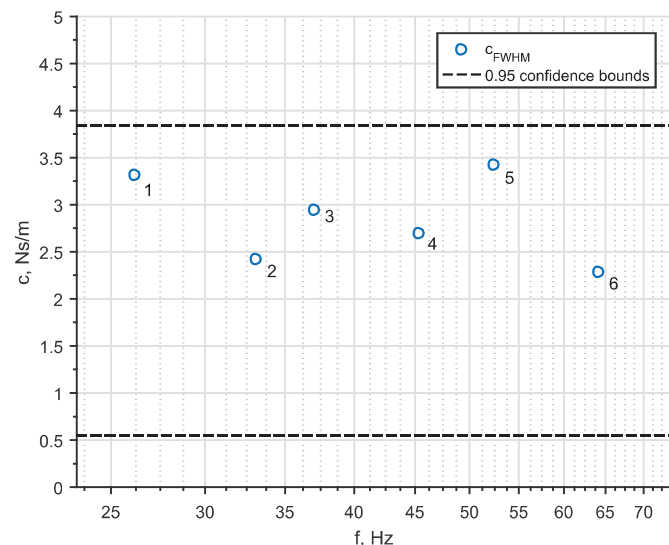


Fig. 11. The damping coefficient determined via FWHM are displayed as a function of the resonance bandwidth. The dotted line represent the 0.95 confidence bound of the model. The numbers correspond with the measurement labels of Fig. 10.

converges to the applied control stiffness, while at high frequencies the responses converge to the inertia of the mass. In-between, a resonance peak is present of which the peak height decays as would be expected from a viscous damper model.

The uncertainty of the modelled damping coefficient presented in Fig. 11 is the result of multiple measurement uncertainties. The figure furthermore shows no non-linearities in the trend or magnitude of the damping coefficients. Some differences can be explained by the assumed constant viscosity, which is not necessarily the case for a ferrofluid [20]. Fig. 12 shows that the damping coefficient stays constant for constant stiffness and varying input amplitude and therefore varying input sliding velocity. This altogether demonstrates that the assumption of a constant viscosity for a ferrofluid bearing is fair under these conditions.

The peak heights in Fig. 10 scales with the stiffness as expected over the measured region. This implies that the damping coefficient stays constant for the used input amplitudes and stiffness. However, the

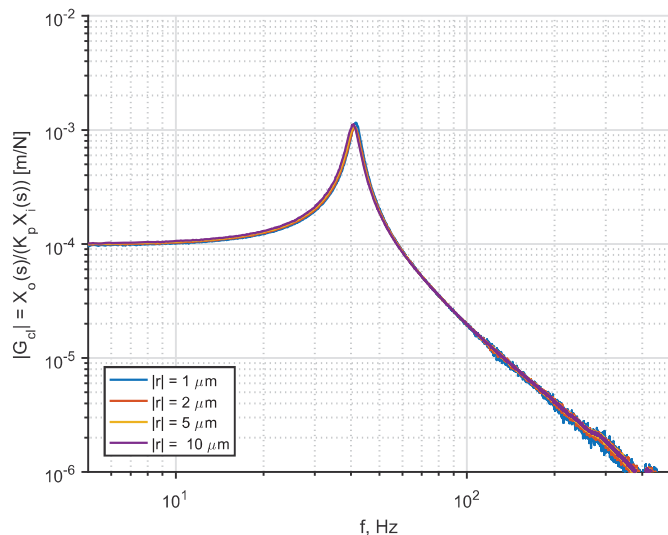


Fig. 12. The effect of a variation in the input signal amplitude on the frequency response with a constant stiffness of $K_p = 10 \times 10^3$. The amplitude varies from 1 up to $10 \mu\text{m}$. This proves the linearity for 1– $10 \mu\text{m}$.

measured damping constant is systematically higher than the modelled coefficient. This implies that a systematic error or another undescribed effect occurs in the method of determining the modelling parameters. A likely candidate for a systematic error is the fluid film thickness, due to the small distance and lack of stiff connection.

The results are measured for stroke lengths up to $\sim 1 \text{ m}$, as a result the maximal input amplitude of $10 \mu\text{m}$ with a maximal Q-factor of ~ 100 . So for large stroke ($\ell \gg 1 \text{ mm}$) additional experiments need to be performed.

The theoretical bearing model presented in this paper requires that the magnetic body force is strong enough to keep the ferrofluid in place. For large speeds, it might be possible that the body force is not large enough to pull back the fluid. In the case of a ferrofluid pocket bearing, this results in leakage of air through the seal, resulting in a permanent change in fly height.

6. Conclusion

A ferrofluid bearing is a low-cost, relatively simple, concept that has been proven to have no discernible stick-slip effects and is therefore well suited for precision positioning systems.

The model as presented in Ref. [17] is expanded to include the magnetic body force, ensuring a Poiseuille flow counteracting the Couette flow resulting in no significant fluid-loss during motion. The resulting flow field is used to derive the in-plane damping coefficient of a ferrofluid bearing. A ferrofluid bearing has no in-plane stiffness, by adding a control stiffness its dynamic behaviour can be modelled as a mass-damper-spring system.

The ferrofluid bearings in the identified system behave like a linear viscous damper for the utilized input amplitudes. Although the viscosity is non-linear as a function of the speed, the expanded model proves a valid approach at quantifying the damping coefficient of a ferrofluid bearing.

The validity of the friction model demonstrates that the load capacity is affected by the translational motion of the bearing. The magnetic body force used for creating load capacity is then additionally used for keeping the fluid in place. This results in a lower net load capacity during translation. It is important to take this effect into account during the design of the bearing.

The presented model allows for better design of precision positioning systems using FF bearings.

Acknowledgements

This research has been supported by the Dutch TKI maritime funding program.

Appendix A. Supplementary data

Supplementary data related to this article can be found at <https://doi.org/10.1016/j.precisioneng.2018.05.013>.

References

- [1] Garagić Denis, Srinivasan Krishnaswamy. Adaptive friction compensation for precision machine tool drive. *Contr Eng Pract* 2004;12(11):1451–64. <https://doi.org/10.1016/j.conengprac.2003.10.006>. ISSN 09670661.
- [2] Rosensweig Ronald E. Bearing arrangement with magnetic fluid defining bearing pads. 1971.
- [3] Ridler Keith Douglas, Gosling Alexander Bennet, Edge Gordon Malcom. Linear bearing for parallel tracking arm. 1977.
- [4] Sudo Seiichi, Takaki Yuji, Hashiguchi Yasunari, Nishiyama Hideya. Magnetic fluid devices for driving micro machines. *JSME International Journal Series B* 2005;48(3):464–70. <https://doi.org/10.1299/jsmeb.48.464>. ISSN 1340-8054.
- [5] Uhlmann E, Bayat N. High precision positioning with ferrofluids as an active medium. *CIRP Ann - Manuf Technol* 2006;55(1):415–8. [https://doi.org/10.1016/S0007-8506\(07\)60448-X](https://doi.org/10.1016/S0007-8506(07)60448-X). ISSN 00078506.
- [6] Simon van Veen. Planar ferrofluid bearings for precision stages. PhD thesis, MSc thesis, Delft University of Technology; 2013.
- [7] Assadsangabi B, Tee MH, Takahata K. Ferrofluid-assisted levitation mechanism for micromotor applications. *Transducers & eurosensors XXVII: the 17th international conference on solid-state sensors. Actuators and Microsystems*; 2013. p. 2720–3.
- [8] Assadsangabi Babak, Tee Min Hian, Takahata Kenichi. Electromagnetic micro-actuator realized by ferrofluid-assisted levitation mechanism. *Journal of Microelectromechanical Systems* 2014;23(5):1112–20. <https://doi.org/10.1109/JMEMS.2014.2305112>.
- [9] Café Max. Nanometer precision six degrees of freedom planar motion stage with ferrofluid bearings Master thesis Delft University of Technology; 2014
- [10] Georges Stefan, Lampaert Emile, Café Max, Ostayen Ron A J van, Spronck Jo W. (2+4) DOF precision motion stage with ferrofluid bearings 2016 Spring Meeting: Precision Mechatronic System Design and Control 2016. p. 7–10.
- [11] Habib Haris. Design of a three Degrees of Freedom planar precision stage using a single Position Sensitive Detector Master thesis Delft University of Technology; 2015
- [12] Georges Stefan, Lampaert Emile, Habib Haris, Spronck Jo W, Ostayen Ron A J van. XY360 planar positioning stage with ferrofluid bearings. *DSPE-Conference* 2016. 2016. p. 57–61.
- [13] Mok Gihin. The design of a planar precision stage using cost effective optical mouse sensors. Msc thesis, Delft University of Technology; 2015.
- [14] Alvarez-Aguirre Alejandro, Mok Gihin, Hassan HosseinNia S, Spronck Jo. Performance improvement of optical mouse sensors: application in a precision planar stage. 2016 international conference on manipulation, automation and robotics at small scales, MARSS 2016 2016. <https://doi.org/10.1109/MARSS.2016.7561698>.
- [15] van Moorsel Len. A planar precision stage using a single image sensor. Msc thesis, Delft University of Technology; 2017.
- [16] Huang Wei, Shen Cong, Wang Xiaolei. Study on static supporting capacity and tribological performance of ferrofluids. *Tribol Trans* 2009;52(5):717–23. <https://doi.org/10.1080/10402000902913337>. ISSN 1040-2004 <http://www.tandfonline.com/doi/abs/10.1080/10402000902913337>.
- [17] Georges Stefan, Lampaert Emile. Planar ferrofluid bearings modelling and design Principles Msc thesis, MSc thesis Delft University of Technology; 2015
- [18] Georges Stefan, Lampaert Emile, Spronck Jo W, Ostayen Ron A J van. Load and stiffness of a ferrofluid pocket bearing. *The 17th nordic symposium on tribology*. 2016. p. 11.
- [19] Lampaert SGE, Spronck JW, van Ostayen RAJ. Load and stiffness of a planar ferrofluid pocket bearing. *Proc IME J J Eng Tribol* 2018;232(1):14–25. <https://doi.org/10.1177/1350650117739200>. ISSN 1350-6501 <http://journals.sagepub.com/doi/10.1177/1350650117739200>.
- [20] Odenbach Stefan. Magnetoviscous and viscoelastic effects in ferrofluids. *Int J Mod Phys B* 2000;14(16):1615–31. <https://doi.org/10.1142/S0217979200001692>. ISSN 0217-9792.
- [21] Shliomis MI. Effective viscosity of magnetic fluids. *Sov Phys - JETP* 1972;24(6):1291–4. ISSN 00319015.
- [22] Albert Einstein. On the motion of small particles suspended in a stationary liquid, as required by the molecular kinetic theory of heat. *Ann Phys* 1905;322(8):549–60. <https://doi.org/10.1002/andp.19053220806>. ISSN 1521-3889.
- [23] Odenbach Stefan, Thurm Steffen. Magnetoviscous effects in ferrofluids. In: Odenbach Stefan, editor. *Ferrofluids SE - 10*, volume 594 of *lecture Notes in physics*. Springer Berlin Heidelberg; 2002. p. 185–201. ISBN 978-3-540-43978-3 https://doi.org/10.1007/3-540-45646-5_10.
- [24] Odenbach Stefan, Störk H. Shear dependence of field-induced contributions to the viscosity of magnetic fluids at low shear rates. *J Magn Magn Mater* 1998;183(12):188–94. [https://doi.org/10.1016/S0304-8853\(97\)01051-2](https://doi.org/10.1016/S0304-8853(97)01051-2). ISSN

0304-8853 <http://www.sciencedirect.com/science/article/pii/S0304885397010512>.

- [25] Jordan Peter C. Association phenomena in a ferromagnetic colloid. *Mol Phys* January 2015;25:961–73. <https://doi.org/10.1080/00268977300100821>. 1973. ISSN 0026-8976.
- [26] Yu Zubarev Andrey, Odenbach Stefan, Fleischer J. Rheological properties of dense ferrofluids. Effect of chain-like aggregates. *J Magn Magn Mater* 2002;252(0):241–3. ISSN 0304-8853 [https://doi.org/10.1016/S0304-8853\(02\)00674-1](https://doi.org/10.1016/S0304-8853(02)00674-1)<http://www.sciencedirect.com/science/article/pii/S0304885302006741>.
- [27] Welch Peter D. The use of fast fourier transform for the estimation of power spectra: a method based on time averaging over short, modified periodograms. *IEEE Trans Audio Electroacoust* 1967;AU-15(2):70–3.

TASTINGS AND THEORY

AUTHORS' NOTE

Stefan G.E. Lampaert (Ph.D. candidate), Ron A.J. van Ostayen (assistant professor) and Jo W. Spronck (associate professor) are all part of the Mechatronic System Design research group of the Department of Precision and Microsystems Engineering at Delft University of Technology, the Netherlands.

s.g.e.lampaert@tudelft.nl
www.pme.tudelft.nl

Ferrofluid bearings have recently been successfully implemented in precise positioning systems. This article gives an overview of systems built in the Department of Precision and Microsystems Engineering at Delft University of Technology in the Netherlands. Most applications are in microscope stages, where high accuracy is important while stroke and speed attain only moderate levels. Furthermore, some basic theory is provided on ferrofluid bearings that can help engineers incorporate ferrofluid bearings in their designs.

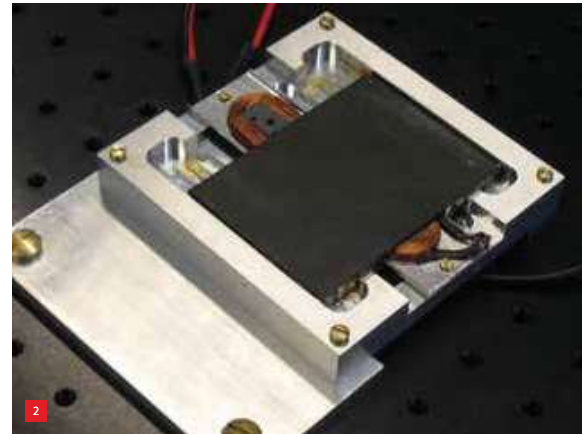
STEFAN LAMPAERT, RON VAN OSTAYEN AND JO SPRONCK

A ferrofluid is a type of fluid with magnetic properties, and its most important property is that it is attracted by a magnet (Figure 1). This is due to the tiny magnetic nanoparticles about 10 nm in size suspended in the fluid.

Ferrofluids can be used to make bearings that generally differentiate themselves from other bearings by their simplicity, low cost, inherent stability, viscous damping with low friction and absence of stick slip [1] [2]. These characteristics make ferrofluid bearings a low-cost alternative in systems with a moderate stroke and speed that are currently using air bearings or magnetic bearings to achieve similar specifications.

Precise positioning systems

The first in the Delft series of precise positioning systems with ferrofluids was built by M.Sc. student Simon van Veen (Figure 2) [4]. The primary goal of his work was to understand and demonstrate the behaviour of ferrofluid



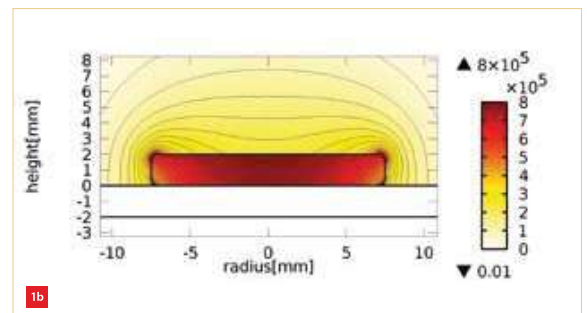
1 Ferrofluid bearing principle.

(a) A disc magnet with ferrofluid on a steel plate. The ferrofluid (black) is drawn towards the highest magnetic field strength, at the edge of the magnet. The disc positioned in the centre is the magnet.

(b) The associated magnetic field. The colours show that the magnetic field intensity is highest at the corners of the magnet, which confirms that the ferrofluid follows the contour lines of the magnetic field. The model was made using COMSOL Multiphysics® [3].

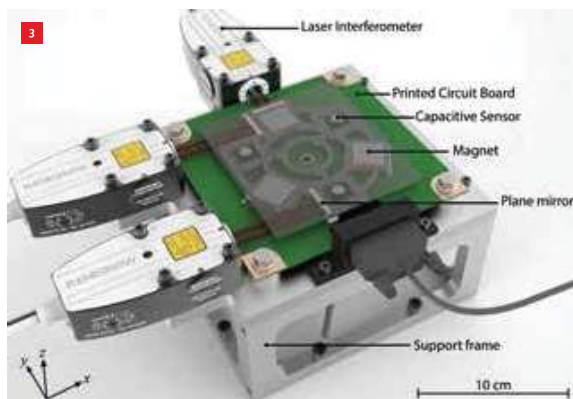


2 Overview of the 1-DoF positioning system built by Simon van Veen [4]. The black body in the middle is the dynamic part of the system. The system is actuated electromagnetically; the coil is visible underneath the black body.



THEME – PRECISION APPLICATIONS OF FERROFLUID BEARINGS

3 Overview of the (2+4)-DoF positioning system built by Max Café [5]. A printed circuit board with coils is used to actuate the magnets placed on the moving part of the system. The magnets are additionally used to create a ferrofluid bearing. Three laser interferometers and three capacitive sensors are used to measure the position and orientation of the system.

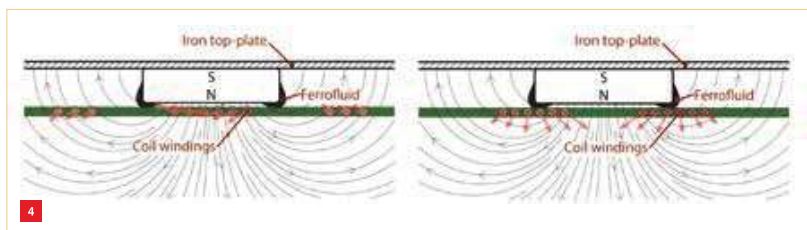


4 The actuation system of Figure 3 consists of three magnets and six coils in a PCB board: two layers contain coils for the out-of-plane actuation and two layers contain the coils for the in-plane actuation. Both sets of coils use the same magnet, which is also used to hold the ferrofluid for the bearing [5].

DoFs (Figure 3). In this system, the magnets fulfil a dual role: they hold the ferrofluid for the bearing function and they provide the magnetic field for the coils of the 6-DoF Lorentz actuators (Figure 4).

The primary goal in this instance was to understand and demonstrate the behaviour of the ferrofluid bearings in a multi-DoF positioning system. An additional goal was to solve the problem of so-called trail formation of the bearing. When moving, the ferrofluid bearing leaves behind a trail of ferrofluid on the contact surface that reduces the amount of ferrofluid actually used in the stage's support. This causes the bearing to slightly decrease in fly height, i.e. 2 μm per mm translation for this system. This decrease in fly height can be compensated for by active control of the Lorentz actuators. The final system was able to take in-plane steps of 0.1 mm with a control bandwidth of 500 Hz with a 1% settling time of 0.02 s, and out-of-plane steps of 250 nm with a bandwidth of 100 Hz with a 1% settling time of 0.1 s.

5 Renderings of the planar 2-DoF positioning system built by Gihin Mok [6]. (a) Overview of the complete stage. (b) The base.

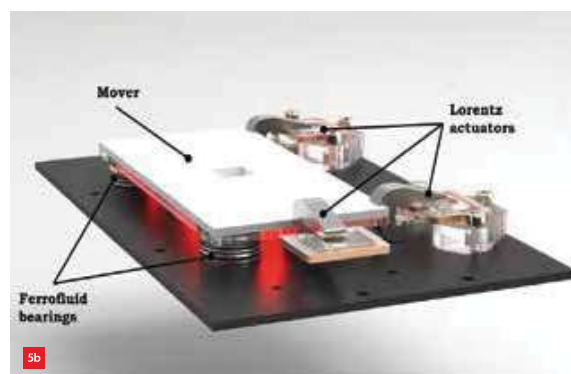
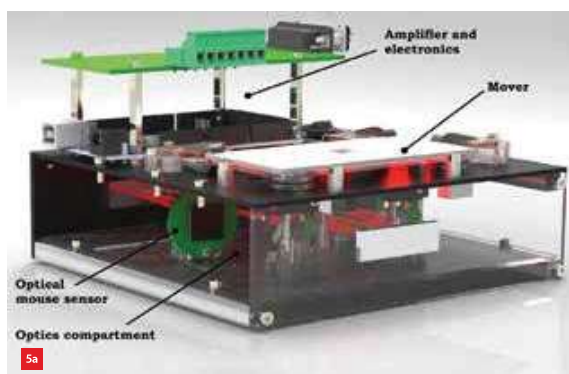


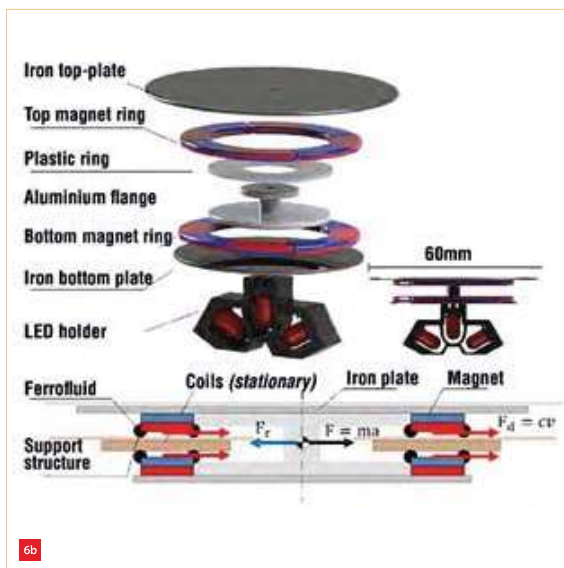
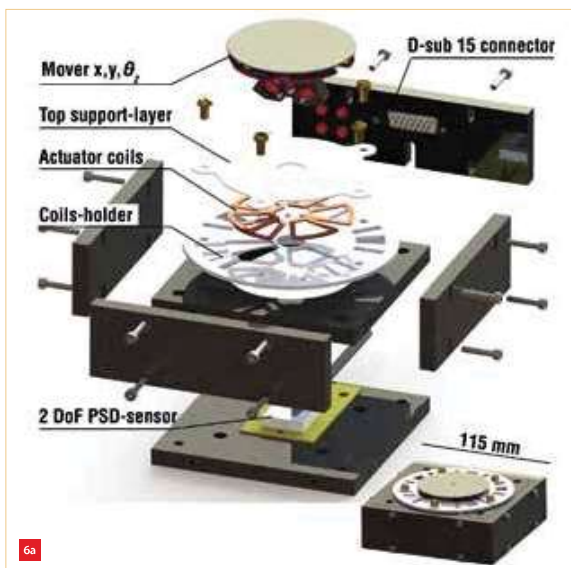
The system's planar performance was mainly limited by the performance of the actuator and the sensors, and not by the performance of the bearings. This showed that the ferrofluid bearing is an interesting concept for high-speed precise positioning in multiple DoFs. It also showed that good system integration can be achieved by using the magnets required for Lorentz actuation to also generate the magnetic field used in the ferrofluid bearings.

The successful completion of these projects created a certain confidence in the properties of ferrofluid bearings. As a result, ferrofluid bearings have been used in subsequent projects as a simple bearing solution in positioning systems. One such example is Gihin Mok's project [6], which examined the potential of using a low-cost optical mouse sensor for a positioning sensor. A full stand-alone positioning system with two DoFs was realised, using three ferrofluid bearings to accommodate planar movements only (Figure 5).

A second example is Haris Habib's project [7], in which an XY360 3-DoF positioning system was designed, built and tested. Here, the goal was to demonstrate the concept of measuring a planar position and orientation with a 2-DoF optical position-sensitive detector (PSD) (Figure 6). The sensor and actuation system allowed for a full rotation in combination with a translational range of 9 mm x 9 mm.

The final system was able to take planar steps of 0.1 mm with a settling time of less than 0.1 s and with an accuracy of 0.2 μm (3σ). A rotational step of 10° took 0.18 s to settle with an accuracy of 0.15 mrad (3σ). The speed of the system was mainly limited by the friction in the bearings. This friction was apparently higher than was modelled using the basic model developed in advance. This eventually caused excessive heat to develop during operation.





6 Renderings of the XY360 3-DoF positioning system built by Haris Habib [7].

(a) Overview.
 (b) Cross-section showing two LEDs used to sequentially illuminate the PSD so that the location and the orientation can be measured, and a third LED used to increase the range of motion.

7 The 3-DoF (XYθ) positioning system built by Len van Moorsel [10].

The moving part of the system contains magnets that are used for the ferrofluid bearing and the Lorentz actuator. The other half of the Lorentz actuator consists of a PCB board in which coils have been etched.

(a) Overview showing the black body in the middle as the moving part of the system.

(b) Rendered cross-section showing the image sensor, located underneath the black body, used for contactless optical measurement of the position of the system.

For this reason, a new project was launched by Stefan Lampaert, the aim of which was to draw up improved theoretical models to be used for generating an accurate prediction of the bearing properties (see below) [8]. This work resulted in validated models that accurately describe the load and stiffness of ferrofluid bearings. A friction model directly derived from these improved models was later validated in [2] [9] by a redesign of the system presented in [4] to obtain an accurate measurement for the friction of the bearings.

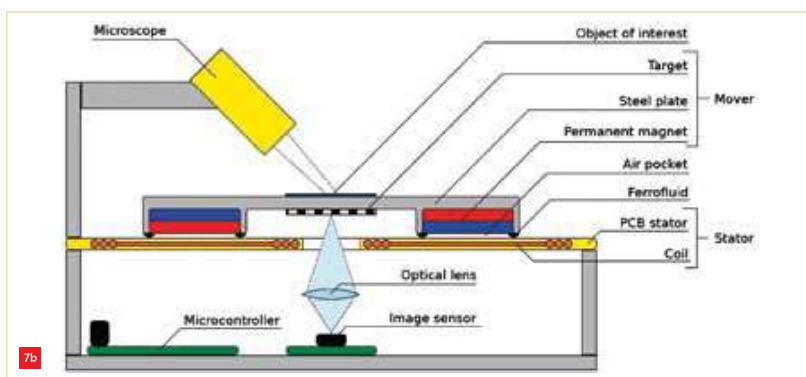
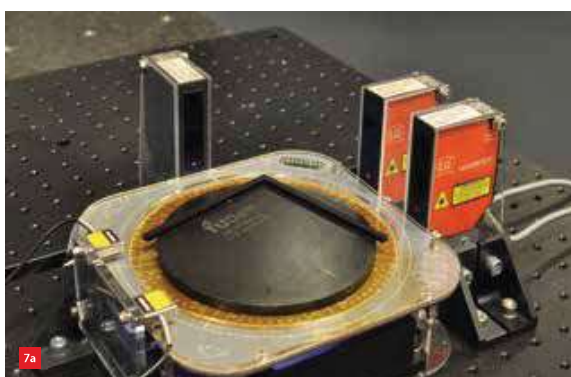
A third example in which ferrofluid bearings and an improved understanding of their functioning has been used is Len van Moorsel's project. Here, the newly derived models of ferrofluid bearings were used in the design of a 3-DoF precise positioning system using fully contactless vision with a single image sensor as position sensor [10]. The final system had a mover that could be actuated in all the in-plane DoFs; commutation of the Lorentz actuators made it possible to make infinite rotations (Figure 7). All the remaining DoFs were constrained using a ferrofluid

bearing. The theoretical models facilitated a more balanced design between actuator and bearing so that no excessive heat developed during operation.

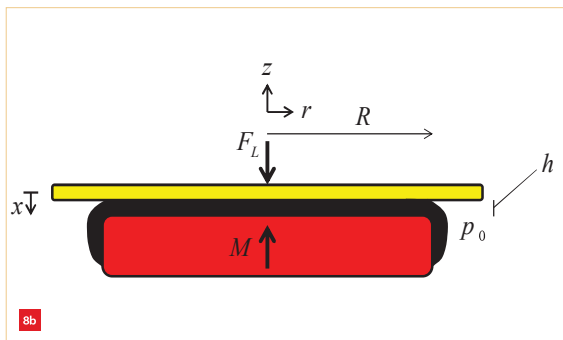
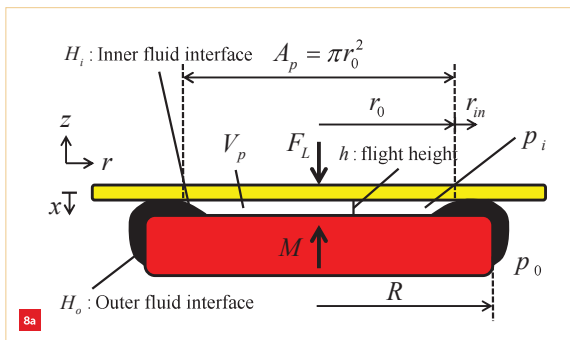
Basic theory

A ferrofluid can basically be used in two different types of bearings [11] [12]. In both bearing types, the ferrofluid acts as a lubricant and a load-carrying component, even at zero speed. The first bearing type is the so-called ferrofluid pocket bearing that encapsulates a pocket of air to carry a load (Figure 8a). The second one is a so-called pressure bearing that works solely by floating the mover on a layer of magnetically pressurised ferrofluid (Figure 8b).

The load capacity of a pocket bearing ($F_{L,pocket}$) is generally a function of the surface area of the pocket of air A_p and the pressure difference that is built up across the seal. This pressure difference is a function of the magnetisation strength of the fluid (M) and the difference in field intensity between the inner fluid interface (H_1) and the outer fluid interface (H_0). The load capacity of a ferrofluid pressure



THEME - PRECISION APPLICATIONS OF FERROFLUID BEARINGS



- 8 Schematic representation of two types of ferrofluid bearing [8].
- (a) Pocket bearing: the load is carried by an encapsulated pocket of air.
- (b) Pressure bearing: the load is floated on a layer of magnetically pressurised ferrofluid.
- 9 Translating the bearing leaves behind a trail of ferrofluid [8].
- 10 Fluid flow profile with no net fluid transport along the length of the bearing [8].

bearing ($F_{L,pressure}$) is solely defined by the pressure built up in the fluid due to the magnetic field at the load-carrying surface of the bearing.

$$F_{L,pocket} = \mu_0 M A_p (H_i - H_o)$$

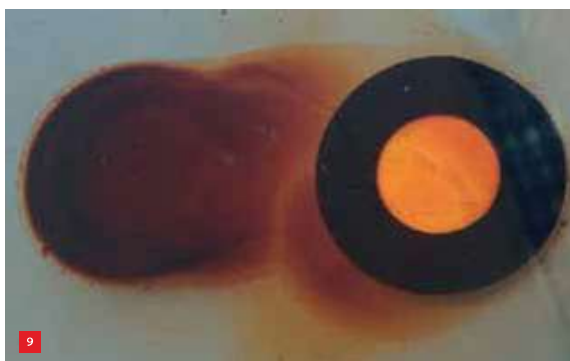
$$F_{L,pressure} = \mu_0 M \int H dA$$

The stiffness for a pocket bearing (k_{pocket}) is mainly defined by the change in pressure across the seal with a change in fly height. This means that this stiffness is mainly defined by the gradient of field intensity across the seal. In general, only the inner fluid interface contributes to the stiffness. The term dr_o/dz in the formula below is called the pneumatic leverage and relates to the movement of the inner fluid interface with the change in fly height. The stiffness for a ferrofluid pressure bearing ($k_{pressure}$) is mainly defined by the gradient in the magnetic field at the load-carrying surface.

$$k_{pocket} = -dF_{L,pocket} / dz = -\mu_0 M A_p (dH_i / dr_o) (dr_o / dz)$$

$$k_{pressure} = -dF_{L,pressure} / dz = -\mu_0 M \int (dH / dz) dA$$

Translating the bearing leaves behind a trail of ferrofluid that has three effects on the bearing's performance (Figure 9). The first is a reduction in fly height due to a reduced load capacity caused by less fluid being available for levitation. The second is an increase in damping due to the reduced fly height. The third effect is a time- and path-



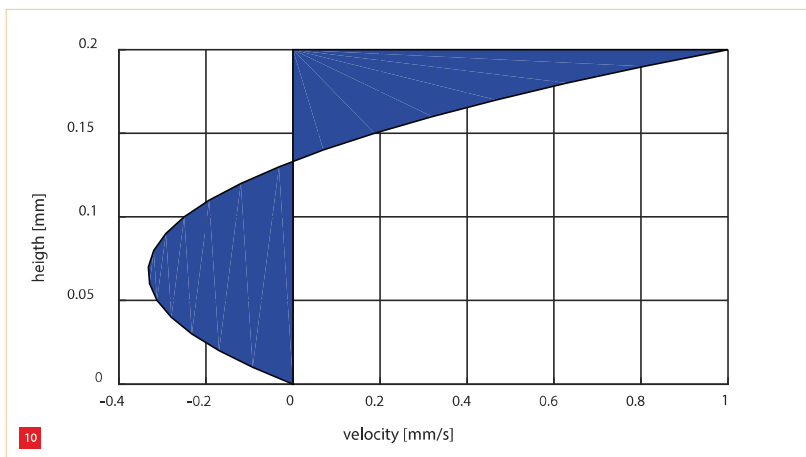
dependent force between the ferrofluid trail and the magnet. Upon translation of the bearing, it appears that the majority of the fluid remains between the bearing surfaces.

This means that there is a fluid flow with no net fluid transport along the length of the bearing. Figure 10 presents the flow profile that meets this condition. This flow profile basically consists of the summation of a Couette flow caused by the relative movement of the bearing surfaces and a Poiseuille flow caused by the magnetic body force. The model is validated by the work presented in [2] [9]. The viscous-like friction force can be described as follows:

$$F_{fric} = c U = 4 \eta (A / h) U$$

Conclusion

The various systems described in this article demonstrate that ferrofluids can provide a simple and cost-effective bearing solution for high-precision positioning. The models presented can be used in the design of ferrofluid bearings. The equations show that the magnitude of the magnetic field is important for the load capacity, while the gradient of the magnetic field is important for the stiffness. The model for the friction shows that the bearing can be taken as a pure viscous damper.



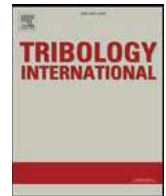
Current and future developments

What started as a simple research project on ferrofluid bearings is now growing into a new research area at Delft University of Technology. Projects have been started that focus on the application of magnetic fluids in different industries. These projects now also include the application of magnetorheological fluids, a type of non-Newtonian magnetic fluid that becomes more viscous in response to a magnetic field. Applications currently being investigated include seals, large-scale bearings and active dampers. ■

REFERENCES

- [1] S.G.E. Lampaert, J.W. Spronck, and R.A.J. van Ostayen, "Load and stiffness of a planar ferrofluid pocket bearing", *Proc. Inst. Mech. Eng. Part J J. Eng. Tribol.*, vol. 232 (1), pp. 14-25, 2018.
- [2] S.G.E. Lampaert, B.J. Fellingner, J.W. Spronck, and R.A.J. Van Ostayen, "In-plane friction behaviour of a ferrofluid bearing", *Precis. Eng.*, under review, 2018.
- [3] www.comsol.com
- [4] S. van Veen, "Planar Ferrofluid Bearings for Precision Stages", M.Sc. thesis, Delft University of Technology, 2013.
- [5] M. Café, "Nanometer precision Six Degrees of Freedom Planar Motion Stage with Ferrofluid Bearings", M.Sc. thesis, Delft University of Technology, 2014.
S.G.E. Lampaert, M. Café, R.A.J. van Ostayen, and J.W. Spronck, "(2+4) DOF precision motion stage with ferrofluid bearings", *2016 Spring Meet. Precis. Mechatron. Syst. Des. Control*, pp. 7-10, 2016.
- [6] G. Mok, "The design of a planar precision stage using cost effective optical mouse sensors", M.Sc. thesis, Delft University of Technology, 2015.
A. Alvarez-Aguirre, G. Mok, S.H. Hosseinnia, and J.W. Spronck, "Performance improvement of optical mouse sensors for position measurement", *euspen Int. Conf.*, 2015.
A. Alvarez-Aguirre, G. Mok, S.H. Hosseinnia, and J.W. Spronck, "Performance improvement of optical mouse sensors: Application in a precision planar stage", *2016 Int. Conf. Manip. Autom. Robot. Small Scales, MARSS 2016*, 2016.
G. Mok, "Mouse precision", *Mikroniek*, vol. 56 (6), pp. 14-18, 2016.
- [7] H. Habib, "Design of a three Degrees of Freedom planar precision stage using a single Position Sensitive Detector", M.Sc. thesis, Delft University of Technology, 2015.
S.G.E. Lampaert, H. Habib, J.W. Spronck, and R.A.J. van Ostayen, "XY360 planar positioning stage with ferrofluid bearings", *DSPE Conference on Precision Mechatronics 2016*, pp. 57-61, 2016.
- [8] S.G.E. Lampaert, "Planar Ferrofluid Bearings Modelling and Design Principles", M.Sc. thesis, Delft University of Technology, 2015.
S.G.E. Lampaert, J.W. Spronck, and R.A.J. van Ostayen, "Load and Stiffness of a Ferrofluid Pocket Bearing", *17th Nord. Symp. Tribol.*, p. 11, 2016.
S.G.E. Lampaert, J.W. Spronck, and R.A.J. van Ostayen, "Friction and trail formation of a planar ferrofluid bearing", *Leeds-Lyon Symp. 2016*, 2016.
S.G.E. Lampaert, "Modelling and Design Principles of planar ferrofluid bearings", *DSPE Conference on Precision Mechatronics 2016*, pp. 157-158, 2016.
- [9] B.J. Fellingner, "Validation of in-plane friction behaviour of a ferrofluid bearing", M.Sc. thesis, Delft University of Technology, 2017.
- [10] L. van Moorsel, "A planar precision stage using a single image sensor", M.Sc. thesis, Delft University of Technology, 2017.
L. van Moorsel, N. Saikumar, H. Polinder, and J.W. Spronck, "Axial Flux Permanent Magnet Motor Design for 30mm Planar Translations and Infinite Rotation", *IEEE Trans. Ind. Electron.*, under review, 2018.
- [11] R.E. Rosensweig, "Bearing arrangement with magnetic fluid defining bearing pads", U.S. Patent 3,612,630, 1971.
- [12] K.D. Ridler, A.B. Gosling, and G.M. Edge, "Linear bearing for parallel tracking arm", U.S. Patent 4,065,188, 1977.

Appendix A3



Increasing the load capacity of planar ferrofluid bearings by the addition of ferromagnetic material

A.S.T. Boots, L.E. Krijgsman, B.J.M. de Ruiter, S.G.E. Lampaert*, J.W. Spronck

Department of Precision and Microsystems Engineering, Delft University of Technology, Mekelweg 2, 2628CD, Delft, the Netherlands

ARTICLE INFO

Keywords:

Precision engineering
Hydrostatic bearing
Mathematical modelling
Magnetics
Optimization

ABSTRACT

Ferrofluid pocket bearings are a type of bearing that are able to carry a load using an air pocket encapsulated by a ferrofluid seal. Previously designed ferrofluid bearings show the great potential of the stick-slip-free and low viscous friction bearings, however until now the load capacity is limited. In this article a method is presented to increase the load capacity in a simple and cost effective way by the addition of ferromagnetic material around the magnet. First, a mathematical model of the bearing is presented and is validated by experiments using an axially magnetized ring magnet surrounded by two steel rings. The model is used to optimize the dimensions of the added ferromagnetic material for maximum load capacity. Depending on the fly height, the load capacity has been increased by a factor three to four by the addition of steel rings to the ferrofluid pocket bearing configuration.

1. Introduction

The kerosene based magnetic fluid or so called ferrofluid that NASA developed in the 1960s appeared to be interesting to apply in seals and bearings as shown by Rosensweig et al. in the 1970s [1–4]. A ferrofluid can be defined as a fluid with paramagnetic properties that are generated by being a colloidal suspension of small magnetic nanoparticles (10 nm) [5,6]. The application of an external magnetic field increases the pressure inside the fluid after which the fluid is capable of carrying loads [7–9], thus can act as an actuator [10–16] or seal [17–21]. Ferrofluid can be used to yield mechanisms that have complete absence of both stick slip and mechanical contact resulting respectively a potential high precision and high lifetime [7,8,22,23].

Because the fluid in ferrofluid bearings is contained by the presence of a magnetic field that is generated by for example a permanent magnet, no seals or active components are required. Therefore, a ferrofluid bearing is a passive, simple, and cost effective alternative to traditional bearings. Examples of these ferrofluid bearings can be found in literature, but despite the great potential, application is still very limited [7–9,24–29]. One reason for this is that the load capacity and stiffness is relatively limited. Lampaert et al. recently developed a mathematical model to describe the load and stiffness characteristics of ferrofluid bearings, which makes it now possible to design for maximum load capacity [7,8,22,23,26,30–33].

The load capacity of a ferrofluid bearing is created by the

pressurized air pocket(s) encapsulated by the ferrofluid seals. The shape of the magnetic field and the number of air pockets between non-connected seals seem to be of great importance to the load capacity. The goal of this article is to increase the load capacity of ferrofluid bearings by the addition of ferromagnetic material.

The addition of ferromagnetic material, in this case steel, has the ability to concentrate the magnetic field generated by the permanent magnet and could therefore increase the load capacity [34,35]. Furthermore, steel could alter the shape of the magnetic field such that multiple air pockets can be created. Steel has a high magnetic saturation and a high relative permeability which makes this material suited for improving the load capacity.

First, a model is presented to calculate the load capacity of a ferrofluid double pocket bearing. This model is validated by experiments and will then be used to optimize the geometries of the steel rings. The acquired knowledge can be used as design rules for increasing the load capacity of planar ferrofluid bearings by the addition of ferromagnetic material.

2. Methods

First, an analytical model for the load capacity of a ferrofluid double pocket bearing is presented based on the available literature. Second, the four different bearing models, model A through D, are presented after which the FEM analysis, using COMSOL Multiphysics, is

* Corresponding author.

E-mail address: s.g.e.lampaert@tudelft.nl (S.G.E. Lampaert).

<https://doi.org/10.1016/j.triboint.2018.07.048>

Received 7 May 2018; Received in revised form 18 July 2018; Accepted 30 July 2018

Available online 01 August 2018

0301-679X/ © 2018 The Authors. Published by Elsevier Ltd. This is an open access article under the CC BY-NC-ND license

(<http://creativecommons.org/licenses/by-nc-nd/4.0/>).

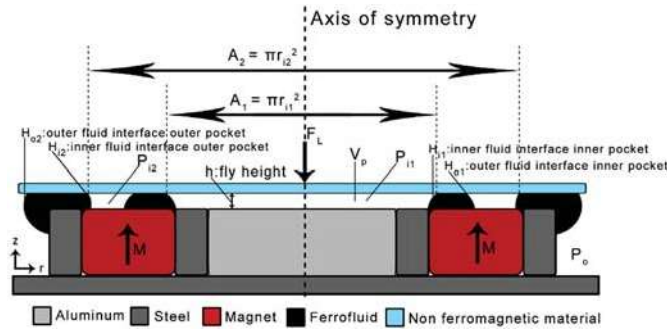


Fig. 1. This figure presents the cross section of the ferrofluid bearing with the defined parameters. The ring magnet is surrounded by two ferromagnetic rings, in this case steel, with an aluminum disk placed inside. The entire setup is mounted on a steel baseplate. Important parameters are the pressures and areas of the air pockets and the magnetic field intensities at the different fluid interfaces.

introduced to calculate the magnetic field intensities. These magnetic field intensities in combination with the analytical model are used to calculate the load capacity. Next, the experimental setup used for the validation of the described model is presented after which the optimizations of models A-D are described.

2.1. Analytical model

The analytical model for a ferrofluid single pocket bearing [8,9,24] is extended to a model predicting the load capacity of a ferrofluid double pocket bearing, schematically represented in Fig. 1. The Navier-Stokes equations for incompressible magnetic Newtonian fluids can be simplified to equation (1) assuming a stationary, low Reynolds number incompressible flow with a Newtonian fluid model. The relation presents the pressure gradient ∇p as the product of the magnetic permeability of vacuum μ_0 , the magnetization strength of the fluid M_s and the magnetic field gradient ∇H .

$$\nabla p = \mu_0 M_s \nabla H \quad 1$$

Application of the Fundamental theorem of calculus gives the relationship used for calculating the load capacity of the air pockets,

equation (2).

$$F_{pocket} = \int_A (p_i - p_0) dA_{pocket} = \mu_0 M_s \Delta H A_{pocket} \quad 2$$

Both the pressure inside the air pocket and the pressure inside the ferrofluid ring contribute to the total load capacity of the bearing. Although the load carrying contribution of the seal is relatively small in comparison to that of the pocket, it will be included in the calculation to get the most accurate prediction of the total load capacity. Equation (3) shows the approximation of the load capacity of the seal as described by Lampaert et al. [7].

$$F_{seal} = \int_A (p_s - p_0) dA_{seal} \approx \mu_0 M_s \Delta H \frac{A_{seal}}{3} \quad 3$$

For a bearing configuration with two seals and two pockets the total load capacity is simply obtained by adding the load capacities of both pockets and both seals. Each contribution to the total load capacity is calculated by integrating the pressure difference over the area, as can be seen in equation (4). This is visually shown in Fig. 5, where the load capacities of the ferrofluid bearing for the magnet only and for the magnet with steel rings correspond to the orange and red surface respectively. The pressure distribution is a result of the magnetic field intensities of the fluid-air interfaces (H_{i1} H_{i2} H_{o1} H_{o2}), see Fig. 1. By integrating this pressure distribution, the total load capacity is calculated.

Implementation of a second ferrofluid seal has the advantage that the pressure can be increased twice, one time over each ferrofluid seal. It is important to note that the pressure contribution of the doughnut shaped second pocket, A_{p2} , as given in equation (4) can be rewritten to equation (5), in which the pressure contributions of both pockets act on a circular surface as defined in Fig. 1. To illustrate this, the pressure distribution which is given in Fig. 5 corresponds to the magnetic field intensities at the interfaces between ferrofluid and air, given in Fig. 4.

$$F_{load} = \int (p_{i1} - p_0) dA_{p1} + \int (p_{s1} - p_0) dA_{s1} + \int (p_{i2} - p_0) dA_{p2} + \int (p_{s2} - p_0) dA_{s2} \quad 4$$

$$F_{load} \approx \mu_0 M_s \left((H_{i1} - H_{o1}) \left(A_1 + \frac{A_{s1}}{3} \right) + (H_{i2} - H_{o2}) \left(A_2 + \frac{A_{s2}}{3} \right) \right) \quad 5$$

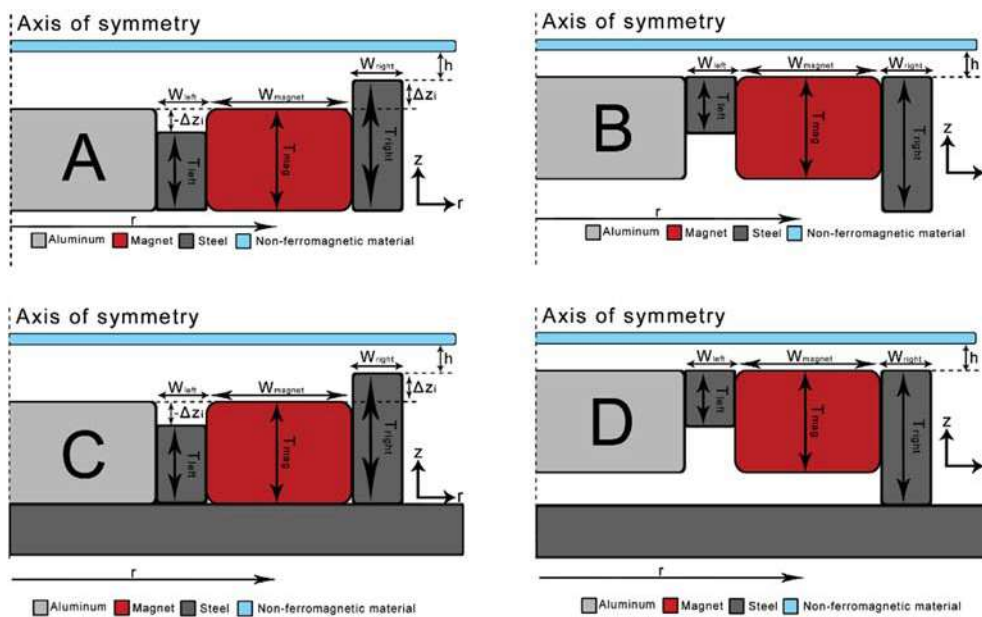


Fig. 2. This figure presents the four different bearing models and their design variables. In contrast to Model C and D, model A and B have no ferromagnetic baseplate. Model A and C are defined from bottom up and model B and D are defined from top down.

Table 1

This table presents a list of variables which are considered to be constant for the different bearing models A-D.

Optimization constants Optimization: Constants	
M_s	= 35 kA/m
μ_0	= $4\pi \cdot 10^{-7} \text{N/A}^2$
W_{mag}	= 8.5mm
T_{mag}	= 6mm
T_{base}	= 3mm
h_{fly}	= 0.2mm
$B_{saturation,steel}$	= 2.4T
M_{magnet}	= 1.25T
p_0	= 10^5Pa

2.2. Bearing models

There are four distinct bearing models presented in this section, which will be referred to as model A, model B, model C and model D (Fig. 2). In all the models the ring magnet is sandwiched between two steel rings with varying widths and thicknesses. Both steel rings are attached to the magnet such that no volume exists between the steel rings and magnet.

The variables which are considered to be constant during the optimization of the bearing models A-D can be found in Table 1.

In model A the rings are fixed with respect to the bottom surface of the magnet. The thickness of the steel rings is defined with T_{left} and T_{right} and the width of the steel rings is defined with W_{left} and W_{right} . An additional parameter Δz_i is defined in equation (6), in which T_i indicates the thickness of the steel rings for either the left or right side.

$$\Delta z_i = T_i - T_{mag} \quad 6$$

It can be concluded from the results of the model presented in section 3.2 that the top surface of the steel rings has to be at equal height as the surface of the magnet such that no steel protrudes beyond the thickness of the magnet. Therefore, model B is introduced. The steel rings are now fixed with respect to the top surface of the magnet and extended downwards.

To investigate the influence of a ferromagnetic baseplate on the load capacity, model C and D are introduced. Model C and D correspond to model A and B respectively, however with a 3 mm steel plate added. The baseplate is directly attached underneath the lowest part of the ferrofluid bearing (Fig. 2).

2.3. FEM analysis and load calculation

The magnetic fields generated by the different bearing configurations are calculated using the numerical analyses package COMSOL 5.3. The magnetic field intensity at the different fluid-air interfaces (H_{i1} H_{i2} H_{o1} H_{o2}) have to be evaluated in order to calculate the total load capacity according to equation (5).

The low grade steel of the rings surrounding the magnet is modelled by using the BH curve from the soft iron (with losses) material in the COMSOL library. Fillets are constructed at all the corners to prevent singularities in the calculations [36]. The model and the result of a single simulation example can be seen in Fig. 3 and Fig. 4. This example corresponds to model C as defined in Fig. 2. The bearing models are parameterized and controlled by Matlab (2017b) using the Livelink toolbox to find an optimal geometry.

The distribution of the magnetic field given in Fig. 3 is evaluated along a horizontal line at a specified height above the highest surface of the bearing, the so called fly height as defined in Fig. 1. An example of this line evaluation is given in Fig. 4 and is used to extract the magnetic strengths of the different interfaces. The ferrofluid will position itself at maximum load such that the inner fluid interfaces H_{i1} and H_{i2} are located at the maximum field intensities thus the peak values of Fig. 4.

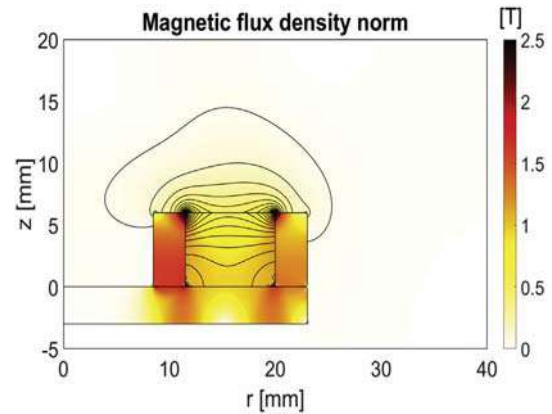


Fig. 3. This figure presents the distribution of the magnetic field expressed in Tesla for the bearing testing setup of model C consisting of the ring magnet, steel rings and baseplate. The magnet is modelled after HKCM 9963–58947 with an axial magnetization strength of 1.25 T. The magnetic behaviour of the steel rings and baseplate is modelled in COMSOL using the built-in BH-curve of soft iron.

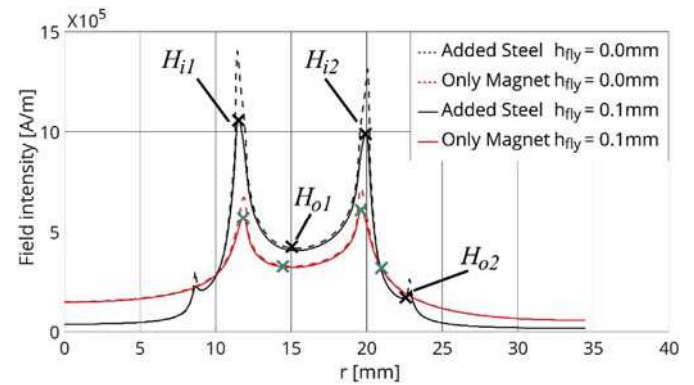


Fig. 4. This figure presents the results of the FEM analysis for the magnetic field intensities, at 2 different fly heights, for the ring magnet (40 mm × 23 mm X 6 mm) with and without the addition of 3 mm × 6 mm steel rings. The magnetic flux density of the magnet is 1.25 T.

H_{o1} is evaluated at the valley between the peaks in the middle of the magnet at a fly height of zero. When the value of H_{o1} is bigger than either H_{i1} or H_{i2} , one seal and one air pocket is created. This comes from the fact that the fluid flows to the outer interface when the peak at a certain fly height is lower than the lowest value of the field intensity at the magnet ($h=0$). The load capacity is then calculated with only the first part of equation (5). When both peaks are higher than the lowest field intensity at the magnet, two seals are created and both terms in equation (5) are taken into account. H_{o2} is evaluated at the fluid interface of the outer seal for a certain fly height. When the flyheight decreases, the ferrofluid seal is pushed outwards. For the magnet only, the outer interface of the ferrofluid seal increases from a radial distance of 21 mm–21.2 mm for fly heights of 1 mm–0 mm respectively. When steel rings are added, the radial distance of the outer interface remains 21.5 mm for a fly height of 1 mm, but increases to the radial distance of the outer steel ring at a fly height of 0 mm due to the steel rings. These values are observed experimentally and are interpolated linearly.

The radial position of the different field intensities are used to calculate the areas of the seals and the pockets. Finally, the load capacity of the bearing is calculated by combining the different field intensities with the corresponding areas and substituting this in equation (5).

To summarize, the FEM model (Fig. 3) is used to calculate the magnetic field produced by the magnet. This field is then evaluated to obtain the field intensities (Fig. 4), which can be used to calculate the

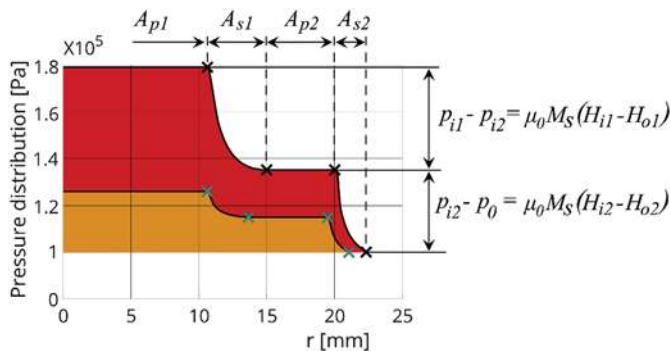


Fig. 5. This figure presents the pressure increase over the ferrofluid seals for both the magnet and the magnet with steel rings. The total load capacities for the magnet only and for the magnet with steel rings are indicated as the red and orange area resp. (For interpretation of the references to colour in this figure legend, the reader is referred to the Web version of this article.)

corresponding pressure distribution (Fig. 5) using the presented analytical model. Finally, the load capacity is obtained by integrating the pressure distribution of the area, indicated by the red area in the figure. Note that in Fig. 5 the pressure distribution and load capacity for the magnet only and for the magnet with steel rings are presented.

2.4. Experimental setup

The analytical model presented in section 2.1 is validated by comparing the predicted load capacity of the bearing with and without steel rings to the results of the measurements. Measurements are done to investigate the maximum load capacity of the bearing and validate the analytical model.

2.4.1. Load capacity

The maximum load capacity of the bearing with and without steel is measured using a tensile testing machine (Zwick/Roell Z005) capable of measuring the force over displacement. To prevent systematic errors, the machine is calibrated before measuring the load capacity. Each measurement is done three times to detect possible random errors. The velocity of the head of the testing machine is set to be 1 mm/min.

The bearing is mounted on top of a steel base plate, which corresponds to bearing model C (Fig. 2), and clamped on the table below the machine, see Fig. 6. Both the rings and the baseplate are made of low grade steel in the test setup, since the material is relatively cheap and has desirable ferromagnetic properties, which approximates the material used in the analytical model. There is assumed that the stiffness of the table is infinite with respect to that of the bearing. Moreover, the mounting is assumed to be rigid. Note that the volume inside the

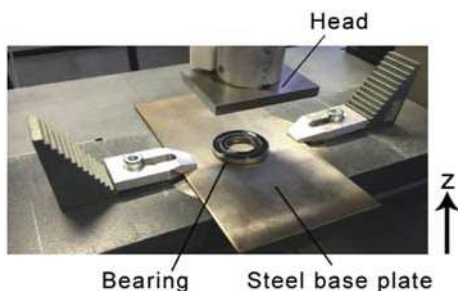


Fig. 6. This figure presents the bearing consisting of a ring magnet, two steel rings and ferrofluid. The ring magnet, HKCM 9963–58947 with dimensions 40 mm × 23 mm × 6 mm and a flux density of $B_z = 1.25$ T, is placed on a steel baseplate. This plate is clamped on the table and placed below the testing machine. 1 mL of ferrofluid is added to the bearing. The velocity of the head of the testing machine is set to be 1 mm/min.

magnet (and steel) in Fig. 6 is reduced by placing an aluminium cylinder inside. This is done in order to minimize the compressibility effect of air by reducing the volume of the inner air pocket [7]. Aluminium is chosen for its non-ferromagnetic properties, high stiffness and availability.

All the components are sealed and mounted with glue to prevent air leakage out of the two pockets. Then, 1 mL of FerroTec EFH1 is added. This amount of ferrofluid is redundant and can therefore create one or multiple air pockets and has a load carrying capacity up to fly heights of 1 mm.

The measurement of the load capacity starts just before the head of the testing machine touches the ferrofluid. No pressure can be build up across the seals at this point yet, because there are no separate air pockets and therefore no difference in magnetic field intensity across the ferrofluid seal ($\Delta H = 0$). The fly height is then decreased until the head of the testing machine starts pushing on the magnet itself. This indicates the end of the measurement of the load capacity.

2.5. Optimization

In this section the validated model, see results in section 3.1, will be used to optimize the geometry of the bearing models given in Fig. 2 for maximum load capacity. For the optimization, the fly height h is set to be 0.2 mm. The optimization of model A shows that the thickness of the steel rings should be equal to the thickness of the magnet, see results in section 3.2. Therefore, bearing model B is introduced. The configuration given in Fig. 2 of model B is optimized in a symmetric and asymmetric way. To investigate the influence of a ferromagnetic baseplate model C and D are introduced, as presented in section 2.2.

2.5.1. Optimization model A and C

The bearing models A and C presented in Fig. 2 will be optimized in both a symmetric and asymmetric configuration. The symmetric optimization is done in order to see the effect of the different variables on the load capacity of the bearing. Symmetric means in this case that the cross section of both steel rings have the same dimensions, thus $W_{left} = W_{right}$, $T_{left} = T_{right}$ and therefore $\Delta z_{left} = \Delta z_{right}$, as can be seen in Fig. 7. The design variables are normalized with respect to the dimensions of the magnet such that the results are easier to interpret. The normalizations are given in equations (7)–(9).

$$T_{ratio} = \frac{T_{steel}}{T_{mag}} \tag{7}$$

$$W_{ratio} = \frac{W_{steel}}{W_{mag}} \tag{8}$$

$$\Delta z_{ratio} = \frac{\Delta z}{T_{mag}} \tag{9}$$

This results in two design variables for the symmetric optimizations, namely: T_{ratio} and W_{ratio} . The design variables for the asymmetric

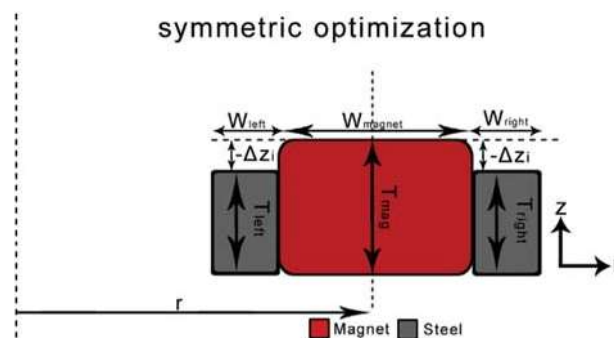


Fig. 7. This figure shows the variables for symmetric optimization and the cross sections of the steel rings.

optimizations for both models are: $T_{ratio-left}$, $W_{ratio-left}$, $T_{ratio-right}$, $W_{ratio-right}$. The Δz_{ratio} is introduced to investigate the height of the steel relative to the height of the magnet.

2.5.2. Optimization model B and D

The bearing models B and D, presented in Fig. 2, will be optimized in a symmetric and asymmetric way. The symmetric optimization is done in order to see the effect of the different variables on the load capacity of the bearing. Due to symmetry, $W_{left} = W_{right}$ and $T_{left} = T_{right}$. The design variables for the symmetric optimization of models B and D are reduced to: T_{ratio} and W_{ratio} and are defined in Fig. 7.

Finally, the asymmetric optimization is performed to see if introducing asymmetry in the system can further improve the load capacity. Note that all the different parameters are again normalized with respect to the magnet in the results. The design variables for the asymmetric optimization of models B and D are: $T_{ratio-left}$, $W_{ratio-left}$, $T_{ratio-right}$, $W_{ratio-right}$, as defined in Fig. 2.

2.5.3. Optimization algorithm

To find an optimum for the configurations described above, an algorithm is designed. The algorithm can be seen as a multi-point approximation method. It evaluates a certain preset subdomain of the design space. The optimal point of the subdomain is considered to be the midpoint of the next subdomain in the next cycle. The process can be seen in Fig. 8. In the asymmetric optimization of the steel rings, this results in a 4D subdomain, consisting of all the design variables. This algorithm solves the optimization problem and is convenient since the function evaluations ask a lot of computational effort.

A subdomain is built using its midpoint, the length of the subdomain and the number of samples. The side length of the subdomain is chosen such that the dimensions of steel increase from no steel rings up to the inner side of the magnet completely filled with steel. Then the subdomain is evaluated and the minimum value is determined. To achieve convergence, the size of the new subdomain must be smaller than that of the previous one. Therefore, the length of each side of the new trust region is scaled. Scaling (< 1) of the subdomain makes the algorithm converge to a certain optimum. The scaling number is determined iteratively by varying this number. A small scaling number makes the subdomain converge too fast and the optimal value is not found ($S < 0.4$). A larger scaling number result in more iterations, but the optimum is found ($0.4 < S < 0.1$).

3. Results

3.1. Load capacity

The load capacity has been analytically calculated and

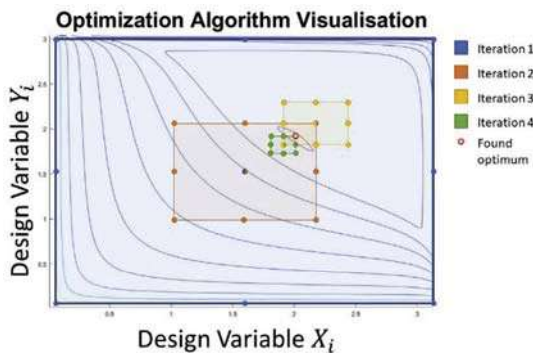


Fig. 8. This figure presents the way the optimization algorithm works. In the first step the entire domain is considered in which 9 points are evaluated. The best point will be the centre of the next iteration step in which the domain will be smaller. These steps will be repeated until an optimum is found.

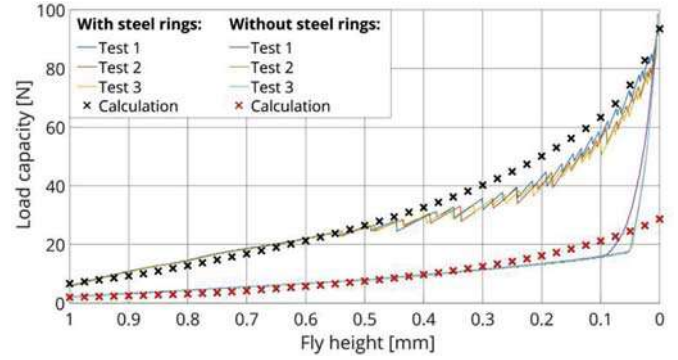


Fig. 9. This figure presents the load capacity predicted by the analytical model and measured by the testing machine versus different fly heights for the magnet only and the magnet with 3 mm wide inner and outer steel rings that have the same z-position as the magnet.

experimentally measured for both the single magnet and the magnet with steel rings for several fly heights. These results can be seen in Fig. 9. The results of the different experiments are indicated with continuous lines while the calculations are indicated with crosses.

Notable is that adding a 3 mm wide inner and outer ring of steel improves the load capacity of the bearing at fly height 0.2 mm with approximately a factor 4. For higher fly heights this factor ranges approximately from 3 to 4. This is a significant improvement compared to the ferrofluid pocket bearing without the steel rings. Also note the zig-zag pattern in the measurements for the improved bearing at lower fly heights.

The overall behaviour of the load capacity of the improved bearing is predicted well by the calculations and both the model and measurements are in good accordance with each other.

3.2. Optimization

The results of the optimization of model A are given in Fig. 10. From this plot it can be concluded that the load capacity is the highest for $\Delta z = 0mm$ for all the different normalized widths of the steel rings. Note that the load capacity significantly decreases if Δz_{ratio} deviates from zero.

The results of the symmetric optimization of model B are given in Fig. 11, Figs. 12 and 13. Fig. 11 shows the load capacity for the two design variables in a single surface plot. Figs. 12 and 13 show side views or cut troughs of the surface plot in Fig. 11.

Fig. 13 shows that the T_{ratio} needs to be approximately 1.2 or higher. The load capacity decreases significantly when the T_{ratio} decreases. In combination with Fig. 13 this leads to the conclusion that for a

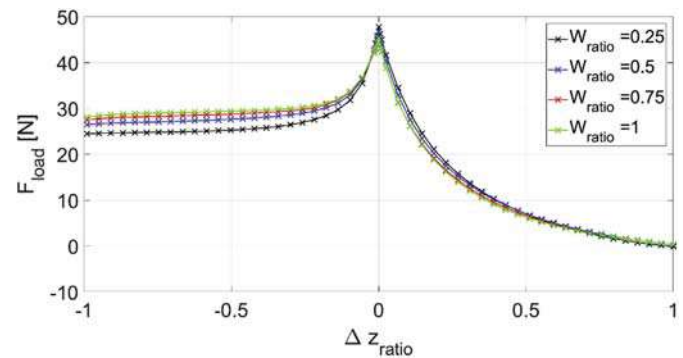


Fig. 10. This figure presents the load capacity of the ferrofluid bearing with additional steel rings for varying thicknesses and widths of the rings. These dimensions are normalized with respect to the thickness and width of the magnet.

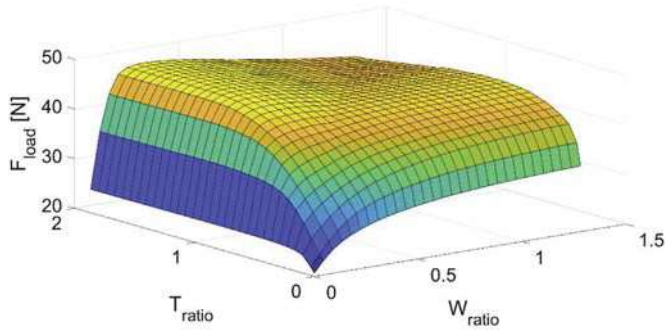


Fig. 11. This figure presents a surface plot of the load capacity of model B with varying dimension parameters H_{ratio} and W_{ratio} .

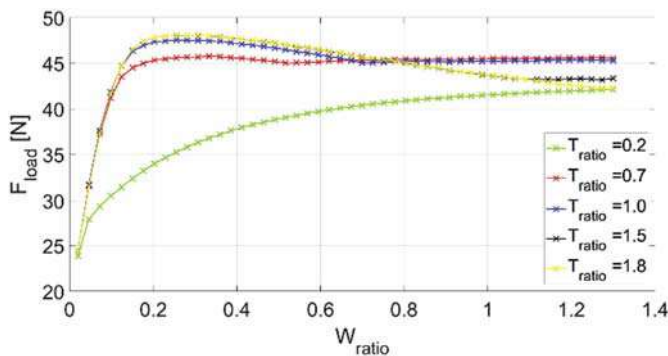


Fig. 12. This figure presents the load capacity of model B versus W_{ratio} for different H_{ratio} .

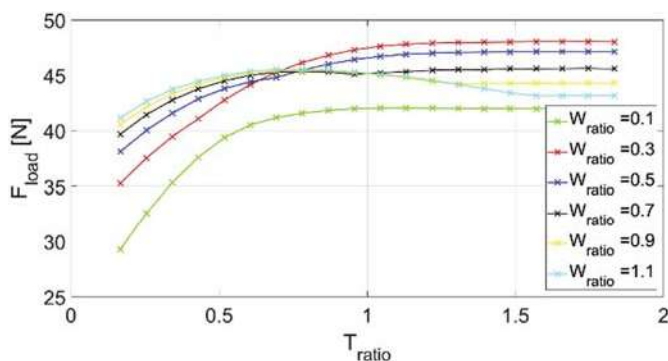


Fig. 13. This figure presents the load capacity of model B versus H_{ratio} for different W_{ratio} .

symmetric configuration of steel rings without baseplate the maximum load capacity of approximately 48N is achieved for $T_{ratio} \approx 1.8$ and $W_{ratio} \approx 0.26$.

The results of the symmetric and asymmetric optimization of model A, B, C and D are given in Table 2. It can be concluded that the addition of the ferromagnetic baseplate changes the optimal geometry of the added ferromagnetic rings as can be seen in Figure 14. Furthermore, when the baseplate is added, an additional 3 N ($\approx 6\%$) increase in load capacity can be obtained.

A visual representation of the optimized bearing configurations for the bearing models is given in Figure 14. The dimensions of the steel rings and the load capacities can be found in Table 2.

4. Discussion

4.1. Analytical model and measurements

Overall, the measurements show that the load capacity of the ferrofluid double pocket bearing is increased 3 to 4 times depending on the fly height by the addition of steel rings around the ring magnet. Addition of these ferromagnetic rings increases the difference in magnetic field intensities over the ferrofluid seal. This increase has the advantage that capillary effects can be overcome such that two air pockets are created. Both the increase in difference in field intensities and the addition of the second seal contribute to the total load capacity, leading to an increase of a factor 4.

The measured load capacity of the bearing with and the bearing without steel rings correspond well to the calculated load capacity. However, the calculations do slightly differ from the actual measurements for both models. From the results it can be seen that at lower fly heights the load capacity for both models is overestimated. This overestimation is probably due to the fact that capillary effects are not taken into account in the mathematical model. Moreover, these capillary effects increase when the fly height decreases.

Also for a magnet with steel rings, the load capacity is overestimated. It seems that the capillary effects are overcome and two seals are formed. However, for low fly heights, the ferrofluid is pushed outwards too far due to the steel rings and do not participate in the load capacity anymore. Therefore, the volume of effective ferrofluid decreases during the measurements, leading to an overestimation of the load capacity. When the amount of effective ferrofluid is overestimated, the realistic value of the H_{o1} is not the lowest value for the field intensity at the magnet and is therefore not located at the valley. The outer interface of the ferrofluid will be located at a higher field intensity, leading to a lower load capacity.

On top of that, the steel rings are modelled in COMSOL as soft iron. In reality, there will be a difference in material properties between the steel rings and the material used in the model. The overall behaviour/shape of the predicted load capacity of the bearing with steel does correspond well to the measurements, and therefore the model can be seen as valid and is used for optimization. It is likely that finding a better BH curve will reduce the overestimation of the load capacity. Another possible error in the FEM model is the applied radius of the fillets, which might also differ from the actual fillets of the steel rings and magnet used in the experimental setup. Note that in general the FEM model starts to become unreliable when the fly height is approaching zero. This is due to effects in the FEM analysis near boundaries and corners of the magnet.

When the fly height is decreased in the measurements, the assumed incompressible ferrofluid is pushed outwards. The fluid-air interfaces get displaced outwards, this increases the areas of the seals and changes the magnetic field intensities at the different interfaces. These effects are included in the analytical and numerical model. In the model, the most outer interface is assumed to linearly increase from a radial distance of 21 mm–21.2 mm and 21 mm to the radial distance of the edge of the outer steel ring for the magnet only and the magnet with steel rings respectively. Implementation of a more realistic gradient in this outer interface will probably yield better results.

When the fly height is decreased the air pressure inside the pockets increases until the point that the seals cannot withstand the pressure anymore. Air escapes out of the pocket and causes the ripples or zig-zag pattern in the measurements in Fig. 9.

4.2. Optimization model A and C

When the W_{ratio} is (very) small there is simply very little steel added to the bearing resulting in that the influence of the steel on the magnetic field is almost negligible. To prevent instant saturation, the W_{ratio} has to be higher than a certain value. Approximately a W_{ratio} of 0.3

Table 2

This table presents the overview of the optimization of the load capacities for the different bearing models discussed in this article **without and with** baseplate.

Model	Design variables	Field intensities				Result				
		$T_{ratio-left}$	$W_{ratio-left}$	$T_{ratio-right}$	$W_{ratio-right}$	$H_{i1} \left[\times 10^5 \frac{A}{m} \right]$	$H_{o1} \left[\times 10^5 \frac{A}{m} \right]$	$H_{i2} \left[\times 10^5 \frac{A}{m} \right]$	$H_{o2} \left[\times 10^5 \frac{A}{m} \right]$	LOAD CAPACITY [N]
A	Symmetric	1	0.27	1	0.27	8.268	3.652	7.581	1.486	47.29
	Asymmetric	1	0.24	1	0.29	8.238	3.648	7.585	1.417	47.65
B	Symmetric	1.8	0.26	1.8	0.26	8.53	3.708	7.692	1.547	48.06
	Asymmetric	1.71	0.27	1.71	0.31	8.500	3.702	7.700	1.5	48.31
C	Symmetric	1	0.37	1	0.37	8.835	4.225	8.198	1.420	51.19
	Asymmetric	1	0.35	1	0.37	8.822	4.224	8.203	1.420	51.20
D	Symmetric	1	0.37	1	0.37	8.835	4.225	8.198	1.420	51.19
	Asymmetric	1	0.35	1	0.37	8.822	4.224	8.203	1.420	51.20

balances complete magnetic saturation and diffusion of the magnetic field into the steel when the width of the steel rings becomes to large.

Regardless of the width of the steel rings, the thickness of the steel rings has to be equal to the thickness of the magnet to obtain the maximum load capacity (section 3.2). When the thickness of the steel rings is less than that of the magnet, the magnetic field is less concentrated at a fly height just above the magnet because the field lines have to travel a greater distance through the air to close the magnetic circuit using the steel. Also due to the low relative permeability of air, the magnetic field lines diffuse into the air, which lowers the load capacity. On the other hand, when the thicknesses of the ferromagnetic rings are higher than the magnet, the fly height is defined as the distance between the non-ferromagnetic plate and the top of the steel rings instead of the magnet (Fig. 2). The magnetic field will in this case be concentrated within the volume above the magnet and between the steel rings surrounding the magnet while the load capacity is determined by the fly height above the steel rings where the magnetic field is much weaker. Therefore, taking the thickness of the steel rings smaller than that of the magnet is less detrimental to the total load capacity of the ferrofluid bearings than taking the thickness too big.

Besides that, steel rings with the same thickness as the magnet have the advantage that the flat top prevents the ferrofluid from dripping down. In this way, the ferrofluid can be used in an optimal way since the ferrofluid seal is able to span a greater horizontal length which increases the load capacity since the difference in magnetic field increases between both interfaces ($\Delta H = H_i - H_o$).

4.3. Optimization model B and D: symmetric

When the T_{ratio} is (very) small there is simply very little steel added to the bearing resulting in that the influence of the steel on the magnetic field is almost negligible, see Fig. 12. The magnetic field has to travel through the air instead of the added steel. Therefore, increasing the thickness of the steel rings increases the load capacity significantly until a T_{ratio} of 1.2 is reached for the bearing without baseplate (model B). For a T_{ratio} of 1, the thickness of the steel rings and the magnet are equal. In this case, the magnetic field leaves the steel and has to make a 180° turn through the air to close the magnetic circuit. Steel rings which are slightly thicker than the magnet reduce this turn to 90°. Therefore a T_{ratio} of at least 1.2 results in the highest load capacity. Further increasing the thickness of the steel beyond a ratio of 1.2 has no influence on the load capacity since the magnetic field does not protrude into the added steel since this would increase the path by the magnetic field lines to close the magnetic circuit. When a baseplate is added below the bearing the thickness of the steel rings has to be equal to the thickness of the magnet.

This can be explained by looking at the magnetic properties of the added material. Once the width of the rings is too small, magnetic saturation of the rings occurs which can be seen in Fig. 12. After the ferromagnetic material is saturated, the magnetic field is not influenced by the material anymore. Therefore, the magnetic saturation of the ferromagnetic material limits the load capacity. Increasing the width increases the load capacity. However, when the width of the rings is too large, the field lines are not concentrated at the edges of the magnet where the ferrofluid will be placed, but distributed into the steel rings,

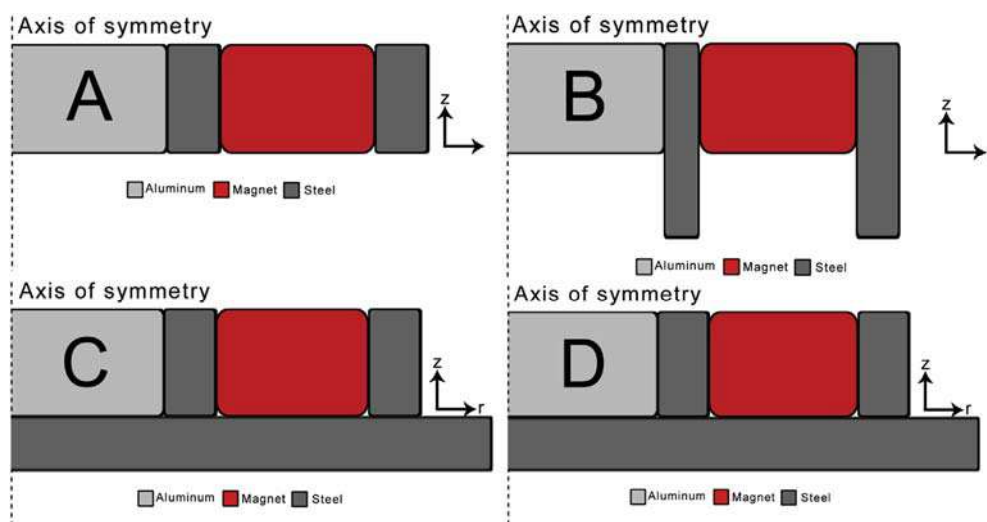


Fig. 14. This figure presents the optimal bearing configurations to achieve maximum load capacity for the ring magnet sandwiched between steel rings without being placed on top of a baseplate (model A and B) and placed on top of a baseplate (model C and D).

which decreases the load capacity. When the width of the rings is increased even further, the dispersion does not increase and therefore the load capacity remains constant which explain the behaviour in Fig. 12 for increasing widths of the steel rings.

Therefore, it can be concluded that the steel needs to have a certain minimum width to prevent magnetic saturation. The optimal width of the rings for the symmetric model B is $W_{ratio} = 0.26$ which balances the magnetic saturation and dispersion of the magnetic field. When a baseplate is added (Model D) the rings need to be a little bit wider (Table 2), namely $W_{ratio} \approx 0.37$. Note that when the inner ring is increased such that the magnet is completely filled with steel, the magnetic field is short circuited and the load capacity decreases.

4.4. Optimization model B and D: asymmetric

The optimal thickness of the rings in the asymmetric optimization of model B happens to be symmetric, namely $T_{ratio} = 1.71$ for the bearing without baseplate, see Table 2. The thickness of the rings exceeds the thickness of the magnet such that it is easier for the magnetic field to close the magnetic circuit. Only a turn of 90° is required for the magnetic field when it leaves the steel ring instead of a full 180° turn. When an additional ferromagnetic baseplate is added the optimal thickness of the rings is equal to the thickness of the magnet which is quite convenient when mounting the bearing. This way the entire magnet is surrounded by steel except for the top surface where the ferrofluid is placed. Besides that the addition of the baseplate changes the optimal thickness significantly such that the bearing can be mounted much more easily, the load capacity is increased by approximately $3N$ ($\approx 6\%$) therefore it is recommended to choose the thickness of the rings equal to the thickness of the magnet and to mount the bearing on a ferromagnetic baseplate.

The optimal width for the steel rings also depends on the presence of a baseplate. As earlier mentioned, a certain minimum value for the width is required to prevent magnetic saturation. If the width is too large the concentration of the magnetic field is decreased which decreases the load capacity but this effect is not as detrimental as the magnetic saturation of the steel. When a baseplate is present, the optimal widths of the steel rings is slightly bigger with respect to a bearing without baseplate, namely $W_{ratio} \approx 0.27$ (model A) & $W_{ratio} \approx 0.26$ (model B) versus $W_{ratio} \approx 0.37$ (model C) & $W_{ratio} \approx 0.37$ (model D) respectively. Introducing asymmetry into the system only increases the load capacity marginally (0.1%) and one can therefore argue whether it is worth the trouble to implement this in practice.

The load capacity can even be increased further if the strength of the magnet and the magnetic saturation of the ferromagnetic material are increased. A larger magnet (a larger T_{mag} or W_{mag}) has a bigger volume and therefore higher magnetic field intensities which increases the load capacity. This is not investigated in this article since it is not a cost effective way to increase the load capacity. Also, a stronger magnet results in an increase of the optimal width of the rings in order to prevent complete magnetic saturation. Increasing the magnetic saturation of the ferromagnetic material does exactly the opposite, namely resulting in a smaller optimal width. This comes from the fact that less material is needed to prevent saturation. Thus, choosing materials with better magnetic properties for the rings can increase the load capacity of the described ring magnet even more. However, using different ferromagnetic materials than steel could increase the costs, which makes the increase in load capacity by adding a ferromagnetic material less cost effective. These and many other possible improvements are not discussed in this article since the goal was to increase the load capacity of a ferrofluid bearing in a cheap and easy manner.

5. Conclusion

The experiments show that the model is in good accordance for the bearing with and without the ferromagnetic rings.

Overestimation of the load capacity is probably caused by capillary effects, an overestimation of the amount of effective ferrofluid and a mismatch between the modelled magnetic saturation and the actual material properties of the steel used in the test setup. The bearing furthermore shows excellent repeatability after an initial compression.

The addition of steel rings does not only increase the differences in field intensities, but also gives the opportunity to overcome the capillary effects and give rise to a second seal. Therefore, it can be concluded that the load capacity of the ferrofluid pocket bearing can be improved by the addition of steel rings up to a factor of 3–4, depending on the fly height and the dimensions of the steel.

Optimization shows that the maximum load capacity is reached if the thickness of the steel is equal to the thickness of the magnet and if the bearing is mounted on a ferromagnetic baseplate. Moreover, the optimal width depends on the magnetic saturation of the rings and the strength of the magnet. Ideally, the rings are on the verge of being completely saturated which optimally concentrates the magnetic field at the corners of the magnet. The optimal width of the steel for the ring magnet described in this report is approximately a third of the width of the magnet.

Acknowledgments

This research has been supported by the Dutch TKI maritime funding program.

References

- [1] Rosensweig R. Bearing arrangement with magnetic fluid defining bearing pads. 1971. 3 612 630.
- [2] Rosensweig R. Magnetic fluid seals. 1971.
- [3] Papell S. Low viscosity magnetic fluids obtained by the colloidal suspension of magnetic particles. 1965. 3 215 572.
- [4] Rosensweig RE. Non-bursting ferrofluid seal. 2001. US6543782B1.
- [5] Rosensweig RE. Ferrohydrodynamics. Dover Publications Inc; 2013.
- [6] Rinaldi C, Chaves A, Elborai S, He X, Zahn M. Magnetic fluid rheology and flows. Curr Opin Colloid Interface Sci 2005;10:141–57. <https://doi.org/10.1016/j.cocis.2005.07.004>.
- [7] Lampaert SGE, Spronck JW, van Ostayen RAJ. Load and stiffness of a planar ferrofluid pocket bearing. Proc Inst Mech Eng Part J J Eng Tribol 2017. <https://doi.org/10.1177/1350650117739200>. 1350650117739200.
- [8] Lampaert SGE, Fellingner BJ, Spronck JW, Ostayen RAJ Van. In-plane friction behaviour of a ferrofluid bearing. Precis Eng 2018<https://doi.org/10.1016/j.precisioneng.2018.05.013>.
- [9] Lampaert SGE. Modelling and Design Principles of planar ferrofluid bearings. DSPE-Conference. 2016 2016.
- [10] Cheng HC, Xu S, Liu Y, Levi S, Wu ST. Adaptive mechanical-wetting lens actuated by ferrofluids. Optic Commun 2011;284:2118–21. <https://doi.org/10.1016/j.optcom.2010.12.073>.
- [11] Uhlmann E, Bayat N. High precision positioning with ferrofluids as an active medium. CIRP Ann - Manuf Technol 2006;55:415–8. [https://doi.org/10.1016/S0007-8506\(07\)60448-X](https://doi.org/10.1016/S0007-8506(07)60448-X).
- [12] Torres-Díaz I, Rinaldi C. Recent progress in ferrofluids research: novel applications of magnetically controllable and tunable fluids. Soft Matter 2014;10:8584–602. <https://doi.org/10.1039/C4SM01308E>.
- [13] Sudo S, Takaki Y, Hashiguchi Y, Nishiyama H. Magnetic fluid devices for driving micro machines. JSME Int J Ser B 2005;48:464–70. <https://doi.org/10.1299/jsmeb.48.464>.
- [14] Olaru R, Petrescu C, Hertanu R. A novel double-action actuator based on ferrofluid and permanent magnets. J Intell Mater Syst Struct 2012;23:1623–30. <https://doi.org/10.1177/1045389X12449916>.
- [15] Liu Q, Alazemi SF, Daqaq MF, Li G. A ferrofluid based energy harvester: computational modeling, analysis, and experimental validation. J Magn Mater 2018;449:105–18. <https://doi.org/10.1016/j.jmmm.2017.09.064>.
- [16] Jayhooni SMH, Assadsangabi B, Takahata K. A stepping micromotor based on ferrofluid bearing for side-viewing microendoscope applications. Sensors Actuators, A Phys 2018;269:258–68. <https://doi.org/10.1016/j.sna.2017.11.020>.
- [17] Mitamura Y, Takahashi S, Amari S, Okamoto E, Murabayashi S, Nishimura I. A magnetic fluid seal for rotary blood pumps: effects of seal structure on long-term performance in liquid. J Artif Organs 2011. <https://doi.org/10.1007/s10047-010-0526-8>.
- [18] Ravaut R, Lemarquand G, Lemarquand V. Mechanical properties of ferrofluid applications: centering effect and capacity of a seal. Tribol Int 2010. <https://doi.org/10.1016/j.triboint.2009.04.050>.
- [19] Yang R, Hou H, Wang Y, Fu L. Sensors and Actuators B: Chemical Micro-magneto-fluidics in microfluidic systems: A review vol. 224. 2016. p. 1–15.
- [20] Potma OGR. To. Designs for rotary shaft fluid seals in an aqueous environment

- using ferrofluid vol. 98. 2017.
- [21] Urreta H, Aguirre G, Kuzhir P, Lopez de Lacalle LN. Seals based on magnetic fluids for high precision spindles of machine tools. *Int J Precis Eng Manuf* 2018. <https://doi.org/10.1007/s12541-018-0060-9>.
- [22] Lampaert SGE, Spronck JW, van Ostayen RAJ, Café M. (2 + 4) DOF precision motion stage with ferrofluid bearings department of precision and microsystems engineering delft university of technology. 5–8. 2014.
- [23] Café M. Nanometer precision six degrees of freedom planar motion stage with ferrofluid bearings. Technical University Delft; 2014.
- [24] Lampaert SGE. Planar ferrofluid bearings modelling and design principles. Technical University Delft; 2015.
- [25] Lampaert SGE, Spronck JW, van Ostayen RAJ. Hydrostatic bearing with MR texturing. B abstr 16th ger ferrofluid work. 2017. p. 94–5.
- [26] Lampaert SGE, Spronck JW, van Ostayen RAJ. Load & stiffness of a planar ferrofluid pocket bearing S.G.E. 17th nord symp Tribol 2016. <https://doi.org/10.1017/CBO9781107415324.004>.
- [27] Lampaert SGE, Spronck JW, van Ostayen RAJ. Virtual textured hybrid bearings. 44th Leeds-Lyon Symp. Tribol 2017;30:84.
- [28] Millet G, Hubert A. Design of a 3 DOF displacement stage based on ferrofluids. *Actuators* 2006;06:656–9.
- [29] Alvarez-Aguirre A, Mok G, HosseinNia SH, Spronck J. Performance improvement of optical mouse sensors: application in a precision planar stage. 2016 int conf manip autom robot small scales, MARSS. 2016 2016. <https://doi.org/10.1109/MARSS.2016.7561698>.
- [30] Mok G. The design of a planar precision stage using cost effective optical mouse sensors. Technical University Delft; 2015.
- [31] Lampaert SGE, Spronck JW, van Ostayen RAJ. Friction and trail formation of a planar ferrofluid bearing. Leeds-Lyon Symp. 2016. p. 4. 2016.
- [32] Lampaert SGE, Spronck JW, van Ostayen RAJ, Habib H. Planar Positioning Stage with a PSD sensor and ferrofluid bearings. DSPE-Conference 2016:57–61. 2016.
- [33] Van Veen S. Planar ferrofluid bearings for precision stages. Technical University Delft; 2013.
- [34] Olaru R, Petrescu C, Arcire A. Maximizing the magnetic force generated by an actuator with non-magnetic body in a ferrofluid pre-magnetized by permanent magnets. *Int Rev Electr Eng* 2013;8:904–11.
- [35] Arcire A, Olaru R, Petrescu C. Study of the influence of ferromagnetic material on the characteristics of an actuator based on ferrofluid and permanent magnets. *EPE 2012 - Proc 2012 Int Conf Expo Electr Power Eng* 2012. p. 776–80. <https://doi.org/10.1109/ICEPE.2012.6463838>.
- [36] Andersson L. Fillet away your electromagnetic field singularities. 2014.

Operational range of a ferrofluid pocket bearing

A S T Boots, J W Spronck, R A J van Ostayen and S G E Lampaert 

Department of Precision and Microsystems Engineering, Delft University of Technology, Mekelweg 2, 2628CD, Delft, The Netherlands

E-mail: S.G.E.Lampaert@tudelft.nl

Received 17 December 2018, revised 8 April 2019

Accepted for publication 20 June 2019

Published 16 October 2019



CrossMark

Abstract

Ferrofluid pocket bearings are interesting for fast and precise positioning systems thank to the absence of stick-slip, the low viscous friction and their cost-effective nature. However, the characteristics of the bearing change due to over(de)compression since air escapes out of the enclosed pocket. This article presents an experimentally validated model that includes the air mass inside the pocket in the calculation of the equilibrium position of the ferrofluid bearing. Moreover, a simple and efficient way to obtain the operational range of the bearing is presented and a sensitivity analysis was performed. The sensitivity analysis showed that ferrofluid pocket bearings are always self-aligning and that the tilt stiffness increases when the fly height decreases or the tilt angle increases.

Supplementary material for this article is available [online](#)

Keywords: precision engineering, numerical modelling, hydrostatic bearing, magnetism, sensitivity analysis, rotational stiffness, sealing capacity

(Some figures may appear in colour only in the online journal)

1. Introduction

A ferrofluid is a colloidal suspension of small magnetic particles inside a carrier fluid. The magnetic particles (3–15 nm), often covered with a layer of dispersant, give the fluid paramagnetic properties [1–3].

Numerous applications have been suggested for ferrofluids over the years [4–7], ranging from sensors [8, 9] and actuators [10–14] to the use of ferrofluid as a lubricant [15] or an energy harvester [16]. Another frequently suggested application is to make staged [17] and non-bursting [18] ferrofluidic seals. This enables rotary shafts to be sealed without the common disadvantage of wear [19, 20], like in vacuum feedthrough [21] or aqueous environments [22]. Ferrofluid bearings and seals can be optimised by maximising the magnetic force generated by permanent magnets using ferromagnetic material [23–25]. The absence of stick-slip also

makes ferrofluid bearings useful in high precision systems [26–30].

Ferrofluid bearings can be classified as either pressure bearings or pocket bearings [31]. Ferrofluid pressure bearings only rely on the pressure inside the ferrofluid to carry a load. Pocket bearings on the other hand rely on both the pressurised air pocket, which is encapsulated by the ferrofluid seal, and the pressure inside the seal itself. The pressure is a result of the magnetic body force which depends on the external magnetic field and the boundary condition of the magnetic fluid [32, 33].

Lampaert *et al* [34] presented a mathematical model to calculate the maximum load capacity of ferrofluid pocket bearings. Over(de)compression of a ferrofluid pocket bearing resulted in air escaping in and out of the pocket which subsequently changed the behaviour of the bearing. However, the bearing also showed good repeatability over multiple compression-decompression cycles when the mass inside the pocket is unaltered. In practice, this is the operational range of the bearing.

In this article, the behaviour of the bearing after over(de)compression is modelled to determine its operational range. First, an experimentally validated model is presented to



Original content from this work may be used under the terms of the [Creative Commons Attribution 3.0 licence](#). Any further distribution of this work must maintain attribution to the author(s) and the title of the work, journal citation and DOI.

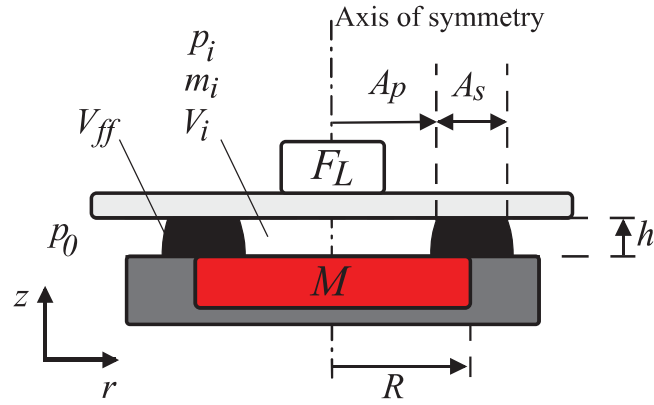


Figure 1. A cross-section of the ferrofluid pocket bearing defines the parameters used in this article. The cylindrical magnet, with magnetisation M , is placed in a non-ferromagnetic base (grey).

calculate the position of the ferrofluid seal depending on the air mass inside the pocket. Next, this position will be used to calculate the load capacity of the ferrofluid bearing according to literature. Moreover, a simple and efficient way to obtain the operational range is presented based on only the strength of a ferrofluid seal and the mass inside the pocket. Finally, a sensitivity study was performed in order to see how different variables affect the load capacity and operational range of the bearing.

2. Methods

First, the calculation of the strength of a ferrofluid seal in the presence of an external magnetic field is described. Subsequently, the load capacity of the bearing is derived and the sensitivity of the load capacity with respect to tilt is analysed. The sensitivity can be used to determine how the bearing performs in practice where disturbances are present. The ideal gas law is introduced to calculate the air mass enclosed by the ferrofluid seal. Next, the finite element method (FEM) model is introduced, which will be used to calculate the positions of the interfaces between ferrofluid and air. The magnitude and positions of the interfaces will subsequently be used to calculate the load capacity and torque of the bearing. The load capacity is calculated according to Lampaert *et al* [34]. Finally, the experimental set-up that was used to validate the predicted load capacity of the bearing is introduced. Figure 1 shows the schematic of the bearing including all the important parameters.

2.1. Mathematical model

2.1.1. Ferrofluid seal. The pressure inside a stationary ferrofluid seal can be derived from the Ferrohydrodynamic Navier–Stokes equations for incompressible Newtonian fluids [2, 35]. In the derivation, it is assumed that the ferrofluid is completely saturated and that the only body force present is the magnetic body force. The result is equation (1) for the pressure distribution inside a ferrofluid [24, 34]. In this equation, the pressure ($p(r)$) inside the ferrofluid at a specific

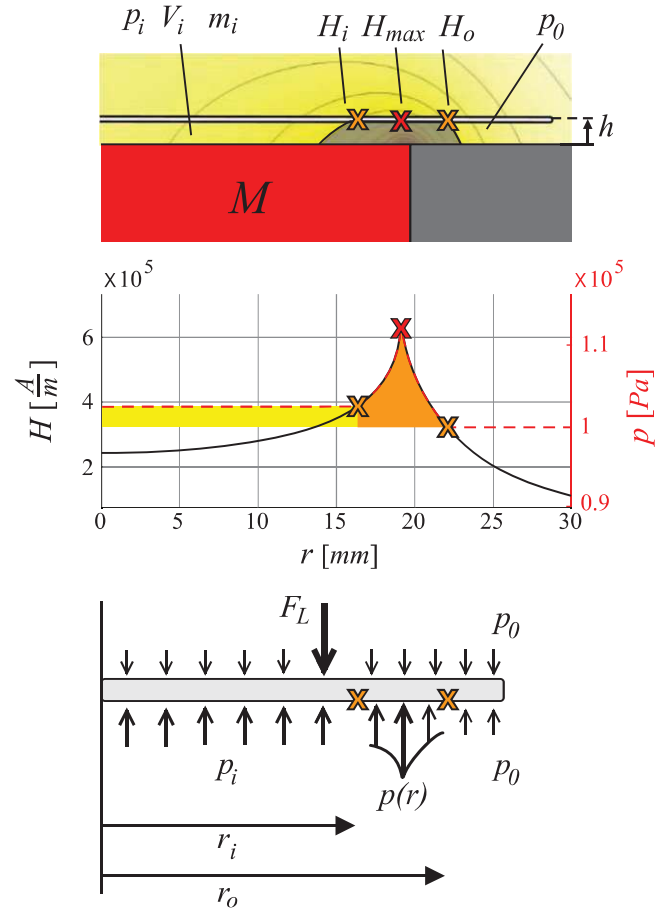


Figure 2. The pressure distribution (middle figure), acting on the plate above the bearing (bottom figure), is a result of the shape and placement of the ferrofluid seal (top figure). The total load capacity is obtained by integrating the pressure distributions given in the bottom figure. The coloured areas in the middle figure represent visually the contributions of the seal and pocket to the total load capacity of the bearing.

radial position (r) and fly height (h), is dependent on the magnetic field intensity ($H(r)$) at that specific location and the magnetic field intensity of the outer fluid–air interface (H_o). Moreover, μ_0 is the permeability of vacuum and M_s the saturation magnetisation of the ferrofluid.

$$p(r) - p_0 = \mu_0 M_s (H(r) - H_o). \quad (1)$$

Equation (1) can be used to calculate the pressure difference over a ferrofluid seal (Δp or $p_i - p_0$) by evaluating the magnetic field intensity at the inner interface (H_i) and at the outer interface (H_o), equation (2). Figure 2 shows the location and shape of the ferrofluid seal for an arbitrary H_i and H_o . The figure also shows the resulting pressure distribution.

Next, equation (2) can be used to calculate the maximum pressure difference that a ferrofluid seal can withstand. The maximum pressure difference ($p_{i,max} - p_0$) is determined by the maximum pressure difference in magnetic field intensity that can be achieved across the ferrofluid seal (ΔH or $H_i - H_o$). For the geometries discussed in this article, this maximum is obtained when the inner ferrofluid interface is located at the maximum magnetic field intensity at that specific fly height, thus when $H_i = H_{max}$. This results in equation (4) for the

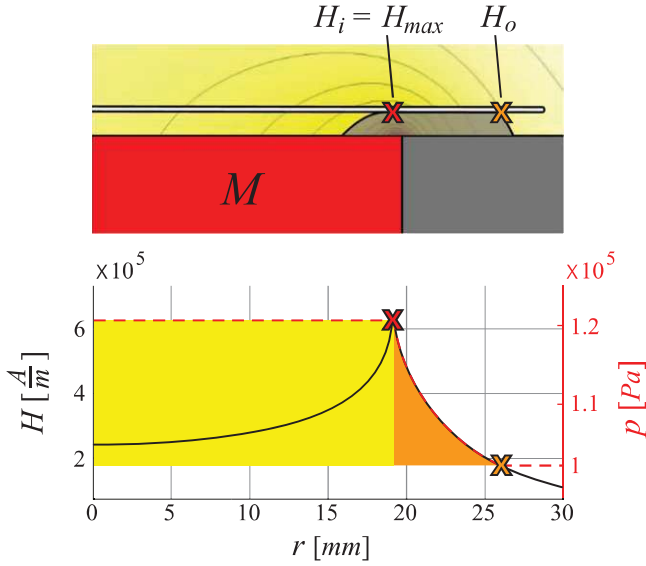


Figure 3. The shape of the ferrofluid seal and the resulting pressure distribution over the seal for a maximum pressurised pocket at a height h . The corresponding load capacity of the seal and the pocket are indicated in orange and yellow.

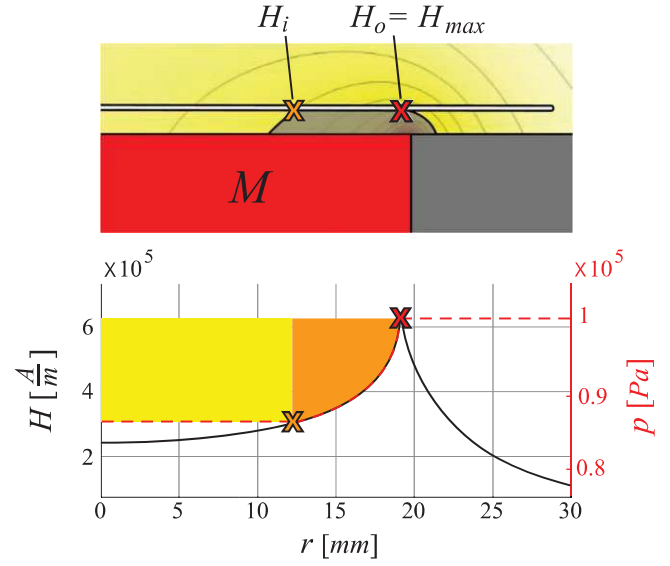


Figure 4. The shape of the ferrofluid seal and the resulting pressure distribution over the seal for a minimum pressurised pocket at a height h . The corresponding load capacity of the seal and the pocket are indicated in orange and yellow.

calculation of the maximum strength of the seal. Note that the value of H_{max} is dependent on the the magnetic field generated by the permanent magnet and the fly height. The value of H_o is dependent on the amount of ferrofluid present in the system (V_{ff}). Figure 3 shows the corresponding location and shape of the seal, the pressure distribution and magnetic field intensity over the seal

$$p_i - p_0 = \mu_0 M_s (H_i - H_o), \quad (2)$$

$$m_i = p_i V_i \frac{M_{air}}{RT}. \quad (3)$$

The same reasoning applies to the calculation of the minimum pocket pressure, given in equation (6). In that case, the magnetic field intensity at the outer interface equals the maximum magnetic field intensity at that fly height ($H_o = H_{max}$). This results in a negative pressure drop over the seal, since $H_o > H_i$. Figure 4 shows the shape of the ferrofluid seal for a minimum pressure inside the pocket and once again the pressure distribution and magnetic field for that specific configuration. Note that the pressure inside the pocket is lower than the ambient pressure. The corresponding pressure difference the seal has to withstand is referred to as the minimum strength of the ferrofluid seal

$$p_{i,max} - p_0 = \mu_0 M_s (H_{max} - H_o), \quad (4)$$

$$m_{i,max} = p_{i,max} V_{i,max} \frac{M_{air}}{RT}, \quad (5)$$

$$p_{i,min} - p_0 = \mu_0 M_s (H_i - H_{max}), \quad (6)$$

$$m_{i,min} = p_{i,min} V_{i,min} \frac{M_{air}}{RT}. \quad (7)$$

2.1.2. Load capacity. Integration of all the different forces that act on the plate (figure 2) results in the total load capacity of the bearing (F_L), equation (8). Combining equations (2) and (8) results in equation (9) for the load capacity expressed in a cylindrical coordinate system. The total load capacity is made up of the contribution of the air pocket and the contribution of the ferrofluid seal. The radial position of the inner interface is denoted by r_i and the outer interface by r_o

$$F_L = \int_0^{2\pi} \int_0^{r_o} (p(r) - p_0) r dr d\theta, \quad (8)$$

$$F_L = \underbrace{\mu_0 M_s (H_i - H_o) \pi r_i^2}_{\text{Air pocket}} + \underbrace{2\pi \mu_0 M_s \int_{r_i}^{r_o} (H(r) - H_o) r dr}_{\text{Ferrofluid seal}}. \quad (9)$$

Figures 2–4 visually show how the load capacity is calculated using equation (8) or (9). The contribution of the pocket to the total load capacity is indicated by the yellow marked area, while that of the seal is marked orange.

The stiffness of the ferrofluid bearing can be calculated by taking the derivative of the load capacity with respect to the vertical position, equation (10)

$$k_z = -\frac{dF_L}{dh}. \quad (10)$$

2.1.3. Tilt. The plate at height h above the magnet is now tilted around the y -axis in clockwise direction by a tilt angle α , figure 5. The tilt angles are assumed to be small ($\alpha \leq 1^\circ$), therefore at an angle θ , α is reduced to γ according to equation (11). A cross-section of the bearing at angle θ is

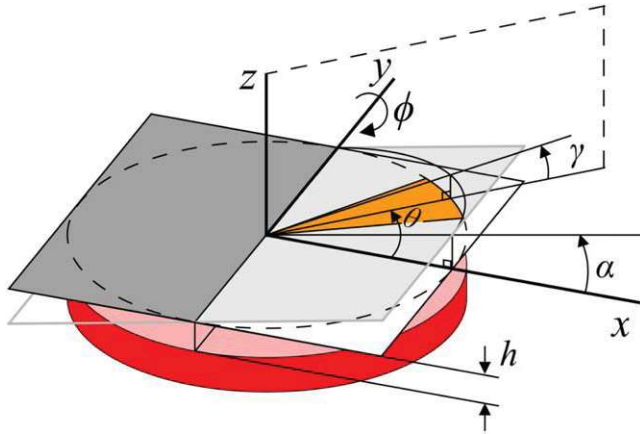


Figure 5. Schematic representation of the tilted bearing. The plate is tilted around the y -axis by an angle α . A cross-section of the bearing at the angle θ is shown in figure 6.

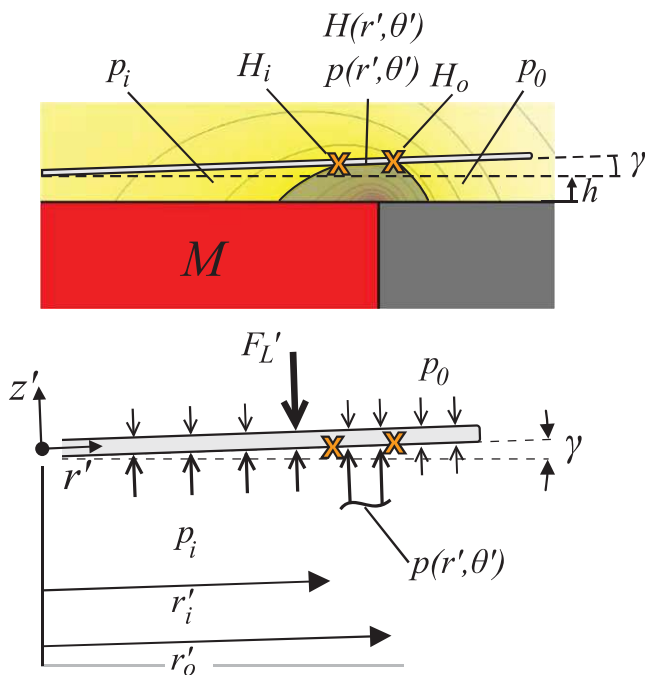


Figure 6. The shape of the ferrofluid seal and the resulting pressure distribution over the seal for a tilted bearing. Note that a body fixed frame of reference is introduced in the center of mass of the plate and that the tilt angle γ is introduced.

given in figure 6. This figure presents the pressure distribution that acts on the plate. Moreover, a body fixed frame of reference (r', θ', z') is introduced which will be used to calculate the load capacity and torque.

In contrast to equation (8), the pressure is now dependent on the angular coordinate θ' , since the system is not axisymmetric any more. The total load capacity of the bearing perpendicular to the surface of the plate is obtained by combining equations (2) and (12), (13). The load capacity in vertical direction is approximately the same as the load capacity perpendicular to the surface of the plate for small tilt angles ($F_L \approx F'_L$). Note that in this analysis, part of the resultant force F'_L , acting in r -direction due to the tilt, is neglected. This force accelerates the plate and possibly results

in the plate gliding off the ferrofluid

$$\gamma = \alpha \cos(\theta), \quad (11)$$

$$F'_L = \int_0^{2\pi} \int_0^{r'_o(\theta')} (p(r', \theta') - p_0) r' dr' d\theta', \quad (12)$$

$$F'_L = \mu_0 M_s (H_i - H_o) \int_0^{2\pi} \int_0^{r'_i(\theta')} r' dr' d\theta' + \mu_0 M_s \int_0^{2\pi} \int_{r'_i(\theta')}^{r'_o(\theta')} (H(r', \theta') - H_o) r' dr' d\theta'. \quad (13)$$

Next, the torque that acts on the plate around the y -axis (M_y) can be calculated by multiplying the pressure distribution with its lever arm and integrating it over the entire area of the bearing, equation (14). Note that this is easily done in the body fixed frame of reference since the pressure distribution acts normal to the plate. Due to symmetry the resulting torque around the x -axis is zero

$$M_y = \int_0^{2\pi} \int_0^{r'_o(\theta')} -(p(r', \theta') - p_0) r' \cos(\theta') r' dr' d\theta'. \quad (14)$$

Finally, the tilt stiffness of the bearing (k_ϕ) around the y -axis (ϕ -direction) can be calculated by taking the derivative of the torque with respect to the tilt angle, equation (15). The negative sign is missing since the angle α is defined in the negative ϕ -direction

$$k_\phi = \frac{dM_y}{d\alpha}. \quad (15)$$

The sensitivity of the load capacity and operational range with respect to tilt will be included in the sensitivity analyses. Moreover, the effects of the saturation magnetisation and the applied volume of ferrofluid are included, see the results in section 3.

2.1.4. Mass inside pocket. If the pressure inside the pocket exceeds the maximum pressure the seal can withstand with respect to ambient pressure (equations (4) and (16a)), the seal breaks, air escapes and the bearing loses mass until equilibrium can be obtained again (figure 3 and equation (5)), as observed by Lampaert *et al* [34]. Consequently, this mass loss changes the characteristics of the bearing, namely the load capacity and stiffness. Mass gain also changes the characteristics. When the pressure difference over the seal exceeds the minimum strength of the seal (equations (6) and (16c)) it breaks. The result is that air surrounding the bearing moves through the seal into the air pocket. This process continues until the bearing gained sufficient air mass such that equilibrium can be obtained again, (figure 4 and equation (7)).

By introducing the ideal gas law in the calculations, the equilibrium position of the seal becomes dependent on the air mass enclosed by the ferrofluid seal, equations (3) and (16b). Compression and decompression of the bearing are assumed to be done in a slow fashion, such that the system can

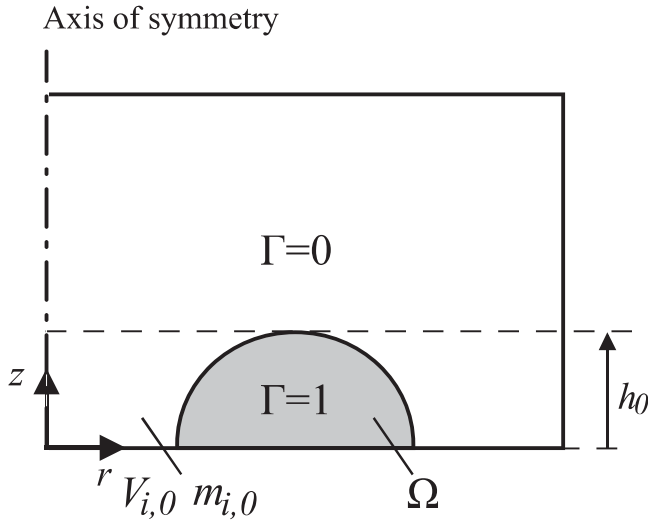


Figure 7. Air and ferrofluid are distinguished by the function Γ in the FEM.

continuously adjust itself to the temperature of the surroundings. Therefore, it is reasonable to assume an isothermal process, $\bar{R}T = \text{Constant}$, with the temperature assumed to be room temperature, $T = 293 \text{ K}$. The molar mass of air is denoted by M_{air} and the universal gas constant by \bar{R} . Initially, the mass of air inside the pocket is $m_{i,0}$, which is defined as the mass encapsulated by the seal at the fly height h_0 , figure 7

$$p_i > p_{i,max} \text{ Loosing mass,} \quad (16a)$$

$$p_{i,min} \leq p_i \leq p_{i,max} \text{ Constant mass,} \quad (16b)$$

$$p_i < p_{i,min} \text{ Gaining mass.} \quad (16c)$$

2.2. FEM implementation

The goal of the FEM is to calculate the magnetic field produced by the magnet and subsequently to calculate the equilibrium position of the ferrofluid seal for varying m_i , V_{ff} , α , M_s and h . Using the position of the seal, the load capacity and torque can be calculated and the total behaviour of the bearing is obtained.

The shape and position of the ferrofluid seal for an arbitrary fly height h , is completely defined by the two variables H_i and H_o , figure 8. Therefore, an additional formulation (Γ), dependent on these variables, is introduced in the FEM, in order to distinguish air and ferrofluid, figure 7 and equation (17). $\Gamma = 1$ for all the coordinates which are part of the union of the sets Ω_1 and Ω_2 and indicates ferrofluid. Air is defined by $\Gamma = 0$, therefore volume integration of Γ results in the total amount of ferrofluid present in the system, equation (18). Next, the solving strategies for a perfectly aligned bearing as well as a tilted bearing will be discussed

$$\Gamma(r, z, \theta) = \begin{cases} 1 & \text{if } (r, z, \theta) \in (\Omega_1 \cup \Omega_2) \text{ Ferrofluid} \\ 0 & \text{if } (r, z, \theta) \notin (\Omega_1 \cup \Omega_2) \text{ Air} \end{cases}, \quad (17)$$

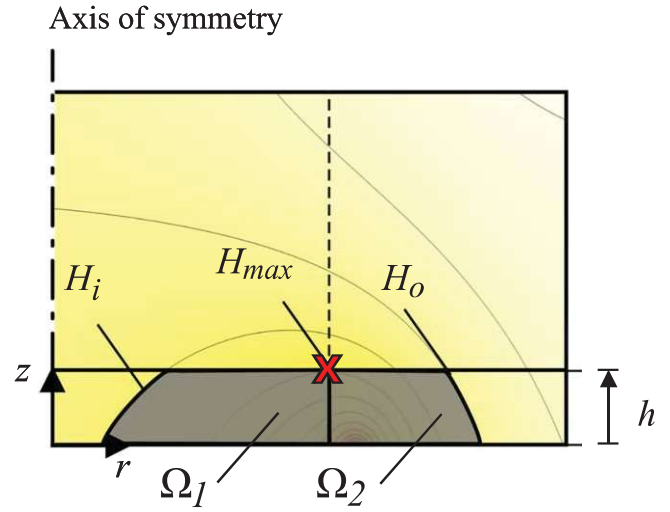


Figure 8. The ferrofluid domain ($\Gamma = 1$) is divided into the sets Ω_1 and Ω_2 , which are defined by H_i , H_o , H_{max} and h .

$$V_{ff} = \iiint \Gamma(r, z, \theta) dV. \quad (18)$$

2.2.1. Perfect alignment. When there is no tilt, the system is axisymmetric which simplifies Γ to $\Gamma(r, z)$. Therefore, the system is modelled in COMSOL Multiphysics® (COMSOL Inc. version 5.3.1.348) as 2D axisymmetric. First, the magnetic field generated by the magnet is calculated. Subsequently, the equilibrium position of the ferrofluid seal is calculated by combining all the different forces (equations (2) and (3)) with the description for the ferrofluid (equations (17) and (18)). The calculations start from the fly height h_0 with the initial mass $m_{i,0}$ inside the pocket with volume $V_{i,0}$, figure 7. The characteristic of the aligned bearing is obtained by calculating the position of the ferrofluid for different fly heights. An overview of the solving strategy is given in figure 9.

2.2.2. Tilt. Due to the tilt, the system is not axisymmetric any more, figure 5. Therefore, the previously described solving strategy cannot be used any more. The problem can still be solved by modelling it in 3D, however this becomes computational expensive when more accuracy is needed. In order to reduce computational cost, the tilted bearing will be approximated by implementing a 2D (middle) Riemann sum, in which the pressure distribution at the centerline of each individual part k , represents the pressure distribution of that entire part. The interval and size β of each partition is determined by the number of subdivisions N , figure 11 and equation (19).

To illustrate this, the pressure distribution of partition k simplifies from $p(r', \theta')$ to $p(r', \theta = \beta k)$ on the interval between its lower boundary (θ_l, k) and upper boundary (θ_u, k) . Note that the tilt angles are small ($\alpha \ll 1^\circ$), therefore the angular coordinate θ is approximately the same in the global and body fixed frame of reference ($\theta' \approx \theta$). The cross-section presented in figure 6 corresponds to the centerline of the

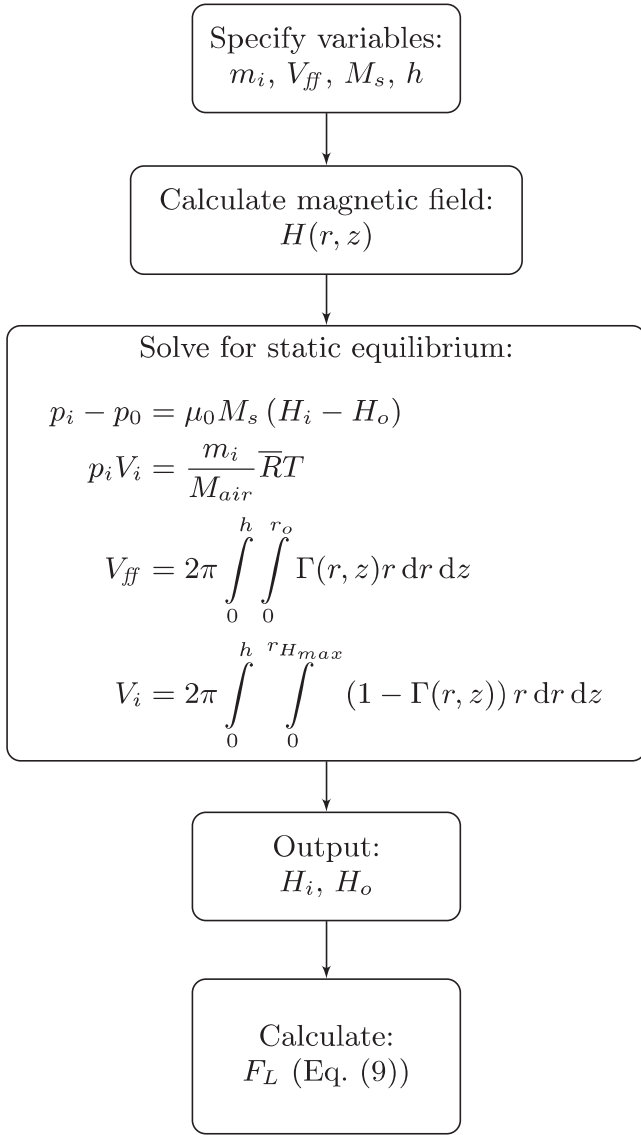


Figure 9. The solving strategy for the aligned (axisymmetric) ferrofluid bearing.

orange partition presented in figures 5 and 11. Note that increasing the number of elements increases the accuracy of the approximation but also increases computational time. The convergence study showed that a physics-controlled mesh size 5 and $N = 16$ are required to obtain a relative error below 0.5%, see result in figure 15. The torque of the bearing (M_y) showed to be the most sensitive to small variations in the calculated equilibrium position of the ferrofluid. Therefore, M_y is used to quantify the convergence of the calculation. Note that M_y is scaled with respect to the finest and therefore assumed the most accurate calculation. This calculation was performed using a physics-controlled mesh size 1 and $N = 56$.

The advantage of the discretization is that each partition can be modelled using a 2D axisymmetric model, each with a

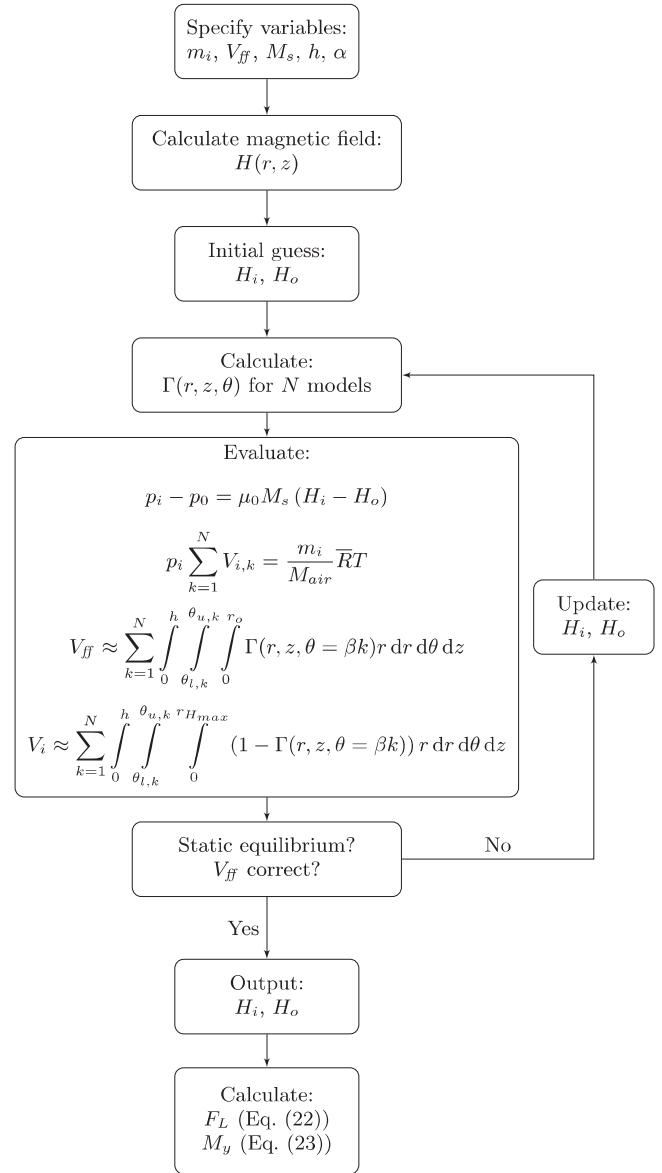


Figure 10. The solving strategy for the tilted (asymmetric) ferrofluid bearing.

slightly different tilt angle ($\gamma_k \approx \alpha \cos(\theta = \beta k)$, equation (11)). The disadvantage is that N calculations are needed. The model is solved for static equilibrium in an iterative fashion for the variables H_i and H_o , figure 10. The fminbnd algorithm in the MATLAB® R2018a Optimisation Toolbox™ (The MathWorks Inc.) is used in combination with the Livelink for the finite element calculations in COMSOL Multiphysics®. When H_i and H_o are known, both the load capacity and torque of the tilted bearing (equations (13) and (14)) can be calculated using the discretization, equations (20) and (21). Note that the lever arm of the pressure distribution can be approximated as $r' \cos(\theta)$ for small tilt angles

$$\beta = \frac{2\pi}{N}, \quad (19)$$

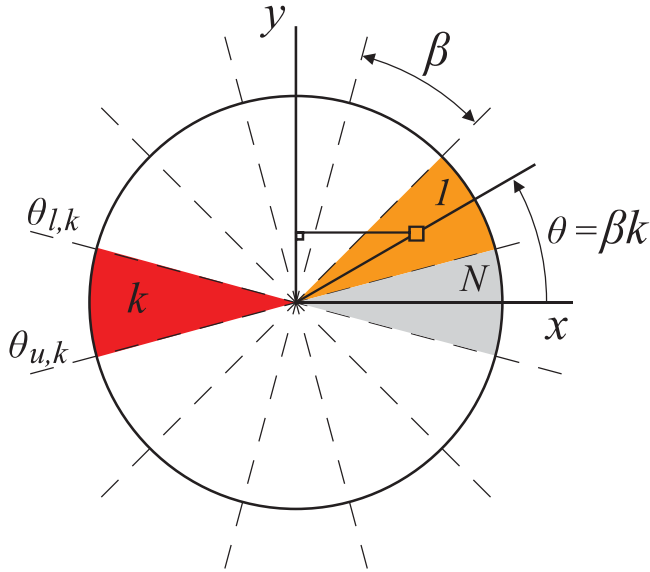


Figure 11. The discretization of the tilted bearing (figure 5) in a top view. The lever arm around the y-axis of a small pressure element is displayed.

$$F_L \approx \sum_{k=1}^N \int_{\theta_{l,k}}^{\theta_{u,k}} \int_0^{r'_o(\theta=\beta k)} (p(r', \theta = \beta k) - p_0) r' dr' d\theta, \tag{20}$$

$$M_y \approx \sum_{k=1}^N \int_{\theta_{l,k}}^{\theta_{u,k}} \int_0^{r'_o(\theta=\beta k)} (p(r', \theta = \beta k) - p_0) r' \cos(\theta) r' dr' d\theta. \tag{21}$$

2.3. Experimental set-up

The presented model was validated by comparing the results of the theoretical model and the experiments that were performed as described below. In the validation, both the load capacity and stiffness were compared and discussed.

Experiments were performed using a test set-up as shown figures 12 and 13. A Zwick/Roell Z005 was used to measure the force over displacement behaviour of the bearing. The relative accuracy of the force measurement is 0.21%, whereas the repeatability has an accuracy below 0.33%. For the displacement measurement, the repeatability is 0.3 μm and the accuracy is 0.6 μm.

The ferrofluid bearing under testing consisted of a cylinder magnet, HKCM 9961-835, with a radius of 40 mm, a height of 10 mm and a remanent flux density of 1.28 T, placed in an aluminium casing. Next, the magnet attached to the aluminium casing, chosen for its non-ferromagnetic properties, was placed onto a low-grade steel plate. This is convenient since no glue or other connections were needed for the connection of the base plate and magnet. Finally, the magnet was mounted onto the testing machine using stainless steel bolts and aluminium clamps, figure 12. It is important to note that the head of the tensile testing machine was made of aluminium. If the material would be ferromagnetic, the force measurement would be errored, since the magnet would attract the head of the machine.

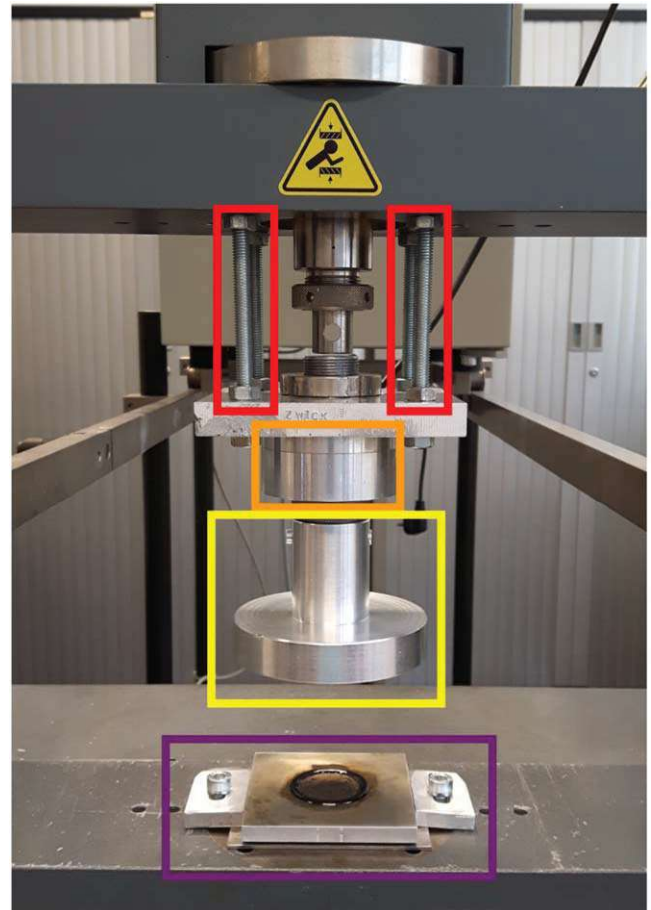


Figure 12. The test set-up consists of the ferrofluid bearing (purple), the head of the tensile testing machine (yellow) and the load cell (orange). The stiffness of the test set-up is approximately $2 \times 10^6 \text{ N m}^{-1}$.

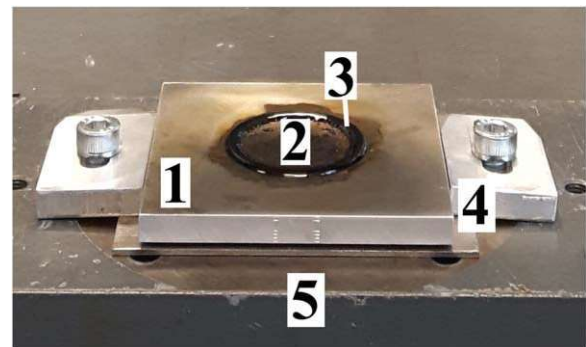


Figure 13. The ferrofluid bearing consists of the cylinder magnet (2) which is placed inside the aluminium casing (1) and the ferrofluid (3). The bearing is mounted to tensile testing machine (5) using clamps, bolts and a steel base plate (4).

2.3.1. Initialisation. Before the measurement started, the test set-up had to be prepared properly, meaning alignment of the machine and bearing, application of the ferrofluid and determination of the position of the surface of the bearing. This was done in the following manner: the head of the tensile tester was pressed onto the bearing with a force of 100 N, in

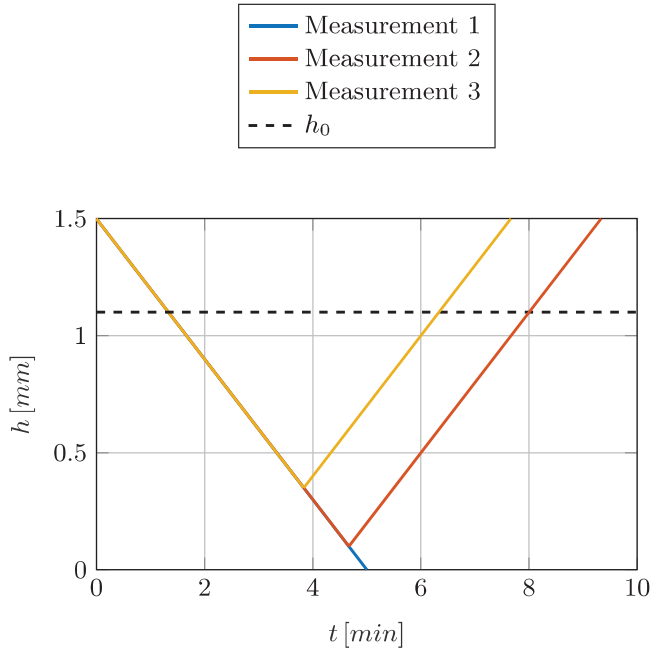


Figure 14. The position of the tensile testing machine (fly height h) versus the time for the different measurements. All three measurements start 1.5 mm above the surface of the magnet. h_0 indicates the height of the ferrofluid seal.

order to determine the position of the surface of the bearing, $h = 0$ mm, and the stiffness of the test set-up, approximately $2 \times 10^6 \text{ N m}^{-1}$. At $h = 0$ mm, the surface of the head was aligned to the surface of the bearing using the nuts and bolts, red marking in figure 12.

Next, the head was retracted and ferrofluid was applied to the system using a pipette. The pipette is slightly inaccurate, since the ferrofluid was pulled out of the nozzle due to the magnetic attraction of the magnet onto the ferrofluid. Therefore, the mass of the pipette filled with ferrofluid was measured before and after application of the ferrofluid, using a weigh scale with an uncertainty of 0.005 g. By combining the density of the ferrofluid, $\rho = 1380 \text{ kg m}^{-3}$, and the difference in mass, which corresponds to the applied mass of ferrofluid, the applied volume could be calculated.

The ferrofluid used in the measurements is the Ferrotec APG 513A, which has a saturation magnetisation of $M_s = 32 \text{ kA m}^{-1}$ at a temperature of 300 K. The applied volume of ferrofluid in the measurements was 0.38 ml.

2.3.2. Measurements. Before the actual measurements, an initial pre-wetting step was performed. This means compressing the bearing maximally until the head reaches $h = 0$ mm. This was done in order to apply a thin film of ferrofluid onto the head of the tensile testing machine, such that the experiments performed afterwards were repeatable. The thin film of ferrofluid only has to be applied once. Effectively, this means that the applied volume of 0.38 ml is slightly decreased.

After the pre-wetting step, three different measurements were performed, figure 14. First, the maximum load capacity

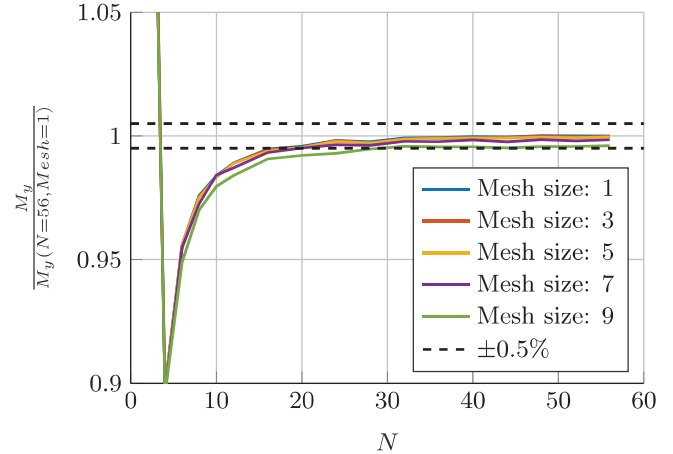


Figure 15. The accuracy of the discretized model (figure 11) with respect to the number of discretizations N . The convergence of the mesh size and discretization is determined by scaling the torque M_y with respect to the finest and therefore assumed the most accurate result, obtained using mesh size 1 and $N = 56$.

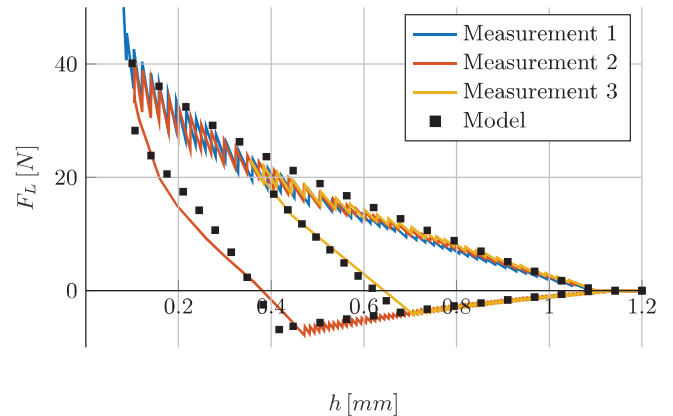


Figure 16. The modelled load capacity is compared to the measurement results. The maximum load capacity is given in blue, while red and yellow indicate two different compression and decompression cycles.

of the bearing was measured by completely compressing the bearing until $h = 0$ mm. During the second and third measurement, the bearing was compressed until heights of 0.1 mm and 0.35 mm respectively, after which the bearing was fully decompressed. All the measurements were performed with a speed of 0.3 mm min^{-1} .

3. Results

The results of the convergence study are given in figure 15. Initially, when the number of discretizations N is small the relative error is $>5\%$. Increasing the number of discretizations increases the accuracy of the model. In contrast, the convergence is fairly independent of the chosen physics-controlled mesh size. A physics-controlled mesh size 5 and $N = 16$ result in an error below 0.5%.

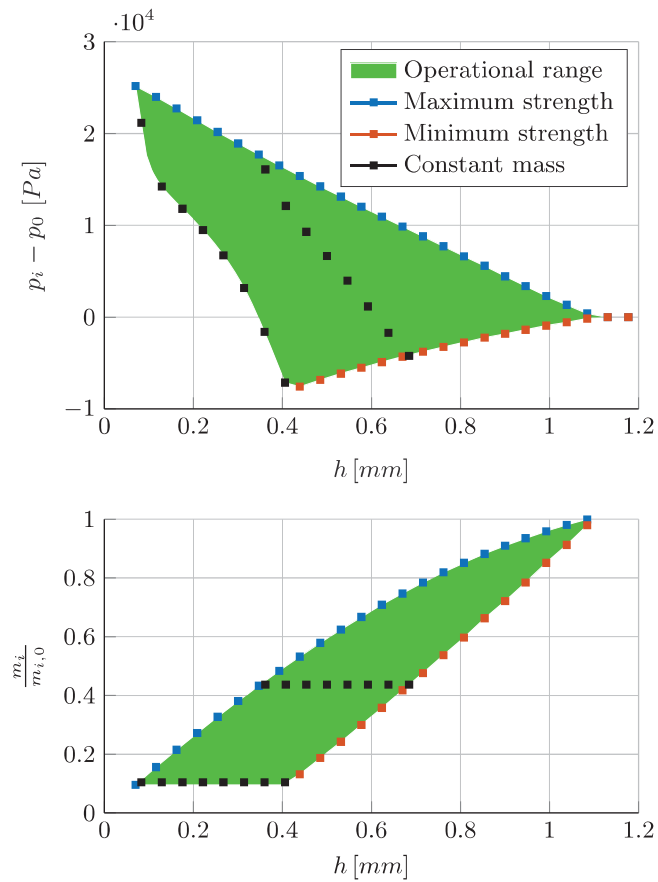


Figure 17. The pressure difference the ferrofluid seal can withstand calculated using the presented model (top figure) ket bearing (bottom figure). Decreasing the fly height increases the maximum and minimum strength of the ferrofluid seal, but decreases the air mass inside the pocket. The black markers correspond to measurements 2 and 3 from figure 16.

Next, the results of the measurements described in section 2.3.2 are given in figure 16. In this figure, the load capacity of the ferrofluid pocket bearing is shown versus the fly height for both the measurements and the model. The expected load capacity, calculated using the suggested model, is shown with black markers, while the different measurements are indicated with continuous lines.

Figure 17 shows the pressure and mass inside the pocket of the ferrofluid bearing versus the fly height. Note that the values correspond to the values of the model given in figure 16. These results are used to explain and interpret the behaviour of the bearing, namely the mass loss and operational range. In the top figure, the blue colour indicates the maximum pressure that the ferrofluid seal can withstand at that fly height, see also figure 3. The corresponding mass inside the pocket at maximum pressure is given in the bottom figure in blue. Note that the mass is normalised with respect to the initial mass $m_{i,0}$, figure 7. The red colour indicates the minimum pressure that the seal can withstand, see also figure 4. The corresponding mass inside the pocket is given in the bottom figure in red. The black lines correspond to

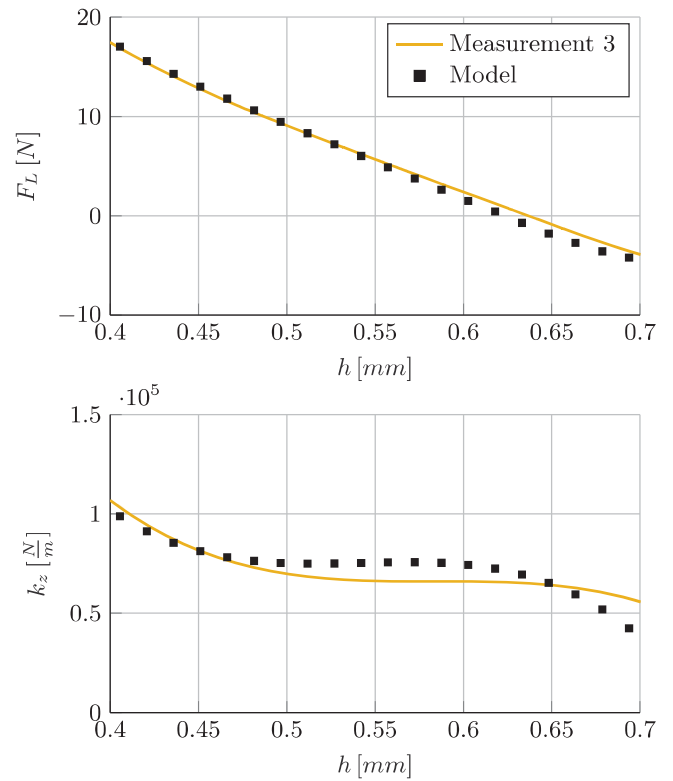


Figure 18. The load capacity (top figure) and stiffness (bottom figure) of the bearing, in the operational range of measurement 3 (figure 16), are compared to the model.

measurements 2 and 3 of figure 16. The operational range of the ferrofluid pocket bearing is coloured green.

In the top figure of figure 18, the part of measurement 3 (figure 16) that is located in the operational range of the bearing according to figure 17, is presented. The bottom figure of figure 18 shows both the stiffness of the bearing derived from the load capacity measurements, as well as the stiffness derived from the load capacity predicted by the model.

Lastly, the sensitivity of the load capacity and operational range with respect to the saturation magnetisation of the ferrofluid (figure 19), the applied volume of ferrofluid (figure 20) and the tilt (figure 21) are given. The load capacity of the bearing significantly increased when the saturation magnetisation increased. The operational range did not change significantly when the saturation magnetisation was increased from 20 to 40 kA m^{-1} . Figure 20 shows that increasing the amount of ferrofluid increases both the load capacity and operational range. In contrast, figure 21 shows that tilt decreases both.

Figures 22 and 23 present the torque and the tilt stiffness with respect to the tilt angle for both the maximally and minimally pressurised pockets. Both figures globally show the same behaviour. When the tilt angle is positive, the torque and tilt stiffness are positive for all the different fly heights. The torque and tilt stiffness increase when the fly height is decreased or when the tilt angle is increased. When the pocket of the bearing was minimally pressurised, the magnitude of

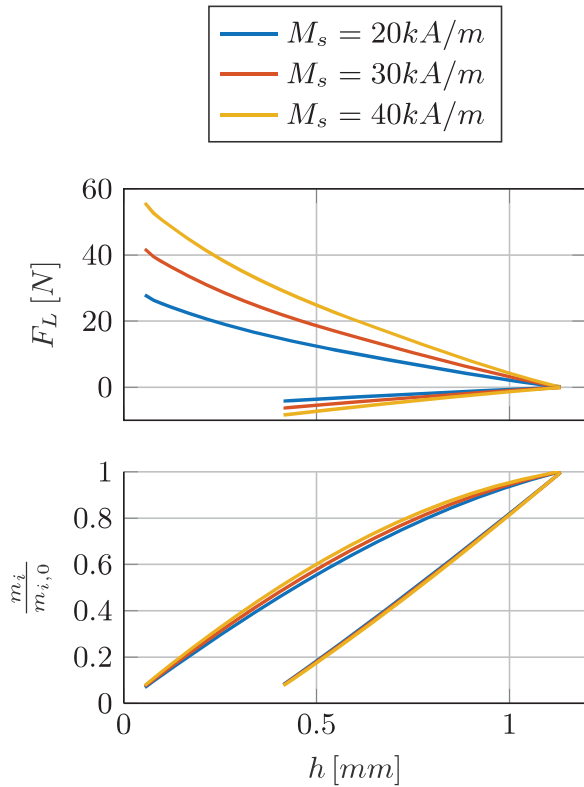


Figure 19. The modelled sensitivity of the load capacity (top figure) and the operational range (bottom figure), with respect to the saturation magnetisation. The other parameters correspond to the measurements, $V_{ff} = 0.38 \text{ ml}$ and $\alpha = 0^\circ$. The air mass inside the pocket is normalised with respect to the initial mass of $M_s = 40 \text{ kA m}^{-1}$.

both the torque and tilt stiffness are lower when compared to the maximally pressurised pocket.

4. Discussion

4.1. Model validation: load capacity and operational range

All three measurements given in figure 16 show a zig-zag pattern, indicating that the mass of air inside the pocket changes. Either mass is gained or mass is lost. When the bearing is compressed, the pressure inside the pocket increases and the load capacity increases. When the pressure increases such that the strength of the ferrofluid seal is exceeded, mass escapes out of the pocket, as described in section 2.1.4. During decompression, the pressure inside the pocket decreases. When the ferrofluid seal cannot withstand the pressure difference any more, mass is gained. Thus, the strength of the ferrofluid seal defines the maximum and minimum load capacity of the bearing, which increase when the fly height is decreased. Overall, both the load capacity and stiffness of the ferrofluid pocket bearing seem to be accurately described by the suggested model, figures 16 and 18.

Measurements 2 and 3 showed that the behaviour of the bearing during decompression differs from the behaviour

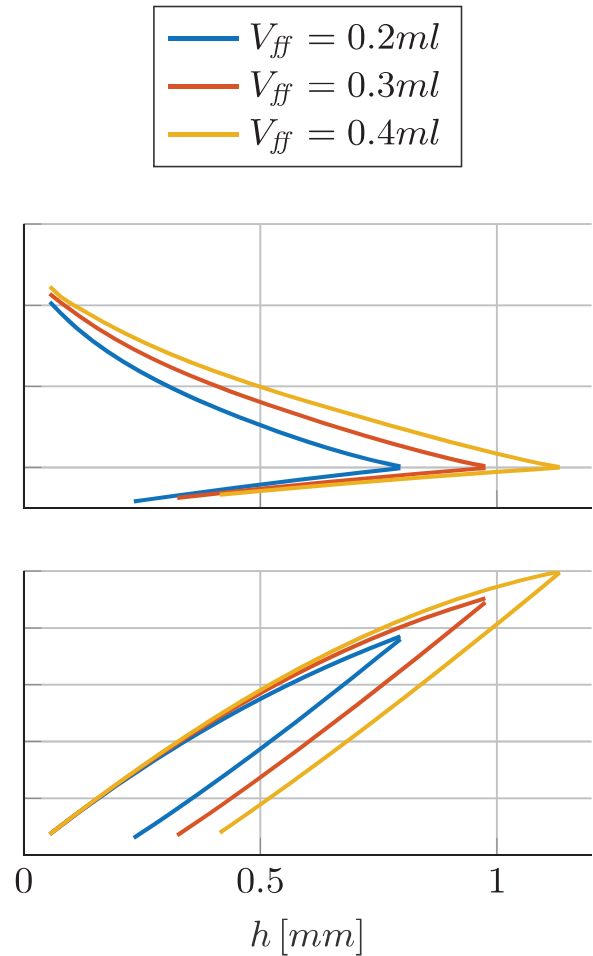


Figure 20. The modelled sensitivity of the load capacity (top figure) and the operational range (bottom figure), with respect to the applied volume of ferrofluid. The other parameters correspond to the measurements, namely $M_s = 0.32 \text{ kA m}^{-1}$ and $\alpha = 0^\circ$. The air mass inside the pocket is normalised with respect to the initial mass of $V_{ff} = 0.4 \text{ ml}$.

found during the initial compression. This phenomenon can be explained by the fact that mass is lost during the initial compression, which changes the system and therefore its characteristics. The zig-zag pattern is not present in the measurements during decompression of the bearing, indicating constant mass. After the minimum strength of the seal gets exceeded, or minimum load capacity, mass is gained and the system changes again. The behaviour of the bearing is repeatable and predictable in the operational range.

The operational range of measurement 3 is well described by the model. In contrast, measurement 2 shows that decompression of the bearing, after almost maximum compression, is less accurately described by the model. Inaccuracy of the model at these low fly heights could possibly be explained by the neglected surface effects, like capillary effects and surface tension. Also, the FEM model neglects magnetisation of the ferrofluid in the calculations. Moreover, the FEM model is sensitive to sharp edges in the geometry and the relative mesh size at those edges, particularly at low fly heights. The measurement itself can also be errored at low

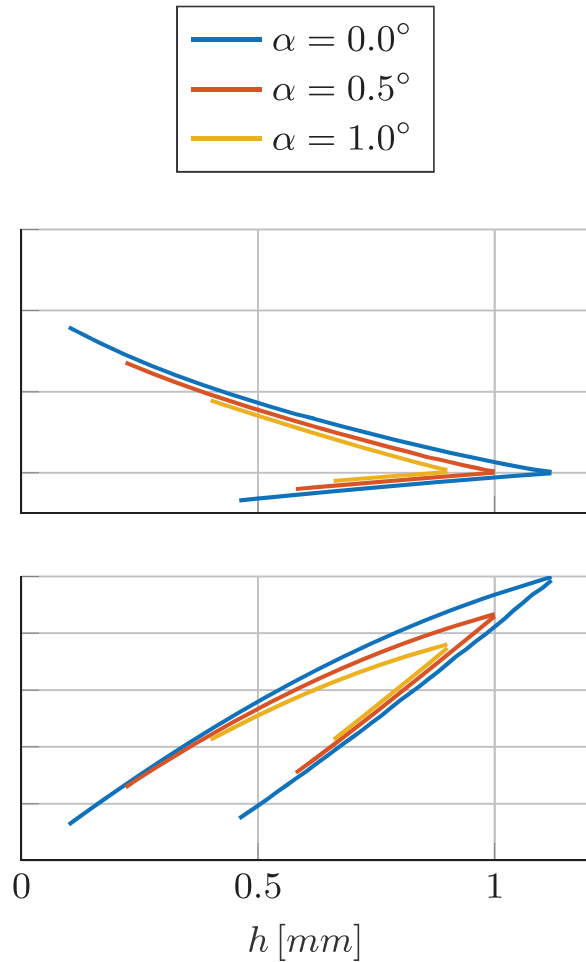


Figure 21. The modelled sensitivity of the load capacity (top figure) and the operational range (bottom figure), with respect to the tilting of the bearing. The other parameters correspond to the measurements, namely $V_{ff} = 0.38$ ml and $M_s = 0.32$ kA m⁻¹. The air mass inside the pocket is normalised with respect to the initial mass of $\alpha = 0.0^\circ$.

fly heights due to for example a damaged magnet. Dents in the magnet result in magnetic field concentrations near the magnet. This effect becomes less pronounced further away from the magnet.

The stiffness of the test set-up is approximately 10 times the stiffness of the bearing. A force of 40 N, which is the approximately the load capacity of the bearing at a fly height of 0.1 mm, results in a displacement error of maximally 20 μ m. Other uncertainties in the model are the saturation magnetisation of the steel base plate and the temperature of the environment. The temperature was not measured during the experiments, but is assumed to be approximately 293 K. The FEM model is able to calculate both static and dynamics problems. However, it is important to note that the model is limited to dynamic problems with relative low accelerations such that the problem can be approximated as quasi-static. This is because the FEM finds the positions of the interfaces between ferrofluid and air by solving for static equilibrium. In contrast, the FEM description makes it possible to include other forces, like capillary forces and surface tension, and to include magnetisation of the ferrofluid.

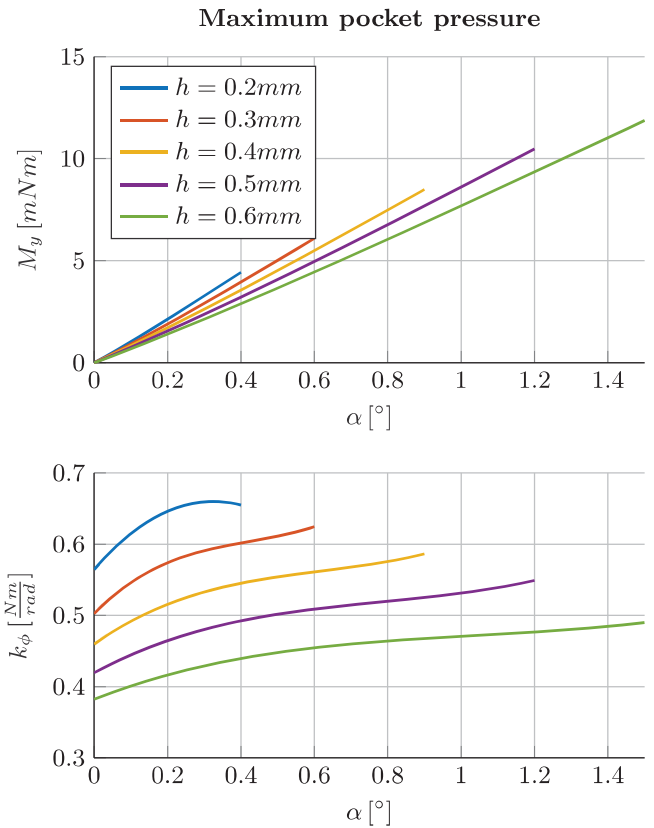


Figure 22. The tilt stiffness (bottom figure) of a maximally pressurised ferrofluid pocket bearing is a result of the torque around the y-axis (top figure), equation (15).

Figure 17 will be used to illustrate and explain the behaviour of figure 16 and to determine the operational range of the bearing. The operational range is indicated in green and is determined by the minimum and maximum pressure difference that the ferrofluid seal can withstand. When the fly height is decreased, the ferrofluid is pushed radially outwards causing ΔH to increase subsequently increasing the strength of the seal. Moreover, the magnetic field is stronger near the magnet thus compression of the bearing will also result in an increased ΔH . The combination of these two effects explains the increase in strength of the ferrofluid seal given in the top figure of figure 17.

The operational range of the bearing can easily be determined from figure 17, by looking at different constant mass lines or horizontal lines in the bottom figure. The intersection between a constant mass line and the green area indicates the operational range for that specific mass. Two examples are given with two sets of black markers. If the fly height is decreased beyond the operational range, mass is lost according to the set of blue markers. Afterwards, the new constant mass line can be used to determine the new operational range of the bearing. If the fly height is increased beyond the operational range, mass is gained according to the set of red markers. Thus, the operational range and behaviour of the bearing is determined by the initial compression, during which mass is squeezed out of the pocket. Note that ferrofluid bearings can easily be reset by separating the bearing and the plate.

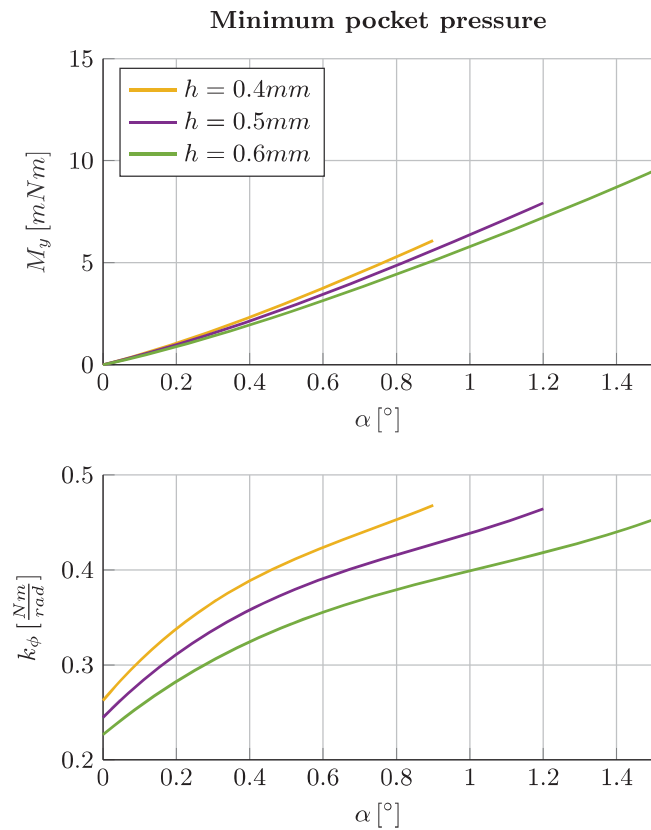


Figure 23. The tilt stiffness (bottom figure) of a minimally pressurised ferrofluid pocket bearing is a result of the torque around the y-axis (top figure), equation (15).

It can be concluded that the model properly describes the behaviour of the bearing, except at very low fly heights. It might be interesting for further research to model and measure the behaviour of multiple seals and pockets, or to use an incompressible fluid instead of air inside the pocket. In both cases, it might be convenient to measure the actual pressure inside the pocket instead of only measuring the force and displacement.

4.2. Sensitivity analysis

Only the three variables that are assumed to be the most erroneous during the actual measurements are discussed in the sensitivity analysis. Other variables, for example surface effects, are neglected in the sensitivity analysis, since they are either neglected or included in the derivation of the model on which the rest of the analysis is based on. The presented values in figures 19–21 are a bit exaggerated for errors that might occur in practice. However, this way the effect of the different errors becomes clearly visible. It is important to note that the effects the variables have on the load capacity and operational range of the bearing are evaluated individually. Combined effects are beyond the scope of this research, however they should be modelled and kept in mind when designing ferrofluid bearings for high precision systems.

Both tilt and the applied volume of ferrofluid have a significant influence on both the load capacity and the operational range. In contrast to increasing the tilt angle,

increasing the amount of ferrofluid increases the operational range and load capacity. Addition of more ferrofluid increases the height of the ferrofluid ring, thus results in earlier contact and establishment of both the seal and air pocket. However, the effect of adding more ferrofluid decreases at low fly heights. When the bearing is almost entirely compressed, the outer interface H_o is nearing zero, so addition of more ferrofluid does not increase ΔH significantly any more. In contrast, both saturation magnetisation and tilt change the behaviour of the bearing at every fly height. The load capacity of the bearing significantly increases when the saturation magnetisation increases. This increase is linear according to equations (1) and (9). It is also worth noticing that the operational range of the bearing is limited by tilting of the plate. Higher tilt angles result in earlier contact of the plate with the bearing surface, thus limiting the operational range. Moreover, tilt decreases the height at which the enclosed air pocket is established, resulting in a decreased load capacity and operational range. Accordingly, some general design guidelines for ferrofluid bearings can be formulated. (1) Tilt of either the plate or the bearing should be minimised, since tilt decreases the load capacity and the operational range. (2) Increasing the volume of ferrofluid increases the load capacity and operational range. Ferrofluid should therefore be added to the system, until the point of diminishing returns.

The small difference between the measured and the predicted load capacity can possibly be explained by the errors discussed here. Since only three possible errors are discussed, no conclusions can be drawn regarding which set of errors was present in the measurements. However, slight overestimation of the amount of ferrofluid is likely, since a ferrofluid trail is left behind on the head of the testing machine after the initial compression.

Figures 22 and 23 show that the tilt stiffness of the bearing is positive for positive tilt angles, for both maximum and minimum pressure inside the pocket. Since the system is symmetric, the tilt stiffness is also positive for negative tilt angles. Therefore, due to the positive tilt stiffness, it can be concluded that the ferrofluid bearing is self-aligning regardless of the pressure inside the pocket. However, in order to be certain that the described behaviour of the ferrofluid bearing is indeed correct, it is recommended that for future work the load capacity and torque of the bearing are actually measured for different tilt angles.

5. Conclusion

This article provides a simple and efficient way to obtain the operational range of a ferrofluid pocket bearing from only the mass versus fly height diagram. The operational range is only dependent on the magnetic field produced by the magnet and the amount of ferrofluid present in the system.

The experimentally validated model accurately describes the load characteristic of a ferrofluid pocket bearing. The model includes the air mass inside the pocket, since both the load capacity and stiffness of the bearing change when the mass changes. Overcompression of the bearing results in mass loss and overdecompression in mass gain. The bearing

shows repeatable and predictable behaviour when the mass inside the pocket does not change. In practice, this is the operational range of the bearing.

The operational range of the bearing is sensitive to errors such as tilt or uncertainty in the applied volume of ferrofluid. The sensitivity analysis shows that tilt decreases both the load capacity and operational range of the bearing. Independent of the pressure inside the pocket, both the torque acting on the plate above the bearing and the resulting tilt stiffness are always positive when tilted. It can be concluded that ferrofluid pocket bearings are always self-aligning. The tilt stiffness increases when the fly height decreases or when the tilt angle increases. Increasing the amount of ferrofluid increases the operational range of the bearing significantly while the load capacity is only increased for higher fly heights.

ORCID iDs

S G E Lampaert  <https://orcid.org/0000-0002-8268-1457>

References

- [1] Rosensweig R E 2013 *Ferrohydrodynamics* (New York: Dover) p 368
- [2] Shliomis M I 1974 *Sov. Phys.—Usp.* **17** 153
- [3] Scherer C and Neto A F 2005 *Braz. J. Phys.* **35** 718
- [4] Raj K, Moskowitz B and Casciari R 1995 *J. Magn. Magn. Mater.* **149** 174
- [5] Raj K and Moskowitz R 1990 *J. Magn. Magn. Mater.* **85** 233
- [6] Rinaldi C, Chaves A, Elborai S, He X and Zahn M 2005 *Curr. Opin. Colloid Interface Sci.* **10** 141
- [7] Urreta H, Aguirre G, Kuzhir P and Lopez de Lacalle L N 2018 *Int. J. Precis. Eng. Manuf.* **19** 495
- [8] Torres-Díaz I and Rinaldi C 2014 *Soft Matter* **10** 8584
- [9] Yang R-J, Hou H-H, Wang Y-N and Fu L-M 2016 *Sensors Actuators B* **224** 1
- [10] Cheng H C, Xu S, Liu Y, Levi S and Wu S T 2011 *Opt. Commun.* **284** 2118
- [11] Jayhooni S M H, Assadsangabi B and Takahata K 2018 *Sensors and Actuators A* **269** 258
- [12] Olaru R, Petrescu C and Hertanu R 2012 *J. Intell. Mater. Syst. Struct.* **23** 1623
- [13] Sudo S, Takaki Y, Hashiguchi Y and Nishiyama H 2005 *JSME Int. J. B* **48** 464
- [14] Uhlmann E and Bayat N 2006 *CIRP Ann.—Manuf. Technol.* **55** 415
- [15] Tipei N 1982 *J. Lubr. Technol.* **104** 510
- [16] Liu Q, Alazemi S F, Daqaq M F and Li G 2018 *J. Magn. Magn. Mater.* **449** 105
- [17] Rosensweig R 1970 *US Patent* US3620584A
- [18] Rosensweig R E, Raj K and Black T J 2003 *US Patent* US6543782B1
- [19] Mitamura Y, Takahashi S, Amari S, Okamoto E, Murabayashi S and Nishimura I 2011 *J. Artif. Organs* **14** 23–30
- [20] Ravaut R, Lemarquand G and Lemarquand V 2010 *Tribol. Int.* **43** 76–82
- [21] Rosensweig R 1987 *Annu. Rev. Fluid Mech.* **19** 437
- [22] Potma O G R 2017 Designs for rotary shaft fluid seals in an aqueous environment using ferrofluid *Msc Thesis* Technical University Delft
- [23] Arcire A, Olaru R and Petrescu C 2012 *EPE 2012—Proc. 2012 Int. Conf. Exposition on Electrical and Power Engineering* p 776
- [24] Boots A, Krijgsman L, de Ruiter B, Lampaert S and Spronck J 2019 *Tribol. Int.* **129** 46–54
- [25] Olaru R, Petrescu C and Arcire A 2013 Maximizing the magnetic force generated by an actuator with non-magnetic body in a ferrofluid pre-magnetized by permanent magnets *Int. Rev. Electr. Eng.* **8** 904
- [26] Alvarez-Aguirre A, Mok G, HosseinNia S H and Spronck J W 2016 *2016 Int. Conf. on Manipulation, Automation and Robotics at Small Scales, MARSS 2016* (<https://doi.org/10.1109/MARSS.2016.7561698>)
- [27] Deng R, van Veen S, Café M, Spronck J W and Schmidt R H M 2014 Linear nano-positioning stage using ferrofluid bearings *14th Euspen Int. Conf. (Dubrovnik, June 2014)* p 4
- [28] Lampaert S, Spronck J, van Ostayen R and Café M 2014 (2+4) DOF precision motion stage with ferrofluid bearings *American Society for Precision Engineering* 63
- [29] Lampaert S, Spronck J, van Ostayen R and Habib H 2016 XY360 – Planar Positioning Stage with a PSD sensor and ferrofluid bearings *DSPE Conference on Precision Mechatronics* p 57
- [30] Millet G and Hubert A 2006 *Actuators'06* June, 656–59
- [31] Lampaert S G E, Fellingner B J, Spronck J W and van Ostayen R A J 2017 *Precis. Eng.* **54** 163–70
- [32] Petit M, Kedous-Lebouc A, Avenas Y, Tawk M and Artega E 2011 *Prz. Elektrotech.* **9b** 115–19
- [33] Yu J, He X, Li D and Li W 2018 *Phys. Fluids* **30** 092004
- [34] Lampaert S G E, Spronck J W and van Ostayen R A J 2017 *Proc. Inst. Mech. Eng. J* **232** 14–25
- [35] Neuringer J L and Rosensweig R E 1964 *Phys. Fluids* **7** 1927

Design of a passive alternative for long stroke linear aerostatic stages based on ferrofluid bearings

Stefan W.M. van den Toorn^a, Jo W. Spronck^a, Ron A.J. van Ostayen^a and Stefan G.E. Lampaert^a

^aDepartment of Precision and Microsystems Engineering, Delft University of Technology, Delft, The Netherlands

ARTICLE INFO

Keywords:

Magnetic fluid
Passive bearing
Ferrofluid linear stage
Air bearing alternative
Ferrofluid design

ABSTRACT

The objective of this research is to demonstrate the capability of a long stroke linear ferrofluid (FF) stage. This stage can be a passive alternative to existing linear aerostatic stages and can be used in low loaded CNC devices, pick and place machines, microscopy or scanner applications. To compete with aerostatic stages the bearing must be repeatable and achieve sufficient stiffness for the application. The effects of FF trail formation were countered with the use of a FF reservoir located on the mover. To increase stiffness a specially designed magnet configuration is used. A stage was built with outer dimensions of 180x600x80 mm (WxLxH), a mover of 1.8 kg without actuator and payload having 430 mm stroke. The load capacity of the stage was measured to be 120 N, with a stiffness of 0.4 N/ μm . The maximum height delta after a stroke with 1 kg payload and a mover velocity of 0.25 m/s was measured to be less than $\pm 3 \mu\text{m}$, with 1.75 kg payload and a velocity of 0.5 m/s the height delta was within $\pm 7 \mu\text{m}$. Using a rheometer, it was shown that the effects of evaporation in FF can be reversed by adding carrier fluid, within certain limits of mass loss. The damping is shown to be a function of payload and velocity and was measured to be between 2 and 4 N·s/m for velocities between 0.2 and 0.5 m/s. In comparison to a linear aerostatic stage it can be concluded that while the linear FF stage is outperformed in stiffness and out-of-plane repeatability, the FF stage doesn't require a continuous supply of air and has lower fabrication tolerances due to the higher fly height. Thus, the linear FF stage is a cost-effective alternative to a linear aerostatic stage when the stiffness and straightness are of less importance.

1. Introduction

The aerostatic bearing can't be overlooked in current precision positioning systems. The relatively simple concept of floating on top of a cushion of air has obtained a major market share in the past decades [18]. The use of pressurized air however also has its downside, as the bearing seizes when the air pressure is stopped, the manufacturing tolerances are very tight, the system is difficult to implement in vacuum environments and the low damping gives problems in controlling the movement [38]. In the search for alternatives we find that conventional bearings such as ball or journal bearings suffer from stick-slip, magnetic bearing suffer from complexity and flexures suffer from energy storage and a limited range of motion. A bearing type free from all of these issues is the ferrofluid (FF) bearing.

The ferrofluid bearing consists out of a ferrofluid in between bearing surfaces in a magnetic field. FF is a stable colloidal suspension of magnetic particles ($\sim 10 \text{ nm}$) in a carrier fluid [28]. The bearing itself relies on pressure build-up in the fluid as it is attracted by a magnetic field. This pressure build-up is caused by the displacement of the fluid from a position with a high magnetic field to a position with a lower magnetic field. This generates a normal force onto the bearing surface. Alternatively, the FF can be used to seal a pressurized pocket of air which provides the normal force. The first concept is known as the FF pressure bearing [33], the second is known as the FF pocket bearing [34]. The working principle of these bearings is illustrated in figure 1.

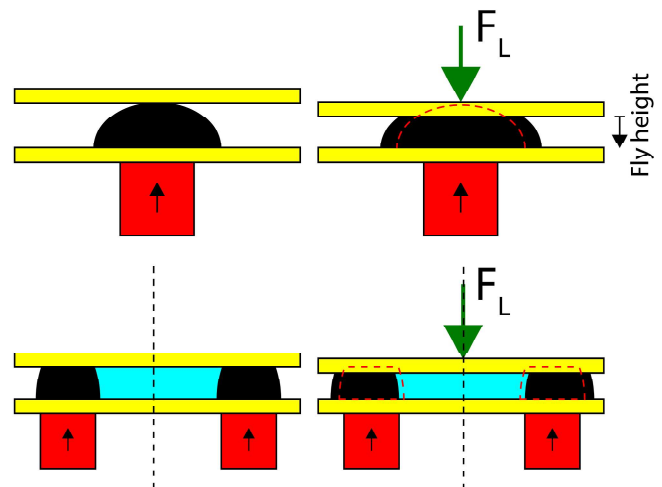


Figure 1: Working principle pressure bearing (up) and pocket bearing (down).

The relation between the ferrofluid bearing and other bearing solutions can be seen in table 1. The table shows that the aerostatic bearing outperforms the ferrofluid bearing in load capacity and stiffness. However, the ferrofluid bearing can fill a niche that has been left open by the other bearing types i.e. low-cost passive applications requiring a smooth motion without demand for high stiffness. These applications can range from low loaded CNC devices such as 3D printers or laser cutters to optical devices such as microscopy or scanners. An entirely different field of application would be the

✉ stefanvandent@gmail.com (S.W.M. van den Toorn)
ORCID(s):

Table 1

Ferrofluid bearings in comparison to other bearing solutions for precision positioning [43, 29, 32, 3, 5]. The ferrofluid bearing is taken as benchmark, a better performance in precision positioning applications is denoted with +.

	Ferrofluid	Active magnetic	Hydrostatic	Aerostatic	Roller bearing
Load	0	+	++	0	+
Stiffness	0	++	++	+	++
Static friction	0	0	0	0	--
Dynamic friction	0	--	0	--	-
Surface finish requirement	0	++	-	--	--
Complexity	0	--	-	-	0
Advantage	No stick slip	UH vacuum compatible	Large loads	Contactless	Standardized
Disadvantage	Low stiffness	Inherently unstable	Lubrication oil	Supply Pressure	Stick-slip

use in zero gravity environments, as the fluid is contained in the magnetic field.

The FF bearing has some other advantages. The magnetic field necessary for a Lorentz actuator is already available. The system has a relatively low required tolerances in relation to similar high precision bearings due to the relatively large (~0.5 mm) distance between bearing surfaces. The FF itself acts as a lubricant. The large surface area in contact with the fluid allows for heat transfer between the bearing surfaces. The broad choice in carrier fluid makes it possible to tune the bearing for different environments, for example a fluid with a low vapour pressure for use in a vacuum, or a fluid with a low viscosity for fast motion. The amount of physical damping makes controlling the system easier. It decreases the sensitivity to high frequency disturbances, thus reducing the need for complicated filtering [35, 10, 36, 13] or external damping [37, 41].

In the last decade FF bearings were implemented into various planar positioning systems [7, 6, 23, 1, 24, 42] and into linear stages [44, 9, 2], the behaviour in load capacity and damping were studied [27, 31, 26, 45, 4, 16, 17], and finally basic design rules for FF bearings were formulated by Lampaert [15]. Still all existing demonstrators suffer from a low repeatability in the constrained directions and a limited range of motion. These issues are the result of the loss of air from the pocket bearings and loss of FF due to trail formation.

In this study a passive long stroke linear stage based on ferrofluids is proposed. The challenges in the long stroke bearing primarily are achieving a sufficient stiffness, repeatability and stroke length. Problems and implementations of the solutions are discussed, designed and build in a demonstrator stage for the purpose of verification. The specifications for this demonstrator stage are based on those of a commercially available aerostatic linear stage.

2. Stage design

The proposed demonstrator is based on an existing linear bearing stage from Physical Instrumente, the A-110. This air bearing stage is marketed as a high performance affordable nanopositioning stage. The aim of the demonstrator stage is

made to be interchangeable with this aerostatic stage, thus conforming to the same or better specifications. These specifications can be seen in table 2.

2.1. Challenges

In the design of the stage some specific challenges were considered. The most pressing matters were air loss, trail formation and evaporation. Air loss is distinctive for FF pocket bearings, where the fly height is permanently reduced once the bearing is loaded beyond the load capacity of the ferrofluid seal. The fly height is defined as the distance between bearing surfaces and can be seen in figure 1. Trail formation is the occurrence where fluid is left behind as the bearing is translated. Evaporation changes the composition of the ferrofluid suspension and alters the fluid properties such as viscosity and saturation magnetization. If left unaddressed, each problem can severely compromise the performance and repeatability of the stage. Solutions for each of these problems have been implemented in this bearing stage.

The problem of air loss is distinctive to FF pocket bearings only, the FF pressure bearing does not suffer from this problem. In terms of load capacity and stiffness, the pocket bearing outperforms the pressure bearing. As the repeatability of the bearing is considered more desirable than load capacity or stiffness the pressure bearing is the preferred bearing type for this application.

The trail formation problem is solved by the creation of a reservoir on the mover itself. By assuming a Couette flow between the bearings and base the total amount of fluid loss is estimated at 20 ml. As the amount of fluid required is low, this reservoir can be incorporated into the pressure bearings themselves. The ferrofluid can move freely between the individual pressure bearings. This ensure a repeatable behaviour and redistributes the collected trail.

A ferrofluid with a low viscosity is used to decrease trail formation and to limit damping. As this fluid has a higher vapor pressure than is desired the evaporation problem needs to be addressed. In order to do this, the effect of resupplying the evaporated carrier fluid is researched.

The design of the stage is a double u shape as shown in figure 2. The preload increases stiffness and the symmetric design reduces tilt under movement. The in-plane length of

Table 2
Specifications of A-110.300 linear air bearing stage [30]

Model	A-110.300
Travel	300 mm
Maximum payload	10 kg normal
Flatness	$< \pm 2 \mu\text{m}$
Moving mass	2.6 kg
Maximum velocity	1 m/s
Outer dimensions	160 × 575 × 60 mm (W × L × H)
Mover dimensions	160 × 200 × 60 mm (W × L × H)

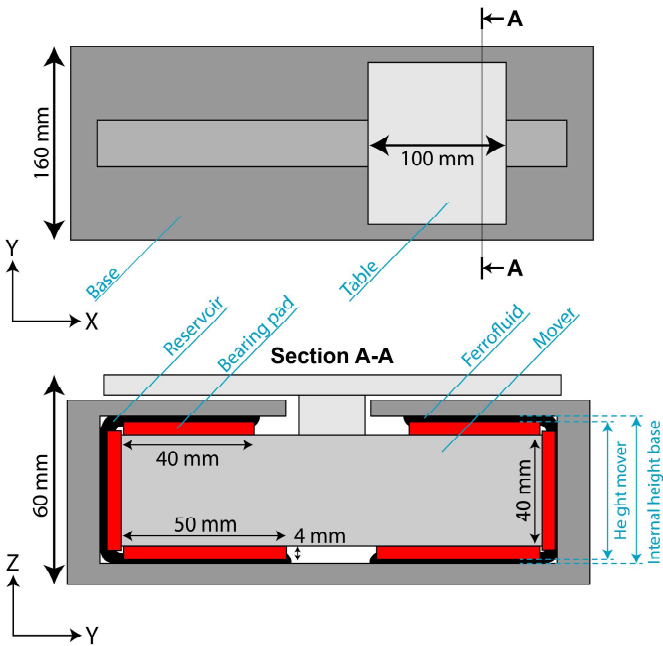


Figure 2: Schematic bearing design with areas reserved for bearing in red.

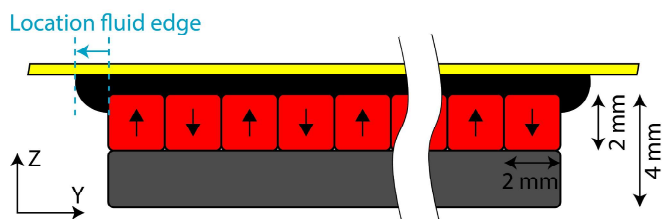


Figure 3: Bearing pad cross-section showing the layout. The in-plane length of the bearing pad is 100mm.

the mover is 100 mm, to save weight and to reduce damping. The areas marked in red are reserved for 6 bearing pads, two of 50x100x4 mm (W x L x H) for the bottom bearings and four 40x100x4 mm (W x L x H) for the side and top bearings. For this research the kerosene based EFH3 fluid from Ferrotec is chosen. This FF has a relative high saturation magnetization of 66 mT and a viscosity of 12 mPa·s [11].

2.2. Bearing pad

Each bearing pad consists out of 50x2x2 mm magnets from HKCM [14]. These magnets are arranged in an ‘up-down’ magnetization configuration with the long side in the movement direction as can be seen in figure 3. The bottom bearing pads are arranged in a 2x25 grid (x*y), the top and side bearing pads are slightly smaller and are arranged in a 2x20 grid (x*y). The use of many small magnets results in a concentrated magnetic field close to the magnets with a large gradient in the direction of the fly height. This results in a high load capacity and stiffness for a ferrofluid pressure bearing. Instead of an up-down magnetization configuration, the magnets can also be magnetized facing each other, all in the same way or by means of a Halbach array. Alternatively, also iron can be used in between the magnets to shape the magnetic field. It was found that from these possible configurations the up-down configuration with an iron bottom plate is the most cost-effective way to achieve a high stiffness and load capacity while also having little moving mass [40]. A second benefit of this arrangement is the low stray field, as the individual magnets cancel each other at larger distances. Magnets with a smaller cross-section can increase stiffness of the bearing, but the brittleness and increased number of magnets would make assembly complex. Ferritic stainless steel is used instead of iron due to rust. Although 0.5 mm thickness of the bottom plate would already have yielded the same performance, for assembly purposes a relative thick bottom plate of 2 mm is used. As the pressure bearings are located close together, the magnetic field intensity is relatively high at the adjoining corners of the bearing pad as can be seen in figure 2. The ferrofluid that accumulates there has a negligible effect on the load capacity of the stage, this is used as a reservoir of ferrofluid to counter the effects of trail formation. As this reservoir bridges the different bearing pads it also can transport fluid between the bearing pads, ensuring a repeatable performance.

2.3. Modelling stage load capacity and stiffness

Using a mathematical model of the magnetic field in COMSOL [8] and Matlab [39], the load capacity and stiffness of the bearing pads were determined. The geometry of the pad was built in Matlab using the COMSOL Livelink interface, the magnetic field was then calculated in COMSOL and afterwards post-processed in Matlab. In the model several assumptions are made for the remanent flux density of the magnets (1.17 T), saturation magnetization of the ferrofluid (66 mT) and the location of the fluid edge (5mm). The definition of the fluid edge location is shown in figure 3. The FF itself is modelled as air, having a relative permeability of 1. For the ferritic stainless steel, a relative permeability of 4000 is used with a saturation magnetization of 1.4 T.

The chosen bearing stage design gains added stiffness through a preload. This preload can be varied by varying the difference in height of the mover and the internal height of the base as can be seen in figure 2. The design of the demonstrator is made such that this height difference can be varied easily. Decreasing the height difference decreases the

fly height of the top and bottom bearing pads and thus increases the applied preload. As the ferrofluid bearing can be seen as a spring this increases the stiffness of the bearing. The increased stiffness however comes at the cost of less load capacity and more viscous damping. Decreasing the fly height also reduced the amount of fluid necessary as the physical volume between the bearing surfaces decreases. An additional effect of the preload is a more stable fly height as the trail formation will also occur on the top side and thus, the fluid loss is symmetrical. As the bearing pads on top and bottom differ in size and gravity acts on the mover, the equilibrium position of the top and bottom pad will not be exactly the same.

Table 3 shows the bearing characteristics as function of the fly height according to the model. In order to achieve the same specifications as the A-110 aerostatic stage the fly height in vertical direction will need to be somewhere between 0.5 mm and 0.25 mm. As no horizontal payload is known for this stage a fly height of 1 mm in the horizontal pads is assumed to be sufficient.

Table 3

Bearing characteristics in horizontal and vertical plane for different fly heights. Stiffness is evaluated around equilibrium position. Load capacity is evaluated at the minimum fly height of 0.1 mm.

Horizontal			
Fly height left pad [mm]	Fly height right pad [mm]	Load [N]	Stiffness [N/ μm]
0.1	1.9	120	0.23
0.1	0.9	92	0.27
0.1	0.4	49	0.34
0.1	0.15	11	0.43
Vertical			
Fly height bottom pad [mm]	Fly height top pad [mm]	Load [N]	Stiffness [N/ μm]
0.1	0.9	231	0.68
0.1	0.4	146	0.81
0.1	0.15	69	0.97

2.4. Eddy current damping in stage

Aluminium is the preferred material for the demonstrator stage due to its availability and machinability. The relative velocity between the good conducting aluminium and the magnetic fields induced by the bearing pads can create eddy currents. The damping induced by these eddy currents is investigated using a COMSOL model. Figure 4 illustrates this model and the direction of the relative velocity between the bearing pad and conductor. In the model the used bearing pad is translated past a long aluminium block. The bearing pad consists out of 2x25 magnets ($x*y$) of 50x2x2 mm with a remanent flux density of 1.17 T. The results of the modelling can be seen in table 4.

In table 4 can be seen that the simulated eddy current damping is low. The low damping is caused by two factors. Firstly, as the eddy currents are induced by a change in mag-

Table 4

Simulation of eddy current damping in full size pressure bearing pad. Magnet dimensions 50x2x2 mm, arranged in a 2*25 ($x*y$) grid with long edge in x -direction, magnetized alternating between positive and negative z -direction.

Fly height [mm]	Eddy current damping coefficient [N·s/m]
0.10	0.22
0.25	0.13
0.50	0.07
1.00	0.03

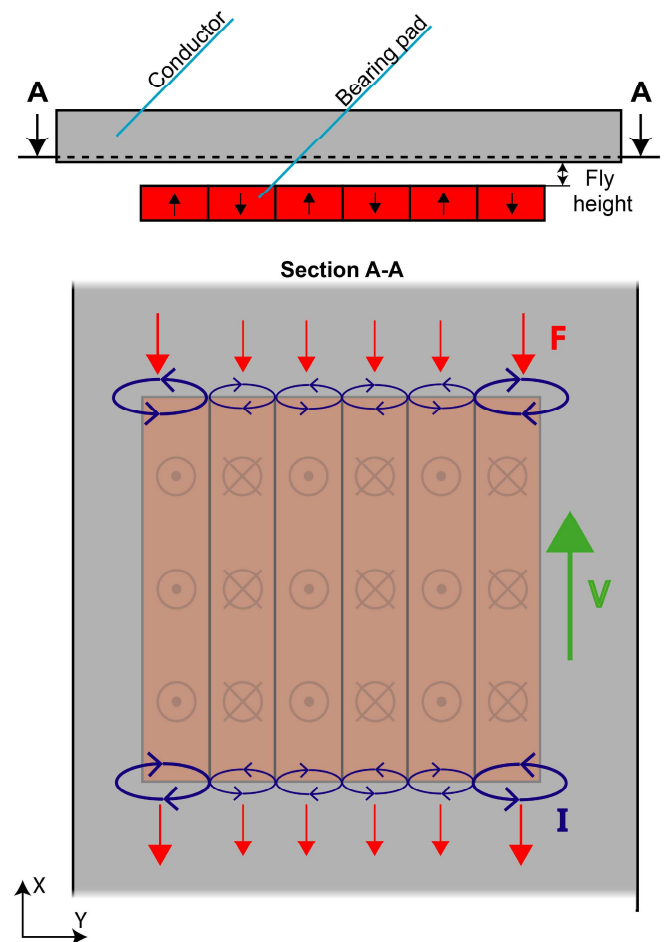


Figure 4: Illustration of the location and magnitude of the eddy currents (I) on the surface of the conductor. With the direction of the relative velocity between conductor and bearing pad (V) in green and damping force (F) direction in red.

netic field the current loops can only occur at the start and end of the bearing pad. Secondly, as the magnetization direction of the magnets alternate the direction of the current alternates as well. This prevents large current loops from forming. Both factors can be seen in figure 4.

3. Methods for design validation

To verify that the functioning of the stage is as intended, first the load capacity and stiffness model of an individual pressure bearing pad are validated. This same model then is used in the verification of the load and stiffness of the full stage. To gain insight in the performance of the stage when in use, the effects of trail formation and evaporation will be measured. Finally, the damping and flow profile between bearing surfaces will be experimentally determined. This can benefit the future actuation of the stage.

3.1. Single pressure bearing pad

The individual tested pressure bearing pad is assembled of 23 50x2x2 magnets [14] with a remanent flux density of 1.17 T structured as seen in figure 3. The pad is tested with 5 ml of EFH3 fluid and with the same amount of APG 513A ferrofluid. The load-fly height curve of the bearing is measured using a materials test frame and compared to the model.

For the modelling of the pressure bearing path the location of the outer fluid edge is needed. This variable is defined in figure 3, and represents the starting point of the pressure build-up in the fluid. The location is primarily dictated by the equilibrium between the gravitational pull and the magnetic body force on the fluid. The effect of surface tension and surface roughness on this location is negated. Using COMSOL the magnetic field surrounding the bearing pad is simulated, resulting in a location of the outer fluid edge of 0.9 mm outside the magnet. The magnetization saturation of the ferrofluid is modelled as 32 kA/m [25] for the APG 513A and 52.5 kA/m for the EFH3 [12].

3.2. Demonstrator stage

The demonstrator as seen in figure 5 was constructed from aluminium with ferritic stainless-steel bottom plates for mounting the magnets. The top plate could be raised using shims to increase the fly height of the top and bottom bearing pads. The total material cost for the ferrofluid demonstrator stage are slightly over €1000, the magnets attribute €150.

Table 5
Physical properties of realized demonstrator stage

Travel	460 mm
Moving mass	1.84 kg
Outer dimensions	180 × 640 × 80 mm (W × L × H)
Mover dimensions	139 × 124 × 60 mm (W × L × H)

In table 5 the physical properties of the realized stage can be seen. The base and mover have both been overdesigned. Thicker metal is used in in order to increase production efficiency and to allow for more freedom in the fine-tuning of the height difference between mover and base. Because of this, the width and height of the outer dimensions could both be reduced with 20 mm without any performance loss.

Figure 5 shows the demonstrator and the three Micro-Epsilon optoNCDT 1420 laser distance sensors [21] used.

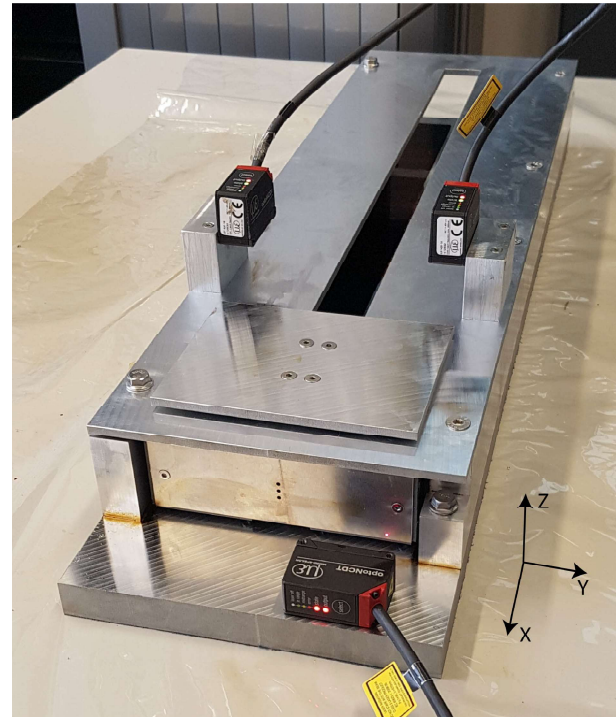


Figure 5: Measurement setup of demonstrator with 3 laser distance sensors for position and roll of the mover.

2 sensors with a range of 10mm were fitted above the table on either side. These sensors measure the position of the table relative to a fixed frame. From this the fly height and roll of the stage could be found. One sensor with a range of 200 mm was mounted in front of the mover and was used to measure displacement and velocity of mover. The demonstrator stage was connected to an actuator using a thin wire. By setting the demonstrator at a slight incline, it could thus be actuated in both directions with negligible disturbance to the measurements.

Unless mentioned otherwise, all experiments are conducted using the EFH3 ferrofluid from Ferrotec.

3.2.1. Load and stiffness

The load and stiffness of the stage is determined using three different methods. The first method is by using a materials test frame. In the second method weight is added to the table manually while measuring the height using the later distance sensors. The third method is to set the stage at very small inclination and to add weight until the mover stops moving freely.

3.2.2. Trail formation

Figure 6 shows the trail formation in the bearing. The trail thickness can be deduced from the colour of the trail. The light brown on the right and almost black on the left indicate a strong correlation between the amount of fluid loss and the movement velocity. The influence of this trail formation is experimentally determined by measuring the height of the stage at the end of a stroke. This is done for different amounts of fluid in the system and for different translation

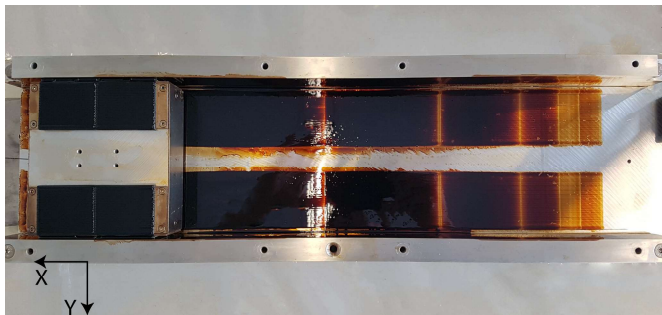


Figure 6: Trail formation in stage. The mover has been displaced in steps increasing in velocity from right to left. The table and top plate were removed before the displacement.

speeds.

3.2.3. Evaporation

The evaporation rate of the ferrofluid was determined by placing five grams of fluid in a Petri dish. The fluid-air interface was 58 cm² and the temperature was kept between 18 and 22 degrees Celsius. The Petri dish with fluid is weighed at several moments in time. The effects of evaporation on the fluid viscosity and magnetic properties are investigated using a rheometer. This rheometer is capable of generating a magnetic field comparable to the field at the surface of the pressure bearing pads. The evaporation rate is established by the mass loss in a controlled volume over time. Fluid with different percentage of mass loss is then evaluated in the rheometer. This same experiment is redone for fluid with the same percentage of mass loss, this time resupplied to original mass by addition of paraffin oil.

3.2.4. Damping

The damping of the stage is evaluated by setting the stage under a defined incline. The external stage is used to pull the mover onto the slope and to release it at the highest point. Gravity will accelerate the stage until it reaches terminal velocity, which is measured using the 200 mm laser distance sensor. This is done for several times for a combination of three different inclinations and three different amounts of payload. As the weight of the stage is known, the driving force can be calculated. The damping coefficient then follows from the terminal velocity and the driving force.

The flow profile in between the bearing plates is derived by combining the data from the damping in the stage with the damping model from Lampaert [16]. The damping model used assumes a Couette flow with negative pressure gradient and derives the pressure gradient by assuming zero trail formation. As can be seen in figure 6, this assumption is invalid for this bearing. Thus, data from the damping in the stage is used to derive the pressure gradient.

In equation 1 shows the velocity profile of the fluid, u_x according to the damping model from Lampaert. With η the shear rate dependent viscosity of the ferrofluid, h the height

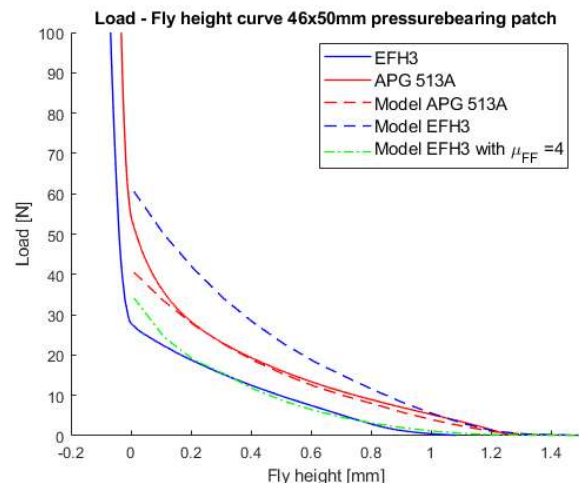


Figure 7: Load-fly height curve of 23x1 pressure bearing pad with EFH3 and APG 513A ferrofluid.

of the FF film and U the velocity of the mover.

$$u_x = \frac{1}{2\eta} \frac{\partial p}{\partial x} (z^2 - hz) + \frac{U}{h} z \quad (1)$$

The $\frac{\partial p}{\partial x}$ describes the pressure drop in the flow direction. This term can be determined based on data from the experiment. Based on initial testing and observations in the trail formation it is assumed that the relation between the damping coefficient and velocity is linear. This results in a quadratic relation between the velocity and the damping force. The damping force can be derived using formula 2 and taking $z=h$, giving following formula 3.

$$\tau_{zx} = \eta \frac{\partial u_x}{\partial z} \quad (2)$$

$$\tau_{zx} = \frac{1}{2} \frac{\partial p}{\partial x} h + \eta \frac{U}{h} \quad (3)$$

The friction force on the mover will be measured by measurement of the terminal velocity. The contribution of a single bearing pads to the friction force can be determined by assuming it is proportional to the contribution when assuming a Couette flow over the bearing pads. The pressure drop term can then be determined using equation 3 and the friction force on a single bearing pad.

4. Bearing design validation

4.1. Single pressure bearing pad

Figure 7 shows the results of the testing of the individual pressure bearing pad. Zero displacement was taken to be the point at which the pressure plate touches the magnets in the measurement.

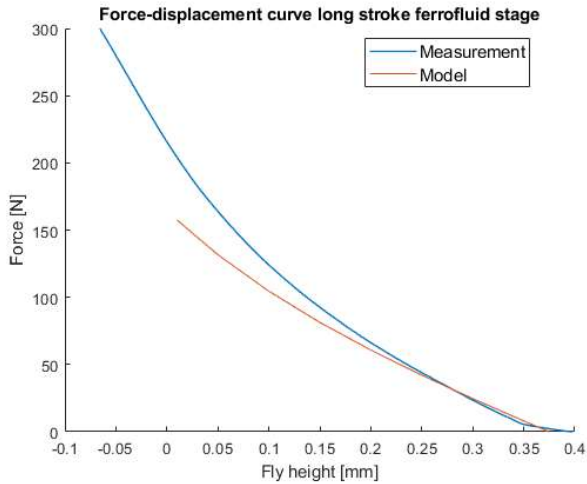


Figure 8: Load-fly height curve of stage. The crosshead velocity of the materials test frame was set to 0.5 mm/min. The initial fly height without payload is 0.39 mm for the bottom bearing pad and 0.36 mm for the top bearing pad. The bearing pads are modelled with a relative permeability of 4 for the ferrofluid.

4.2. Demonstrator stage

4.2.1. Load capacity and stiffness

The experiment from section 4.1 was repeated for the full stage. The results of this is shown in figure 8. The individual fly heights of the top and bottom pad are taken to be such that the modelled load generated by the bottom pad is equal to the modelled load of the top pad combined with the gravity forces. This result in 0.39 mm for the bottom pad and 0.36 mm for the top pad. The fly height of the bottom pad is larger than the top pad as the size of these bearing pads differ.

The maximum sustained load capacity was determined by adding mass to the stage whilst being under a small incline and was found to be 140 N for a stroke of under 100 mm and 120 N for the full stroke.

The stiffness was also determined at different initial fly heights by using the laser displacement sensors and a weight of 3 kg. The model parameters were chosen to be the same as in figure 8. Table 6 shows the results of these measurements. It can be seen that the model corresponds well with the measurements at larger fly heights. When the fly height decreases, the model and measurement diverge.

Table 6

Measured and modelled stiffness of stage for different fly heights for the bottom and top bearing pad.

Fly height	[mm]	0.3/0.25	0.4/0.35	0.55/0.50
Measured Stiffness	[N/ μ m]	0.73	0.44	0.31
Modelled Stiffness	[N/ μ m]	0.57	0.42	0.36

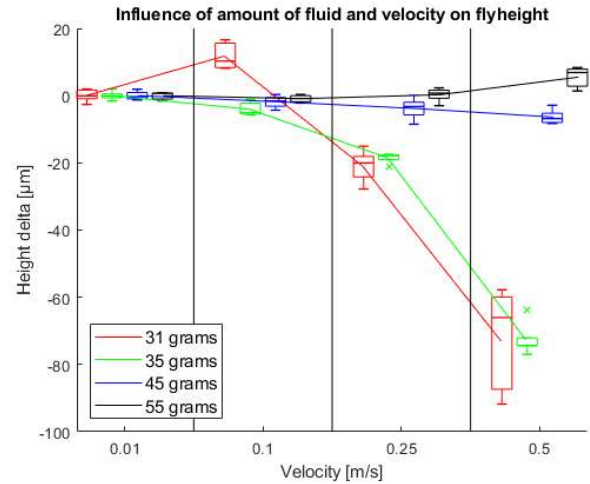


Figure 9: Height delta of the mover height under translation at different speeds for different amounts of fluid. No payload was added to mover.

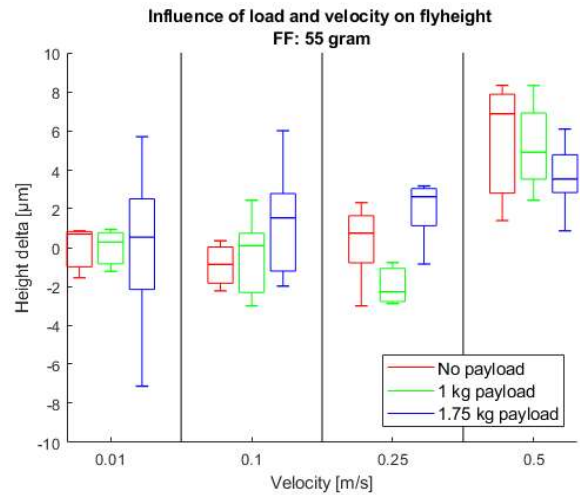


Figure 10: Height delta of the mover height under translation at different speeds when filled with 55 grams of FF.

4.2.2. Trail formation

Figure 9 shows a significant height drop at higher translation velocities using a limited amount of FF. Figure 10 shows the relative height of the stage for 55 grams of fluid and different payload amounts. It can be seen that the payload has no noticeable influence on the repeatability of the height. The zero in these figures is taken as the mean at 0.01 m/s. The initial fly height was set to 0.55 mm for the bottom pad and 0.50 mm for the top pad.

4.2.3. Evaporation

The evaporation measurement resulted in an evaporation rate in the initial 74 hours of $9.0 \cdot 10^{-5}$ g/(cm²·h) for the EFH3 fluid. The evaporation rate in the next 43 hours was $5.6 \cdot 10^{-5}$ g/(cm²·h). Using a rheometer, the properties of the ferrofluid were evaluated when subjected to evaporation.

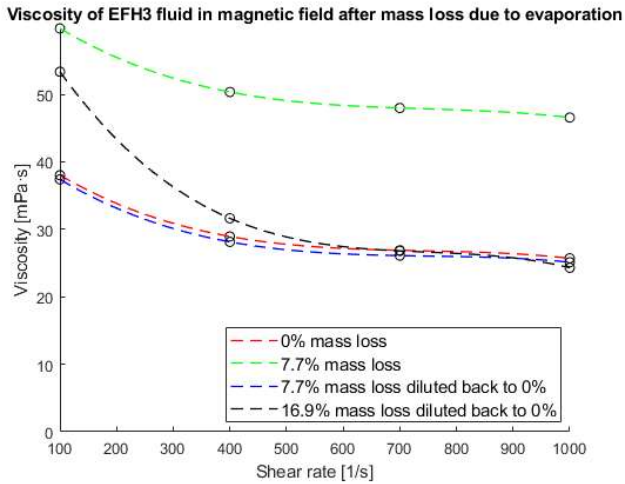


Figure 11: Viscosity of EFH3 fluid for different levels of evaporation and dilution.

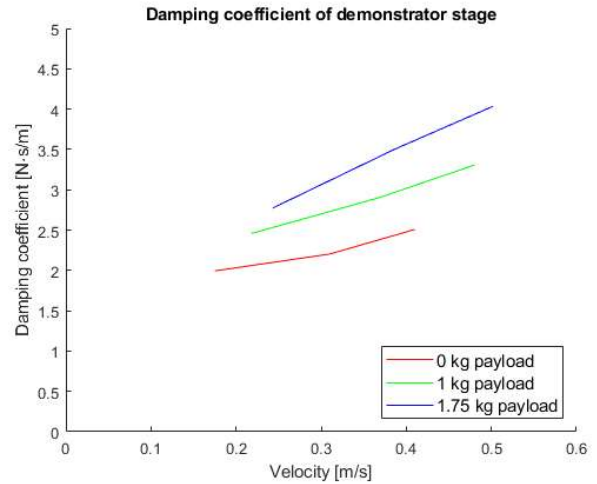


Figure 13: Damping coefficient of demonstrator stage for different loads.

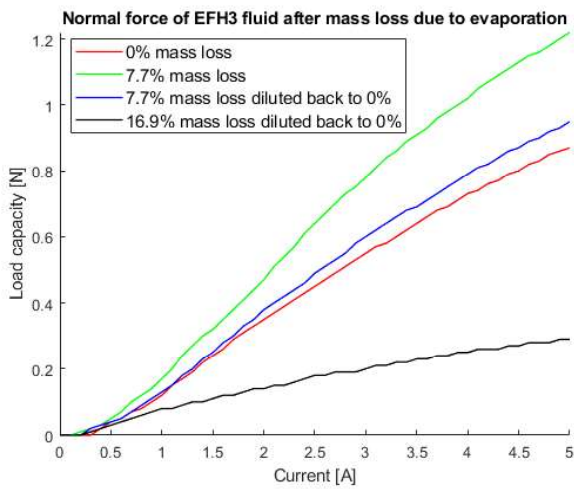


Figure 12: Normal force exerted by EFH3 fluid on the rheometer for different levels of evaporation and dilution.

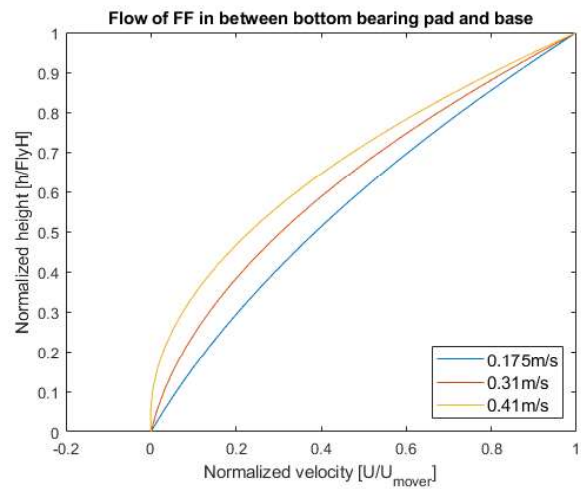


Figure 14: Flow in ferrofluid in between the bottom bearing pad and base based on equation 1 and the data presented in figure 13 for the damping coefficient without payload to fit the pressure drop term.

This was done for the EFH3 fluid subjected to 7.7 % mass evaporation and 16.9 % mass evaporation and can be seen in figures 11 and 12. Figure 11 shows the viscosity in the ferrofluid as a function of the shear rate. Figure 12 shows the normal force exerted on the rheometer by the ferrofluid.

4.2.4. Damping

The results of the damping experiment can be seen in figure 13, the stage was filled with 45 grams of FF and has an unloaded fly height of 0.55 mm for the bottom pad and 0.50 mm for the top pad. There is a strong correlation between the damping coefficient and the load and velocity of the stage.

The pressure drop term is fitted to the data, the found values for the bottom bearing in the measurement without payload are $1.9 \cdot 10^4$, $5.2 \cdot 10^4$ and $9.4 \cdot 10^4$ Pa/m for respective 0.175, 0.31 and 0.41 m/s mover velocity.

5. Discussion

5.1. Single pressure bearing pad

The data from the pressure bearing test using the APG 513A ferrofluid results in a load capacity of 40 N, resulting in 1.8 N/cm^2 . The load capacity and stiffness of the bearing could have potentially been higher by opting for pocket bearings instead of pressure bearings. Though, the values for load and stiffness are comparable to a previous implementation of a single pocket bearing stage [24] where a load capacity of 100 N was achieved using a surface area of 84 cm^2 , resulting in 1.2 N/cm^2 . Thus, to improve over the current design more complex pocket bearings with multiple seals would be required. This would result in more pockets of air which all need to be managed to maintain repeatability.

The load capacity using the EFH3 fluid is lower than with the APG 513A. This is unexpected as the EFH3 has a higher saturation magnetization. This behaviour might be explained by the loss of colloidal stability due to the high gradient in the magnetic field [22]. Magnetic particles will then accumulate at the corners of the magnets. This accumulation can be problematic in this specific magnet geometry as a large build-up of particles in between the two oppositely magnetized magnets will cause a short circuit in the magnetic field.

This behaviour is simulated in the model using an increase of relative permeability. A relative permeability of 4 is in close agreement with the measurement of the EFH3 fluid. This can be seen in figure 7

5.2. Demonstrator stage

5.2.1. Load capacity & Stiffness

The force-fly height curve shows the behaviour of the stage is behaves similar to the model at larger fly heights, the model and measurement diverge when the fly height of the stage approaches zero. This behaviour can be explained by squeeze film damping.

It can be seen that in the sense of load capacity, an FF stage can achieve similar load capacity to a comparable aerostatic stage. The stiffness of the aerostatic stage however is several times higher. The high stiffness is required in the aerostatic stage to move resonance spikes from the underdamped eigenmodes to a frequency well above the desired bandwidth. As the ferrofluid stage uses relatively viscous fluid, the eigenmodes are overdamped and much less of a problem. Thus, from a control point of view the stiffness doesn't necessarily need to be high. As the stiffness of the stage is known and stable under translation, it can easily be compensated for.

The stiffness of the stage can be increased by decreasing the fly height of the top and bottom bearing pads. This can be done by decreasing the difference in height between mover and base. This way a stiffness of up to $0.73 \text{ N}/\mu\text{m}$ can be achieved. The increase in stiffness comes at the cost of a reduce in load capacity. The fly height can be chosen based on the application, a larger fly height for applications requiring higher load capacity and a smaller fly height for applications requiring stiffness.

The load capacity in lateral direction isn't directly measured, but can be determined by using the bearing pad model. At a fly height of 1 mm this load capacity would be 80 N. When taking account fluid loss in translation, the effective lateral load capacity would be slightly lower. As the lateral pad is smaller and the reservoir in the mover remains equal in size, the drop in lateral load capacity is estimated to be less than 20 N. Resulting in an estimated 60 N load capacity in lateral direction.

5.2.2. Trail formation

Figure 9 shows that for a limited amount of FF, there is a significant drop in the height of the mover at higher translation velocities. The higher velocity induces more shear

and as a result less fluid is present to support the load of the stage. Using a larger volume of ferrofluid eliminates this height drop, a height increase can even be observed in the height for an increase in pull back velocity. This height gain can partly be explained by the weight reduction associated by the loss in fluid. The loss of 30 grams of fluid would give an increase in fly height of $1 \mu\text{m}$ at a stiffness of $0.3 \text{ N}/\mu\text{m}$. A further explanation would be a difference in fluid loss and fluid supply in the top and bottom bearing pads. When the top pad has less fluid relatively to the bottom pad, the height of the mover will increase.

The increased stability in fly height can be explained by the reservoirs at the corners of the bearing pads as seen in figure 2. A larger volume of ferrofluid ensures there is an excess amount of fluid available on the mover to replace lost ferrofluid due to trail formation.

Figure 10 shows the relative height of the mover for 55 grams of fluid and different payload amounts. It can be seen that the payload has limited influence on the repeatability of the height of the mover. This figure shows the stage can accommodate a payload of 1 kg at a maximum velocity of 0.25 m/s with an out-of-plane height stability of $\pm 3 \mu\text{m}$, and $\pm 7 \mu\text{m}$ for a payload of 1.75 kg at a maximum velocity of 0.5 m/s .

In past implementations of ferrofluid bearings into precision movement stages, the performance has been severely limited by trail formation. Typical values are a stroke of several centimetres and the loss of mover height is in the order of $1 \mu\text{m}/\text{mm}$ translation [24, 44]. In comparison, both the attained stroke and stability of the mover height in the realized demonstrator stage are of exceptional performance.

5.2.3. Evaporation

Figure 11 shows a severe increase in viscosity, both with and without magnetic field under evaporation of the fluid. When the fluid is diluted back to the original mass the viscosity of the fluid also reverts back to original, but this was observed only for the 7.7 % evaporated fluid. A very probable explanation is the loss of colloidal stability of the fluid when evaporation exceed a certain value. Individual particles then agglomerate and no longer disperse when diluted back to original mass.

Figure 12 shows the normal force exerted on the rheometer by the ferrofluid. This endorses the theorized refilling of the carrier fluid for small levels of evaporation. Again, here can be seen that there is less normal force for the further evaporated fluid, which can also be caused by agglomerations in the fluid.

Due to the relatively large wetted surface in the bearing, the overall mass loss due to evaporation using the EFH3 fluid will be in the order of a percent per day. This means that after a week the viscosity in the fluid has doubled. After a few more days the fluid will lose colloidal stability and the individual particles will agglomerate. This process can be reversed by 'lubricating' the bearing occasionally through the addition of carrier fluid. The properties of the fluid will then return to their original specification. This has yet to be tested

Table 7

Comparison of specifications of aerostatic bearing stage and ferrofluid demonstrator stage. * No actuation is added to the demonstrator stage at this stage. ** Outer dimensions of demonstrator can be reduced without loss of performance.

	Unit	PI aerostatic bearing A-110.300	Ferrofluid demonstrator stage	Goal achieved
Travel	mm	300	460	✓
Maximum payload	N	100 normal	120 normal, 60 lateral	✓
Stiffness	N/ μm	30-60 (estimated)	0.4	X
Moving mass	kg	2.6	1.8*	✓
Outer dimensions (W \times L \times H)	mm	160 \times 575 \times 60	180 \times 600 \times 80	✓**
Mover dimensions (W \times L \times H)	mm	160 \times 200 \times 60	139 \times 124 \times 60	✓
Straightness & Flatness	μm	$< \pm 1$	$< \pm 8$ (Fluid loss only)	X
Maximum velocity	m/s	1	-	?

inside a working bearing system, however experiments using a rheometer look very promising.

Alternatively, a different solution to the evaporation problem would have been the use of a ferrofluid with a very low vapor pressure. Where kerosene based EFH3 ferrofluid has a vapour pressure of 0.1 kPa [11], the vapour pressure of the H9-LT ferrofluid from Liquid-Research has a vapour pressure of $\sim 1 \cdot 10^{-7}$ kPa [19]. Based on the difference in vapour pressure the evaporation rate of the H9-LT ferrofluid will be several orders higher than the evaporation rate of the EFH3 ferrofluid [20]. This would make a system for resupplying unnecessary as the effects of evaporation will only be noticeable after several years. Low vapour pressure ferrofluids however are expensive and have a high viscosity. The H9-LT ferrofluid has a viscosity of 300 mPa·s, which is 25 times higher than the used EFH3 ferrofluid. Primarily the high viscosity is problematic as it will increase damping and trail formation, thus reducing the possible stroke length and mover velocity.

5.2.4. Damping

The damping in the system is relatively constant and predictable, a function of movement velocity and payload. This makes open loop controlling a possibility in systems with lower positioning requirements. For high precision requirements, the damping attenuates high frequency noise and makes implementing a PID controller less difficult [35]. The strong correlation of the damping coefficient with the velocity however is puzzling, no explanation could be found for this occurrence.

Figure 14 shows the flow profile in the ferrofluid as modelled using a Couette flow with back pressure. Due to the limited back pressure at a low velocity the flow profile approximates that of a Couette flow. As the velocity increases the back pressure increases and the flow profile becomes similar to the flow profile theorized by Lampaert [16]. These flow profiles would indicate less fluid loss at higher velocities, which is in contrast with observations in the demonstrator (figure 6) where the fluid loss was seen to increase with velocity.

The modelled flow profile in the fluid between mover and base suggests the presence of a recirculation of the fluid on the sides of the bearing pad. Figure 15 shows an explanation

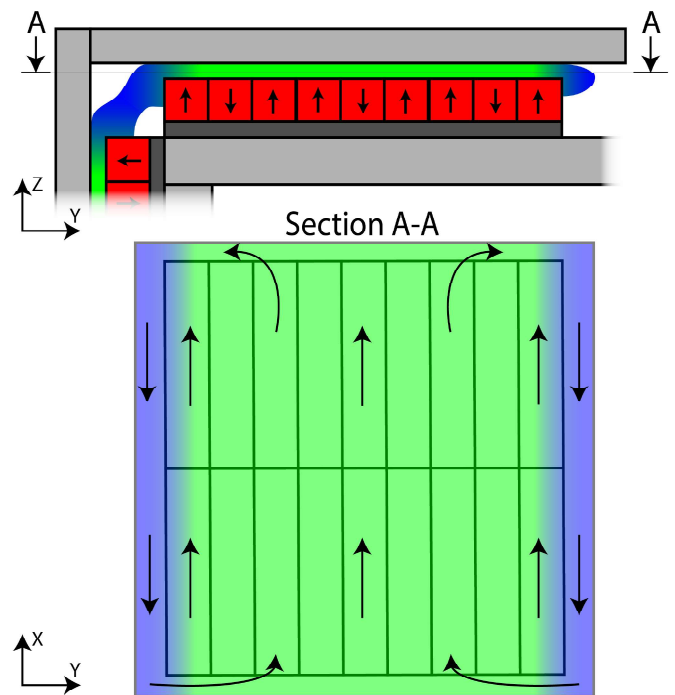


Figure 15: Top and front view of a pressure bearing pad with a reverse flow channel (blue). The arrows show the direction of net fluid flow for a mover translation in positive x-direction. Fluid coloured green flows in the positive x-direction, blue flows in the opposite direction.

of this recirculation path using reverse flow channels.

The existence of a reverse flow channel on the magnet pads would allow the fluid to circulate almost freely at low speeds. While at higher speeds, the volume flow in the reverse flow channels increases and a significant back pressure is created. This increase in pressure increases the loss of fluid as well. The circulation of the fluid is observed when the top of the bearing is removed. The fluid then uses the free top surface to circulate fluid from the side and bottom bearing pads

5.3. Comparison with aerostatic stage

The goal of this research was to demonstrate the possibility of a passive linear guide using ferrofluid pressure bearings capable of competing with an existing aerostatic stage. Table 7 shows the comparison between the realized demonstrator model and the PI linear stage with air bearings. It can be seen that the stage is only outperformed by the aerostatic bearing stage at 2 points, stiffness and straightness. The maximum velocity of the stage has yet to be determined.

6. Conclusion

In comparison to previous implementations of ferrofluid bearings, the realized stage greatly improves the stroke length and out-of-plane stability in mover height. Though, the attained stability and stiffness is less than an aerostatic bearing stage can achieve. Thus, the use of this stage is not recommended in applications where this is very critical, such as in sub-micrometre lithography stages. However, in comparison to aerostatic stages, the ferrofluid bearing can provide the same stick-slip-free motion without the need for a constant supply of air and tight manufacturing tolerances. Moreover, the ferrofluid bearing approaches the same out-of-plane stability for a lower payload and velocity. There can be concluded that the ferrofluid bearing is a feasible alternative to aerostatic bearings, depending on the demands of the application.

From the findings in this research the following conclusions can be drawn:

- Optimized ferrofluid pressure bearings can compete with single seal pocket bearings
- Magnets can be used in close proximity to conductors without significant eddy current damping by choosing the geometry and orientation of the magnets properly.
- The use of a reservoir on the mover results in a stable fly height under translation.
- The magnetic and viscous properties of ferrofluids subjected to moderate evaporation can be restored by re-supplying with carrier fluid.
- The damping in the stage is purely viscous in nature and primarily affected by velocity and size of payload.
- It is possible to design and manufacture a linear ferrofluid stage to specification.

References

- [1] Alvarez-Aguirre, A., Mok, G., HosseinNia, S.H., Spronck, J., 2016. Performance improvement of optical mouse sensors: Application in a precision planar stage. 2016 International Conference on Manipulation, Automation and Robotics at Small Scales, MARSS 2016 doi:10.1109/MARSS.2016.7561698.
- [2] Assadsangabi, B., Tee, M.H., Takahata, K., 2013. Ferrofluid-assisted levitation mechanism for micromotor applications. 2013 Transducers and Eurosensors XXVII: The 17th International Conference on Solid-State Sensors, Actuators and Microsystems, TRANSDUCERS and EUROSENSORS 2013 17, 2720–2723. doi:10.1109/Transducers.2013.6627368.
- [3] Boots, A., 2018. Operational range of a ferrofluid pocket bearing (MSc Thesis).
- [4] Boots, A.S., Krijgsman, L.E., de Ruiter, B.J., Lampaert, S.G., Spronck, J.W., 2019. Increasing the load capacity of planar ferrofluid bearings by the addition of ferromagnetic material. Tribology International 129, 46–54. URL: <https://doi.org/10.1016/j.triboint.2018.07.048>, doi:10.1016/j.triboint.2018.07.048.
- [5] Brian Rowe, W., 2012. Hydrostatic, Aerostatic and Hybrid Bearing Design. Elsevier Inc. doi:10.1016/C2011-0-07331-3.
- [6] Café, M., 2014. Nanometer precision Six Degrees of Freedom Planar Motion Stage with Ferrofluid Bearings. Technical Report. TU Delft.
- [7] Café, M., Spronck, J., 2014. Nanometer precision Six Degrees of Freedom Planar Motion Stage with Ferrofluid Bearings. DSPE Conference on Precision Mechatronics, 43–46.
- [8] COMSOL AB., 2019. COMSOL Multiphysics 5.4. URL: www.comsol.com.
- [9] Deng, R., Van Veen, S., Café, M., Spronck, J.W., Munnig Schmidt, R.H., 2014. Linear nano-positioning stage using ferrofluid bearings. Conference Proceedings - 14th International Conference of the European Society for Precision Engineering and Nanotechnology, EU-SPEN 2014 1, 372–375. URL: <https://news.microsoft.com/apac/features/putting-digital-transformation-on-the-business-agenda/>.
- [10] Dong, Z., Liu, P., Ding, H., 2009. Kalman estimator-based state-feedback high-precision positioning control for a micro-scale air-bearing stage, in: Lecture Notes in Computer Science (including sub-series Lecture Notes in Artificial Intelligence and Lecture Notes in Bioinformatics), pp. 765–775. doi:10.1007/978-3-642-10817-4(_)76.
- [11] Ferrotec, 2011. Ferrofluid data sheet EFH series.
- [12] Ferrotec, 2013. Data Sheet APG 2100 series.
- [13] Fleming, A.J., Aphale, S.S., Moheimani, S.O., 2009. A new robust damping and tracking controller for SPM positioning stages, in: Proceedings of the American Control Conference, pp. 289–294. doi:10.1109/ACC.2009.5159934.
- [14] HKCM Engineering e.K., 2019. Magnet-Cuboid Q50x02x02Ni-N35. URL: https://www.hkcm.de/HKCM_allinone.php?l=&id=53809&tolerance=1&flux=1&coating=1&bh=1&l=en.
- [15] Lampaert, S., 2015. Planar Ferrofluid Bearings Modelling and Design Principles (MSc Thesis).
- [16] Lampaert, S.G., Fellingner, B.J., Spronck, J.W., van Ostayen, R.A., 2018a. In-plane friction behaviour of a ferrofluid bearing. Precision Engineering 54, 163–170. doi:10.1016/j.precisioneng.2018.05.013.
- [17] Lampaert, S.G., Spronck, J.W., van Ostayen, R.A., 2018b. Load and stiffness of a planar ferrofluid pocket bearing. Proceedings of the Institution of Mechanical Engineers, Part J: Journal of Engineering Tribology 232, 14–25. doi:10.1177/1350650117739200.
- [18] Lentini, L., Moradi, M., Colombo, F., 2018. A historical review of gas lubrication: From reynolds to active compensations. doi:10.24874/ti.2018.40.02.01.
- [19] Liquids Research Ltd., . Ferrofluids for sealing applications SI. URL: https://www.liquidsresearch.co.uk/en-GB/for_sealing_applications_si-61.aspx.
- [20] Mackay, D., Van Wesenbeeck, I., 2014. Correlation of Chemical Evaporation Rate with Vapor Pressure. Environ. Sci. Technol 48, 10259–10263. URL: <https://pubs.acs.org/sharingguidelines>, doi:10.1021/es5029074.
- [21] Micro-Epsilon, . Datasheet optoNCDT 1420. URL: <https://www.micro-epsilon.com/download/products/cat--capaNCDT--en.pdf>.
- [22] Moeser, G.D., Roach, K.A., Green, W.H., Alan Hatton, T., Laibinis, P.E., 2004. High-gradient magnetic separation of coated magnetic nanoparticles. AIChE Journal 50, 2835–2848. URL: <http://doi.wiley.com/10.1002/aic.10270>, doi:10.1002/aic.10270.
- [23] Mok, G., 2015. The design of a planar precision stage using cost effective optical mouse sensors (MSc Thesis).
- [24] van Moorsel, L., 2017. A planar precision stage using a single image sensor (MSc Thesis).
- [25] Odenbach, S., 2004. Recent progress in magnetic fluid research. Jour-

- nal of Physics Condensed Matter 16. doi:10.1088/0953-8984/16/32/R02.
- [26] Odenbach, S., 2009. Colloidal Magnetic Fluids. Number 763 in Lecture Notes in Physics, Springer Berlin Heidelberg, Berlin, Heidelberg. URL: <http://link.springer.com/10.1007/978-3-540-85387-9>, doi:10.1007/978-3-540-85387-9.
- [27] Osman, T.A., Nada, G.S., Safar, Z.S., 2001. Static and dynamic characteristics of magnetized journal bearings lubricated with ferrofluid. Tribology International 34, 369–380. doi:10.1016/S0301-679X(01)00017-2.
- [28] Papell, S.S., 1965. Papell - 1965 - Low viscosity magnetic fluids obtained by the colloidal suspension of magnetic particles. US patent .
- [29] Peijnenburg, A.T., Vermeulen, J.P., van Eijk, J., 2006. Magnetic levitation systems compared to conventional bearing systems. Microelectronic Engineering 83, 1372–1375. doi:10.1016/j.mee.2006.01.248.
- [30] Physik Instrumente, 2019. PIGlide Air Bearing Technology datasheet.
- [31] Ravaut, R., Lemarquand, G., Lemarquand, V., 2010. Mechanical properties of ferrofluid applications: Centering effect and capacity of a seal. Tribology International 43, 76–82. URL: <http://dx.doi.org/10.1016/j.triboint.2009.04.050>, doi:10.1016/j.triboint.2009.04.050.
- [32] Reck, M., . Air Bearings : When to Use and Air Bearings: When to Use and When to Avoid in Your Motion Application.
- [33] Rosensweig, R., 1966. Buoyancy and stable levitation of a magnetic body immersed in a magnetizable fluid. doi:10.1038/210613a0.
- [34] Rosensweig, R., 1971. Bearing arrangement with magnetic fluid defining bearing pads.
- [35] Schmidt, C., Heinzl, J., Brandenburg, G., 1999. Control approaches for high-precision machine tools with air bearings. IEEE Transactions on Industrial Electronics 46, 979–989. doi:10.1109/41.793347.
- [36] Sorensen, K.L., Singhose, W., Dickerson, S., 2007. A controller enabling precise positioning and sway reduction in bridge and gantry cranes. Control Engineering Practice 15, 825–837. doi:10.1016/j.conengprac.2006.03.005.
- [37] Sung, E., Seo, C.h., Song, H., Choi, B., Jeon, Y., Choi, Y.M., Kim, K., Lee, M.G., 2019. Design and experiment of noncontact eddy current damping module in air bearing–guided linear motion system. Advances in Mechanical Engineering 11, 1687814019871424. URL: <http://journals.sagepub.com/doi/10.1177/1687814019871424>, doi:10.1177/1687814019871424.
- [38] Tan, K.K., Huang, S., Liang, W., Yu, S., 2012. Development for precise positioning of air bearing stages, in: 2012 IEEE International Conference on Mechatronics and Automation, ICMA 2012, pp. 1943–1948. doi:10.1109/ICMA.2012.6285119.
- [39] The Mathworks Inc., 2018. Matlab R2018b.
- [40] van den Toorn, S.W.M., 2020. Ferrofluid linear long stroke stage (MSc Thesis).
- [41] Tsumura, T., Yoshioka, H., Shinno, H., Sawano, H., 2014. Magnetically preloaded aerostatic guideway for high speed nanometer positioning. Journal of Advanced Mechanical Design, Systems and Manufacturing 8, JAMDSM0054–JAMDSM0054. URL: <http://jlc.jst.go.jp/DN/JST.JSTAGE/jamdsm/2014jamdsm0054?lang=en&from=CrossRef&type=abstract>, doi:10.1299/jamdsm.2014jamdsm0054.
- [42] Uhlmann, E., Bayat, N., 2006. High precision positioning with ferrofluids as an active medium. CIRP Annals - Manufacturing Technology 55, 415–418. doi:10.1016/S0007-8506(07)60448-X.
- [43] Van Beek, A., 2012. Engineering Design Lifetime Performance and Reliability. TU Delft, Delft.
- [44] van Veen, S., 2013. Planar Ferrofluid Bearings (MSc Thesis).
- [45] Wang, Z., Hu, Z., Huang, W., Wang, X., 2017. Elastic support of magnetic fluids bearing. Journal of Physics D: Applied Physics 50. doi:10.1088/1361-6463/aa86f9.

Design considerations for ferrofluid pressure bearing pads

Stefan W.M. van den Toorn^a, Jo W. Spronck^a, Ron A.J. van Ostayen^a and Stefan G.E. Lampaert^a

^aDepartment of Precision and Microsystems Engineering, Delft University of Technology, Delft, The Netherlands

ARTICLE INFO

Keywords:
Magnetic fluid
Air bearing replacement
Stick-slip

ABSTRACT

This research discusses different magnet configurations to improve the load and stiffness of a ferrofluid pressure bearing. It is shown that magnets with a small cross-section magnetized alternatively up and downwards combine a high load capacity and moderate stiffness while being low on material cost and complexity. Magnets magnetized alternatively left-right alternated with iron give the highest load capacity and stiffness, albeit at the cost of weight and complexity. It is shown that an increase in the number of magnets and is beneficial for the stiffness in both magnetization configurations, as is an increase in remanent flux density of the magnet. A metal bottom plate made of iron reduces the necessary height of the magnet in the up-down magnetization configuration. The model was validated using bearing pad arranged in the up-down configuration. The force-displacement curve of this pad was measured in a load frame, using the APG 513A ferrofluid from Ferrotec. A load capacity of 1.75 N/cm² was achieved, this exceeds previous pressure bearing implementations and performs comparable or better than implementations of single seal ferrofluid pocket bearings. Thus, making this the ferrofluid pressure bearing a passive alternative in motion systems where the designer otherwise would have had to use an active bearing.

1. Introduction

Bearings regularly used in precise positioning systems suffer from high cost, need for active components or the presence of stick-slip [1]. The stick-slip phenomenon prevents a smooth continuous motion of the bearing, especially at low speeds [2]. The ferrofluid bearing has none of these issues and thus could be an interesting alternative.

The ferrofluid bearing consists out of a magnet array and a magnetic fluid. This fluid is a colloidal suspension consisting of magnetic particles in a carrier fluid [3]. In a magnetic field these particles are drawn to the highest field intensity and as a result produce a pressure in the fluid. A bearing can be created by placing the fluid in a magnetic field in between two bearing surfaces [4]. As the bearing is loaded, the surfaces move closer together and the fluid is displaced from the equilibrium position, which in turn inducing a reaction force. This is called the ferrofluid pressure bearing. Alternatively, the pressure in the fluid can be used to seal a pocket of air and a displacement of the bearing surface will pressurize this air resulting in a normal force. This is called the pocket bearing [5].

Figure 1 shows the working principle of the ferrofluid pressure bearing. Using equation 1 and 2 the load and stiffness of the pressure bearing can be calculated [6]. In these formulas F_L is the load capacity, μ_0 the permeability in vacuum, M_s the saturation magnetization of the ferrofluid and H the magnetic field intensity. The area is defined as the surface area of the ferrofluid on the top bearing surface. It can be seen in figure 1 that an increase in payload causes the bearing surfaces to move closer together, thus increasing the area over which the integral is taken, as well as the increasing the overall magnetic field intensity. In practice only the latter will be significant as the outer fluid edge is at low

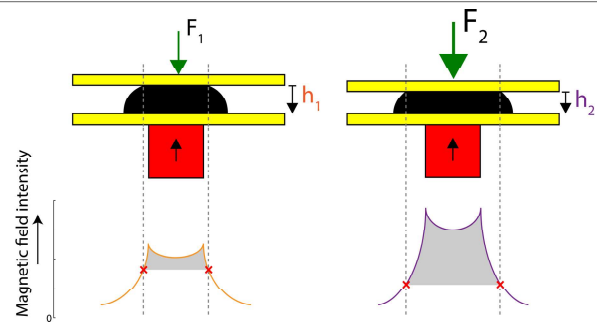



Figure 1: Effect of increase in payload in ferrofluid pressure bearing with magnetic field intensity at the location of the top bearing surface. With $F_1 < F_2$ and $h_1 > h_2$

magnetic field intensity.

$$F_L = \mu_0 M_s \int_S H dA \quad (1)$$

$$k = -\mu_0 M_s \frac{d}{dh} \int_S H dA \quad (2)$$

Although ferrofluid pressure bearings can be found in literature [4, 7, 8], the actual implementation of this bearing type is very limited in load capacity and stiffness [9–12]. When an application demands a certain load capacity and stiffness the ferrofluid pocket bearing is seen as the preferred bearing type [5], although in comparison with the pocket bearing, the out of plane repeatability of the pressure bearing is much higher as no air can escape. For a similar surface area, a pressure bearing will also have more tilt stiffness. While the optimal configuration of pocket bearings has been researched by Boots [13], this has yet to be done for the pressure bearing.

 s.w.m.vandentoorn@student.tudelft.nl (S.W.M.v.d. Toorn)
ORCID(s):

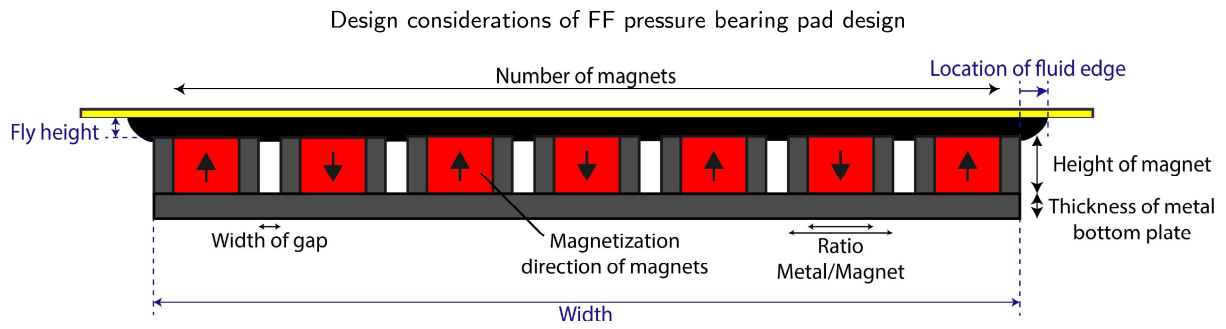


Figure 2: Design variables (black) and model constants (blue) in a cross-section of the bearing pad. The length of the pad is defined into the plane.

Table 1
Design variables and their respective ranges.

Variable	Symbol	Type	Range	Unit	Range based on
Number of magnets	N_{mag}	Discrete	1-50	-	Manufacturability
Magnetization direction of magnets	Mag_{dir}	Discrete	$\uparrow\downarrow, \uparrow\uparrow, \uparrow\leftarrow, \leftarrow\rightarrow$	-	Assumed optimum
Width of gap	W_{gap}	Continuous	0-3	mm	Assumed optimum
Ratio metal/magnet	$R_{\frac{Met}{Mag}}$	Continuous	0-0.5	-	Assumed optimum
Thickness metal bottom plate (MBP)	H_{mbp}	Continuous	0-2	mm	Assumed optimum
Height of magnet	H_{mag}	Continuous	0.5-4	mm	Manufacturability
Remanent flux density of the magnet	Mag_{str}	Continuous	1.1-1.5	T	Manufacturability

Table 2
Model constants.

Constant	Value	Unit
Width	50	mm
Length	100	mm
Fly height	0.1	mm
Relative permeability ferrofluid	1	-
Saturation magnetization ferrofluid	52.5	kA/m
Relative permeability metal	4000	-
Saturation magnetization metal	1.4	T
Relative permeability magnets	1	-
Location fluid edge	5	mm

The optimal pressure bearing consists of an optimal fluid in an optimal magnetic field. Research has been done on the magnetic fluid. Although not specifically for bearing applications, there are some fluids that are well suited. Less is known about the optimal magnetic field. The purpose of this paper is to give an insight in the design of the magnetic field for application in a pressure bearing pad and to provide a direct comparison between the pressure and pocket bearing.

2. Modelling of pressure bearing pad

The magnetic field can be manipulated by arranging multiple magnets in relation to each other with the addition of metal with high permeability. In order to obtain an understanding of the influence of the different variables, a model has been made.

The pressure bearing model is based on a 2D simulation of a cross-section of the bearing pad using COMSOL

Multiphysics [14]. This simulation assumes the bearing pad continues infinitely in and out of the plane as seen in figure 2. Using the LiveLink interface, a COMSOL model is parametrically coded in Matlab [15], then run in COMSOL and again post processed in Matlab. In this model several variables were varied, these are listed in figure 2 and table 1. The Halbach magnetization configuration was left out as it produces a constant field with little gradient, which would result in a low stiffness bearing [16]. The build volume was taken to be 50x100x4 mm (width x length x height), the length being defined as in and out of the plane as seen in figure 2. The used constants in modelling the pressure bearings can be seen in table 2 and figure 2. As the minimum fly height is dictated by manufacturing tolerances and damping, it is set at 0.1 mm for all parameter configurations. The error in simulation caused by the finite bearing length is evaluated in a 3D model and found to be negligible. For the metal between the magnets and for the bottom plate iron has been chosen for its high permeability and saturation magnetization. The gaps are modelled as air.

The width of the metal and magnets is defined using the variables and can be found using equation 3 and 4 respectively. The definition of the symbols used can be seen in table 1.

$$W_{mag} = (Width - W_{gap} (N_{mag} - 1)) \frac{1 - R_{\frac{Met}{Mag}}}{N_{mag}} \quad (3)$$

$$W_{met} = \frac{1}{2} R_{\frac{Met}{Mag}} W_{mag} \quad (4)$$

Table 3

Optimized magnet configuration for stiffness subjected to constraints: load capacity > 100N, cost < €50, weight < 150 grams. Using the constants in table 2. Fly height for all configurations is 0.1 mm.

Variable	Values	Unit				
Magnetization direction of magnets	↑↓, ↑↑, ↑←, ←→	-	Up-Down	Up-Up	Up-Left	Left-Right
Number of magnets	5, 15, 30, 40, 50	-	50	30	30	50
Remanent flux density of the magnet	1, 1.15, 1.3, 1.5	T	1.5	1.5	1.5	1.5
Height of magnet	1, 2, 3	mm	1	1	2	3
Ratio metal/magnet	0, 0.2, 0.4	-	0	0.4	0.2	0.4
Thickness metal bottom plate	0, 1	mm	1	1	0	0
Width of gap	0, 0.1, 0.2	mm	0	0	0.2	0
Material cost		€	24.19	17.28	35.64	51.83
Weight		g	77.5	78.2	67.0	114.6
Load capacity		N	149.63	117.09	128.22	216.46
Stiffness		N/μm	0.52	0.52	0.68	0.76

2.1. Initial optimization

To gain an initial understanding, a parameter sweep performed using several evaluation points in the range of each variable. From the parameter sweep could be concluded that the magnetization direction of the magnets has a great influence on the design of the bearing pad. The results of the parameter sweep were used in an optimization for stiffness. Constraints were added using a penalty method. The imposed constraints were a minimum load of 100N, a maximum weight of 150 grams and a maximum material cost of €50. These constraints are based on a linear stage design where the pressure bearing pads are placed on the mover. Equation 5 relates the cost of the magnetic material per gram (Y) as a function of the remanent flux density of the magnet (M_{str}).

$$Y = (2.4 \cdot 10^{-3}) e^{3.7293 \cdot M_{str}} \quad (5)$$

This function was determined based on data from the on-line design tool of HKCM [17]. The material cost of metal was assumed to be negligible. Table 3 shows the results of the parameter sweep for different magnet magnetization directions. Some interesting things can be seen:

- All magnetization directions use the highest remanent flux density of the magnet available.
- A gap in between magnets is unwanted in all magnetization directions except up-left, this is a result of a slight increase in stiffness as the gap increases.
- The up-down magnetization array is relatively simple compared to the others, no additional ferromagnetic material or gaps are used.
- The left-right magnetization direction shows the best performance. This however comes at the cost of complexity as small features are required. Much material is required relative to the other magnetization directions, resulting in a higher weight.

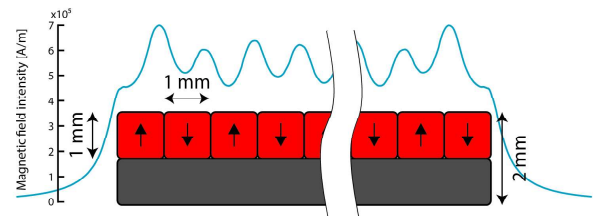


Figure 3: Magnet configuration for up-down magnetization direction with magnetic field intensity at 0.1 mm above magnet surface.

From the initial parameter sweep thus can be concluded that each magnetization direction produces a different optimal configuration of magnets, metal and gaps. The choice of magnetization direction is based on the trade-off between weight, material cost, load capacity, stiffness and complexity. The up-down magnetization configuration for the relatively low material cost and complexity while still having a moderate load capacity. The combination of low material cost and low complexity can result in a very cheap to produce bearing design. The absence of gaps and metal makes for a potentially monolithic producible bearing. The magnetization can then be 'written' on a single block of Ne-Fe-B [18–20]. A single magnet block can significantly reduce assembly as well as improve tolerances. The up-down and left-right magnetization configurations are both suited for bearing applications and they will be discussed next.

2.2. Up-down magnetization configuration

Figure 3 shows the magnet configuration using the variables in table 3 with the magnetic field intensity at 0.1 mm. The neighbouring magnets provide a low reluctance path which results in a spike in the magnetic field intensity. Due to the large number of magnets, many low reluctance paths are created. This moves the overall magnetic field intensity closer to the magnet, increasing load capacity and stiffness.

Table 4

Logarithmic sensitivity of an increase in the individual variables for the stiffness of the up-down magnetization configuration.

	N_{mag}	W_{gap}	H_{mag}	$R_{Met/Mag}$	Mag_{str}	H_{mbp}	Fly height
Stiffness	0.843	-0.002	0.113	-0.010	1	0.002	-0.282
Load capacity	-0.138	-0.001	0.105	-0.008	1	0.002	-0.280

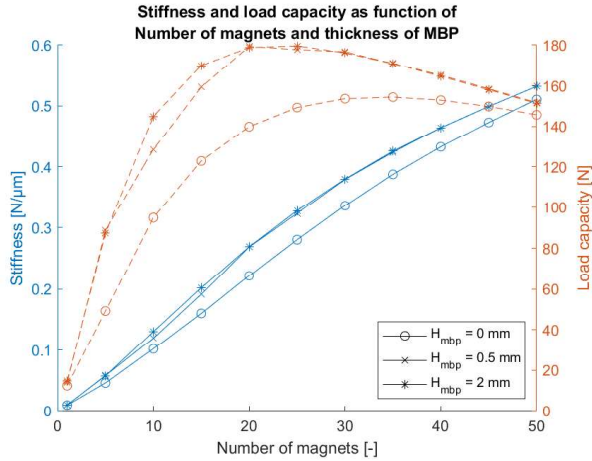
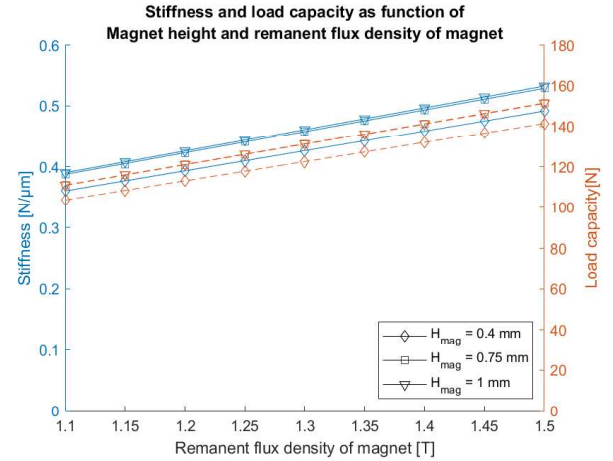
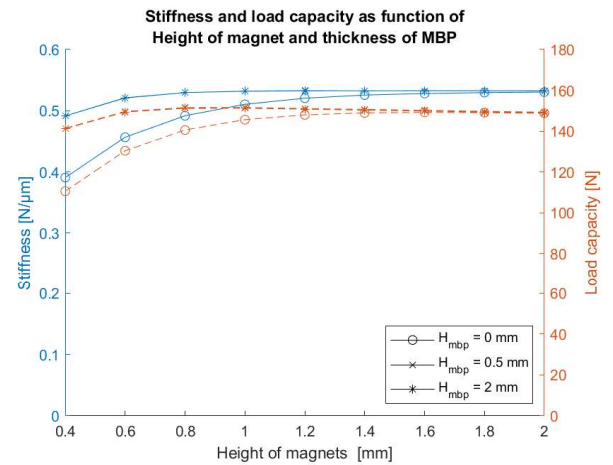

Figure 4: Stiffness and load capacity as a function of the number of magnets for different thicknesses of the metal bottom. For up-down magnetization configuration.

Figure 5: Stiffness and load capacity as a function of the remanent flux density of the magnet for different heights of the magnets. For up-down magnetization configuration. The lines for magnet height of 0.75 mm and 1 mm coincide.

Table 4 shows the effect of the different variables on the stiffness normalized using logarithmic sensitivity. The sensitivities are determined around the up-down configuration in table 3. As the gap and the factor metal/magnets are already minimal, only the number of magnets, height of magnets, remanent flux density and fly height can improve the stiffness of the bearing. Use of a metal bottom plate has no significant effect on the bearing performance but does add moving mass if the bearing pads are mounted on the mover. An increase in the number of magnets also decreases the load capacity. Thus, a compromise has to be made.

Figure 4 and figure 5 show the influence of the different variables on the stiffness and load capacity. The metal bottom plate is more efficient for a lower of magnets. A relative thin bottom plate of 0.5mm is enough to prevent effects of saturation. Figure 4 again stresses the importance of many small magnets. It can be seen that the optimum for load capacity lies around 20-25 magnets. The optimum for stiffness however is located outside of the graph. From figure 5 we see that the stiffness and the load capacity scale linearly with the remanent flux density of the magnet. The height of the magnets shows an optimum around 1mm. Further increase of the height reduces the stiffness slightly.

Figure 6 shows the relation between the height of the magnets and the bearing performance for different thicknesses of the MBP. Up to 25% performance gain can be achieved by only 0.5 mm MBP thickness. It can be seen that in most cases it is more economical efficient to use less magnetic material and a thin MBP. Figure 5 and figure 6 contain all


Figure 6: Stiffness and load capacity as a function of height of magnet for different thicknesses of the metal bottom plate. For up-down magnetization configuration. The lines for 0.5 mm and 2 mm bottom plate thickness coincide.

significant variables concerning the respective material cost and weight. It can be seen that a cost-effective bearing is to favour remanent flux density of the magnet over magnet height, while using a metal bottom plate. The same goes for optimizing towards weight, thin magnets combined with a thin MBP.

Table 5

Logarithmic sensitivity of an increase in the individual variables for the left-right magnetization configuration.

	N_{mag}	W_{gap}	H_{mag}	$R_{\frac{Met}{Mag}}$	Mag_{str}	H_{mbp}	Fly height
Stiffness	0.548	-0.012	0.343	-0.063	1	-0.006	-0.550
Load capacity	-0.590	-0.089	0.551	-0.146	1	-0.006	-0.284

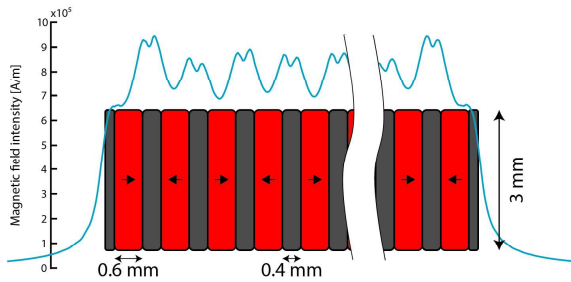


Figure 7: Magnet configuration for left-right magnetization with magnetic field intensity at 0.1 mm above magnet surface.

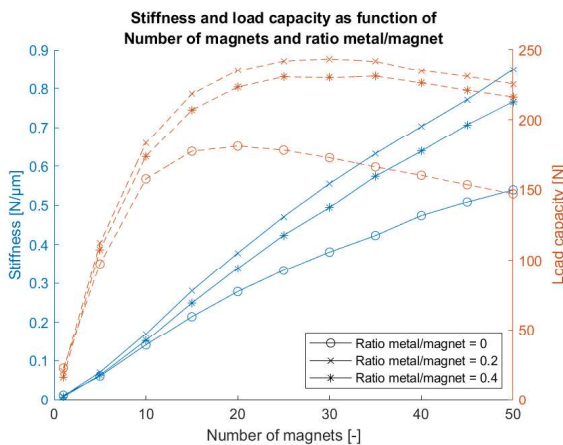


Figure 8: Stiffness and load capacity as a function of the number of magnets for different ratios of metal/magnet. For left-right magnetization configuration.

2.3. Left-right magnetization configuration

Figure 7 shows the left-right magnetization configuration for the values of the variables in Table 3. The study from the previous section is repeated here for the left-right magnetization configuration.

Table 5 shows the logarithmic sensitivity of the stiffness for the different variables with the configuration in table 3 as initial value. The width of the gap and thickness of the MBP are already zero, thus the ideal configuration doesn't include gaps or an MBP. The response of the load capacity and stiffness on change in the height of the magnet, number of magnets, factor metal/magnet and remanent flux density of the magnet are shown in Figure 9 and Figure 10.

The same dependence of the number of magnets can be observed in figure 8 as with the up-down configuration. There is a distinct difference in the optimum of the load capac-

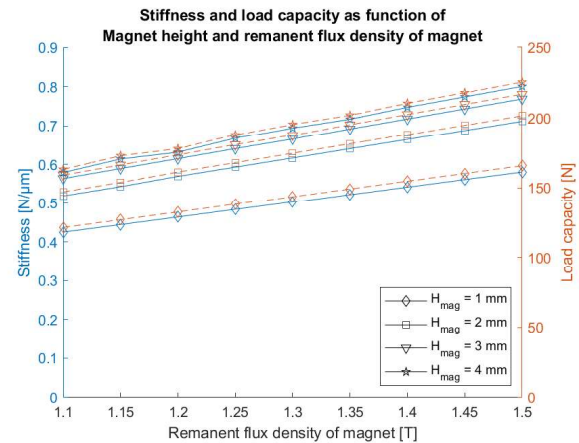


Figure 9: Stiffness and load capacity as a function of the remanent flux density of the magnet for different heights of the magnets. For left-right magnetization configuration.

ity and the stiffness. The addition of metal in between the magnets shows an increase in bearing performance. Some metal is needed to guide the magnetic field. Increasing of the width of this metal reduces the amount of magnetic material in the bearing configuration eventually leading to a reduction of performance. Figure 9 also shows similar behaviour for the remanent flux density of the magnet compared to the up-down configuration.

As the specific weight of neodymium magnets and metal are very similar, the weight of the configuration is determined by the height of the magnets. The material cost is determined by the remanent flux density of the magnet, height of magnets and the factor metal/magnet.

From the influence of the specific variables can be concluded that the configuration using a left-right magnetization depends largely on the cost and weight constraints. As the MBP reduces the bearing performance, remanent flux will be larger using this type of bearing. The stability will also be an issue when choosing a configuration with a small metal/magnet factor.

3. Method for validation

A materials test frame is used to validate the model of the pressure bearing pad. This is done by a fly height sweep of a pad made up of 23 magnets with the dimensions 50x2x2mm (LxWxH) and a remanent flux density of 1.17 T [21]. The magnets are arranged in the up-down magnetization configuration. The pad is placed on a ferritic stainless-steel (AISI 410s) bottom plate and is filled with 5 grams of either the

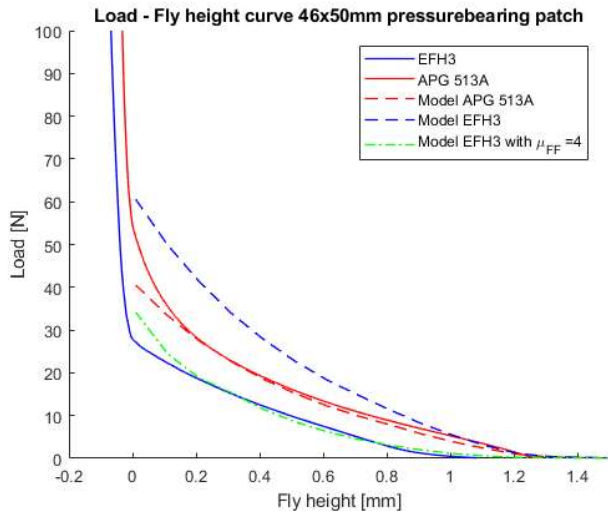


Figure 10: Load-fly height curve of pressure bearing pad with EFH3 and APG 513A ferrofluid and modelled performance of the ferrofluid. pad consists of 23 50x2x2mm magnets from HKCM[21] arranged in up-down configuration. The remanent flux in the magnets is 1.17T, the location of fluid edge is modelled 0.9 mm outside magnet.

EFH3 or the APG 513A ferrofluid.

Both the APG 513A and EFH3 fluid are manufactured by Ferrotec. The APG 513A fluid is chosen as its common in literature and its properties are well known. [22] The EFH3 fluid is chosen for its high magnetic saturation and low viscosity, making it a more suitable ferrofluid for use in bearings in comparison to the APG 513A.

The load of the bearing at the same fly height sweep is modelled. The magnet dimensions, pad dimensions and remanent flux density are modelled as described above. As the location of the ferrofluid edge is found at the point where the magnetic body force acting on the fluid is overcome by the gravity force, it can be determined using a COMSOL simulation of the magnetic field surrounding the bearing pad. This location was found at 0.8 mm outside the bearing pad for the APG 513A fluid and 0.9 mm for the EFH3 fluid. The magnetic saturation of the ferrofluids are set to 32 kA/m for the APG 513A fluid[22] and 52.5 kA/m for the EFH3 fluid [23].

4. Results and discussion

Figure 10 shows the results of the of the fly heights sweep and the calculated load capacity according to the model. Zero fly height was taken to be the point at which the pressure plate touches the magnets in the measurement.

The modelling of the bearing pad using the APG 513A fluid is in close agreement with the measurement. There is a slight divergence of the model and measurement as the fly height approaches zero that can be explained by the squeeze film damping from the relatively viscous (150 mPa·s) ferrofluid.

As can be seen in formula 1, the load capacity of a bearing pad should be proportional to the saturation magnetization. This can be observed when looking at the modelled load vs fly height curve for the APG 513A and EFH3 ferrofluid. When looking at the measurements it can be seen that while the APG 513A measurement and model are in good agreement, the same is not true for EFH3 measurement and model.

The probable cause of this difference is the accumulation of magnetic particles in areas of high magnetic field gradients. The largest gradients in the bearing pad are located at the corners in between two magnets. Accumulation of the magnetite particles there causes effectively a short circuit of the magnetic field, reducing the magnetic field elsewhere. A relatively good approximation of the accumulation can be done by increasing the relative permeability of the ferrofluid, this can be seen in the dash-dot line in figure 10.

The APG 513A fluid achieves a load capacity of 1.75 N/cm². This bearing configuration exceeds previous implementations of pressure bearings [9, 24, 25] and performs comparable or better than implementations of single seal pocket bearings [26–28]. Still, pocket bearings can be made with an even higher load capacity by stacking seals. The downside of this bearing design is the creation of more pockets of air that all need to be managed in order to have a repeatable stage behaviour.

5. Conclusion

The orientation of the different magnets in relation to each other is an important variable in the design of pressure bearing pads. Two distinct magnetization configurations both prove promising. The up-down magnetization configuration for its simplicity, and the left-right configuration for performance.

The up-down magnetization configuration consists out of an array of magnets combined with a metal bottom plate. The number of magnets is the most important variable in this configuration, combined with the remanent flux density of the magnet. Higher amounts of magnets slightly reduce load capacity, but offer more stiffness in return. Current state of the art allows for the ‘writing’ of the magnetization in the magnets, this technology can allow for monolithic pressure bearings [19, 20].

In the left-right magnetization configuration instead of providing low reluctance paths like in the up-down magnetization configuration, the magnets counteract each other. This can prove problematic as the configuration can become unstable when designing with a small metal/magnet ratio. This configuration though potentially has more stiffness and load capacity compared to the up-down magnetization configuration.

In the bearing design, cost and weight are important factors. Due to the low height of the magnets required and the ability to be produced monolithically, the up-down configuration performs the best in cost effectiveness and weight effectiveness. If the cost and weight are of less importance the

left-right magnetization configuration is the better choice.

The model is validated for use with the APG 513A ferrofluid. The EFH3 fluid shows effects that can be linked to accumulation of particles at the magnet surface. Using the APG 513A ferrofluid a load capacity of 1.75 N/cm^2 was achieved. Potentially this can be higher when the bearing pad is combined with a ferrofluid with a high magnetization saturation and a high colloidal stability in order to prevent accumulation.

The bearing pad that is created using the design guidelines developed in this paper can be used instead of single seal pressure bearing pads without a loss in load capacity, but with an improvement in the repeatability in fly height. Although some precision systems require more load capacity and stiffness, the achieved performance will satisfy the demands in many applications.

This paper has given insight into the variables that go into the design of a pressure bearing pad. This ferrofluid bearing pad is a passive alternative bearing to motion systems that otherwise would have been forced to use an active bearing to eliminate the effects of stick-slip.

References

- [1] Frank Wardle. *Ultra Precision Bearings*. Elsevier Ltd, 2 2015.
- [2] B Armstrong. Stick Slip and Control in Low-Speed Motion. *IEEE Transactions on Automatic Control*, 38(10):1483–1495, 1993.
- [3] Solomon S Papell. Papell - 1965 - Low viscosity magnetic fluids obtained by the colloidal suspension of magnetic particles. *US patent*, 1965.
- [4] R. Rosensweig. Buoyancy and stable levitation of a magnetic body immersed in a magnetizable fluid, 1966.
- [5] S. G.E. Lampaert, J. W. Spronck, and R. A.J. van Ostayen. Load and stiffness of a planar ferrofluid pocket bearing. *Proceedings of the Institution of Mechanical Engineers, Part J: Journal of Engineering Tribology*, 232(1):14–25, 2018.
- [6] Ronald E. Rosensweig. *Ferrohydrodynamics*. Dover Publications, 2013.
- [7] S Odenbach. *Colloidal Magnetic Fluids*. Number 763 in Lecture Notes in Physics. Springer Berlin Heidelberg, Berlin, Heidelberg, 2009.
- [8] Zhuang Wang, Zhengdong Hu, Wei Huang, and Xiaolei Wang. Elastic support of magnetic fluids bearing. *Journal of Physics D: Applied Physics*, 50(43), 2017.
- [9] S van Veen. Planar Ferrofluid Bearings (MSc Thesis), 2013.
- [10] Joe S. Hunter and Little J. Little. Magnetic fluid bearing accelerometer, 2010.
- [11] B. Assadsangabi, M. H. Tee, and K. Takahata. Ferrofluid-assisted levitation mechanism for micromotor applications. *2013 Transducers and Eurosensors XXVII: The 17th International Conference on Solid-State Sensors, Actuators and Microsystems, TRANSDUCERS and EUROSENSORS 2013*, 17(June):2720–2723, 2013.
- [12] G Millet and Arnaud Hubert. Design of a 3 DOF displacement stage based on ferrofluids. *Actuators'06*, pages 656–659, 2006.
- [13] A. S.T. Boots, L. E. Krijgsman, B. J.M. de Ruiters, S. G.E. Lampaert, and J. W. Spronck. Increasing the load capacity of planar ferrofluid bearings by the addition of ferromagnetic material. *Tribology International*, 129(May 2018):46–54, 2019.
- [14] COMSOL AB. COMSOL Multiphysics 5.4, 2019.
- [15] The Mathworks Inc. Matlab R2018b, 2018.
- [16] Z. Q. Zhu and D. Howe. Halbach permanent magnet machines and applications: A review. In *IEE Proceedings: Electric Power Applications*, volume 148, pages 299–308, 7 2001.
- [17] HKCM.de. HKCM Engineering e.K. Online magnet design.
- [18] Larry W. Fullerton and Mark D. Roberts. Magnetizing printer and method for re-magnetizing a least a portion of a previous magnetized magnet., 2016.
- [19] Larry W. Fullerton, Mark D. Roberts, and Jason N. Morgan. System and method for producing magnetic structures, 2019.
- [20] H Meng, J N Morgan, Q F Wei, and C H Chen. Design of Smart Magnetic Devices. In *Proceedings of 25th International Workshop on Rare-Earth and Future Permanent Magnets and Their Applications*, number Repm, 2018.
- [21] HKCM Engineering e.K. Magnet-Cuboid Q50x02x02Ni-N35, 2019.
- [22] S. Odenbach. Recent progress in magnetic fluid research. *Journal of Physics Condensed Matter*, 16(32), 2004.
- [23] Ferrotec. Data Sheet APG 2100 series, 2013.
- [24] J. M. Guldbakke and J. Hesselbach. Development of bearings and a damper based on magnetically controllable fluids. *Journal of Physics Condensed Matter*, 18(38), 2006.
- [25] E. Uhlmann and N. Bayat. High precision positioning with ferrofluids as an active medium. *CIRP Annals - Manufacturing Technology*, 55(1):415–418, 2006.
- [26] L van Moorsel. A planar precision stage using a single image sensor (MSc Thesis), 2017.
- [27] R. Deng, S. Van Veen, M. Café, J. W. Spronck, and R. H. Munnig Schmidt. Linear nano-positioning stage using ferrofluid bearings. *Conference Proceedings - 14th International Conference of the European Society for Precision Engineering and Nanotechnology, EUSPEN 2014*, 1(June):372–375, 2014.
- [28] Max Café and Jo Spronck. Nanometer precision Six Degree s of Freedom Planar Motion Stage with Ferrofluid Bearings. *DSPE Conference on Precision Mechatronics*, pages 43–46, 2014.

Method for transport of Ferrofluid in a liquid contactless rotational seal

Olivier G.R. Potma^a Stefan G.E. Lampaert^a and Ron A.J. van Oostyaen^a

a Department of Precision and Microsystems Engineering, Delft University of Technology, Mekelweg 2, 2628CD Delft

Keywords: Environmentally friendly, zero leakage, zero wear, low friction, **ferrofluid seal, experimental and numerical analysis.**

Mots clés: Ecologique, fuite nulle, usure nulle, faible frottement, **joint ferrofluid, analyse expérimentale et numérique.**

Ferrofluid (FF) can effectively be used as a liquid seal for rotary shafts to seal off gasses. The technology tends to be less effective when sealing off liquids, where one major problem is the degradation of FF when it comes into contact with the liquid. This paper presents a method for replacing the FF in the seal without pressure loss, in order to improve the lifetime of the seal. A test setup has been designed to comply with all the contemporary knowledge on FF/water interface seals and to improve on it by adding a FF replenishment method. Using a FEM model to predict the pressure capacity the results show the measured capacity to conform with the model. The setup shows promising results on stability of the seal when water is used as a medium in the pressure chamber.

Les ferrofluides (FF) peuvent être utilisés dans les joints dynamiques pour étancher des gaz. Cette technologie est moins efficace pour étancher des liquides. Dans ce cas un des problèmes majeurs est la dégradation des FF en contact avec les liquides. Ce papier présente une méthode pour le remplacement des FF dans le joint sans perte de pression pour augmenter la durée de vie. Un montage expérimental a été conçu pour satisfaire toutes les connaissances contemporaines des interfaces FF/eau et de les améliorer en ajoutant une méthode renouvellement du FF.

Un modèle d'éléments finis pour prédire la limite en pression du joint montre la capacité de reproduire les essais. Le montage expérimental montre des résultats prometteurs de la stabilité du joint quand l'eau est le fluide à étancher.

1 Introduction

The use of Ferrofluid (FF) in rotational shaft seals is still a new field when used to seal of liquids. Yet there is an interest from industry to implement this technology for propulsion shafts in ships, as well as many other applications.

The major problem is the failure of the seals in aqueous environment due to degradation [1], which affect the lifetime of these type of seals when in direct contact with water. In [2] a mechanism was developed to refresh the FF in the seal, to prevent leaking of the seal over time. The setup however remains stationary and does not take into account the dynamic effects on the seal. Speed differences of the fluids at the seal interface can initiate instability [3], which can lead to mixing of FF with the fluid [4], [5]. Very high rotational speeds can cause centripetal forces [5] to act on the fluid. These phenomena have an adverse effect on the seal lifetime or the pressure drop and are primarily dependent on the peripheral speed of the shaft.

This paper will expand on the mechanism of fluid transport by increasing the seal lifetime by removing degraded FF at the water interface through pumping. A new test setup that more closely resembles the real-world application where the effects of rotational speed of a shaft will be tested on the FF transport mechanism will be introduced.

2 Method

The concept of FF sealing and transport, as well as specific design requirements will be discussed in the following section. This will set the basis for a design which can remove degraded FF to prolong the lifetime of the seal.

2.1 FF transport concept

The setup will consist of a rotary shaft with the seal fixed coaxially around it. The setup has a pressure chamber attached to the front end to simulate pressurized fluids at the seal. FF is added at the front end of the assembly Fig 1, facilitating the flow of FF to the seals while also diminishing discharge into the pressure chamber. At a certain point, the added FF will travel towards the adjacent magnet that attracts the fluid, thus transporting the FF over the seal assembly. After the last seal the FF can be collected for recycling.

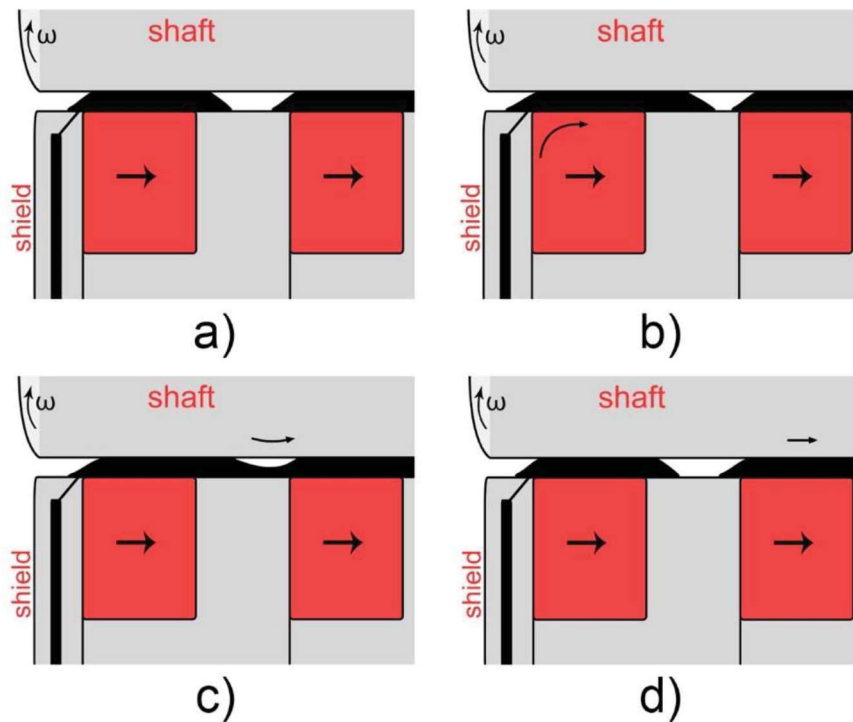


Fig 1 The seal is first a) at equilibrium. Then FF is added b) to the first seal, moving the interface. Magnetic forces c) of the second magnet become more prevalent on the fluid, pulling excess towards it. Finally equilibrium restores d) with the excess fluid now on the second magnet

2.2 Sealing concept

The rotation of the shaft will have an influence on the performance of the seal where it can lower the pressure capacity and/or reduce the lifetime of the seal. The pressure capacity is modelled on the static case where the shaft rotational speed is zero. The gradient of the pressure becomes

$$\nabla p = \mu_0 M_s \nabla H$$

where μ_0 is the permeability of air and M_s is the saturation magnetization of the FF. It is important to note is that this equation is only valid for a saturated FF. For a single magnet and a specific FF, the pressure gradient at a seal is only dependent on the gradient of the magnetic intensity H . Expanding the pressure difference capacity over multiple seals is a summation of the magnets in series. The equation becomes

$$p_i - p_0 = \mu_0 M_s \sum_{i=1}^n H_{i,i} - H_{o,i}$$

where H_i is the intensity at the higher pressure side of the seal, H_o at the lower pressure side, n is the number of sealing rings and i indicate a specific sealing ring. The highest magnet field strength of a magnet is located at the edges. This phenomenon can be used to form a seal close to the magnet where a high value of H is available.

2.3 Interface instability

The shafts rotation has an effect on the behaviour of the fluids at the interface where the fluids meet. When the relative velocity between two fluids at the interface becomes sufficient large, waves form at the interface, and instability occurs. When this instability has fully formed, the fluids start mixing, decreasing the amount of FF in the seal and increasing the contact area at the interface. The point of instability can be predicted by obtaining its criterion using the Rosensweig instability

$$(U_1 - U_2)^2 > \frac{\rho_1 + \rho_2}{\rho_1 \rho_2} \left\{ \sqrt{2g(\rho_2 - \rho_1)\sigma} + \frac{(\mu_1 - \mu_2)^2}{\mu_1 + \mu_2} H^2 \right\}$$

Where U and ρ are the speed and density of the fluid, respectively, g is the gravity, σ is the surface tension between the two fluids, μ is the permeability of the fluid and H is the magnetic intensity at the interface. The H direction should be parallel to the interface.

The design of the seal should be such that the relative velocity difference between the two fluids is enough to prevent the onset of instability. Peripheral speeds on specifically ships hafts can reach speeds of up to 6 m/s, therefore the design of the seal has to be adapted to mitigate these issues. This can be done by adding a shield to the front end of the seal assembly [4], as is shown in Fig 1.

2.4 Seal tightness

In the works of [6] it is claimed that, when there is contact with water, FF seals slowly lose some pressure, coined as tightness loss, while the shaft is in motion without failure of the seal. This loss stabilizes over time. Another observation by [6] is that the critical pressure is dependent on the speed of the shaft, decreasing with increasing speed with the critical pressure at standstill having the highest value. These phenomena should be reproducible in the setup.

3 Experimental approach

3.1 Setup design

The design of the demonstrator (Fig 2), contains a rotary shaft driven by a motor. The Shaft rotates in a pressure chamber that can hold liquids and pressures.

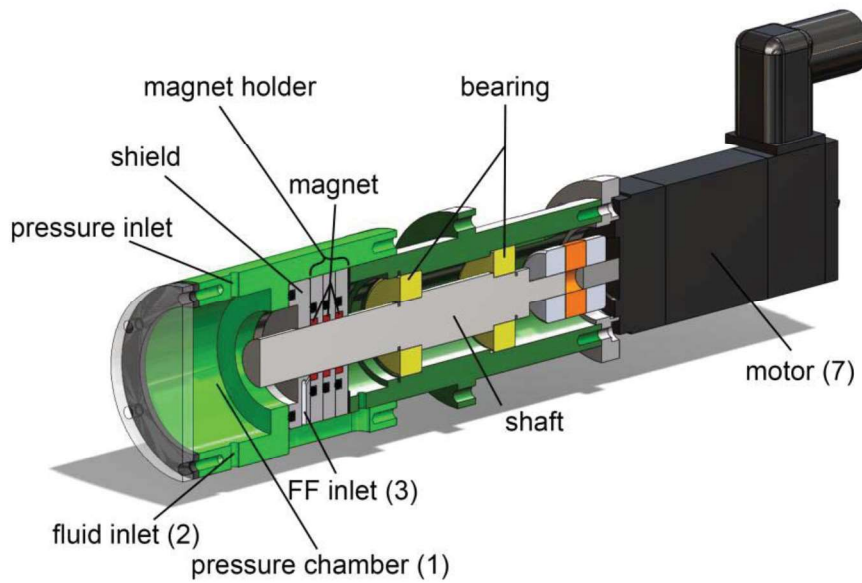


Fig 2 A cut-through of the FFP 02. Colours and tags are used to differentiate between the different components.

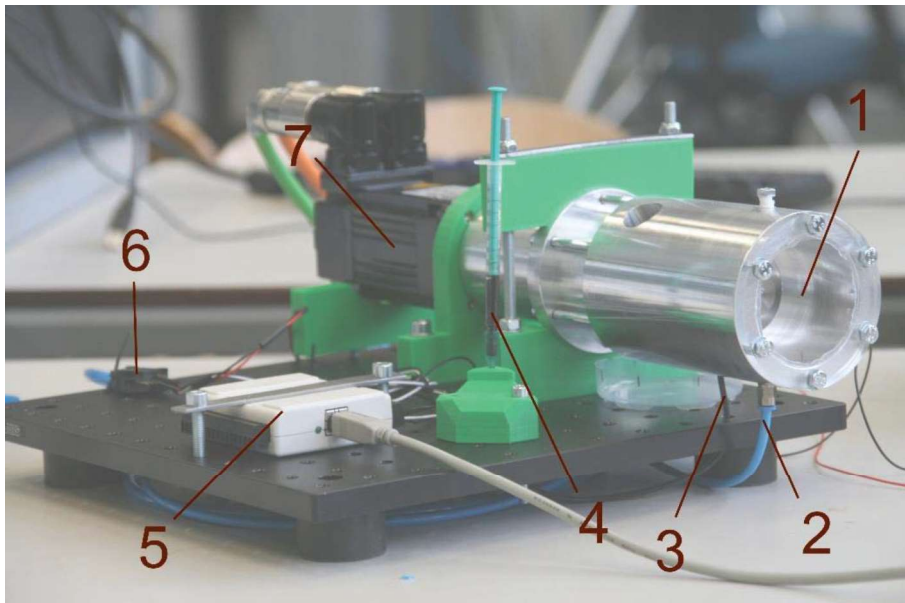


Fig 3 Top image is A cutthrough of the FFP 02. Colours and tags are used to differentiate between the different components. Numbers correspond with the bottom image. Here, the pressure chamber 1 is fed by the inlet 2. The inlet of the FF 3 is connected to the syringe 4, used as FF reservoir and pump. A relative pressure sensor 6 is connected to a data processor 5. The motor 7 drives the setup.

A seal assembly, containing the shield and 3 magnetic seals, is placed around the shaft to seal of the chamber. FF can be added at the shield. The pressure chamber can be filled with water and pressurized using compressed air. The seals are created by adding FF via the syringe while slightly increasing the pressure in the pressure chamber, thus spreading the FF over all the seals. The intermittent chambers are then pressurized by increasing the pressure further until all seals start leaking. This pressure is denoted as the p_c of the setup. The completed setup with FF seals can be seen in Fig 3.

3.2 Experiments

The experiments will be divided in a static and a dynamic case. In the static case the shaft remains at standstill. In the the dynamic case, experiments are conducted at speeds between 1000 and 6000RPM, with increments of 1000RPM.

In the static case the critical pressure p_c can be determined. This is done by steadily increasing the pressure until air starts leaking through the seal. This failure of the seal can be observed by a sharp decrease in pressure in the chamber, as well as by a bubble sounds coming from at the back end. Another experiment is the testing of the lifetime at standstill, where the chamber is pressurised until $0.95p_c$ and measured until seal failure.

In the dynamic case, in a first experiment, a FF transport test is conducted at a sub critical pressure of $0.5p_c$. At each incremental velocity step, FF is added to the seal in a small burst of 0.1 ml . If the pressure in the chamber decreases with the addition of FF and bubbles can be heard at the back end of the seal, a leak is determined. In a second experiment, the dynamic critical pressures $p_{c,d}$ at the different velocity increments is determined. At each speed, the pressure is gradually increased until failure of the seal.

Finally, the performance of the setup with water is tested. An dynamical case experiment is performed where the seal is tested in a water environment at 6000RPM to determine the lifetime of the seal in water. Lastly the FF transport experiment is repeated, now with water in the pressure chamber.

3.3 Comsol model

In order to know the magnetization gradient a FEM model is devised. Figure Fig 4 is a 2D model that represents a cutthrough figure of the demonstrator. Only half is modelled due to axis symmetry. With the magnetic iso-lines, the figure shows the high gradient near the edges of the magnet and a low point in between the magnets. A total of 3 magnets with thickness $b = 4 \text{ mm}$ are modelled with a flux density of $B_r = 1.17 \text{ T}$ and have the same orientation.

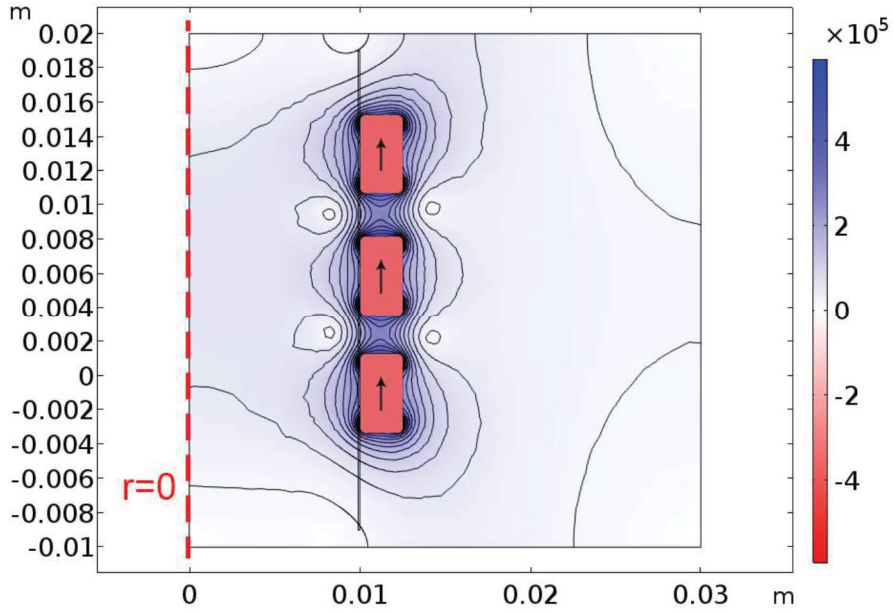


Fig 4 Magnetic field lines of the 2D model. Half of the cuttrough has been modelled because of symmetry. Dotted line represents the symmetry line at the center of the shaft. The vertical black line represents the gap of the seal.

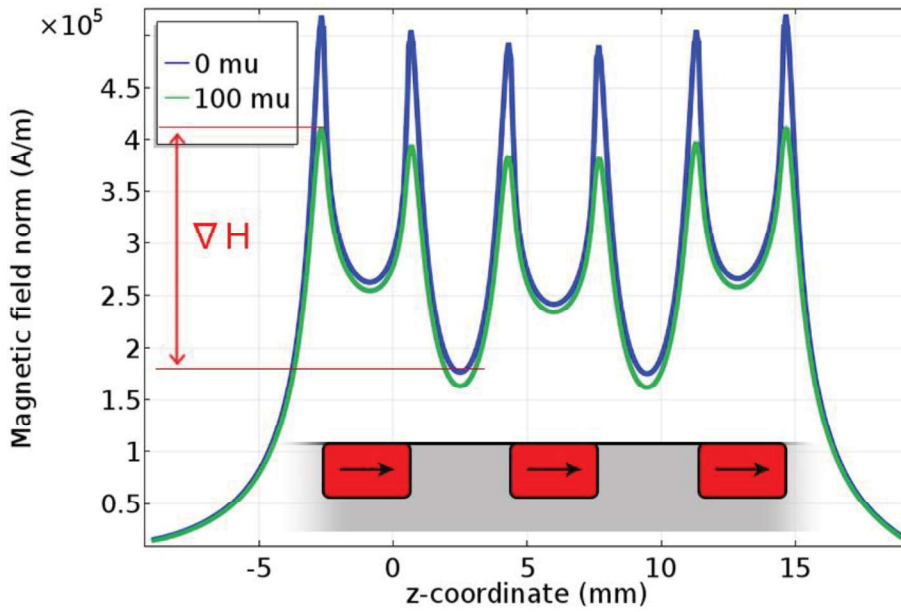


Fig 5 Graphs of the magnetic intensity at the top and bottom surfaces in the gap of the seal. Peaks correspond to the edges of the magnets, shown in red. Height is measured from the surface of the magnet.

Tab 1 Magnetization values from the FEM model for calculating the theoretical maximum pressure.

Seal	$H_i \times 10^5$ [A/m]	$H_o \times 10^5$ [A/m]	Δp [kPa]
1	4.11	1.77	10.3
2	3.84	1.76	9.09
3	4.11	0	18.08

The magnetization field intensity of the model in the gap between magnet and shaft is displayed Fig 5. Each spike corresponds to the edge of a magnet and the valley to the furthest distance between two magnet edges. Taking the the first peak from the green line and its corresponding lowest valley on the blue line forms the H at the two interfaces of the first sealing ring. Repeating this for each seal seal ring gives the values in table Tab 1. The assumption is that there is one sealing element per magnet. Two elements will give a slightly higher pressure drop, but is negligible. These values result in a theoretical maximum pressure of 37.47 kPa. The interaction between the sealing rings, resulting from the distance between them, entails in that each ring does not contain the maximum amount FF. This is caused by the attraction forces of the neighbouring rings. The actual p_c thus tends to be lower.

4 Results & Discussion

4.1 Static critical pressure

An average critical pressure of $p_c = 34.15\text{kPa}$ was obtained by increasing the pressure in the chamber until leaking of the seal, which lead to a sharp drop in the graph (Fig 6). The leaking was accompanied by the sound of air bubbles escaping from the back end of the seal. The difference in critical pressures measured derives from differences in the amount of FF in the seal during the experiments. The small eccentricity in the shaft has also led to different results depending on the rotational orientation of the shaft.

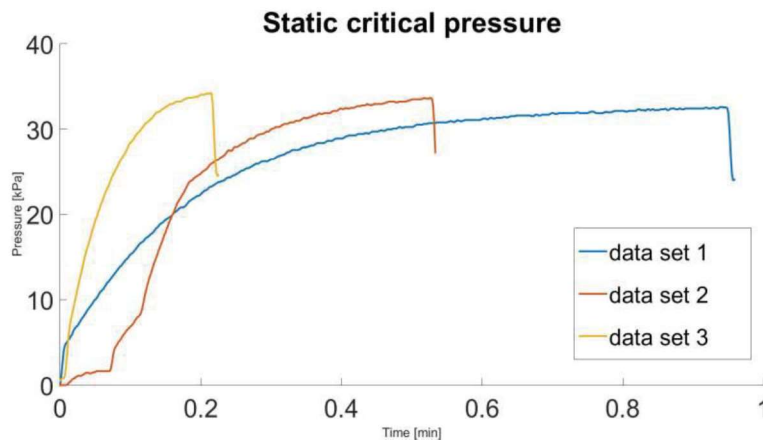


Fig 6 An example of three datasets used in calculating the average of p_c . The sharp drop is the result of a leak of the seal. The pressure rise differs because of the fact that the pressure valve is operated manually.

Keeping the setup at a sub-critical pressure of $0.95p_c$ resulted in leakage after several minutes that continued to leak over several hours. Having the seal at standstill, entices the FF to diffuse slightly towards the magnet, decreasing the pressure drop capacity of a sealing ring. Furthermore gravity will create an asymmetric sealing ring, weakened at the top due to less FF. This also means that the increased amount at the bottom can lead to undesired FF transport, further decreasing the Pressure drop capacity. If a sealing ring fails, it jettisons FF in the direction of the back end of the seal, which is another form of unwanted FF transport and also has a negative effect on the pressure drop capacity.

4.2 Dynamic critical pressure

For the p_c the values for each speed interval, as well the pressures for p_c can be found in Fig 7. The graph shows the pressure drop decreasing with each speed increase. The p_c for lower speeds was measured at a higher pressure than the p_c , which was predicted to be the highest pressure. It is suggested that the rotation of the shaft limits the amount of diffusion and asymmetry in the sealing ring, increasing the performance of the seal. This could explain in the higher sealing capacity. The p_c gradually dropped over speed. This drop is comparabel to the findings of [6].

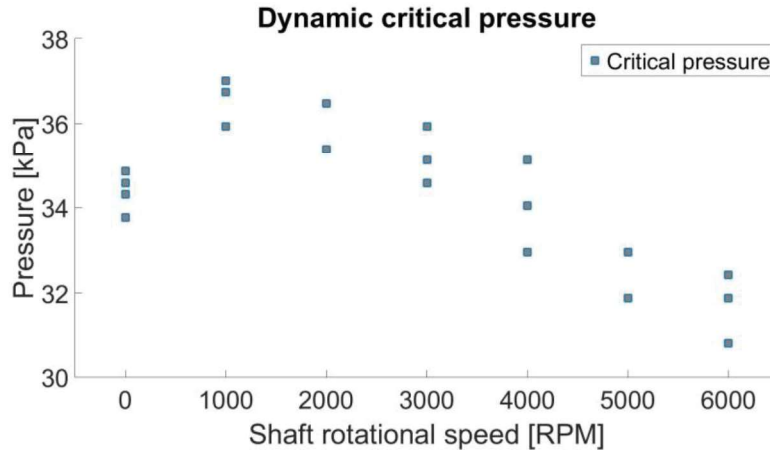


Fig 7 At each speed interval a leak test was carried out, resulting in the p_c . The slope indicates the p_c decreases with speed increase.

4.3 FF addition

When adding FF to the seal while the shaft is rotating, no sharp drop in pressure is detected in Fig 8 for each speed increment. A positive slope for some of the speeds is visible. This has been attributed to the heating of the air by the setup, that is generated by viscous friction of the seal. For experiments at 3000 RMP and 6000 RPM the pressure was reset to 20 kPa. The graph shows that for a FF/air interface the FF transport method works at the given sub critical pressure.

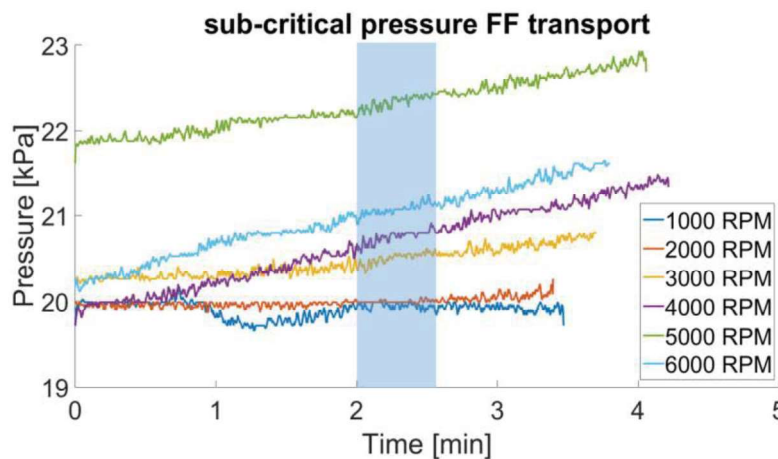


Fig 8 Set up is pressurized to p_c and is run at different speeds where after a certain time (blue area) FF is added to the seal. The rising of the pressure is due to the heating of the setup by viscous friction.

4.4 Performance with water

To determine if the design was correctly designed according to the specifications mentioned in previous chapters a lifetime experiment was conducted. The first test plotted in figure Fig 9 is a stepwise increase of the speed at a sub critical pressure. It showed no sharp pressure decrease although a slight negative slope is visible in accordance with the predictions by [6]. After the maximum speed was attained, the test was ended. A full lifetime test was then performed at maximum speed. The graph in Fig 10 shows the negative slope as before, but later the slope changes in to a positive slope due to the heating of the

water. After 51 minutes the seal fails, shown by the sharp pressure decrease in the graph. The seal can hold a sub critical pressure of 22.69 kPa with an FF/water interface for several minutes, demonstrating that the design behaves comparable to contemporary setups, without further optimisation.

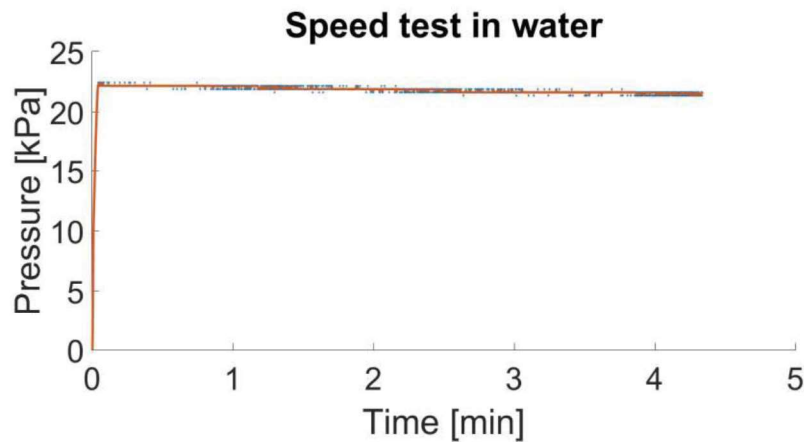


Fig 9 Starting at 0 RPM, the speed is increased by increments of 1000 every 30 seconds until 6000\$ RPM. A slight negative slope is visible.

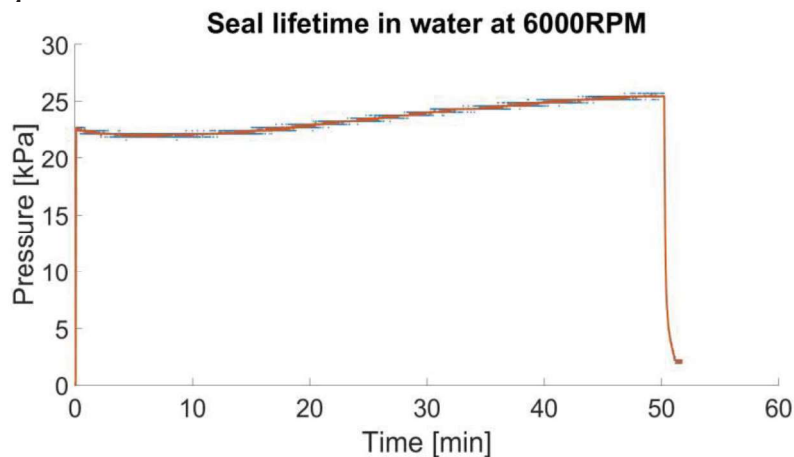


Fig 10 At the sub-critical pressure the speed is increased to 6000\$ RPM. The speed is then maintained until failure of the seal.

Addition of FF with a water interface showed comparable results with respect to the slight negative slope over time. Adding FF at first doesn't lead to failure. However, Fig 11 shows at 3000 RPM that, while the FF is being added, the pressure sharply decreases and water droplets begin to emerge from the back end of the seal. The relatively quick failure (compared to the lifetime of 51 minutes at max. speed) indicates that the addition of FF was the prime cause for failure. The amount of FF added to the first ring at each interval and the flow rate at which it was administered can have a severe effect. FF that isn't directly taken in the sealing ring and transported further towards the back end acts as excess fluid in front of the seal which can more easily mix with water because it being further away from the magnet. The mixture then can be pressed back into the seal after the addition has stopped, weakening the seal. The location of the FF inlet is also a possible culprit. The inlet resides on the front end of the seal, which could more easily facilitate mixing with the water when FF is administered to the first ring.

Fig 11 has also shown that the seal regains a new equilibrium and the leaking stop. The new equilibrium is stable, and it can hold the new pressure, also at higher speeds. The seal is however weakened because now there is water in the chambers. Also some FF has been washed away by the leaked water through the seal. This means small pressure increases lead again to pressure a drop and more droplets forming, further weakening the seal.

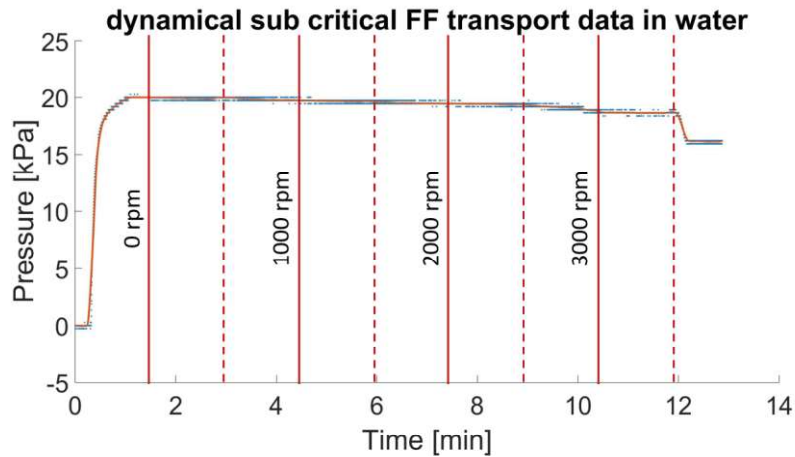


Fig 11 Set up is filled with water and pressurized to $0.5 p_{c,s}$. At certain moments (solid line) speed is increased, and inbetween (dotted line) FF is added to the seal. At 3000 RPM the seal fails at the moment of FF addition.

A failed seal at standstill was measured to still be able hold a pressure of 15.67kPa before failing again. Adding FF to the seal causes the seal to increase its pressure holding capacity to a pressure of 32.42kPa. This indicates that a failed seal can be repaired to a certain degree by adding FF to the seal.

5 Conclusion

A rotation setup was created to observe the effects of FF transport in a liquid seal. The design has been based on the literature under similar conditions to obtain a seal with a high seal life. This includes the of a shield for improved seal stability and also a small gap size to maximize the pressure drop and minimize the interface area. The critical pressure was found to match the analytical model for the static case and in the dynamic case the critical pressure showed to be depended on the rotary speed of the shaft. FF transport was shown to successfully work without seal failure independent on the shaft speed.

The performance of the seal with a water interface showed the capacity to function for 51 minutes without failure at full speed. The addition of FF however, while the shaft was in motion, has led to the failure of seal prematurely. This suggest that the method for administering the FF has room for improvements and has great possibilities designing a seal with long lifetime.

6 References

- [1] Y. Mitamura *et al.*, "Sealing Performance of a Magnetic Fluid Seal for Rotary Blood Pumps," *Artif. Organs*, vol. 33, no. 9, pp. 770–773, 2009.
- [2] O.G.R. Potma, "Designs for rotary shaft fluid seals in an aqueous environment using ferrofluid," Delft University of Technology, 2017.
- [3] J. Kurfess and H. K. Muller, "Sealing Liquids with Magnetic Liquids," *J. Magn. Magn. Mater.*, vol. 85, pp. 246–252, 1990.
- [4] Y. Mitamura, S. Takahashi, S. Amari, E. Okamoto, S. Murabayashi, and I. Nishimura, "A magnetic fluid seal for rotary blood pumps: Effects of seal structure on long-term performance in liquid," *J. Artif. Organs*, vol. 14, no. 1, pp. 23–30, 2011.
- [5] T. Borbáth, D. Bica, I. Potencz, L. Vékás, I. Borbáth, and T. Boros, "Magnetic nanofluids and magnetic composite fluids in rotating seal systems," *IOP Conf. Ser. Earth Environ. Sci.*, vol. 12, p. 012105, 2010.
- [6] M. Szczech and W. Horak, "Tightness testing of rotary ferromagnetic fluid seal working in water environment," *Ind. Lubr. Tribol.*, vol. 67, no. 5, pp. 455–459, 2015.

Ferrofluid Rotary Seal with Replenishment System for Sealing Liquids

K. van der Wal, R. A. J. van Ostayen, and S. G. E. Lampaert

Department of Precision and Microsystems Engineering, Delft University of Technology, The Netherlands

Ferrofluid rotary seals are mechanical contact-free magnetic liquid seals that are characterised by their simple structure, low friction and ability to hermetically seal. Although ferrofluid rotary seals for sealing vacuum and gases are part of a well established industry, the sealing of liquids has not been implemented yet. Literature learns that degradation of the ferrofluid seal over time when it dynamically contacts a liquid results into premature seal failure. This paper presents a new type of ferrofluid rotary seal in which a ferrofluid replenishment system is implemented that renews the ferrofluid in the sealing ring while sealing capacity is maintained. By replacing the degraded ferrofluid in the seal at a sufficient rate, service life of the ferrofluid rotary seal can theoretically be unlimited. An analytical model and FEM analysis are used to design the ferrofluid sealing device and to predict its sealing capacity. An experimental test setup has been built on which the sealing capacity and service life of the device has been tested for different sealing conditions. It is demonstrated that the ferrofluid replenishment system successfully extends and controls the service life of the ferrofluid rotary seal that dynamically seals pressurised water.

Keywords: magnetic liquid seal, lip seal, water, ferrofluid transport, magnetics

1 Introduction

In the 1960's the world's first patented magnetic fluid was created by adding magnetic properties to rocket fuel, enabling control of the fluid in outer space using magnets [1]. Funded by space agency NASA Ronald E. Rosensweig led the development of a wide variety of magnetic fluids and the research to the fluid mechanics of magnetic liquids [2, 3]. Ferrofluid is a magnetic fluid that consists of ferromagnetic nanoparticles suspended in a carrier liquid [4]. The three main technical application areas of ferrofluids are sealing, damping and heat transfer [5]. In most of these applications ferrofluid is positioned magnetically and secondary properties of the fluid are then exploited. An example of application are ferrofluid planar bearings, where absence of both stick slip and mechanical contact result in respectively a high precision and high durability [6, 7].

Since the 1930's radial lip seals are industries standard to retain lubricant and exclude contamination in rotating shaft and bearing applications [8]. This contact-based rotary seal is inherently subjected to wear, which limits its service life and causes leaks. Ferrofluid rotary seals are contact-free magnetic liquid seals and are characterised by their simple structure, low friction and ability to hermetically seal. Ferrofluid rotary seals operating in vacuum and gas environments already have proven themselves in industry [9, 10, 11]. Ferrofluid sealing is also considered to be very important in preserving the environment, since ferrofluid is able to create hermetic sealing for hazardous gases [12].

However, literature learns that ferrofluid rotary

seals fail prematurely when they are used for sealing liquids [13, 14, 15, 16, 17]. The driving mechanisms causing this premature failure are not fully understood and prevent current implementation for sealing liquids. Many authors attribute this limited service life to the arise of interfacial instabilities between the liquid that is sealed and the ferrofluid of the seal [18, 13]. When the liquid-ferrofluid interface becomes unstable, ferrofluid emulsifies with the liquid sealed which results in failure of the seal. Mitamura et al. have shown that a shielding structure in front of the ferrofluid rotary seal can be used to stabilise the interface between the two fluids [19, 20, 21]. Although shielding prevents instant seal failure caused by interfacial instability, the service life of the seal is still limited and unpredictable.

It is reported in literature that the magnetic properties of ferrofluid in contact with water decrease [22]. Also it is suggested that the existence of shearing forces at the interface of the ferrofluid seal and liquid contained limits its service life [23]. Shear forces between the liquid sealed and ferrofluid could cause gradual removal of ferrofluid [24]. All these effects could attribute to the degradation of the ferrofluid seal when it seals a liquid in dynamic operation conditions. Degradation decreases the sealing capacity of the seal over time and causes seal failure when its sealing capacity becomes lower than the required operational sealing pressure. If service life can be improved ferrofluid sealing technology seems very promising for marine applications [25, 26].

This paper presents a new type of ferrofluid rotary seal in which a ferrofluid replenishment system is implemented that renews the ferrofluid in the sealing

ring while sealing capacity is maintained. By replacing the degraded ferrofluid in the seal at a sufficient rate, service life of the ferrofluid rotary seal that seals liquids can theoretically be unlimited. First an analytical model and FEM analysis of the ferrofluid sealing device is presented. Next the stability of the ferrofluid in the seal, the shielding and the ferrofluid replenishment method is discussed. The acquired knowledge is used to design an experimental test setup for a series of experiments in order to identify both static and dynamic sealing capacity of the system. Finally these results are used to perform an series of experiments in order to validate the hypothesis that the ferrofluid replenishment system improves the service life of the ferrofluid rotary seal that is used to seal high pressure water on a rotating shaft.

2 Methods

In order to design a ferrofluid rotary seal that seals liquids, first an analytical model that describes its sealing capacity is derived. Subsequently the required magnetic field intensities for this analytical model are calculated by FEM analysis performed using COMSOL Multiphysics[®]. Next, the influence of the magnetic field gradient stability of ferrofluid on its sealing capacity is discussed. In order to prevent dynamic seal failure, shielding of the seal is discussed and the new concept of ferrofluid replenishment is introduced. Finally, the experimental test setup and experimental procedures and results are elaborated.

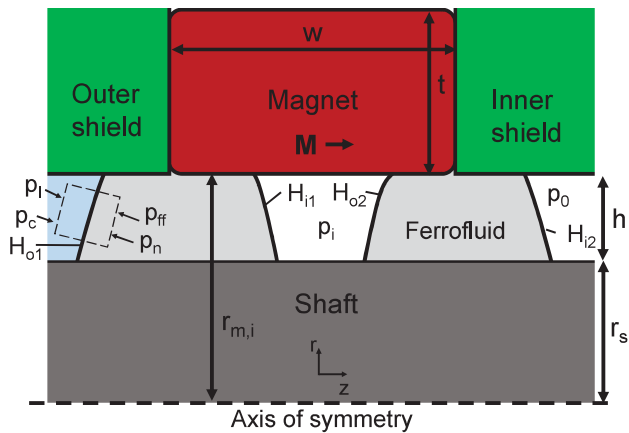


Figure 1: Cross-sectional overview of the ferrofluid rotary sealing system that consists of an axially magnetised ring magnet surrounding a ferromagnetic shaft. Ferrofluid magnetically positioned in the seal gap prevents liquid to leak through the seal gap. The inner and outer shield are made of non-ferromagnetic material.

2.1 Analytical model

A cross-sectional overview of a basic ferrofluid rotary sealing system is presented in figure 1. The system

consists of an axially magnetised ring magnet that is placed around a ferromagnetic shaft and supported by a non magnetic structure (green). Two ferrofluid seals that are located in the gap between the rotating shaft and stationary housing maintain the pressure difference between the liquid with pressure p_l that is sealed and the atmosphere with pressure p_0 . In order to calculate the static sealing capacity of the two ferrofluid seals in the sealing system an analytical model is derived. The behaviour of the ferrofluid in terms of its motion as a function of time can be described using the Navier-Stokes equations for Newtonian incompressible magnetic fluids [27], presented in relation 1.

$$\rho_{ff} \frac{D\mathbf{v}}{Dt} = \underbrace{-\nabla p_{ff}}_{\text{Pressure}} + \underbrace{\eta \nabla^2 \mathbf{v}}_{\text{Viscous}} + \underbrace{\rho_{ff} \mathbf{g}}_{\text{Gravity}} + \underbrace{\mu_0 M \nabla H}_{\text{Magnetic}} \quad (1)$$

$$\nabla \cdot \mathbf{v} = 0$$

The left side term is the density of the ferrofluid ρ_{ff} times the rate of change following the mass motion \mathbf{v} , also known as the material derivative. The right side of equation 1 is the sum of the pressure, viscous, gravity and magnetic body forces normalised to a unit volume. In general gravitational effects are small and can be neglected. For the derivation of the analytical model only non-rotating static shaft conditions are considered, which means that inertial and viscous effects on the pressure distribution can be neglected. The relation presented in equation 1 can now be reduced to the relation shown in equation 2 and only contains the pressure and magnetic terms.

$$\nabla p_{ff} = \mu_0 M \nabla H \quad (2)$$

where p_{ff} is the pressure inside of the ferrofluid, μ_0 the permeability of vacuum, M magnetisation of the ferrofluid and H the magnetic field intensity. The sealing capacity of a ferrofluid seal is defined to be the maximum pressure difference between the high pressure of the fluid (p_{ff}) and the low pressure (p_0) of the ambient gas that can be maintained without leakage. In order to calculate the sealing capacity of both ferrofluid seals combined ($p_l - p_0$), the boundary conditions at the interfaces of the seals have to be investigated. In figure 1 the dashed box indicates the boundary condition at the interface between the liquid that is sealed and the ferrofluid of the first seal. Equation 3 presents this boundary condition.

$$p_l + p_c = p_{ff} + p_n \quad (3)$$

Besides bulk pressures p_l and p_{ff} also interfacial pressures p_n and p_c are present at the liquid-ferrofluid interface. Pressure p_c is the capillary pressure between the liquid that is contained and the ferrofluid and pressure p_n is the normal magnetic pressure.

Capillary pressures will be neglected in the analytical model of the sealing capacity, considering its impact is low compared to the magnetic pressures generated inside of the ferrofluid [28]. The magnetic normal pressure p_n is equal to $\mu_0 M_n^2/2$, where M_n is the normal magnetisation force vector at the interface of the ferrofluid seal. The normal magnetic pressure p_n for the ferrofluid seals can also be neglected since the magnetic field is tangential to the interfaces of the ferrofluid seal [27].

With these assumptions the pressure build up in the first seal can be calculated using equation 2. The magnetisation M of the ferrofluid is a function of the magnetic field intensity. Since magnetic field intensity in the sealing gap is high compared to the saturation magnetisation (M_s) of ferrofluid, it is safe to assume the ferrofluid will be fully magnetically saturated ($M = M_s$). The maximum pressure difference between p_l and p_i then can be calculated by integrating in axial direction along the length of the seal, which is presented in equation 4.

$$p_l - p_i = \int_c \nabla p_{ff} \cdot dz = \mu_0 M_s \int_c \nabla H \cdot dz \quad (4)$$

$$= \mu_0 M_s (H_{o1} - H_{i1})$$

Equation 4 learns that the pressure build up of the first seal depends on the magnetic field intensity H_{o1} at the liquid-ferrofluid interface and the magnetic field strength H_{i1} at the ferrofluid interface on the inside of the seal. The sealing capacity of the second seal can be calculated in a similar way, but now with the magnetic field strength H_{o2} at the interface on the inside of the seal and the magnetic field strength H_{i2} at the ferrofluid-air interface. Relation 5 presents the calculation of the total pressure build up $p_l - p_0$ of both seals combined.

$$p_l - p_0 = \mu_0 M_s ((H_{o1} - H_{i1}) + (H_{o2} - H_{i2})) \quad (5)$$

When pressure difference $p_l - p_0$ on the two ferrofluid seals exceeds the sealing capacity of the two seals that is predicted by relation 5, the seals will burst and the liquid that is sealed will leak through the seal gap.

2.2 FEM Analysis

Equation 5 presented in section 2.1 learns that the magnetic field intensities ($H_{o1}, H_{i1}, H_{o2}, H_{i2}$) at the interfaces of the two ferrofluid seals are required in order to calculate its static sealing capacity. These magnetic field intensities are calculated using the numerical analysis package COMSOL Multiphysics version 5.3.

The magnetic properties of the shaft material have a significant impact on the distribution of the magnetic field intensity in the seal system. Shafts that

operate in aqueous environments and transmit torque often are made of stainless steel. There are four main families of stainless steels which are primarily classified by their crystalline structure. These are ferritic, austenitic, martensitic and duplex stainless steels. Of these four ferritic stainless steels have the best magnetic properties. Therefore the material of the shaft is selected to be ferritic stainless steel (AINSI 430F) and is modelled using the BH curve from the COMSOL material library (stainless steel 430F annealed). The ring magnet is modelled by a remanent magnetisation B_r and is magnetised in axial direction. Fillets of radius r_{fil} of the used ring magnet are constructed in all corners. Seal gap h of the seal system is 100 μm . Table 1 presents an overview of the parameters of the ferrofluid sealing device that is used in the FEM analysis.

Table 1: Parameters of the sealing system which are used in the FEM.

Design Parameters			
r_{fil}	0.3 mm	B_r	1.28 T
r_s	3.9 mm	w	6 mm
$r_{m,i}$	4 mm	h	100 μm
t	3.5 mm	M_s	35 kA/m

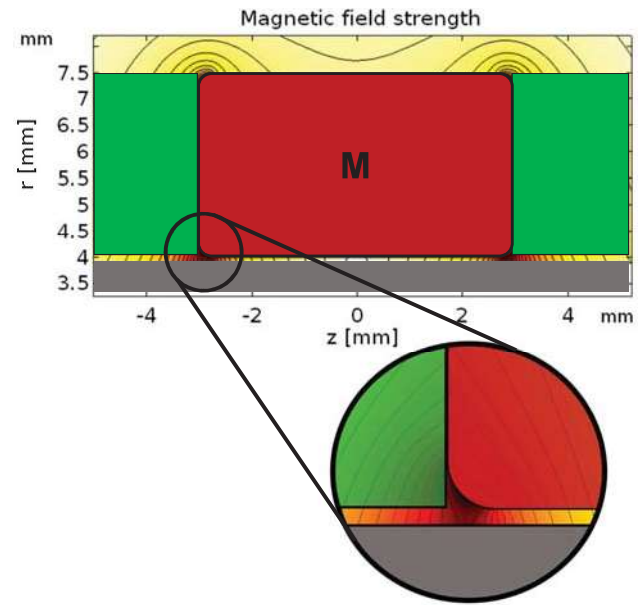


Figure 2: Magnetic field intensity of the seal having a ferritic stainless steel (AINSI 430F) shaft. The isolines of the magnetic field intensity are also the isolines of the pressure distribution in the ferrofluid. Ferrofluid shapes according to these isolines.

Figure 2 presents a two dimensional plot of the magnetic field intensity in the system. The colour scale represents the strength of the magnetic field, where red is highest magnetic field intensity and white the lowest. The black lines in the seal gap represent the magnetic isolines. Equation 2 learns these isolines are equal to the isolines of the pressure distribution in the

system. Ferrofluid shapes according to these isolines. Analysing the distribution and shape of these lines it can be observed that two independent ferrofluid seals can be formed by the magnetic field distribution in the seal.

The magnetic field distribution of the seal system is evaluated along two horizontal lines in the sealing gap, one at the top of the gap (h) and one at bottom. Figure 3 presents a lineplot of these magnetic field intensities. Previous section showed that the sealing capacity of the ferrofluid seals depends on the magnetic field differences $H_{o1} - H_{i1}$ and $H_{o2} - H_{i2}$. Since the seal will start to fail at its weakest spot, the magnetic field intensities that predict the lowest sealing capacity have to be used.

In order to reach the full performance potential of the seal system the magnetic field difference ΔH on each ferrofluid seal has to be as high as possible. The inner shield, also shown in figure 1, makes sure that the ferrofluid of the second seal is forced into a region of low magnetic field intensity (H_{i2}). The magnetic field intensity plot of figure 3 learns that the inner shield has to have a width of around 6 mm in order to create a high magnetic field difference on the second seal and therefore a high sealing capacity.

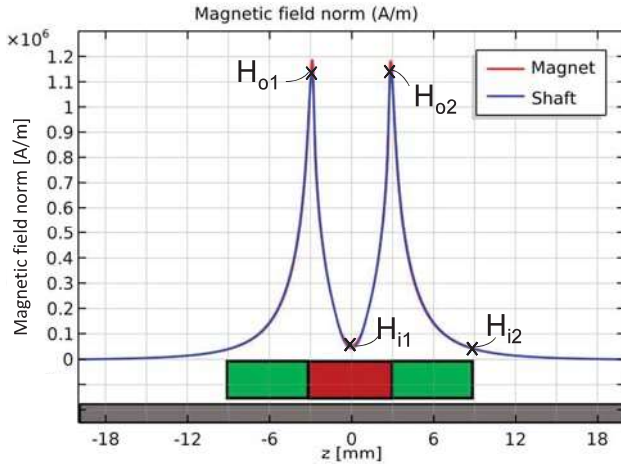


Figure 3: Magnetic field intensity evaluated at two horizontal lines along the axial direction at the top and bottom surfaces of seal gap h . The material of the shaft is ferritic stainless steel (AINSI 430F).

The ferrofluid (Ferrotec EFH1) that will be used in the experimental sealing system consists of a light hydrocarbon carrier liquid with magnetite (Fe_3O_4) suspended particles. The saturation magnetisation of the ferrofluid M_s equals 35 kA/m. Table 2 lists the magnetic field intensities at the two interfaces of both seals which have been found in the FEM analysis. The sealing capacity of both seals now can be calculated using equation 2. The total predicted sealing capacity of the two ferrofluid seals combined equals 96.2 kPa.

Table 2: Magnetic field intensities at the seal interfaces and predicted sealing capacity of both ferrofluid seals.

	$H_o \cdot 10^5$ [A/m]	$H_i \cdot 10^5$ [A/m]	Δp [kPa]
Seal 1	11.4	0.541	47.8
Seal 2	11.4	0.410	48.4

2.3 Magnetic field gradient stability of ferrofluid

Since the ferrofluid in the sealing system is a colloidal dispersion of magnetic particles in a liquid carrier, stability of that colloid is an important property of the seal. In static sealing conditions the magnetic field gradient in the seal generated by the ring magnet, shown in figure 2, can cause migration of the magnetic particles. Particles travel through the fluid to a higher intensity region of the magnetic field [29]. This phenomenon results in a non homogeneous ferrofluid that has a higher effective magnetisation. The sealing capacity that is measured will be higher than predicted using relation 5. By rotating the shaft at sufficient speed the ferrofluid in the seal becomes homogeneous again.

The stability of the magnetic particles in the magnetic field gradient can be analysed by comparing their thermal energy E_{Therm} and magnetic energy E_{Mag} . Thermal motion counteracts the magnetic field force and provides statistical motion that results in a distribution of the particles in the magnetic fluid. In equation 6 the ratio between both energies is presented.

$$\frac{E_{Therm}}{E_{Mag}} = \frac{k_B T}{\mu_0 M_p H V_p} \quad (6)$$

The thermal energy per particle can be calculated by the product of the Boltzmann's constant k_B and absolute temperature T . The magnetic energy represents the work in transferring the particle to the higher magnetic intensity region in the fluid. The magnetic energy per particle E_{Mag} can be calculated by the product of magnetic permeability of vacuum μ_0 , magnetisation of the particle M_p , magnetic field intensity H and particle volume V_p . It can be concluded that particle size is an important property of the ferrofluid that influences its stability in the seal.

2.4 Shielding

A relative velocity between the liquid that is sealed and the ferrofluid of the seal can cause interfacial instability which results in seal failure [13, 30]. By introducing a shield into the design of a ferrofluid seal sealing liquids the liquid-ferrofluid interface can be stabilised and instant seal failure due to interfacial instability can be prevented [21, 19]. The simple outer

shield structure presented in figure 1 is found to be most effective [19]. Experiments and CFD analyses of flow in a ferrofluid seal showed the shield stabilises the interface between water and the ferrofluid. Figure 4 visualises the velocity profiles of the liquid sealed and the ferrofluid of the seal when a no slip condition is assumed. Also it is assumed flows in and in front of the seal gap are laminar and that the velocity profiles are linear in radial direction.

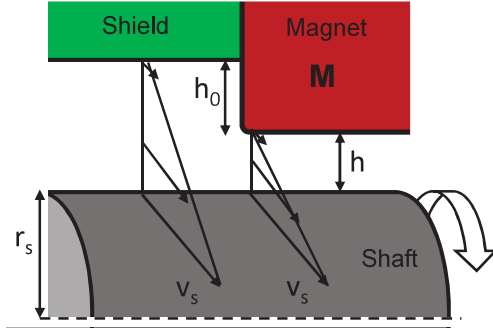


Figure 4: Velocity profiles of the liquid that is sealed and the ferrofluid of the seal. Due to a height difference h_0 between the magnet and shield of the system a relative velocity between the fluids is created.

Equation 7 presents a relation for calculating the relative velocity between the liquid that is sealed and ferrofluid of the system.

$$v_{ff} - v_l = v_s \cdot \frac{h_0}{h_0 + h} \quad (7)$$

where v_{ff} and v_l are the velocities of ferrofluid and liquid that is sealed, v_s the surface speed of the shaft and h_0 the difference in gap height between the shield and seal gap h . If a seal system design is considered with a large ratio between h_0 and h , the velocity difference can be approximated by surface speed v_s . It can be seen that the height difference h_0 is an important design parameter for minimising relative velocity between the liquids and the prevention of premature seal failure.

The Kelvin-Helmholtz instability for magnetic liquids derived by Rosensweig is often used to describe the stability of the liquid-ferrofluid interface [27, 18, 13]. The Kelvin-Helmholtz instability is a hydrodynamic instability in which two inviscid fluids are in relative and irrotational motion. The velocity and density profiles are discontinuous at the interface between the two fluids. Besides preventing instability of the interface between the liquid sealed and ferrofluid, shielding also decreases shearing forces on the ferrofluid. Shearing stress on the ferrofluid is dependent on viscosity, the relative velocity of the fluids and the contact area between the liquids. When shaft diameter and seal gap of the system increases, shear stresses affecting the performance of the seal will also increase.

2.5 Ferrofluid replenishment system

Although shielding of a ferrofluid rotary seal that seals liquids prevents instant dynamic seal failure due to interfacial instability, service life of the seal is still limited. Degradation of the ferrofluid seal decreases the sealing capacity over time and causes failure of the seal when its sealing capacity becomes lower than the required operational sealing pressure.

In order to solve this problem, a ferrofluid replenishment system is introduced here into the design of a ferrofluid rotary seal (also partially presented in [31, 32]). The system replenishes the ferrofluid of the seals by facilitating the axial transport of ferrofluid from one seal to another.

Figure 5 presents an overview of the process of ferrofluid transport through the two seals of the ferrofluid rotary sealing system that also was elaborated in sections 2.1 and 2.2. First an amount of new ferrofluid is radially injected through a supply channel in front of the first seal (step 1). By doing so the same amount of ferrofluid at the lowest pressure region of the first seal (interface of H_{i1}) will jump from the first seal to the second seal. This can be seen in steps 2 and 3 presented in figure 5. When the second seal is supplied with ferrofluid from the first seal, ferrofluid at the lowest pressure region of the second seal (interface of H_{i2}) will be pushed out of the seal to the right through the sealing channel (step 4). This ferrofluid will eventually be pushed to the end of the sealing channel where it can be collected, potentially for recycling.

The sealing capacity of the ferrofluid seals is restored when the degraded ferrofluid is replaced by new ferrofluid. If the ferrofluid in the seal constantly is being replaced at sufficient rate, the service life of the ferrofluid rotary seal theoretically could be extended without limitation.

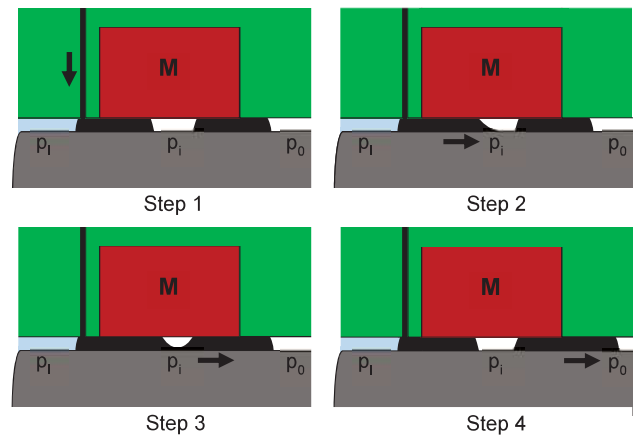


Figure 5: Concept of the axial ferrofluid transport through the seal. During step 1 new ferrofluid is radially added in front of the first seal. In steps 2 and 3 ferrofluid flows from the first seal to the second seal. In step 4 ferrofluid of the second seal is pushed to the ferrofluid outlet at the right.

In order to prevent the ferrofluid from flowing to-

wards the liquid that is sealed instead of through the seals, it is required that the liquid pressure p_l is sufficiently high in order to force the ferrofluid to jump from the first to the second seal. In figure 3 the magnetic field intensity H_{i1} between the two seals can be seen. This magnetic field intensity can be used to calculate a pressure p_{min} , in order to define the operational range of the sealing system to use this axial ferrofluid transport. The sealing capacity of the seal system can be increased when multiple seals are placed after each other [33]. Equation 8 presents a general relation for the upper- and lower-bound of liquid pressure p_l for the ferrofluid rotary sealing system when ferrofluid is axially transported through its seals.

$$p_0 + p_{min} < p_l < p_0 + \sum_{j=1}^n \Delta p_j \quad (8)$$

where p_0 is the atmospheric pressure, p_{min} the minimum pressure, Δp_j the seal capacity of each seal ring j and n the number of seal rings in the system. It can be seen that if the number of seals increases, the operational range of sealing pressure p_l also increases.

Up to now the analysis has been performed assuming a non-rotating shaft. It is important to note that the sealing capacity decreases when the shaft speed increases. This also means that the operational range of the sealing system is different for static and dynamic sealing conditions. The refreshment rate of the seal system has to be sufficiently high in order to compensate for the degradation rate of the seal and thus to prevent seal failure. If the volume of the seal is known the specific replacement time of the ferrofluid seal can be calculated using the relation presented in equation 9.

$$R = \frac{\pi \cdot ((r_s + h)^2 - r_s^2) \cdot w_{seal}}{Q_{ff}} \quad (9)$$

where R is the time constant with which the seal is being replaced, r_s the shaft radius, h the seal gap height, w_{seal} the total seal width and Q_{ff} the ferrofluid supply rate. Without replenishment, the ferrofluid will degrade with a certain time constant, and will fail when the condition of the ferrofluid drops below a certain critical value. Now, with replenishment, the ferrofluid will still degrade but only until there is a balance between the addition of new ferrofluid and the degradation of ferrofluid in the seal, so the critical degradation value will never be reached.

2.6 Experimental test setup

The theory presented before is used to design and manufacture a ferrofluid rotary seal module and test setup in order to validate if the ferrofluid replenishment system improves and controls the service life of a ferrofluid rotary seal. An axially magnetised ring

magnet (HKCM R15x08x06ZnPC-42SH, [34]) with a remanent magnetisation B_r of 1.28 T, also discussed in section 2.2, generates the magnetic field distribution inside of the ferrofluid sealing module. Corrosion of the magnet is prevented by its coating consisting of parylene and zinc. The shaft ($\varnothing = 7.8$ mm) is made of ferritic stainless steel (AINSI 430F), resulting in the magnetic field distribution presented in figure 2. The diametrical clearance between the ring magnet and the shaft is 200 μm and creates a seal gap of 100 μm . The ferrofluid used in the setup and experiments is Ferrotec EFH1 [35] and generates a theoretical sealing capacity of 96.2 kPa, which was calculated during the FEM analysis.

Figure 6 presents an overview of the ferrofluid seal module that has been designed and manufactured. The magnetic ring is contained in an assembly of four layers of transparent acrylic sheets that are bonded by transparent tape-sheet (3M 7955MP). By using transparent structural material good visibility inside of the ferrofluid rotary seal is provided. Layer 1 functions as inner shield and creates a shielding channel that stabilises the liquid-ferrofluid interface. Acrylic sheet layer 2 contains a small milled channel of approximately 1 mm depth and width which is used for radial supply of ferrofluid in front of the first seal. The ring magnet is supported by layer 3 and this layer also contains a brass tube connector for the ferrofluid supply hose. Finally, layer 4 functions as outer shield and makes sure ferrofluid of the second seal is directed towards a low intensity region of the magnetic field. The magnetic field intensity plot of figure 3 showed that a layer thickness of 6 mm is sufficient in order to reach the full potential of the sealing capacity of the second ferrofluid seal.

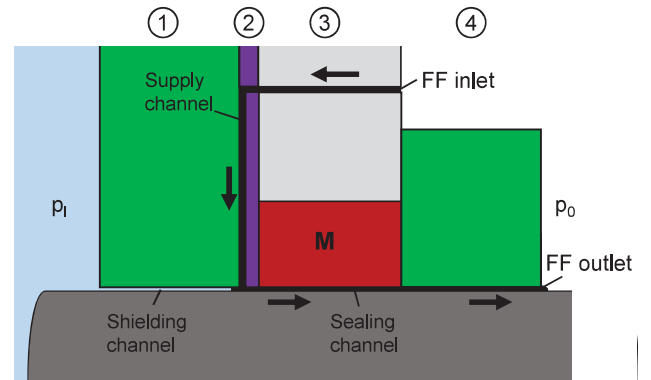


Figure 6: Cross-sectional view of the seal module. The seal module consist of 4 different layers of transparent acrylic sheets.

Ferrofluid flows into the seal module via the inlet of layer 3 and enters through a hole in the supply channel of layer 2, which ends just before the first seal. Subsequently ferrofluid travels through the sealing channel to the ferrofluid outlet where it exists the system. Table 3 presents an overview of the width and function of the four layers.

Table 3: Overview of the transparent acrylic layers used in the sealing module. The layers are bonded by 127 μm transfer tape (3M 7955MP).

Layer	Width	Function
1	6 mm	Outer shield
2	2 mm	Supply channel
3	6 mm	Magnet support
4	6 mm	Inner shield

In order to create the sealing environment the sealing module is mounted on a pressure chamber. Care is taken to ensure that only the shaft is ferro-magnetic, all other materials in the setup are non-magnetic. Figure 7 presents a cross sectional view of the test setup. The transparent acrylic cover end-plate provides good visibility inside of the pressure chamber. The total volume of the pressure chamber is approximately 58 ml. The liquid that is stored in the pressure chamber is pressurised by air through the pressure inlet. The shaft is supported by two pillow block ball bearings made of a zinc alloy. The ferrofluid supply hose is connected to the ferrofluid inlet of the seal module.

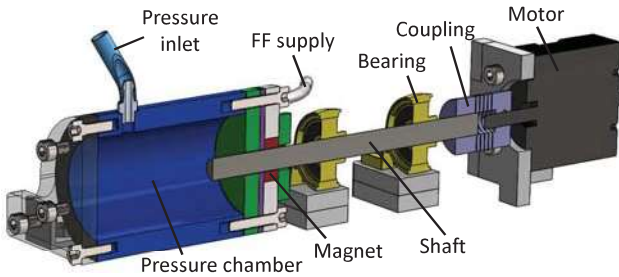


Figure 7: Cross-section of the test setup. The seal module is mounted on a pressure chamber which creates the sealing environment. A DC motor drives the ferromagnetic shaft supported by two ball bearings.

In order to perform consistent experiments it is important that the surface speed of the shaft is constant and therefore is velocity controlled. A 24 V brushless DC motor (Trinamic QBL4208-41-04-006) is connected to the shaft by an aluminum flexible motor coupling. The DC motor is supported by an acrylic structure and controlled using a single axis driver module (Trinamic TMCM-1640). A computer with software (Trinamic TMCL-IDE version 3.0) is connected to the driver module in order to provide instructions to the DC motor.

A rendering of the test setup is presented in figure 8. The pressure chamber is mounted to an acrylic baseplate by supports (6060T66 AlMgSi 0.5). The holes of these supports are slightly larger than the bolts used for mounting, enabling alignment of the seal module in both vertical and horizontal plane around the shaft. Additionally slots have been made in the acrylic support plate for alignment in the horizontal plane. The base consists of an aluminum bread-

board (Thorlabs) with four Sorbothane vibration isolaters (Thorlabs \varnothing 38.1 mm). Non magnetic stainless steel bolts are used throughout the system for mounting. The setup has been placed inside of an aluminum drip tray.

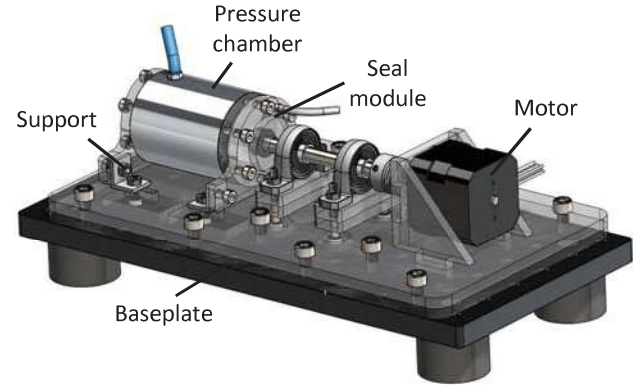


Figure 8: Rendering of the experimental test setup. The setup is mounted on an aluminum breadboard base.

A global overview of the experimental test setup including supporting systems is presented in figure 9. The air pressure that is used in order to pressurise the pressure chamber is generated by a compressor and regulator. A needle valve is added for the manual fine-tuning of the pressure increase. In order to stabilise the pressure a buffer tank with a volume of 2 liters is added. A ball valve is used to shut off the pressure of the pressure chamber after the desired sealing pressure is reached. Ferrofluid is rate controlled added to the system by the combination of a syringe pump (WPI SP100iZ) and a 3 ml syringe (HSW soft-ject). The device allows to set the rate and total volume of ferrofluid supply. The syringe and ferrofluid supply hose are connected by a Huer lock connection in order to make refill of the syringe convenient.

The air inlet hose of the pressure chamber is split and connected to a monolithic silicon gauge pressure sensor (NXP MPX4250DP). The sensor measures the pressure inside of the pressure chamber (p_l) relative to the ambient air pressure (p_0). This means that the sealing capacity of the seal ($p_l - p_0$) is directly measured by the pressure sensor. The sensor is connected to a 16 bit analog I/O device (NI USB-6211). Labview 2013 (version 13.0, 32 bit) has been used to live display the pressure inside of the pressure chamber and to store the sensor data that has been obtained during the experiments. The pressure is sampled at a frequency of 10 Hz.

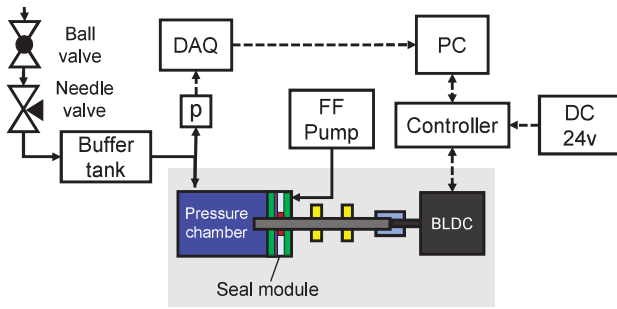


Figure 9: Global overview of the experimental test setup and its supporting systems. Continuous arrows represent flows of air or ferrofluid, dotted arrows represent digital control signals.

2.7 Experimental procedure

2.7.1 Examination of sealing capacity

The first performance parameter of the ferrofluid sealing system that will be experimentally evaluated is its sealing capacity for a number of different static and dynamic sealing conditions. It is important that the exact moment of seal failure is accurately determined. That is why for the experiments evaluating the sealing capacity the buffer tank is removed. The sealing device is prepared for each sealing condition by first transporting ferrofluid through the sealing system. Once the sealing channel is completely filled with ferrofluid the supply is stopped and the seal is considered to be ready. During all experiments that have been performed the alignment between the seal module and shaft has not been changed.

First the static sealing capacity of the system is determined when it seals demineralised water. The sealing capacity is tested 5 times immediately after the test setup is prepared and 3 times 24 hours after the setup is prepared. During this settling time of 24 hours the seal is not pressurised, shaft speed is zero and the ferrofluid replenishment system is not active. These experiments are also conducted for air as sealed medium. The dynamic sealing capacity of the system when demineralised water is sealed is tested at five different shaft speeds, ranging from 500 to 2500 rpm.

In order to obtain the sealing capacity of the system during a certain sealing condition the pressure inside the pressure chamber will be increased until the seal bursts. The rate of pressure increase is manually controlled using the needle valve. The pressure of the pressure chamber is live monitored during the experiments. When the seal bursts during an experiment the needle and ball valve are closed.

2.7.2 Examination of service life

When the static and dynamic sealing capacity of the seal system are determined, the influence of the ferrofluid replenishment system on the service life of the

seal can experimentally be examined. The service life of the seal system that seals demineralised water depends on shaft speed, sealing pressure and rate and duration of ferrofluid transport through the seal.

The pressure p_l of the demineralised water that is sealed is chosen to be at least higher than the sealing capacity of a single ferrofluid seal (48.1 kPa). By doing so, it is ensured that both ferrofluid seals have to contribute to the sealing capacity of the seal system when ferrofluid is transported through the seals. The upper bound of the sealing pressure is determined by the dynamic sealing capacity of the system at 500 rpm. The closer the sealing pressure p_l approaches this dynamic sealing capacity, the faster the seal will fail after the replenishment system is deactivated. The amount of time required to perform the experiments can be reduced this way. Within this range p_l is set at 55 kPa for the service life experiments ($\pm 90\%$ of its dynamic sealing capacity at 500 rpm).

In order to examine the influence of the ferrofluid replenishment system on the service life of the seal, the ferrofluid replenishment system has been deactivated after various running times. These running times are 10, 30 and 60 minutes. The ferrofluid supply rate is set to 2 ml/hr, which theoretically results in a replacement time constant of the ferrofluid in the system of approximately one minute. The experiments are alternated in order to exclude coincidence. Five measurements per running time are performed.

3 Results and discussion

3.1 Static sealing capacity

The static sealing capacities of the seal that have been measured during the four different sealing conditions are listed in table 4. The moments that the seal failed were very obvious, both from observation during the experiments as afterwards in the recorded pressure data. The average sealing capacity measured for water (75.9 kPa) and air (69.8 kPa) slightly differ.

The static sealing capacity that has been measured is lower than that was predicted by the analytical model and FEM analysis (96.2 kPa). Overestimation of the static sealing capacity could be due to wrong assumptions in the FEM analysis, analytical model or manufacturing errors in the test setup. Alignment of the shaft and the sealing module during the experiments was not perfectly concentric. Due to this misalignment the radial seal gap height h is larger than 100 μm at some locations in the seal system. This results in a lower magnetic field gradient at these weakest spots of the seal, thus lowering the sealing capacity of the system. Also the non uniformity of the coating of the ring magnet could introduce error in the height of the seal gap. Other authors have also reported that an increase in seal gap decreases the sealing capacity

of the seal [36].

Table 4: Average sealing capacity measured for four different static sealing conditions. Also the number of experiments per condition is listed.

Static condition	Mean $p_{c,s}$ [kPa]	#
Water	75.9	5
Air	69.8	5
Water (24 hrs)	213	3
Air (24 hrs)	156	3

The FEM analysis did not account for the influence of ferrofluid on the magnetic field distribution in the system. Furthermore in the analytical model capillary effects have been neglected, which theoretically could lower the maximum pressure the sealed liquid can reach before the seal system fails. Other research also indicated that overestimation of the seal capacity of a ferrofluid seal could be due to capillary effects [37, 6]. However, it has been shown that all these assumptions may only result in an acceptable small overestimation of the load capacity. As a consequence, this means manufacturing errors are probably the main reason that the sealing capacity is overestimated.

The average sealing capacity for water and air that was measured after the ferrofluid in the seal system had been allowed to settle for 24 hours, 213 kPa and 156 kPa respectively, are significantly higher than the sealing capacity that is measured when it was tested immediately after preparation. A phenomenon that could attribute to this increase in seal capacity is the magnetic field gradient instability of the ferrofluid, which was presented in equation 6. The particles migrate through the fluid to locations that have a higher magnetic field intensity, which increases the effective magnetisation of the ferrofluid.

Also a difference in the sealing capacity for water and air after 24 hours settling was observed. The sealing capacity measured after water has been sealed for 24 hours (213 kPa) is larger than the sealing capacity when air is sealed for 24 hours (156 kPa). This implies that the increase in static sealing capacity over time when water was sealed can not be attributed exclusively to the migration of particles to a higher magnetic field intensity.

The magnetic field intensity in the sealing gap and thus the sealing capacity of the seal can further be increased by adding pole pieces on both sides of the ring magnet [15]. Pole pieces consist of ferromagnetic material that concentrate the magnetic field in the seal gap. During this research the usage of pole-pieces has not been investigated.

3.2 Dynamic sealing capacity

Figure 10 presents the dynamic sealing capacity of the ferrofluid rotary seal at different shaft speeds ranging from 0 till 2500 rpm. It can be seen that the sealing capacity of the seal drops when the shaft speed increases. The maximum pressure difference in [kPa] can be expressed as a function of the rotation speed in [rpm] by the exponential function $21.4 \cdot e^{-0.0019n} + 54.3$ fitted through the data with a coefficient of determination $R^2 = 0.94$.

The decrease in sealing capacity at higher shaft speeds shows similarities with other results found in literature. Szczech and Horak have proposed a mathematical model that can be used to predict the dynamic sealing capacity of a seal [13]. However, the dynamic sealing capacity that is calculated using this model predicts a faster decrease in sealing capacity at high speeds than is measured. The setup that they have used in order to derive their mathematical model did not contain a shield. This could suggest that a shield can also be used to improve dynamic sealing capacity. Further research is required in order to validate this.

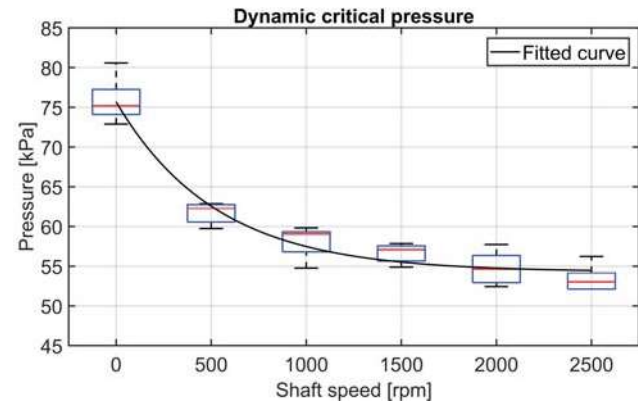


Figure 10: Boxplot of the measured dynamic sealing capacity of the seal system at different shaft speeds. The fitted line through the data is $21.4 \cdot e^{-0.0019n} + 54.3$.

It is not fully understood why the sealing capacity drops when the shaft speed increases. It is possible that higher inertial and viscous effects result into a faster destabilisation of the ferrofluid flow inside of the seal, which affects the sealing capacity of the system. Also some authors consider the Kelvin-Helmholtz instability that was mentioned in section 2.4 as the main reason for the dynamic sealing capacity to decrease [18, 13]. However, since the test setup contains a shield, the relative velocity between the water that is sealed and the ferrofluid of the seal is minimal. Furthermore it is not evident how the pressure of the liquid that is sealed is related to the stability of the interface between the ferrofluid and the liquid.

3.3 Service life

Figure 11 presents the results of the service life experiments on the ferrofluid rotary seal with replenishment system. In the graph 15 measurements of the water pressure inside of the pressure chamber are presented. All measurements start at a water pressure p_l of 55 kPa and for each of the measurements a sudden drop in pressure after a period of time can be seen. This drop indicates the moment the seal has failed and has started to leak water through the sealing channel. After that, when the pressure had dropped sufficiently the ferrofluid that has remained on the ring magnet is able to form a new seal and the pressure inside of the container is again stabilised. It can be observed that during most of the measurements a new seal was formed at a pressure slightly below 20 kPa. After the seal stabilised the measurements were stopped.

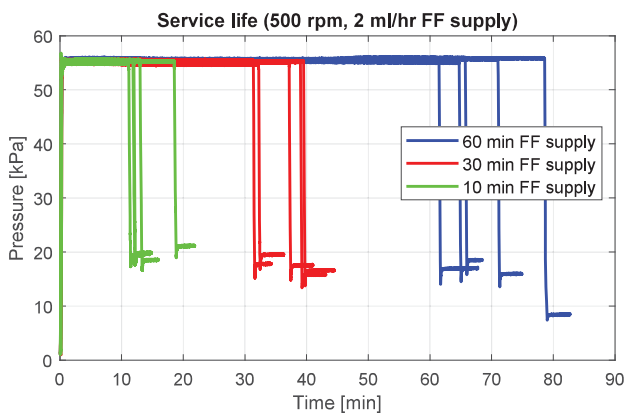


Figure 11: Service life of the ferrofluid rotary seal when the ferrofluid replenishment system is deactivated after 10, 30 or 60 minutes. Water pressurised at 55 kPa is sealed at a shaft speed of 500 rpm. The ferrofluid supply rate is 2 ml/hr.

During the measurements presented in figure 11 ferrofluid transport through the seals of 2 ml/hr was stopped after 10, 30 or 60 minutes respectively. When the ferrofluid supply was stopped after 10 minutes the seal failed within 20 minutes. If the ferrofluid supply was stopped after 30 minutes, service life of the seal increased to approximately 30 to 40 minutes. Finally, if ferrofluid supply was only stopped after 60 minutes, service life ranged from approximately 60 till 80 minutes. The measurement presented in figure 11 show that the ferrofluid rotary seal did not fail while the replenishment system was active.

Because the seal module is transparent and easily accessible it could visually be confirmed that ferrofluid is transported through the seal to the outlet of the seal system while the replenishment system was active. Due to gravity the ferrofluid at the output of the seal leaked along the shield on the base-plate.

The measurements of the pressure in figure 11 show that the moment the seal fails can be controlled by the ferrofluid replenishment system. The ferrofluid supply rate of 2 ml/hr results in a specific replacement

time of approximately one minute. The sealing pressure of 55 kPa during the service life experiments is higher than the sealing capacity of a single ferrofluid seal. This means that at the same time that ferrofluid was transported from one seal to another, both seals still were able to maintain their sealing capacity.

It can be seen that the original service life of the seal without active ferrofluid replenishment system is short and ranges from a few minutes to 20 minutes. This short service life of the seal without ferrofluid replenishment was expected, since the seal was operating at 90% of its dynamic sealing capacity. It also has been found in literature that service life becomes shorter when the sealing pressure becomes higher [14]. The ferrofluid supply rate that is required in order to prevent failure of the ferrofluid seal is dependent on the degradation rate of the seal. It is expected that the required supply rate decreases when the original service life of the seal is higher at lower sealing pressures.

During ferrofluid transport through the seal no water was observed at the ferrofluid outlet of the seal. However, the composition and properties of the ferrofluid leaving the seal and of the water in the pressure chamber were not investigated in this research and therefore the presence or absence of water in the ferrofluid outflow cannot be confirmed.

4 Conclusion

In this research it is demonstrated that the service life of a ferrofluid rotary seal that dynamically seals pressurised water successfully can be improved and controlled by implementing a ferrofluid replenishment system in its design. Degradation of the ferrofluid in the seal ring over time decreases its sealing capacity, which results in seal failure when the sealing capacity becomes lower than the operational sealing pressure. If the ferrofluid seals in the system are completely replaced at a sufficient rate, service life of the seal theoretically will be unlimited.

The increase in static sealing capacity over time that was observed during the experiments could partially be attributed to the migration of particles through the carrier liquid towards higher magnetic field intensities.

Overall, it is believed that the implementation of a ferrofluid replenishment system in ferrofluid rotary seals will pave the way for the development of a new rotary sealing technology for liquids promising low friction in combination with infinite lifetime and zero leakage.

References


- [1] S. Papell, "Low viscosity magnetic fluid obtained by the colloidal suspension of magnetic particles: Us, 3215572."

- [2] R. E. Rosensweig, *Ferrohydrodynamics*. Courier Corporation, 2013.
- [3] R. Rosensweig, "Directions in ferrohydrodynamics," *Journal of Applied Physics*, vol. 57, no. 8, pp. 4259–4264, 1985.
- [4] C. Scherer and A. M. Figueiredo Neto, "Ferrofluids: properties and applications," *Brazilian Journal of Physics*, vol. 35, no. 3A, pp. 718–727, 2005.
- [5] R. Bailey, "Lesser known applications of ferrofluids," *Journal of magnetism and magnetic materials*, vol. 39, no. 1-2, pp. 178–182, 1983.
- [6] S. Lampaert, J. Spronck, and R. van Ostayen, "Load and stiffness of a planar ferrofluid pocket bearing," *Proceedings of the Institution of Mechanical Engineers, Part J: Journal of Engineering Tribology*, vol. 232, no. 1, pp. 14–25, 2018.
- [7] S. Lampaert, B. Fellingner, J. Spronck, and R. Van Ostayen, "In-plane friction behaviour of a ferrofluid bearing," *Precision Engineering*, vol. 54, pp. 163–170, 2018.
- [8] P. Baart, P. Lugt, and B. Prakash, "Review of the lubrication, sealing, and pumping mechanisms in oil- and grease-lubricated radial lip seals," *Proceedings of the Institution of Mechanical Engineers, Part J: Journal of Engineering Tribology*, vol. 223, no. 3, pp. 347–358, 2009.
- [9] Z. Szydło, W. Ochoński, and B. Zachara, "Experiments on magnetic fluid rotary seals operating under vacuum conditions," *Tribotest*, vol. 11, no. 4, pp. 345–354, 2005.
- [10] I. Anton, I. De Sabata, L. Vekas, I. Potencz, and E. Suciú, "Magnetic fluid seals: some design problems and applications," *Journal of Magnetism and Magnetic Materials*, vol. 65, no. 2-3, pp. 379–381, 1987.
- [11] K. Raj, P. Stahl, and W. Bottenberg, "Magnetic fluid seals for special applications," *ASLE TRANSACTIONS*, vol. 23, no. 4, pp. 422–430, 1980.
- [12] K. Raj, B. Moskowitz, and R. Casciari, "Advances in ferrofluid technology," *Journal of magnetism and magnetic materials*, vol. 149, no. 1-2, pp. 174–180, 1995.
- [13] M. Szczech and W. Horak, "Tightness testing of rotary ferro-magnetic fluid seal working in water environment," *Industrial Lubrication and Tribology*, vol. 67, no. 5, pp. 455–459, 2015.
- [14] L. Matuszewski and Z. Szydło, "Life tests of a rotary single-stage magnetic-fluid seal for shipbuilding applications," *Polish Maritime Research*, vol. 18, no. 2, pp. 51–59, 2011.
- [15] T. Liu, Y. Cheng, and Z. Yang, "Design optimization of seal structure for sealing liquid by magnetic fluids," *Journal of Magnetism and Magnetic Materials*, vol. 289, pp. 411–414, 2005.
- [16] Y. Mitamura, K. Sekine, M. Asakawa, R. Yozu, S. Kawada, and E. Okamoto, "A durable, non power consumptive, simple seal for rotary blood pumps," *Asaio Journal*, vol. 47, no. 4, pp. 392–396, 2001.
- [17] K. Heinz, B. Müller, and S. Nau, "Fluid sealing technology principles and applications," 1998.
- [18] J. Kurfess and H. Müller, "Sealing liquids with magnetic liquids," *Journal of Magnetism and Magnetic Materials*, vol. 85, no. 1-3, pp. 246–252, 1990.
- [19] Y. Mitamura, T. Yano, W. Nakamura, and E. Okamoto, "A magnetic fluid seal for rotary blood pumps: Behaviors of magnetic fluids in a magnetic fluid seal," *Bio-medical materials and engineering*, vol. 23, no. 1-2, pp. 63–74, 2013.
- [20] K. Sekine, Y. Mitamura, S. Murabayashi, I. Nishimura, R. Yozu, and D.-W. Kim, "Development of a magnetic fluid shaft seal for an axial-flow blood pump," *Artificial organs*, vol. 27, no. 10, pp. 892–896, 2003.
- [21] Y. Mitamura, S. Takahashi, S. Amari, E. Okamoto, S. Murabayashi, and I. Nishimura, "A magnetic fluid seal for rotary blood pumps: Long-term performance in liquid," *Physica Procedia*, vol. 9, pp. 229–233, 2010.
- [22] Y. Mitamura, S. Arioka, D. Sakota, K. Sekine, and M. Azegami, "Application of a magnetic fluid seal to rotary blood pumps," *Journal of Physics: Condensed Matter*, vol. 20, no. 20, p. 204145, 2008.
- [23] H. Wang, D. Li, S. Wang, X. He, and S. Zhen, "Effect of seal gap on the seal life when sealing liquids with magnetic fluid," *Revista de la Facultad de Ingenieria*, vol. 31, no. 12, pp. 83–88, 2016.
- [24] V. Jarmo, E. Matti, and P. Raimo, "Sealing of liquids with magnetic fluid seals," in *6th Nordic Symposium on Tribology, Szwecja*, pp. 697–702, 1994.
- [25] L. Matuszewski and Z. Szydło, "The application of magnetic fluids in sealing nodes designed for operation in difficult conditions and in machines used in sea environment," *Polish Maritime Research*, vol. 15, no. 3, pp. 49–58, 2008.
- [26] Z. Szydło and L. Matuszewski, "Experimental research on effectiveness of the magnetic fluid seals for rotary shafts working in water," *Polish Maritime Research*, vol. 14, no. 4, pp. 53–58, 2007.
- [27] R. Rosensweig, *Ferrohydrodynamics*. Dover Publications, 5 1998.
- [28] R. Perez-Castillejos, J. Plaza, J. Esteve, P. Losantos, M. Acero, C. Cané, and F. Serra-Mestres, "The use of ferrofluids in micro-mechanics," *Sensors and Actuators A: Physical*, vol. 84, no. 1-2, pp. 176–180, 2000.
- [29] V. Polevikov and L. Tobiska, "Influence of diffusion of magnetic particles on stability of a static magnetic fluid seal under the action of external pressure drop," *Communications in Nonlinear Science and Numerical Simulation*, vol. 16, no. 10, pp. 4021–4027, 2011.
- [30] D. L. Hujun Wang, "Effect of the seal gap on the seal life when sealing liquids with magnetic fluid," *Revista de la Facultad de Ingenieria U.C.V.*, vol. 31, no. 12, pp. 83–88, 2016.
- [31] O. Potma, "Designs for rotary shaft fluid seals in an aqueous environment using ferrofluid," Master's thesis, Delft University of Technology, 2017.
- [32] O. Potma, S. Lampaert, and R. van Ostayen, "Method for transport of ferrofluid in a liquid contactless rotational seal," in *Conference report: 17th EDF-Pprime workshop*, 10 2018.
- [33] M. Szczech, "Experimental study on the pressure distribution mechanism among stages of the magnetic fluid seal," *IEEE Transactions on Magnetics*, vol. 54, no. 6, pp. 1–7, 2018.
- [34] HKCM Engineering e. K., *Magnet-Ring R15x08x06ZnPc-42SH*, 5 2018. Datasheet.
- [35] Ferrotec Corporation, *Ferrofluid EFH1*, 5 2014. Safety datasheet.
- [36] D. C. Li, H. N. Zhang, and Z. L. Zhang, "Study on magnetic fluid static seal of large gap," in *Key Engineering Materials*, vol. 512, pp. 1448–1454, Trans Tech Publ, 2012.
- [37] A. Boots, L. Krijgsman, B. de Ruitter, S. Lampaert, and J. Spronck, "Increasing the load capacity of planar ferrofluid bearings by the addition of ferromagnetic material," *Tribology International*, vol. 129, pp. 46–54, 2019.

Appendix A9

Load and stiffness of a hydrostatic bearing lubricated with a Bingham plastic fluid

Stefan GE Lampaert¹ and Ron AJ van Ostayen

Journal of Intelligent Material Systems and Structures
2019, Vol. 30(20) 3056–3065
© The Author(s) 2019
Article reuse guidelines:
sagepub.com/journals-permissions
DOI: 10.1177/1045389X19873426
journals.sagepub.com/home/jim


Abstract

Using a smart fluid, for example, magnetorheological or electrorheological, in a hydrostatic bearing gives the possibility to actively change the bearing properties during operation. This work presents an analytical model to predict the load and stiffness of a planar hydrostatic bearing lubricated with a Bingham plastic fluid. The model is validated with the use of a numerical model that uses the Bingham–Papanastasiou regularization to achieve convergence. The model gives insight into the size of the operational range of the bearing and the load characteristic.

Keywords

hydrostatic bearing, magnetorheological fluid, electrorheological fluid, mathematical modelling, magnetics

1. Introduction

Generally, when one is designing a bearing system, one is designing a geometry and choosing a proper lubricant such that the optimal performance is achieved (Stachowiak and Batchelor, 2014). The geometry of the bearing causes local variations in fluid flow resistance and in lubricant transportation. Choosing different lubricants changes the amount of resistance and transportation of lubricant at a global level since the rheological behaviour of the lubricant changes in the whole bearing simultaneously.

Smart fluids add an extra design dimension by now adding the possibility of locally changing the rheological behaviour. The three main types of smart fluids are ferrofluids (FF), magnetorheological (MR) fluids and electrorheological (ER) fluids (Chiolerio and Quadrelli, 2017; Stanway, 2004). An FF is a fluid that is attracted to a magnetic field (Rosensweig, 1966), and this behaviour causes an additional body force in the fluid giving rise to a load-carrying capacity (Lampaert et al., 2018a, 2018b). MR and ER fluids are fluids that change their viscous behaviour in response to a magnetic or an electric field, respectively. These fluids behave as Bingham plastic, and they exhibit a yield stress of which the magnitude is dependent on the strength of the applied magnetic or electric field. This locally changes the effective viscosity, locally changing the resistance of the lubricant transportation. In addition, often these effects are accompanied by an attracting force between the fluid and the field, giving rise to an extra body force in the

lubrication layer (Laghrabli et al., 2017a, 2017b). In general, it can be said that locally changing this rheological behaviour has similar effects as locally changing the geometry of the bearing (Lampaert and van Ostayen, 2017a, 2017b).

The additional advantage of using a smart fluid is that it can be used to modify the bearing properties in real time, making it possible to make an active bearing system (Bompos and Nikolakopoulos, 2016; Christidi-Loumpasefski et al., 2017; Wang et al., 2017). Some orienting work on this concept shows some interesting experimental work on an active hydrostatic bearing (Guldbakke et al., 2009; Guldbakke and Hesselbach, 2006; Hesselbach and Abel-Keilhack, 2002, 2003). In Bölter (1999), Guldbakke et al. (2009), Guldbakke and Hesselbach (2006) and Hesselbach and Abel-Keilhack (2002, 2003), a theoretical background was presented for this bearing concept, but no exact solution for calculating the load capacity of the bearing was provided. Similar work is done in Urreta et al. (2009) that demonstrates the difference in using an FF and an MR fluid in a journal bearing. It showed that the internal pressure

Department of Precision and Microsystems Engineering, Delft University of Technology, Delft, The Netherlands

Corresponding author:

Stefan GE Lampaert, Department of Precision and Microsystems Engineering, Delft University of Technology, Mekelweg 2, 2628 CD Delft, The Netherlands.
Email: S.G.E.Lampaert@tudelft.nl

generated in an FF subjected to a magnetic field is not strong enough to be relevant for use as an active lubricant in most journal bearing applications. The work of Becnel et al. (2012) showed that the magnetoviscous effect is still present at shear rates up to $25,000 \text{ s}^{-1}$, a value that is regularly observed in bearing system applications. However, Urreta et al. (2010) showed that the gain of using an MR fluid at high shear rates diminishes due to the large viscous stresses at higher speeds.

A method to model the behaviour of a hydrostatic bearing using MR or ER fluid in an efficient way is to use lubrication theory and model the MR or ER fluids as a Bingham plastic fluid. Some early effort to achieve this was done by Wada et al. (1973a, 1973b) in which a modified Reynolds equation was obtained by only making few additional simplifying assumptions. Tichy (1991) followed up on this work by deriving a Reynolds equation that was an ‘exact’ derivation (that is derived using the exact Bingham plastic fluid model), but this was only valid for a one-dimensional (1D) lubricating film approximation. The two-dimensional (2D) lubricating film was later covered by Dorier and Tichy (1992) using the Bingham–Papanastasiou (BP) approximation for a Bingham plastic fluid. The work of Bompos and Nikolakopoulos (2011) discusses the use of the bi-zone Bingham material model, and the work of Gertzog et al. (2008) discusses the use of the Herschel–Bulkley model in a three-dimensional (3D) computational fluid dynamics (CFD) simulation. The work of Nikolakopoulos and Papadopoulos (1998), Vaz et al. (2017), Wada et al. (1974), Wada et al. (1973b) and Wang et al. (2017) discusses experimental work on bearings lubricated with a yield stress fluid. From the research presented in literature, it follows that it is possible to model the flow of smart fluids, but no proper thin film–based solutions were found to predict the load characteristics of active hydrostatic bearings.

The problem faced in modelling the behaviour of hydrostatic bearings lubricated with MR fluids is that computation times tend to be very time consuming. Simple simulations of the behaviour can easily take hours to compute. This is not convenient in the design of such a bearing. This is especially troublesome during optimization of the design since every call of the objective function is very demanding.

Therefore, this article presents a new thin film–based, and therefore, numerically efficient model to predict the load and stiffness of a planar hydrostatic bearing lubricated with a Bingham plastic fluid. The work provides insight into the potential of using MR or ER fluids in an active hydrostatic bearing. The model furthermore helps to gain insight into how the flow pattern changes in response to changing yield stress due to the applied field. This work finds an experimental validation in the work of Lampaert and van Ostayen (in press).

2. Theoretical model

The derivation of the load capacity of the hydrostatic bearing lubricated with MR fluids starts by deriving the flow field in-between the two bearing faces, followed by integrating the flow field over the fly height of the bearing resulting in the flow rate through the bearing. The derivation assumes a constant recess pressure that makes it possible to calculate the bearing resistance by dividing the pressure gradient across the land by the flow rate. This makes the bearing resistance equal to the land resistance. The last step is to calculate the load capacity by integrating the pressure over the bearing surface.

Figure 1 presents the bearing model used in this article. It consists of two static, axisymmetric bearing faces at which the only pressure gradient is assumed to be over the land area of the bearing; the recess area is assumed to be frictionless, and therefore, a zero pressure gradient is assumed there. A magnetic field may or may not be present to activate the MR fluid. The article refers to ‘Newtonian fluid’ when the fluid shows relatively low non-Newtonian effects. A Newtonian fluid model then accurately describes the behaviour.

2.1. Flow field

The derivation starts from the Cauchy momentum equation

$$\rho \frac{Du}{Dt} = -\nabla p + \nabla \cdot \tau + f \quad (1)$$

Assuming a thin film, low Reynolds number, 1D flow with no body forces in the thin film below the bearing dam reduces this equation to

$$\frac{\partial p}{\partial x} = \frac{\partial \tau}{\partial z} \quad (2)$$

Here, it is assumed that the dam width is narrow compared to the recess radius. And thus, it can be assumed that there is a pure 1D flow across the dam of the bearing. This relation leads to the following shear stress over the height of the fluid profile

$$\tau = \frac{1}{2} \frac{\partial p}{\partial x} (2z - h) \quad (3)$$

The relation demonstrates that the shear stress is high near the walls and zero in the middle of the profile. A Newtonian fluid would result in a parabolic flow profile based on this stress profile. The flow of a Bingham plastic fluid will be different in the sense that flow only occurs when the stress in the material exceeds the yield stress of the material (Ashour et al., 1996; Asma et al., 2016; Kumbhar et al., 2015; Zubieta et al., 2009). The material is assumed isotropic, which is not necessarily the case as shown by Dohmen et al. (2017a, 2017b).

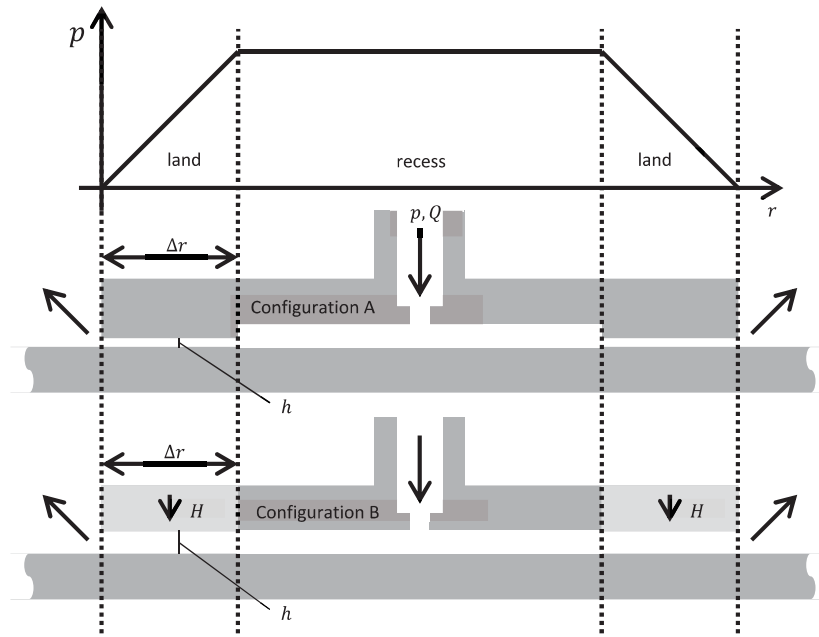


Figure 1. Configuration A is a hydrostatic bearing that works by actively pumping lubricant in-between the two bearing faces to create a load-carrying capacity. The recess area has close to constant pressure since the flow has little resistance there; the land area shows a strong pressure gradient due to the high resistance caused by the small fly height h . Configuration B presents the same hydrostatic bearing geometry but now with magnets in the land area in which an MR lubricant is supplied in-between the two bearing faces to create a load-carrying capacity. The variation of the magnetic field results in a variation of the effective flow resistance across the land area.

The following relation describes this behaviour and demonstrates that only the amount of stress that is above the yield stress contributes to the realization of flow

$$\frac{\partial u_x}{\partial z} = \begin{cases} 0, & |\tau| \leq \tau_y, & \frac{\partial u_x}{\partial z} = 0 \\ \frac{\tau - \tau_y}{\eta}, & |\tau| \geq \tau_y, & \frac{\partial u_x}{\partial z} > 0 \\ \frac{\tau + \tau_y}{\eta}, & |\tau| \geq \tau_y, & \frac{\partial u_x}{\partial z} < 0 \end{cases} \quad (4)$$

From these equations, the location in the profile where the shear stress is equal to the yield stress can be derived. Equations (5) and (6) present the bottom and top location where the shear stress is equal to the yield stress, respectively. The flow is always in the same direction (out of the bearing), and therefore, the pressure gradient is always negative

$$\begin{aligned} \tau &= \tau_y \\ \frac{1}{2} \frac{\partial p}{\partial x} (2z - h) &= \tau_y \\ 2 \frac{1}{2} \frac{\partial p}{\partial x} z &= \frac{1}{2} \frac{\partial p}{\partial x} h + \tau_y \\ z_{bottom} &= \frac{h}{2} + \tau_y \left(\frac{\partial p}{\partial x} \right)^{-1} \end{aligned} \quad (5)$$

$$\begin{aligned} \tau &= -\tau_y \\ z_{top} &= \frac{h}{2} - \tau_y \left(\frac{\partial p}{\partial x} \right)^{-1} \end{aligned} \quad (6)$$

In-between the location of z_{top} and z_{bottom} , the stress is not large enough to exceed the yield stress, and thus, solid material behaviour is the result in this region. Equation (7) calculates the height of this so-called plug by simply taking the difference between the two

$$h_p = z_{top} - z_{bottom} = -2\tau_y \left(\frac{\partial p}{\partial x} \right)^{-1} \quad (7)$$

Based on equation (7), a dimensionless number is defined (equation (8)), which describes the nature of the flow and which is equal to 0 when there is no plug present in the fluid and 1 if the plug covers the total distance between the two bearing surfaces

$$\mathfrak{R}_n = \frac{h_p}{h} = -\frac{2\tau_y}{h} \left(\frac{\partial p}{\partial x} \right)^{-1} \quad (8)$$

Using this dimensionless number (equation (8)), the top and bottom locations for the plug can be written as equation (9)

$$\begin{aligned} z_{top} &= \frac{h}{2} + \frac{h_p}{2} = \frac{h}{2} + \frac{\mathfrak{R}_n h}{2} = \frac{h}{2}(1 + \mathfrak{R}_n) \\ z_{bottom} &= \frac{h}{2} - \frac{h_p}{2} = \frac{h}{2} - \frac{\mathfrak{R}_n h}{2} = \frac{h}{2}(1 - \mathfrak{R}_n) \end{aligned} \quad (9)$$

Subtracting the yield stress from the total stress equation (5) presents the stress in the channel that in the end is available to cause flow. The following relation describes this for the region above and below the plug

$$\begin{aligned} \tau_{flow, bottom} &= \tau - \tau_y \\ &= \frac{1}{2} \frac{\partial p}{\partial x} h \left(\frac{2z}{h} - 1 + \mathfrak{R}_n \right) \end{aligned} \quad (10)$$

$$\tau_{flow, plug} = 0 \quad (11)$$

$$\tau_{flow, top} = \frac{1}{2} \frac{\partial p}{\partial x} h \left(\frac{2z}{h} - 1 - \mathfrak{R}_n \right) \quad (12)$$

And from this and equation (4), the velocity can be derived assuming a zero sliding velocity of both bearing surfaces

$$u_{x, bottom} = \frac{1}{\eta} \int_0^z \tau_{flow, bottom} dz = \frac{1}{2\eta} \frac{\partial p}{\partial x} h \left(\frac{z^2}{h} - (1 - \mathfrak{R}_n)z \right), \quad 0 \leq z \leq z_{bottom} \quad (13)$$

$$\begin{aligned} u_{x, plug} &= u_{x, bottom}(z = z_{bottom}) + \frac{1}{\eta} \int_{z_{bottom}}^{z_{top}} \tau_{flow, plug} dz \\ &= \frac{1}{2\eta} \frac{\partial p}{\partial x} h \left(\frac{z_{bottom}^2}{h} - (1 - \mathfrak{R}_n)z_{bottom} \right), \quad z_{bottom} \leq z \leq z_{top} \end{aligned} \quad (14)$$

$$\begin{aligned} u_{x, top} &= u_{x, plug} + \frac{1}{\eta} \int_{z_{top}}^z \tau_{flow, top} dz \\ &= \frac{1}{2\eta} \frac{\partial p}{\partial x} h \left(\frac{z^2 - z_{top}^2 + z_{bottom}^2}{h} - (1 + \mathfrak{R}_n)(z - z_{top}) - (1 - \mathfrak{R}_n)z_{bottom} \right), \quad z_{top} \leq z \leq h \end{aligned} \quad (15)$$

When the recess pressure is higher than the burst pressure, flow will occur. The part of the fluid that flows behaves as a Poiseuille flow, one-half of the flow profile is above the plug and the other part of the flow is below the plug. The plug flows along with the velocity equal to the maximum velocity of the Poiseuille profile.

2.2. Flow rate

The flow profile can be split into two regions with a parabolic shaped profile and one region with a plug flow shape. The two regions with a parabolic shape are symmetrical, and thus, only one has to be integrated to know the total flow rate of both combined. The flow

rate of the parabolic flow part Q_{pois} is calculated in the following way

$$\begin{aligned} Q_{pois} &= L \int_0^{z_{bottom}} u_{x, bottom} dz + L \int_0^{z_{top}} u_{x, top} dz = 2L \int_0^{z_{bottom}} u_{x, bottom} dz \\ &= -\frac{L}{12\eta} \frac{\partial p}{\partial x} h^3 (1 - \mathfrak{R}_n)^3 \end{aligned} \quad (16)$$

The parameter L presents the circumference of the average outflow radius, which is equal to $2\pi r$ for the circular case presented in this article. The flow rate of the plug flow part is calculated in the following way

$$\begin{aligned} Q_{plug} &= L \int_0^{h_p} u_{x, plug} dz \\ &= -\frac{L}{8\eta} \frac{\partial p}{\partial x} h^3 (1 - \mathfrak{R}_n)^2 \mathfrak{R}_n \end{aligned} \quad (17)$$

The total flow rate in-between the two surfaces can be calculated by now summing up the two flow rates

$$\begin{aligned} Q_{comb} &= Q_{pois} + Q_{plug} \\ &= -\frac{L}{24\eta} \frac{\partial p}{\partial x} h^3 (2 - 3\mathfrak{R}_n + \mathfrak{R}_n^3) \end{aligned} \quad (18)$$

2.3. Bearing or land resistance

The resistance against flow of the bearing R_l is calculated as the ratio of the recess pressure p_r over the flow rate through the bearing Q_b

$$R_l = \frac{p_r}{Q_b} = \frac{p_r}{Q_{comb}} = \frac{24\eta \Delta r}{Lh^3 (2 - 3\mathfrak{R}_n + \mathfrak{R}_n^3)} = \frac{2R_\infty}{(2 - 3\mathfrak{R}_n + \mathfrak{R}_n^3)} \quad (19)$$

where R_∞ is defined by

$$R_\infty = \frac{12\eta \Delta r}{Lh^3} = \frac{6\eta \Delta r}{\pi r h^3} \quad (20)$$

2.4. Load capacity

The load-carrying characteristic of a hydrostatic bearing is defined by the potential (pressure) divider presented in Figure 2. A basic model of the hydrostatic bearing with MR fluid is derived by deriving a relation for the resistance of the bearing R_b .

From this potential divider, the recess pressure p_r can be calculated using (equation (21))

$$p_r = \frac{R_l}{R_l + R_s} p_s = \frac{1}{1 + \frac{R_s}{R_l}} p_s \quad (21)$$

Substituting equation (19) in relation equation (21) results in the following relation

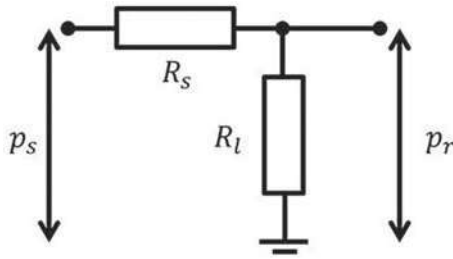


Figure 2. The pressure in the bearing is defined by a potential divider of the supply restrictor resistance R_s and the land resistance R_l .

$$p_r = \frac{1}{1 + \frac{R_s}{2R_\infty}(2 - 3\Re_n + \Re_n^3)} p_s \quad (22)$$

$$p_s = p_r \left(1 + \frac{R_s}{2R_\infty}(2 - 3\Re_n + \Re_n^3) \right)$$

For the system we are analysing, and assuming the pressure gradient across the (narrow) land area is constant, the flow parameter presented with equation (8) is a function of the recess pressure p_r

$$\Re_n = \frac{2\tau_y \Delta r}{h p_r} \quad (23)$$

Or, after substitution of equation (23) in equation (22)

$$p_s = \frac{2\tau_y \Delta r}{h \Re_n} \left(1 + \frac{R_s}{2R_\infty}(2 - 3\Re_n + \Re_n^3) \right) \quad (24)$$

In order to determine the \Re_n as a function of the supply pressure, yield stress and other parameters, the following cubic relation derived from equation (24) needs to be solved

$$\Re_n^3 - \underbrace{\left(3 + \frac{R_\infty h p_s}{R_s \tau_y \Delta r} \right)}_{a_2} \Re_n + 2 \underbrace{\left(\frac{R_\infty}{R_s} + 1 \right)}_{a_3} = 0 \quad (25)$$

This last relation is a cubic relation of which an analytical solution is derived by writing it in its standard form and calculating the following values

$$Q = \frac{3a_2 - a_1^2}{9} = - \left(1 + \frac{R_\infty h p_s}{3R_s \tau_y \Delta r} \right)$$

$$R = \frac{9a_1 a_2 - 27a_3 - 2a_1^3}{54} = - \left(1 + \frac{R_\infty}{R_s} \right)$$

$$D = R^2 + Q^3 = \left(1 + \frac{R_\infty}{R_s} \right)^2 - \left(1 + \frac{R_\infty h p_s}{R_s 3\tau_y \Delta r} \right)^3$$

$$S = \sqrt[3]{R + \sqrt{D}}$$

$$T = \sqrt[3]{R - \sqrt{D}} \quad (26)$$

These values can be used to calculate the following solution

$$\Re_{n1} = S + T - \frac{a_1}{3}$$

$$\Re_{n2} = -\frac{S+T}{2} - \frac{a_1}{3} + \frac{i\sqrt{3}}{2}(S-T) \quad (27)$$

$$\Re_{n3} = -\frac{S+T}{2} - \frac{a_1}{3} - \frac{i\sqrt{3}}{2}(S-T)$$

Only one of these solutions will be physically feasible. To investigate the nature of the solutions, the discriminant can be calculated in the following way

$$D = \left(1 + \frac{R_\infty}{R_s} \right)^2 - \left(1 + \frac{R_\infty p_s h}{R_s 3\tau_y \Delta r} \right)^3 \quad (28)$$

For convenience, equation (23) is used to write the formula in the following form

$$D = \left(1 + \frac{R_\infty}{R_s} \right)^2 - \left(1 + \frac{R_\infty 2p_s}{R_s 3\Re_n p_b} \right)^3$$

$$= \underbrace{\left(\frac{R_\infty}{R_s} \right)^2 \left(1 - \frac{12}{9} \left(\frac{p_s}{\Re_n p_b} \right)^2 \right)}_{\text{always negative}} + 2 \underbrace{\frac{R_\infty}{R_s} \left(1 - \frac{p_s}{\Re_n p_b} \right)}_{\text{never positive}}$$

$$- \left(\frac{R_\infty 2p_s}{R_s 3\Re_n p_b} \right)^3 \leq 0 \quad (29)$$

The value of \Re_n can range between 0 and 1, and the recess pressure p_r can never exceed the source pressure p_s . This means that the first term of equation (29) is always negative and the second term of equation (29) can never be positive. From this, it can be said that discriminant D is always smaller than zero which practically means that there are three different real roots. Of these three real roots, only one will be physically feasible, and this root is used to calculate the load capacity of the system. The value of \Re_n can be substituted back in relation equation (22) to calculate the recess pressure. The load-carrying capacity of the bearing can subsequently be calculated using the following equation

$$W = p_r \left(A_{recess} - \frac{A_{land}}{2} \right) \quad (30)$$

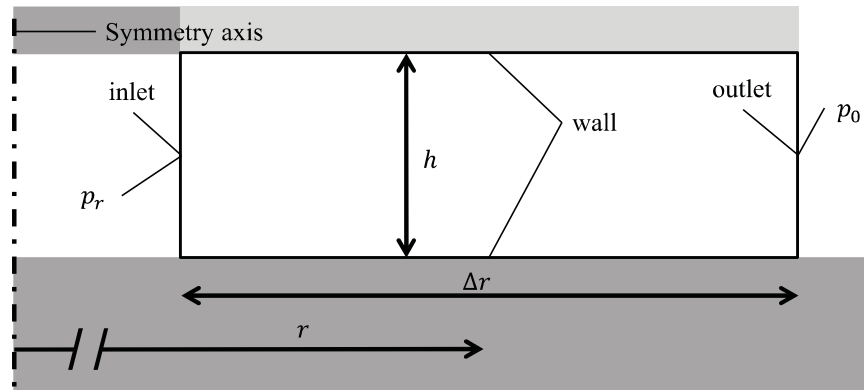
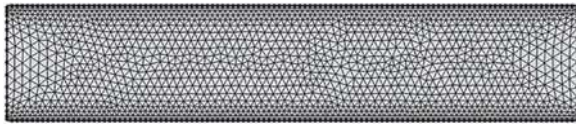
In this relation, the parameters A_{recess} and A_{land} present the surface area for the recess and the land defined in Figure 1, respectively.

3. Method for validation

The static load characteristic of the bearing is calculated using both an analytical model and a numerical model using the parameter values presented in Table 1. The analytical model is based on the theory presented in the previous chapter. In this article, we assume a uniform

Table 1. Table with bearing geometry values used in the article.

Parameter	Symbol	Value	Unit
Average outflow radius	r	0.0225	m
Yield stress	τ	0, 10^1 , 10^2 , 10^3 , 10^4	Pa
Viscosity	η_0	0.1	Pa s
Land width	Δr	0.005	m
Supply pressure	p_s	5×10^5	Pa
Restrictor resistance	R_s	10^{11}	Pa s/m ³
Fly height	h	$10^{-5} \dots 10^{-2}$	m
Regularization factor	m	1	–

**Figure 3.** Schematically overview of the model including all the relevant parameters.**Figure 4.** Example of the mesh build for the numerical model.

magnetic field such that a uniform yield stress is present throughout the fluid film. A full numerical simulation of the magnetic field, in order to determine the yield stress, is not necessary here but easily implemented if required (Bompos, 2015; Bompos and Nikolakopoulos, 2011, 2016; Moles, 2015; Urreta et al., 2010). A numerical model of the bearing system is built using the COMSOL Multiphysics software package. The flow is modelled as an incompressible Stokes flow with the BP viscosity model to achieve convergence of the model (Putz et al., 2009; Smyrnaio and Tsamopoulos, 2001) (equation (31))

$$\eta = \eta_0 + \frac{\tau_y}{|\dot{\gamma}|} (1 - e^{-m|\dot{\gamma}|}) \quad (31)$$

The regularization parameter m , which describes the smooth transition from solid to fluid in the BP model was chosen to be equal to 1. The resistance in the recess is assumed to be constant, and this assumption allows one to only model the land area of the bearing. Figure 3

presents the axisymmetric geometry used for the model. The left edge of the model has a pressure inlet p_b and the right edge has a pressure outlet p_0 . The top and bottom edges are walls with a no-slip boundary condition. The inlet pressure is calculated by subtracting the pressure over the restrictor due to flow from the supply pressure p_s , as described in equation (32). The flow at the outlet of the bearing defines the total flow through the system. Figure 4 presents an example of the mesh used in the computation. The simulation uses a triangular mesh with Lagrange elements of order two for the velocity and order one for the pressure (P2 + P1). The computation was terminated by either reaching a relative tolerance of $1e-5$ or a maximum number of iterations of 4000. Computation is done on an Intel Xeon CPU E5-1620 V3 @ 3.50GHz with 32GB or RAM

$$p_r = p_s - Q_{out}R_s \quad (32)$$

4. Results

Figures 5 to 9 present results calculated using the analytical approximation developed in this article. The figures assume a recess pressure p_b of 3.3 bar, 0.67 bar and 19 mbar together with a yield stress of 1 kPa, respectively. Figure 10 presents results calculated using both the analytical approximation and the numerical

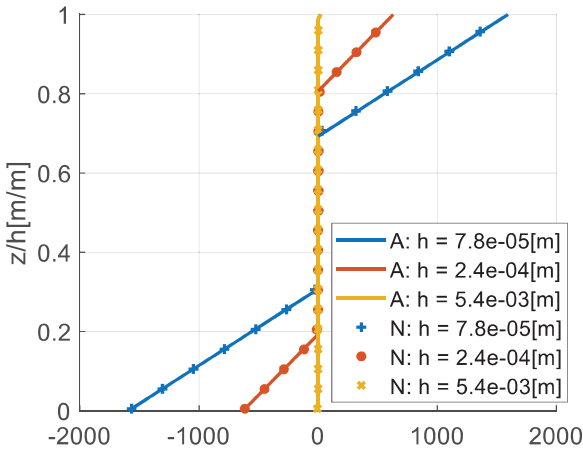


Figure 5. The stress that is available for flow plotted over the height of the channel. Both the analytical (A) and numerical (N) results are shown.

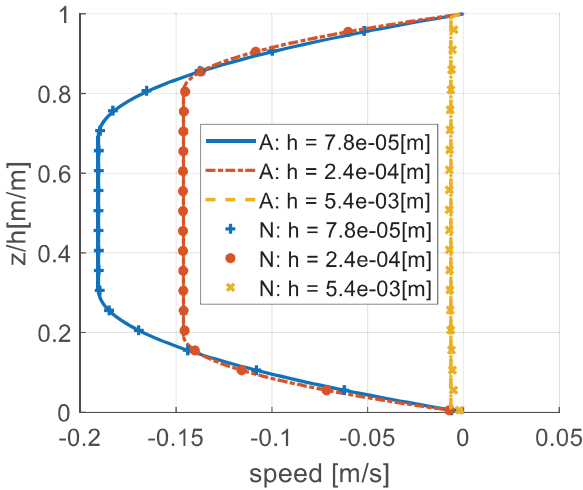


Figure 6. The velocity of the fluid plotted of the height of the channel. Both the analytical (A) and numerical (N) results are shown.

CFD model. The analytical data in this figure took 2 s to solve, and the numerical data took 7 h and 47 min to solve.

5. Discussion

The stress distribution from equation (3) and the flow field of equations (13)–(15) are presented in Figures 5 and 6 for different values of h , respectively. These different values of h correspond also with different values of \mathfrak{R}_n as can be seen from the circles presented in Figure 9. The figures show that for lower values of \mathfrak{R}_n , the flow behaves more similar to a Newtonian flow and for higher values of \mathfrak{R}_n , the flow behaves more like a plug flow. For intermediate values of \mathfrak{R}_n , there is a plug present right in the middle of the flow.

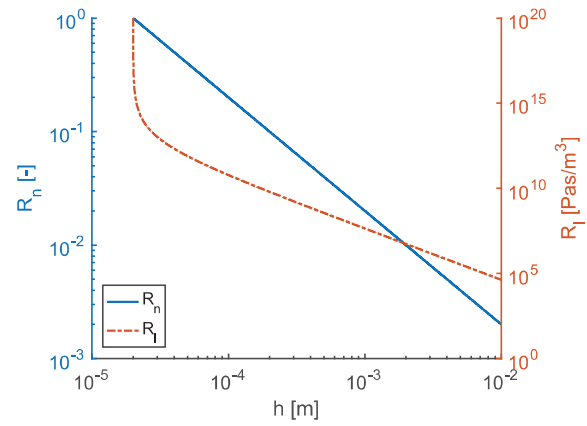


Figure 7. This graph presents the flow parameter \mathfrak{R}_n and the land resistance R_l over the fly height h for a constant pressure supply.

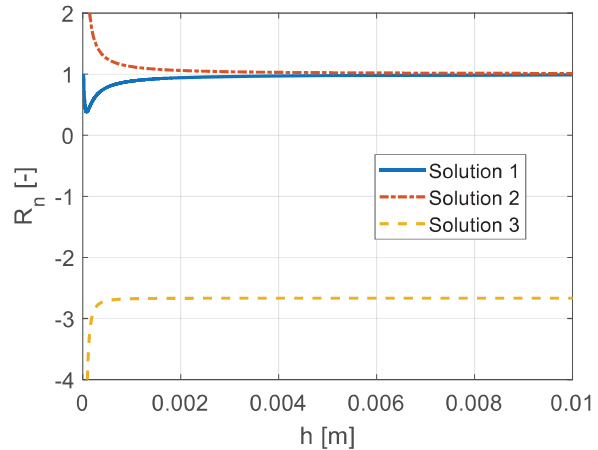


Figure 8. The three solutions of equation (27). The results show that only solution 1 gives a physically correct solution since for that solution, \mathfrak{R}_n stays between 0 and 1.

Figure 7 shows the flow parameter \mathfrak{R}_n and the flow resistance of the land R_l over the fly height of the bearing h for a constant supply pressure. For this situation, a linear relation between \mathfrak{R}_n and h exists as expected from equation (23). The graph furthermore demonstrates that there is a one-to-one relation between h and R_{flow} . The three solutions of equation (27) are visualized in Figure 8 that shows that only one solution satisfies the requirement of \mathfrak{R}_n being between 0 and 1. This can be seen as the only physically correct solution. The physically correct solution of \mathfrak{R}_n can now be used to calculate the bearing or land resistance. Figure 9 presents \mathfrak{R}_n and the R_b in function of h . It demonstrates that, in the situation for a hydrostatic bearing, there is not a linear relation between \mathfrak{R}_n and h anymore, as is expected from equation (23). The main reason for this is that for this situation, both the p_b and h are changing simultaneously (due to the use of a supply restrictor).

Therefore, only h is changing in the situation of Figure 7, whereas both the p_b and h are changing simultaneously in the situation of Figure 9. This has an effect that there is not a one-to-one relation anymore between \mathfrak{R}_n and h , and also p_b should be considered to find the right solution. Interesting to note also in Figure 9 is that the size of the plug is relatively large for both high and low values of h and small only for intermediate values of h .

The recess pressure as a function of the fly height calculated both with the analytical model and the numerical model is given in Figure 10. The graph shows the two models are in good agreement up to a fly height of about 5×10^{-3} m. Above this value, the height of the channel becomes larger than the length, and as a result, the thin film approximation is no longer valid. However, results are still presented to demonstrate the limits of the method. Interesting to note here are the differences in calculation time; the analytical model took a few seconds to solve, while the numerical model took almost 8 h. The analytical model shows to be far more effective to obtain a quick characteristic of the system. Figure 10 furthermore shows that the recess pressure at a low fly height is equal to the feeding pressure. This is explained by equations (21) and (33) that show that for a very high land resistance, the recess pressure becomes equal to the source pressure

$$\lim_{R_l \rightarrow \infty} \frac{1}{1 + \frac{R_s}{R_l}} p_s = p_s \quad (33)$$

Figure 9 shows that for decreasing fly heights, the value of \mathfrak{R}_n approaches the value 1.0 meaning that the size of the plug and the fly height come closer and closer to each other until the moment they are equal. In the limit case where they are equal, equation (34) shows that the land resistance goes to infinity

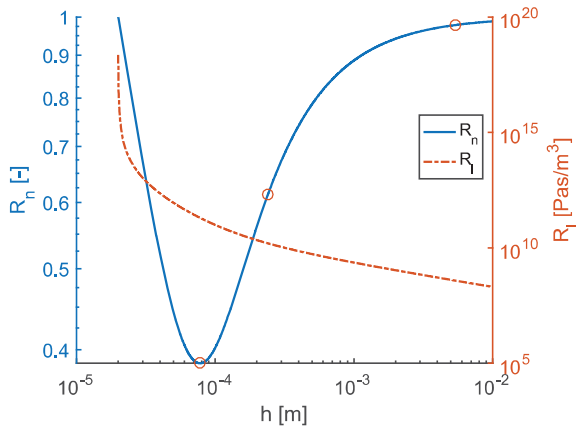


Figure 9. The graph above presents the flow parameter \mathfrak{R}_n and the land resistance R_l over the fly height h . The three circles correspond with the three cases presented in Figures 5 and 6.

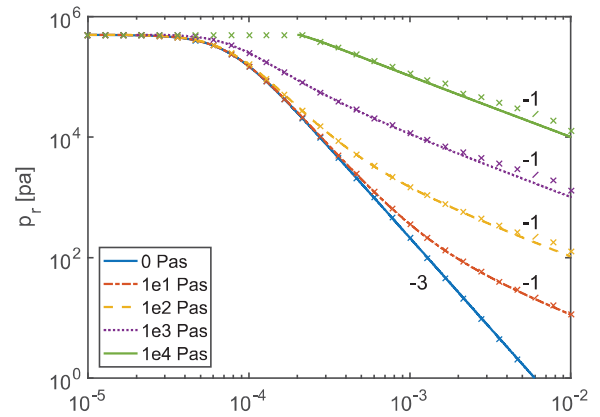


Figure 10. Recess pressure as a function of fly height for different yield strengths. The solid lines present the solution for the analytical model, and the crosses present the solution for the computational model.

$$\lim_{\mathfrak{R}_n \rightarrow 1} R_l = \frac{2R_\infty}{(2 - 3 + 1)} = \infty \quad (34)$$

For higher fly heights, the recess pressure of Figure 10 decreases by either a -3 slope or a -1 slope. The slope steepness implies that there is either a $\sim h^{-3}$ or a $\sim h^{-1}$ relation present. The -3 slope describes the situation where the yield stress of the fluid is set relatively low; the lubricant is close to a Newtonian fluid. This means that the flow value \mathfrak{R}_n is close to 0, which can either mean that the pressure gradient is very high or the yield stress divided by the land width is very low. The limit case of land resistance in that situation converges to that one of the hydrostatic bearings lubricated with a Newtonian fluid as explained with (equation (35))

$$\lim_{\mathfrak{R}_n \rightarrow 0} R_l = \frac{2R_\infty}{(2 - 0 + 0)} = R_\infty \quad (35)$$

Substituting $\mathfrak{R}_n = 0$ in equation (22) gives an equivalent result to equation (35) by providing the relation of a conventional hydrostatic bearing lubricated with a Newtonian fluid

$$p_b \left(1 + \frac{R_s}{R_\infty} \right) = p_s \quad (36)$$

By using a yield stress fluid, the -3 slope gradually transitions into a -1 slope for increasing fly heights. For very high values of the yield stress, the -3 slope even vanishes completely. Figure 9 shows that for increasing fly heights, the value of \mathfrak{R}_n converges to 1.0 meaning that the size of the plug and the fly height come closer and closer to each other but never become equal. Becoming equal would result in an infinite resistance that would increase the pressure and so the pressure gradient in the bearing. This large pressure gradient would cause a lower value of \mathfrak{R}_n and so a

smaller plug in the flow. In region where \mathfrak{R}_n is very close to 1.0, the pressure gradient is proportional to the yield stress divided by the fly height. This causes a situation where the recess pressure is proportional to the yield stress as explained in equation (37). This again is visible in Figure 10

$$\mathfrak{R}_n = \frac{h_p}{h} = -\frac{2\tau_y}{h} \left(\frac{\partial p}{\partial x} \right)^{-1} \approx 1 \quad (37)$$

$$p_b = \frac{2\tau_y}{h} \Delta r$$

For an MR fluid, the yield stress of the fluid is about proportional to the magnetic field intensity. This has a result that the recess pressure is proportional to the magnetic field strength there. Relation equation (30) shows that the bearing characteristic is, apart from the fly height, also dependent on some other parameters like the surface area of the bearing. Since these dependencies are not significantly different from conventional hydrostatic bearing, it is left out of the discussion. Using electromagnets instead of permanent magnets generates the possibility to turn this bearing into an active bearing.

The results of this work demonstrate that changing the rheological behaviour of the lubricant significantly changes the bearing properties. For conventional systems, only the geometrical configuration changed to change the bearing properties. This work demonstrates the effect of introducing the extra design parameter of changing the rheological properties of the lubricant. This is something of which little is known, further research should be conducted to clarify the exact potential of this extra design parameter.

6. Conclusion

The work derives an exact analytical model for the load and stiffness of a hydrostatic bearing using a Bingham plastic fluid. A numerical model validates the analytical model and furthermore shows that the analytical model is much more time efficient. The model shows how the load characteristic is changing with changing yield stress in the fluid. The concept has a higher load capacity at high fly heights compared to a conventional hydrostatic bearing. The model demonstrates the potential of using an MR or ER fluid such that the yield stress is controllable. The article derives a non-dimensional flow parameter that describes the nature of the flow in-between the bearing surfaces.


Declaration of conflicting interests

The authors declared no potential conflicts of interest with respect to the research, authorship and/or publication of this article.

Funding

The author(s) disclosed receipt of the following financial support for the research, authorship and/or publication of this article: The Dutch TKI maritime funding programme has supported this research.

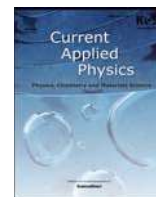
ORCID iD

Stefan GE Lampaert  <https://orcid.org/0000-0002-8268-1457>

References

- Ashour O, Rogers CA and Kordonsky W (1996) Magnetorheological fluids: materials, characterization, and devices. *Journal of Intelligent Material Systems and Structures* 7(2): 123–130.
- Asma S, Leong N, Samin PM, et al. (2016) Synthesis, characterization and magnetorheological properties of carbonyl iron suspension with superparamagnetic nanoparticles as an additive. *Smart Materials and Structures* 25: 025025.
- Becnel A, Hu W and Wereley N (2012) Measurement of magnetorheological fluid properties at shear rates of up to 25000s⁻¹. *Magnetics* 48(44): 3525–3528.
- Bölter R (1999) *Design von Aktoren mit magnetorheologischen Flüssigkeiten Inhaltsverzeichnis*. PhD Thesis, Technischen Fakultät der Universität des Saarlandes, Saarbrücken.
- Bompos DA (2015) *Tribological design of nano/magnetorheological fluid journal bearings*. PhD Thesis, University of Patras, Patras.
- Bompos DA and Nikolakopoulos PG (2011) CFD simulation of magnetorheological fluid journal bearings. *Simulation Modelling Practice and Theory* 19(4): 1035–1060.
- Bompos DA and Nikolakopoulos PG (2016) Rotordynamic analysis of a shaft using magnetorheological and nano-magnetorheological fluid journal bearings. *Tribology Transactions* 59(1): 108–118.
- Chiolerio A and Quadrelli MB (2017) Smart fluid systems: the advent of autonomous liquid robotics. *Advanced Science* 4(7): 1700036.
- Christidi-Loumpasefski O-O, Tzifas I, Nikolakopoulos PG, et al. (2017) Dynamic analysis of rotor – bearing systems lubricated with electrorheological fluids. *Proceedings of the Institution of Mechanical Engineers, Part K: Journal of Multi-body Dynamics* 232(2): 153–168.
- Dohmen E, Modler N and Gude M (2017) Anisotropic characterization of magnetorheological materials. *Journal of Magnetism and Magnetic Materials* 431: 107–109.
- Dohmen E, Borin D and Zubarev A (2017) Magnetic field angle dependent hysteresis of a magnetorheological suspension. *Journal of Magnetism and Magnetic Materials* 443: 275–280.
- Dorier C and Tichy J (1992) Behavior of a Bingham-like viscous fluid in lubrication flows. *Journal of Non-Newtonian Fluid Mechanics* 45(3): 291–310.
- Gertzos KP, Nikolakopoulos PG and Papadopoulos CA (2008) CFD analysis of journal bearing hydrodynamic lubrication by Bingham lubricant. *Tribology International* 41(12): 1190–1204.
- Guldbakke JM, Abel-Keilhack C and Hesselbach J (2009) Magnetofluidic bearings and dampers. In: Odenbach S

- (ed.) *Colloidal Magnetic Fluids: Basics, Development and Application of Ferrofluids*. Berlin: Springer, pp. 405–419.
- Guldbakke JM and Hesselbach J (2006) Development of bearings and a damper based on magnetically controllable fluids. *Journal of Physics: Condensed Matter* 18(38): S2959–S2972.
- Hesselbach J and Abel-Keilhack C (2002) Active hydrostatic bearing with magnetorheological fluid. In: *Proceedings of eighth international conference on new actuators*, Bremen, German, 10–12 June 2002, pp. 343–346.
- Hesselbach J and Abel-Keilhack C (2003) Active hydrostatic bearing with magnetorheological fluid. *Journal of Applied Physics* 93(10): 8441–8443.
- Kumbhar BK, Patil SR and Sawant SM (2015) Synthesis and characterization of magneto-rheological (MR) fluids for MR brake application. *Engineering Science and Technology, an International Journal* 18(3): 432–438.
- Laghrabli S, El Khelifi M, Nabhani M, et al. (2017a) Ferrofluid lubrication of finite journal bearings using Jenkins model. *Lubrication Science* 29: 441–454.
- Laghrabli S, El Khelifi M, Nabhani M, et al. (2017b) Static characteristics of ferrofluid finite journal bearing considering rotational viscosity effect. *Lubrication Science* 29(4): 203–226.
- Lampaert SGE and van Ostayen RAJ (2017a) Hydrostatic bearing with MR texturing. In: *Book of abstracts: 16th German ferrofluid workshop*, Dresden, 17–19 July, pp. 94–95.
- Lampaert SGE and van Ostayen RAJ (2017b) Virtual textured hybrid bearings. In: *Proceedings of the 44th Leeds-Lyon symposium on tribology*, Lyon, 4–6 September, p. 84. Lyon: LaMCoS.
- Lampaert SGE and van Ostayen RAJ (in press) Experimental Results on a Hydrostatic Bearing Lubricated with a Magnetorheological Fluid. *Current Applied Physics*.
- Lampaert SGE, Fellingner BJ, Spronck JW, et al. (2018) In-plane friction behaviour of a ferrofluid bearing. *Precision Engineering* 54: 163–170.
- Lampaert SGE, Spronck JW, van Ostayen RAJ, et al. (2018) Load and stiffness of a planar ferrofluid pocket bearing. *Proceedings of the Institution of Mechanical Engineers, Part J: Journal of Engineering Tribology* 232(1): 14–25.
- Moles N (2015) *Actively Controllable Hydrodynamic Journal Bearing Design Using Magnetorheological Fluids*. Akron, OH: The University of Akron.
- Nikolakopoulos PG and Papadopoulos CA (1998) Controllable high speed journal bearings, lubricated with electro-rheological fluids. An analytical and experimental approach. *Tribology International* 31(5): 225–234.
- Putz A, Frigaard IA and Martinez DM (2009) On the lubrication paradox and the use of regularisation methods for lubrication flows. *Journal of Non-Newtonian Fluid Mechanics* 163(1–3): 62–77.
- Rosensweig RE (1966) Buoyancy and stable levitation of a magnetic body immersed in a magnetizable fluid. *Nature* 210(5036): 613–614.
- Smyrniotis DN and Tsamopoulos JA (2001) Squeeze flow of Bingham plastics. *Journal of Non-Newtonian Fluid Mechanics* 100(1–3): 165–190.
- Stachowiak GW and Batchelor AW (2014) *Engineering Tribology*. 4th ed. Amsterdam: Elsevier.
- Stanway R (2004) Smart fluids: current and future developments. *Materials Science and Technology* 20(8): 931–939.
- Tichy JA (1991) Hydrodynamic lubrication theory for the Bingham plastic flow model. *Journal of Rheology* 35(4): 477.
- Urreta H, Leicht Z, Sanchez A, et al. (2009) Hydrodynamic bearing lubricated with magnetic fluids. *Journal of Physics: Conference Series* 149: 012113.
- Urreta H, Leicht Z, Sanchez A, et al. (2010) Hydrodynamic bearing lubricated with magnetic fluids. *Journal of Intelligent Material Systems and Structures* 21(15): 1491–1499.
- Vaz N, Binu KG, Serrao P, et al. (2017) Experimental investigation of frictional force in a hydrodynamic journal bearing lubricated with magnetorheological fluid. *Journal of Mechanical Engineering and Automation* 7(5): 131–134.
- Wada S, Hayashi H and Haga K (1973a) Behavior of a Bingham solid in hydrodynamic lubrication (Part 1, general theory). *Bulletin of the JSME* 16(92): 422–431.
- Wada S, Hayashi H and Haga K (1973b) Behavior of a Bingham solid in hydrodynamic lubrication (Part 2, application to step bearing). *Bulletin of the JSME* 16(92): 432–440.
- Wada S, Hayashi H and Haga K (1974) Behavior of a Bingham Solid in Hydrodynamic Lubrication (Part 3, Application to Journal Bearing). *Bulletin of the JSME* 17: 1182–1191.
- Wang X, Li H and Meng G (2017) Rotordynamic coefficients of a controllable magnetorheological fluid lubricated floating ring bearing. *Tribology International* 114: 1–14.
- Zubieta M, Eceolaza S, Elejabarrieta MJ, et al. (2009) Magnetorheological fluids: characterization and modeling of magnetization. *Smart Materials and Structures* 18(9): 095019.



Experimental results on a hydrostatic bearing lubricated with a magnetorheological fluid

S.G.E. Lampaert*, R.A.J. van Ostayen

Department of Precision and Microsystems Engineering, Delft University of Technology, Mekelweg 2, 2628CD, Delft, the Netherlands

ARTICLE INFO

Keywords:

Hydrostatic bearing
Magnetorheological fluid
Bingham plastic
Mathematical modelling
Magnetics

ABSTRACT

Magnetorheological fluids can be used as a smart lubricant as a result of the fact that its properties can be changed with the use of a magnetic field. Local flow resistance and local pressure can be generated by applying a local magnetic field. This work presents a hydrostatic bearing in which the pressure profile of a conventional hydrostatic bearing is recreated with solely the use of a magnetic field and a magnetorheological fluid. The magnetic field is applied only locally at the outer edges of the bearing with the use of an electromagnet. The principle is demonstrated with the use of an experimental setup and a model from literature.

1. Introduction

The bearing has made a lot of progress since its inception, and the typical lifetime has increased considerably combined with a significantly reduced friction [1,2]. Still the system is not perfect, and the cost of energy losses due to friction and system failure for society are still huge. In addition, the CO₂ emissions due to friction are especially important nowadays. Estimations show that in total about 23% (119 EJ) of the world's total energy consumption is caused by tribological contacts [3].

One way to improve bearings systems even further be may be with the use of smart fluids. Examples exist that use the addition of magnetic fields together with ferrofluids [4–7] and magnetorheological (MR) fluids [8–17] to boost the performance. Other examples exist that use the addition of electric field together with electrorheological (ER) fluids to boost the performance [18–21].

The common property of these MR and ER lubricated bearings is that the variable rheological properties of the lubricant add an extra design variable to the system. This extra variable opens up a completely new dimension of bearing configuration. Conventional bearing system use local changes in the bearing surface geometry, so called local textures, to create a local change in flow resistance. Bearing systems using MR fluids can create that local change by the application of local magnetic fields, so called MR textures [22–26].

This research demonstrates the potential of this MR texturing by demonstrating the similarities of a hydrostatic bearing using only geometrical surface textures and a hydrostatic bearing using only MR textures (Fig. 1). An experimental setup, a numerical and an analytical

model show the load capacity in function of the fluid film height. This work furthermore shows the potential of the manipulation of the magnetic field to facilitate active control of the bearing properties.

2. Method

Three different methods demonstrate the behaviour of a hydrostatic bearing with MR texturing in this paper. Firstly, an experimental setup is built that is able to measure the load capacity in function of the fluid film height. Secondly, a numerical model is built that simulates the behaviour of the experimental setup as closely as practically possible. Lastly, an analytical model from literature simulates this same situation in a more approximate but time efficient way. Fig. 1 presents the different geometrical parameters used throughout this research.

2.1. Syntheses of the fluid

The MR fluid used in the experiments consists of a mixture of a low viscosity mineral oil (Shell Tellus S2 VX 15) with oleic acid (OA) and fine iron particles (BASF Carbonyl Iron Powder HS, $d_{part} = [1.8 - 2.3] \mu m$). The OA has as function to put the particles easily back into suspension. At rest the particles will slowly settle at the bottom due to the large size of the particles [27]. OA makes this sediment soft and easy to mix again, the absence of OA makes the sediment very hard and almost impossible to mix back into suspension. The substances are mixed in a mass ratio of $\varphi_{iron} = 0.720 kg/kg$, $\varphi_{oil} = 0.228 kg/kg$, $\varphi_{OA} = 0.0520 kg/kg$ into a total mixture of $m_t = 5.48 kg$. The mixture is stirred for 24 h, first by hand, later by using a

* Corresponding author.

E-mail address: S.G.E.Lampaert@tudelft.nl (S.G.E. Lampaert).

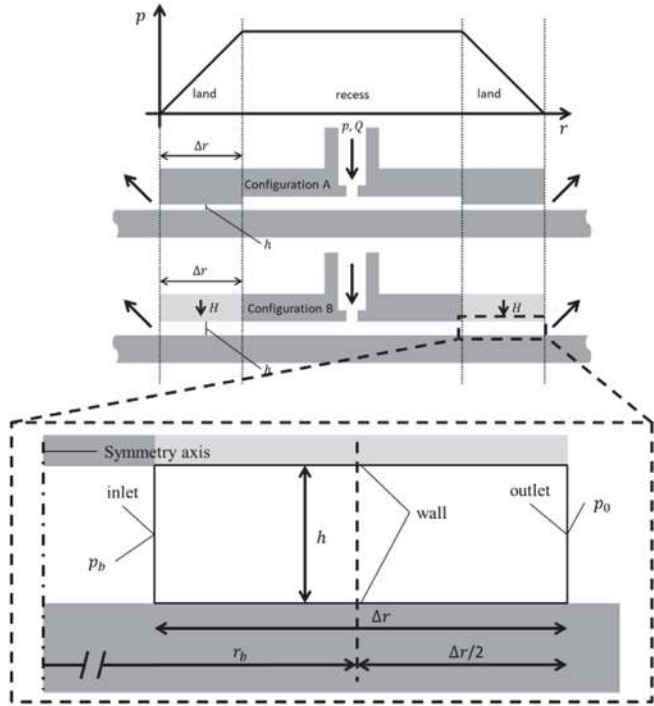


Fig. 1. A set of magnets mimics a geometrical surface structure. Only the outer rim has a magnetic field such that the fluid experiences only resistance at the outer rim of the bearing resulting in a declining pressure there.

mechanical mixer.

Constant mixing was present in the lubricant reservoir during the experiments to minimize the sedimentation. Still some sedimentation occurred. For this reason, a density measurement is performed during the bearing measurements by taking samples $V_{samp} = 0.1\text{ml}$ of lubricant with a micropipette and measuring its weight. The density is measured with a set of 20 measurements that lead to a mean density of $\rho_{lub,exp} = 1,94\text{kg/l}$ with a standard deviation of $0,24\text{kg/l}$. This density is significantly lower than the expected density of $\rho_{lub,ini} = 2,38\text{kg/l}$. From these numbers it is assumed that the realised content of the iron is $\varphi_{iron,exp} = 0.63\text{kg/kg}$ or $\delta_{iron,exp} = 0.15\text{l/l}$.

2.2. Material properties

Table 1 presents the susceptibility and saturation magnetization of different carbonyl iron (CI) particles found in literature. The work of [28] presents the material properties of the same CI particles as used in this research. The particles have a magnetic permeability of $\mu_i = 1 - \chi \approx 3.5$ and an assumed saturation magnetization of $M_{s,CI} = 1600\text{kA/m}$. The Maxwell-Garnett relation given in (EQ (1)) describes the effective permeability of the MR fluid [29]. The saturation magnetization scales with the volumetric particle concentration of the fluid which results in a saturation magnetizing of $M_s = 240\text{kA/m}$ or $B_s = 0.3\text{T}$ (EQ2) [30–34].

Table 1
Susceptibility and saturation magnetization of CI particles.

$d_{part} [\mu\text{m}]$	χ	$M_{s,CI} [\text{kA/m}]$	Source
1	20.46 ± 0.19	1700	[35]
2	5	1600	[36]
2	2.53	n.a.	[28]
2.8 – 3.5	4.76	1500	[37]
1	5	1700	[38]

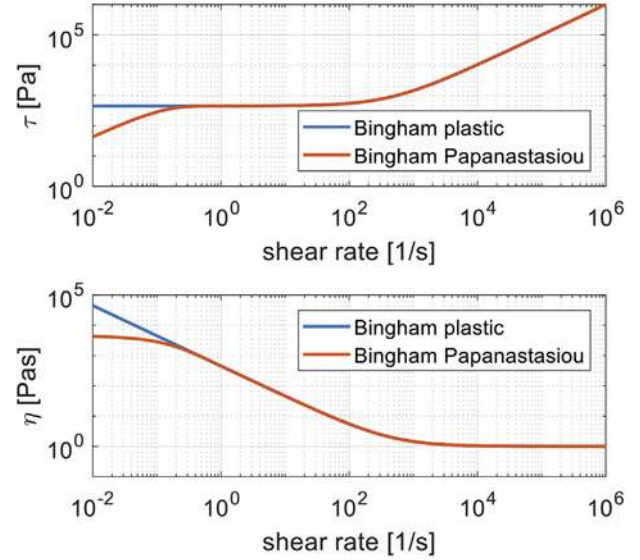


Fig. 2. Comparison between the Bingham plastic fluid model and the Bingham-Papanastasiou model used in the numerical computation.

$$\mu_{eff} = \frac{2\delta_{iron,exp}(\mu_i - 1) + \mu_i + 2}{\delta_{iron,exp}(1 - \mu_i) + \mu_i + 2} = 1.22 \quad (1)$$

$$M_s = \delta_{iron,exp} M_{s,CI} = 240\text{kA/m} \quad (2)$$

A Bingham plastic fluid model (EQ (3)) approximates the viscous behaviour of the MR fluid [39]. Here both the yield stress and the viscosity are a function of the magnetic field intensity. The drawback of this model is that it gives some difficulties during numerical simulation as a result of the non-zero yield stress at zero shear rate. Using the Bingham-Papanastasiou model (EQ (4)) solves this since that approximates the behaviour of the yield stress by generating a very high viscosity at low shear rates [40,41]. A regularization parameter m is chosen such that the Bingham-Papanastasiou model follows the Bingham plastic model down to a shear rate of $\dot{\gamma} = 1\text{s}^{-1}$. Shear rates lower than $\dot{\gamma} = 1\text{s}^{-1}$ are assumed to be of negligible influence to the solution. Fig. 2 presents the Bingham plastic model and the Bingham-Papanastasiou model for a yield stress present at M2 of Table 2 in function of a range of relevant shear rates. A regularization parameter of $m = 10$ is chosen such that the Bingham-Papanastasiou model closely follows the Bingham plastic model down to a shear rate of $\dot{\gamma} = 1\text{s}^{-1}$.

$$\eta = \eta_0 + \frac{\tau_y}{|\dot{\gamma}|} \quad (3)$$

$$\eta = \eta_0 + \frac{\tau_y}{|\dot{\gamma}|} (1 - e^{-m|\dot{\gamma}|}) \quad (4)$$

There are different methods to measure the properties of yield stress fluids [42,43]. In this research, a commercial cone-plate viscometer (Anton Paar MCR302) measures the viscous behaviour of the fluid. The viscous behaviour as a function of shear rate and magnetic field is measured. The shear rate is measured in a range from $\dot{\gamma}_{low,mes} = 0.1\text{s}^{-1}$ to $\dot{\gamma}_{high,mes} = 100\text{s}^{-1}$. The magnetic field is measured in a range from

Table 2
Measurement specific parameter values.

Parameter	Symbol	Value M0	Value M1	Value M2	Unit
Current	I	0	1	2	A
Pressure	P_s	4×10^5	4×10^5	3×10^5	Pa
Average yield stress,	$\tau_{yield,avg}$	0	160	450	Pa
Viscosity	η	0.073	1	3	Pa s
Number of measurement sets	N_{sets}	7	9	5	—

Table 3
General parameter values of the experimental setup.

Parameter	Symbol	Value	Unit
Bearing radius	r_b	0.02	m
Inner cavity	r_i	0.0025	m
Length of land	Δr	0.01	m
Restrictor	R_s	8.3×10^{11}	Pas/m^3
Saturated yield stress	$\tau_{y\infty}$	3355	Pa
Starting yield stress	τ_{y0}	10	Pa
Saturation speed	$\alpha_{\tau y}$	0.0056	T^{-1}
Saturated viscosity	η_∞	10	Pas
Starting viscosity	η_0	0.073	Pas
Saturation speed	$\alpha_{\eta y}$	0.01	T^{-1}

$B_{low,mes} = 0mT$ to $B_{high,mes} = 645mT$. The measurement is done six times for each combination of shear rate and magnetic field. The shear rate range is relatively low due to high thermal dissipation in combination with a high magnetic field strength; the cooling system was not able to cool the fluid properly causing inaccurate results. The magnetic field was measured up to the saturation point of the fluid [44]; the yield stress did not increase further from this point. A fluid sample is taken from the fluid reservoir of the experimental setup during the measurement of the load curve. This made sure that the same fluid properties are measured as present during the load curve measurement.

The Bingham model defines the fluid behaviour in the numerical modelling of the bearing behaviour [34]. The parameters of the Bingham model are fitted to the data measured with the rheometer [45]. This leads to one specific yield stress and one specific viscosity for every measured flux density. The functions presented in (EQ (5)) and (EQ (6)) are fitted to the different yield stresses and viscosities such that the complete rheological behaviour is turned into an analytical relation in function of the magnetic field and the shear rate [46]. See Table 3 for the explanation of the different parameters.

$$\tau_y = \tau_{y\infty} + 2(\tau_{y0} - \tau_{y\infty})(e^{-\alpha_{\tau y} B} - 0.5e^{-2\alpha_{\tau y} B}) \quad (5)$$

$$\eta_y = \eta_\infty + 2(\eta_0 - \eta_\infty)(e^{-\alpha_{\eta y} B} - 0.5e^{-2\alpha_{\eta y} B}) \quad (6)$$

Fig. 3 presents three shear stress vs shear rate measurements performed on the fluid. The points present the different measurements and

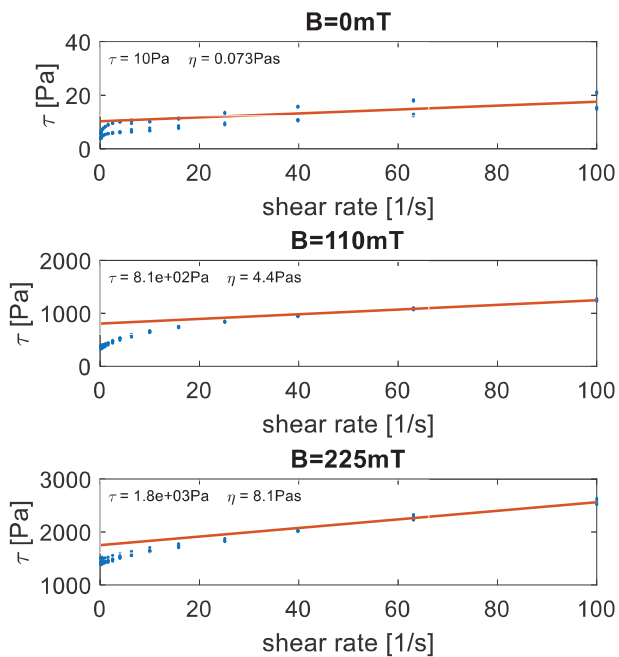


Fig. 3. Three viscosity measurement for different magnetic fields.

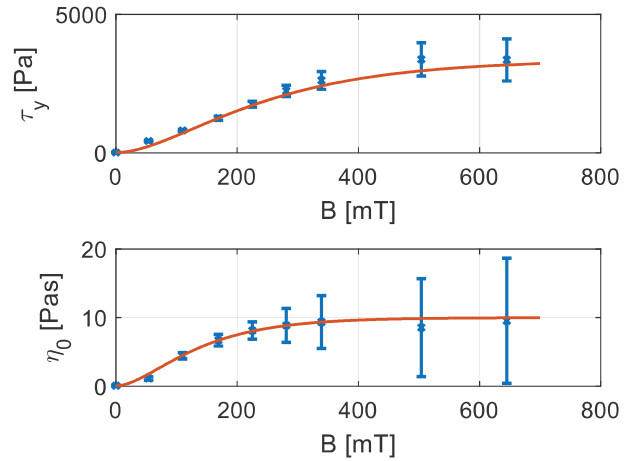


Fig. 4. Yield stress and viscosity values fitted to the viscosity measurements and used in the Bingham model. The confidence interval of the fit is 90%.

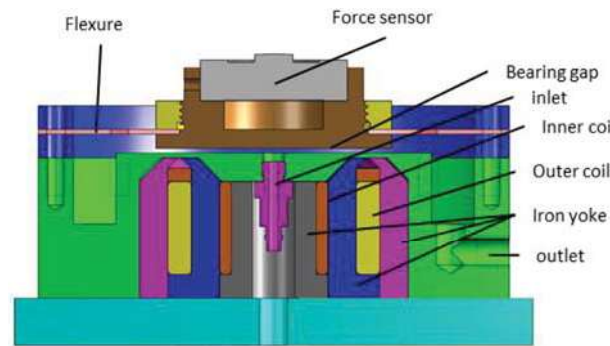


Fig. 5. Schematic of the cross section of the experimental bearing setup.

the solid line presents the resulting fit of that measurement. Fig. 4 presents the fit values of all the viscosity measurements done.

2.3. Experimental setup

The drawing presented in Fig. 5 presents the experimental setup that mimics the behaviour of the mechanical texturing of Fig. 1. The setup consists of two planar disk-shaped bearing surfaces in which a lubricant enters at the center of the bottom surface and leaves at the edge of the surfaces. Two concentric coils under the bearing surface control the magnetic field strength in the bearing gap. A centrifugal pump (SKF FLM12-2000) pressurizes the fluid to a pressure of $p_p = 5 \text{ bar}$. A pressure relief valve (SKF WVN200-10E6) supplies the lubricant at a constant pressure to the system (Fig. 7). The bearing obtains its normal stiffness from a linear restrictor (SKF VD1-105)

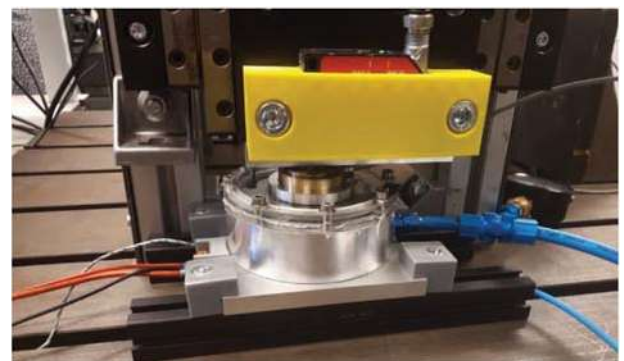


Fig. 6. Picture of the experimental setup.

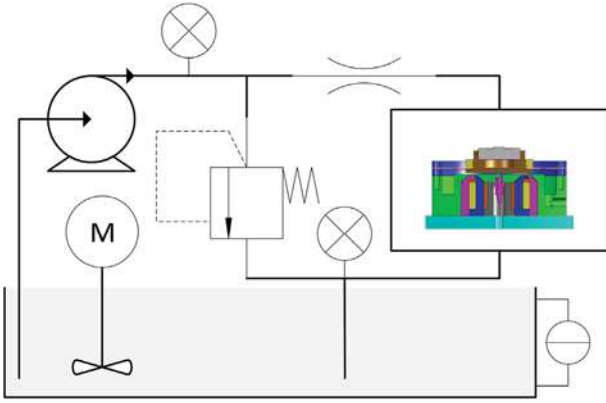


Fig. 7. Hydraulic system used in the experimental setup.

which has a restrictor value of $R_s = 8,3 \times 10^{11} \text{Pas/m}^3$ for the lubricant viscosity when no magnetic field is applied. A cylindrical diaphragm flexure suspends the upper bearing surface such that it can move up and down. The flexure is relatively compliant in the tilting direction of the bearing such that it allows self-aligning of the bearing surfaces. The out of plane stiffness of the flexure is much lower than the stiffness of the bearing such that it does not influence the measurements. The upper bearing surface accommodates a FUTEK LLB400-5001b-FSH03891 button-type force sensor. A precise positioning stage pushes against the force sensor from the top such that all applied force flows through the force sensor. A stepper motor controls the stage using a recirculating ball screw to convert the rotational motion onto a translational motion. The optoNCDT1402 laser sensor from Micro-Epsilon measures the height of the bearing gap. The sensor measures the distance between the moving part of the stage and the side rim of the bearing housing (Fig. 6). The stiffness of the force sensor and the construction is much larger than the stiffness of the bearing, so only the stiffness of the bearing is measured. A basic feedback algorithm makes sure that the bearing gap stays at a constant value. The complete system is able to position with a precision of $1\mu\text{m}$ and measure the force with a precision of 1N . Production of the bearing surfaces with a lathe guarantees the smoothness while finishing by polishing guarantees a low surface roughness. The roughness and flatness of the surface are measured with a Bruker ContourGT-K.

The two coils produce a magnetic field in opposite direction such that there is large field at the sides of the bearing and no field in the middle of the bearing. The ratio between the two coils is derived for the situation that there is no magnetic fluid present in the bearing gap. Adding a magnetic fluid in the bearing causes the field distribution to change slightly due to the magnetic properties of the fluid. The numerical model takes these effects into account. This makes it possible to validate the shape of the magnetic field by using a Goudsmit HGM09 Gaussmeter. The minimum measured magnetic field intensity in the centre and the maximum field intensity at the sides validate the magnetic field intensity of the numerical model.

The experimental procedure consists of three series of measurements. Table 2 presents the measurement specific parameter values and Table 3 presents the general parameter values of the setup. A measurement series consists of multiple measurements sets. One measurement set consists of one sweep of load capacities measured from high fly height to complete contact between the bearing faces. The first series with a current of $I_0 = 0\text{A}$ functions to calibrate and validate the experimental setup. The other two sets function as experimental results of the load characteristic of the hydrostatic bearing with an activated the MR fluid.

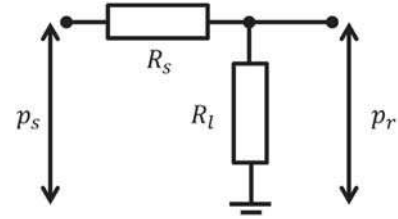


Fig. 8. The pressure in the recess p_r is defined by a potential divider of the restrictor resistance R_s and the land resistance R_l .

2.4. Analytical model

Another paper related to this work and presented in Ref. [25] discusses the analytical model used in the paper extensively. This paper only repeats the important steps in the method. The derivation of the analytical model start from the potential divider of Fig. 8 that makes sure that the bearing systems has stiffness. The linear inlet restrictor R_s and bearing film resistance R_l together define the pressure entering the recess p_r as described by (EQ (7)). The recess pressure finally defines the load capacity of the bearing. The load carrying capacity is calculated for two situations, without and with magnetic field (EQ (7)). is valid for both situations. Figs. 1 and 8, Tables 2 and 3 presents the explanations of the different parameters used.

$$p_r = \frac{R_l}{R_l + R_s} p_s \quad (7)$$

Without the magnetic field, the MR lubricant exhibits no yield stress and thus behaves as a Newtonian fluid. The resistance of a circular hydrostatic bearing as given by (EQ (8)) can reasonable describe the resistance in that situation [47,48].

$$R_l = \frac{6\eta \ln\left(\frac{r_b}{r_0}\right)}{\pi h^3} \quad (8)$$

Substituting (EQ (8)) into (EQ (7)) gives the recess pressure. This result together with the relation given by (EQ (9)) describes the load capacity [47,48].

$$F_{b,\tau_y=0} = \frac{\pi}{2} \frac{(r_b + \Delta r/2)^2 - r_0^2}{\ln\left(\frac{r_b + \Delta r/2}{r_0}\right)} p_r \quad (9)$$

Subjecting the MR lubricant to a magnetic field results in a yield stress for the fluid, and thus the fluid behaves as a Bingham plastic fluid. Solving the set of relations presented in (EQ (10)), (EQ (11)) and (EQ (12)) for either \mathfrak{R}_n or p_b results in an analytical expression for the pressure coming out of the restrictor. These relations are taken from the related work presented in Ref. [25]. These relations practically include the effect of having a plug in the middle of the flow caused by the yield stress of the fluid. Relation (EQ (11)) uses the assumption of modelling the resistance of the bearing by a slit with a length of Δr at a radial distance of r_b . The contribution of the resistance of the inner section (recess) where there is negligible magnetic field is neglected.

$$p_s = \frac{2\tau_y \Delta r}{h \mathfrak{R}_n} \left(1 + \frac{R_s}{2R_\infty} (2 - 3\mathfrak{R}_n + \mathfrak{R}_n^3) \right) \quad (10)$$

$$R_\infty = \frac{12\eta\Delta r}{Lh^3} = \frac{12\eta\Delta r}{\pi r_b h^3} \quad (11)$$

$$\mathfrak{R}_n = \frac{2\tau_y \Delta r}{h p_r} \quad (12)$$

The pressure consequently goes down from the point $r_b - \Delta r/2$ till the edge of the bearing defined by $r_b + \Delta r/2$. The leads to the following relation for the load capacity:

$$F_{b,xy \neq 0} = \frac{\pi}{2} \frac{(r_b + \Delta r/2)^2 - (r_b - \Delta r/2)^2}{\ln\left(\frac{r_b + \Delta r/2}{r_b - \Delta r/2}\right)} p_r \quad (13)$$

2.5. Numerical model

The numerical model package COMSOL Multiphysics 5.3a is used to develop a finite element model of the bearing system. This work again follows the same procedure as presented in the related work [25]. The axisymmetric design of the setup facilitates an axisymmetric numerical model. The first step in the modelling is calculating the magnetic field followed by a flow calculation. Section 2.2 presents the specifications of the magnetic properties and the method of validating the field. This magnetic field functions as an input for the flow calculation since it defines the yield stress of the material. A Stokes flow models the flow of the fluid. The walls of the channel have a zero slip boundary condition. An input pressure in function of the flow that flows through the bearing defines the behaviour of the linear restrictor as presented in (EQ (14)).

$$p_r = p_{in} - Q_{out} R_s \quad (14)$$

A zero pressure condition defines the output of the flow at the outside rim of the bearing surfaces. Section 2.2 presents the properties of the fluid used in the model. The free triangular mesh is very small at the walls in order to account for the high shear gradient expected at the walls due to the expected large size of the plug. The maximum size of the element near the walls scale such that enough elements are present to model the behaviour of the fluid. In addition, the use of P3+P2 elements (third order velocity and second order pressure) increases the form freedom of the elements near the walls. A nonlinear solver accommodates for the nonlinear behaviour of the fluid. Numerical iterations both for the magnetic field and for the flow field are continued until a relative tolerance of 10^{-4} on the residual is reached. The modelling results consists of three series. Table 2 presents the measurement specific parameter values and Table 3 presents the general parameter values of the setup. Computations are done on an Intel Xeon CPU E5-1620 V3 @ 3.50 GHz with 32 GB of Ram.

3. Results

Fig. 9 presents the magnetic field distribution over the radius of the bearing in the presence of a magnetic fluid. The distribution has a minimum in the centre of the bearing and a maximum at the outer radius of the bearing. Table 4 presents the measurements with the Teslometer on the experimental setup without a magnetic fluid present. Again, a minimum is present in the centre and a maximum is present at

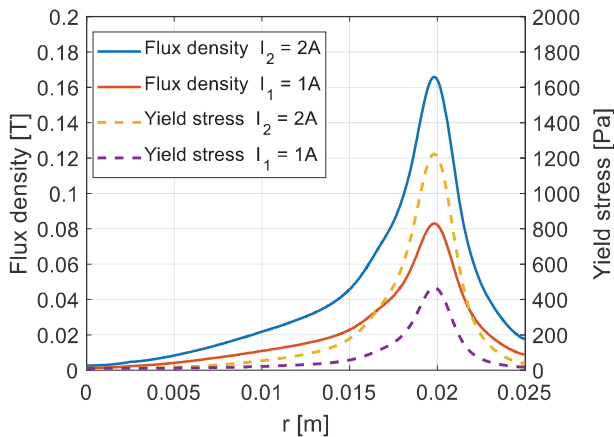


Fig. 9. Magnetic field without a magnetic fluid present in the bearing gap. The solid line presents the magnetic field at a fly height of $h = 0.1 \text{ mm}$ and the dashed line presents the corresponding yield stress.

Table 4
Magnetic flux density measured on the experimental setup without a magnetic fluid present.

Current	Measured flux density centre	Measured flux density side
$I_1 = 1A$	$B_{cent,1} = 3mT$	$B_{Side,1} = 57mT$
$I_2 = 2A$	$B_{cent,2} = 7mT$	$B_{Side,2} = 132mT$

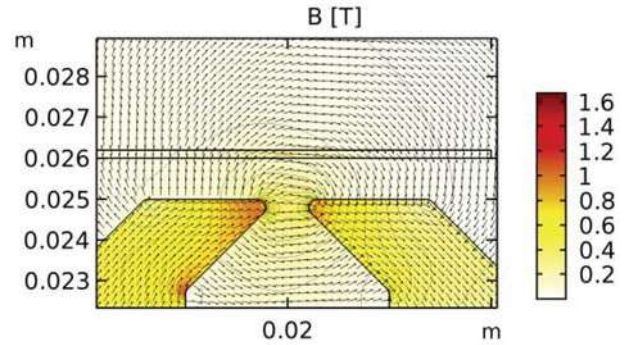


Fig. 10. Plot of the magnetic field produced in the system. The arrows have a normalized size.

the outer radius. The minima and maxima present in the measurement compare well with those in the numerical model, and this validates the magnetic field used in the numerical model.

Fig. 9 also presents the yield stress distribution over the radius of the bearing film for the two different field intensities investigated while there is a magnetic field present in-between the two bearing faces. Fig. 10 presents the flow of the flux in the system. Note that within the bearing gap, the flux flows radially, either inwards or outwards. The realised shape of the magnetic field resembles the mechanical equivalent of Fig. 1.

Fig. 11 presents the first measurement series in the absence of a magnetic field. The graph shows both the raw measurements, the predicted analytical model and the fitted model. The measurements and the predicted analytical model show an offset in force. A correction factor of $f_{fit,force} = 0.9$ has been applied in the fitted model, demonstrating the accurate trend of the predicted model. This shows that the model is about 10% off. The other measurements do not make use of this fitting factor.

Fig. 13 and Fig. 14 present respectively the results of measurement

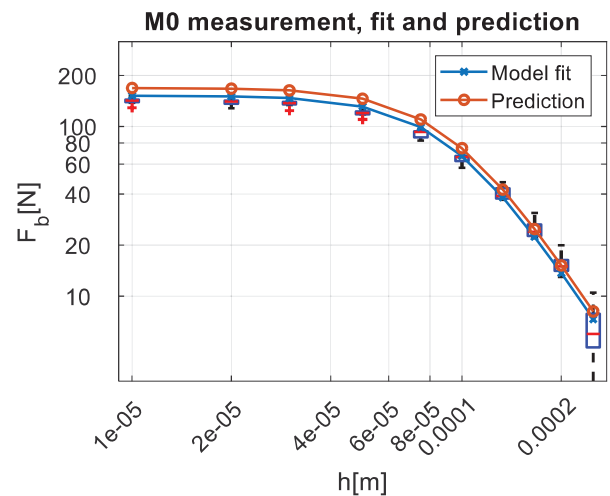


Fig. 11. Load capacity of the bearing in the absence of a magnetic field. The graph shows both the measurements, the predicted model and the fitted model. The boxplots presents the measured data.

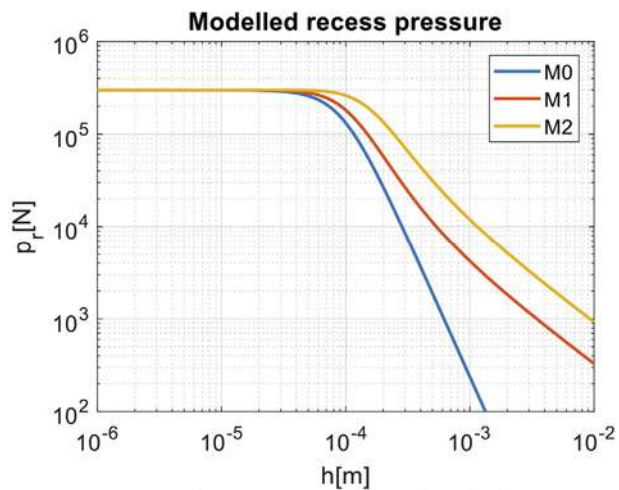


Fig. 12. Load capacity generated with the parameters used in the different graphs.

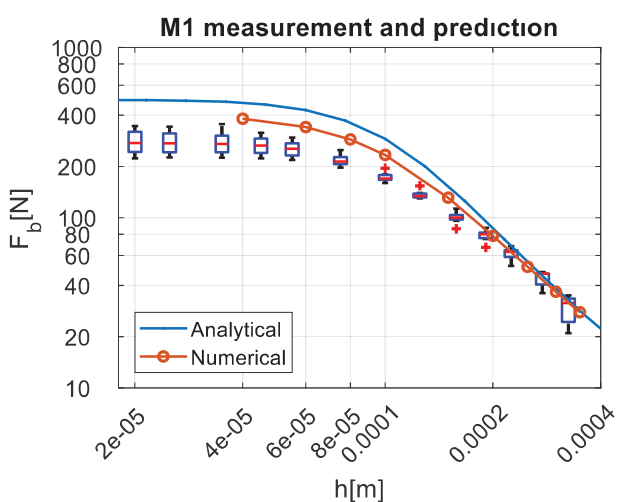


Fig. 13. Load capacity of the bearing in situation M1.

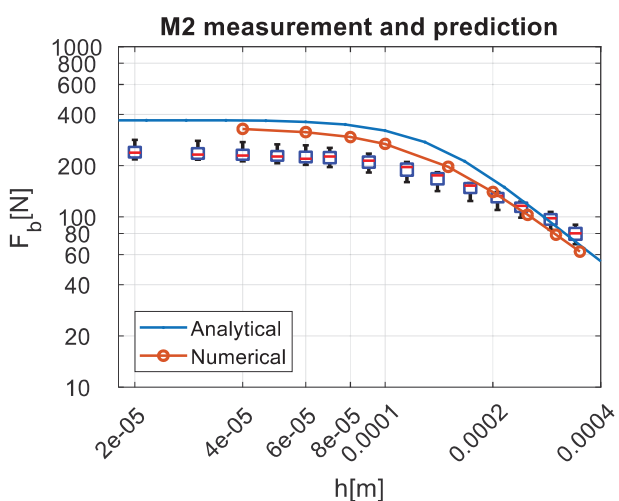


Fig. 14. Load capacity of the bearing in situation M2.

condition M1 and M2 presented in Table 2. The different boxplots present the different performed measurements. The solid line presents the analytical model and the line with circles presents the results from the numerical model. Fig. 12 presents the three analytical models

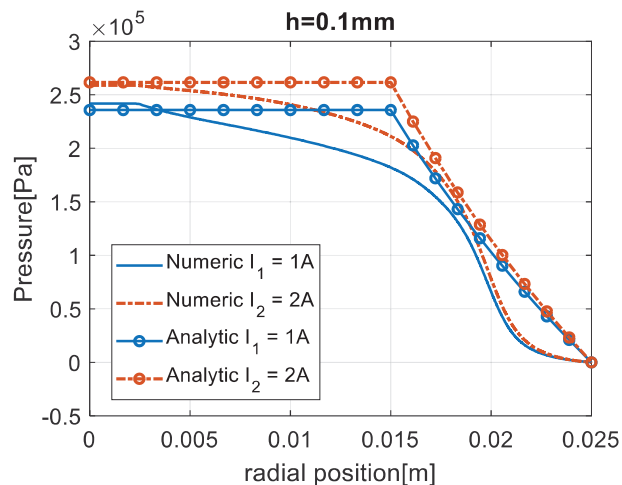


Fig. 15. Pressure distribution in the bearing film over the radius of the bearing for a film height of $h = 0.1\text{mm}$.

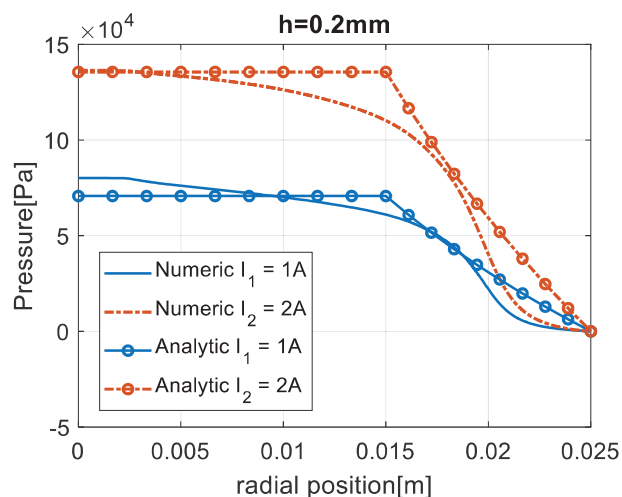


Fig. 16. Pressure distribution in the bearing film over the radius of the bearing for a film height of $h = 0.2\text{mm}$.

discusses in this paper for a wider range of film heights and a constant pressure source, all other parameter values are the same as elsewhere in this paper. Fig. 15 and Fig. 16 presents the pressure distribution in between the bearing surfaces the situation of $I_1 = 1\text{A}$ and $I_2 = 2\text{A}$ for respectively a film height of $h = 0.2\text{mm}$ and $h = 0.1\text{mm}$. Note that the difference between the two situations presented in Fig. 15 is only small due to the difference in source pressure.

4. Discussion

The discussion of this paper first discusses the individual measurements done in this research. It does this by interpreting the individual measurements, analysing the validity and possible relating them to other work. The discussion ends with a general discussion the similarities of a hydrostatic bearing using only geometrical surface textures and a hydrostatic bearing using only MR textures.

The viscous model presented in Fig. 3 seems to overestimate the viscous behaviour of the fluid at lower shear rates ($\dot{\gamma} < 100$). This introduces some error when the flow rates are small resulting in modelling a more viscous fluid than actually is the case. The spread in the viscous behaviour presented in Fig. 4 shows to be very large at high magnetic flux densities. This has no significant effects on the results of the numerical model since the maximum field strength present in the fluid stays well under the 0.2T as can be seen from Fig. 9. Fig. 9

furthermore shows that there is no proportional relation between the yield stress of the fluid and the flux density present. Most of the yield stress is present at the sides of the bearing.

The properties measured with the cone-plate rheometer only measures the fluid properties in the direction tangent to the shear rate and tangent to the speed of the flow. Research showed that the rheological properties are lower in the other two orthogonal direction [49–55]. Applying a magnetic field to an MR fluid causes pillars of magnetic particles to form in the fluid aligning with the magnetic field [56,57]. The work of [51,52] demonstrates that the yield stress can differ as much as a factor 5 in different directions due to this effect. Fig. 10 shows that most of the field is perpendicular to the bearings surfaces but some part of the field (that is near the peak of the field) is parallel to the bearing surfaces. This results in the situation that the resulting yield strength and viscosity near that peak are in reality lower than assumed in the numerical and analytical model. Since the magnetic field in this research is relatively uniform, the effect of the anisotropic behaviour is relatively small. The effect can be large in other systems that do not have a uniform magnetic field; there the anisotropy should be included into the calculations to have accurate representation of the system.

The data presented in Fig. 11 shows a slight offset of 10% between the measured load capacity and the modelled load capacity. This inaccuracy is probably due to some inaccuracies in the experimental setup. Some possible inaccuracies are for example the value of the linear restrictor, the flatness and parallelism of the bearing faces and the hysteresis of the pressure control valve. The magnitude of this error demonstrates that the setup in itself is working properly.

The data presented in Figs. 13 and 14 show a good accordance at higher fly heights. Both the analytical model and the numerical model are well within the inaccuracy of the measurements. The difference between the numerical model and analytical model is larger for a current of $I_2 = 2A$ than for a current of $I_1 = 1A$. Fig. 16 presents a reason for this difference by presenting the pressure distribution of the radius of the bearing for the film height of $h = 0.2mm$. The graph shows that pressure distributions calculated numerically and analytically show more difference in the situation of $I_2 = 2A$ than in the situation of $I_1 = 1A$. This leads to a larger difference in load in the situation of $I_2 = 2A$ than in the situation of $I_1 = 1A$.

The pressure distributions presented in Figs. 15 and 16 show a clear decline in pressure at the locations where the field intensity is high. Still a small decline in pressure is visible where the field strength is small which means that the viscosity in the absence of a magnetic field still causes a significant resistance. These losses are not taken into account in the analytical model, which is the main reason of the differences between the analytical and numerical model. The losses in the absence of a magnetic field can be included in the analytical model but then the big advantage of a simple insightful model is lost.

Offsets between the analytical models, the numerical models and the experimental measurements are large at lower fluid film heights. This indicates that some inaccuracies are present in the pressure distribution over the radius of the bearing. An error in the resistance of the bearing itself is not likely since the resistance does not significantly influence the load capacity at low fly heights. Fig. 15 shows that the pressure distribution assumed in the analytical model is a less good fit to the numerical calculated pressure distribution when compared to the data presented in Fig. 16. The difference between the calculations and the measurements is probably due to the assumption of the Bingham plastic material model. Fig. 3 shows that the difference of the assumed fluid model and the measured fluid model is larger for relatively low shear rates compared to the measured values. The shear rates become lower for lower fluid film heights since both the fluid speed and film height decreases. This causes an error in the yield stress in that situation. This error is larger at the sides of the bearing than in the centre of the bearing since the plug is larger at the sides due to the lower speed there. This results in the situation that the effect of an overestimated yield stress is especially significant at the sides of the bearing. This

means that the pressure should decline faster in radial direction than is currently assumed. A faster declining pressure eventually results in a lower load capacity. This situation might be resolved by using the Herschel-Bulkley model.

Fig. 12 shows the recess pressure calculated with the analytical model for a wider range of fluid film height and the same pressure source. These lines show the effect of applying a magnetic field to the system at a larger scale.

The analytical model is a good addition in the analyses of hydrostatic bearings lubricated with MR fluids. The model might be less accurate compared to the numerical model, but it way less computational demanding. The total computation time of the numerical model is 5.5 h while the total computation time of all other calculations for this research only took a few seconds. This makes it possible to check quickly the effect of certain parameters and the simplicity of the model facilitates the development of some insight into the effects of certain parameters.

In general, the research stated that a hydrostatic bearing with MR structure mimics the behaviour of a hydrostatic bearing with geometrical surface textures. The experimental setup present in this research has only two flat bearing surfaces, a resistance at the outer sides of the bearing surfaces is created by using a MR fluid and applying a magnetic field at the outer locations of the bearing. Figs. 16 and 15 show pressure distributions that are similar to the one found in conventional hydrostatic bearings with geometrical surface textures. The behaviour is similar but not the same since the resistance of a MR structure scales different with the fluid film height and applied pressure compared to a geometrical surface texture as can be seen from Fig. 12.

The magnetic field effects the flow in a similar way as does the geometry of the bearing. This means that for a computation, the shape of the magnetic field should be treated the same as the shape of the geometry of the bearing. This means that both the geometry and the shape of the magnetic field function as inputs of the flow modelling in the bearing.

Interesting to note is that the theory presented in this research is also applicable to hydrostatic bearings lubricated with a Bingham plastic lubricant. A hydrostatic bearing configuration using a geometrical texture as a resistance at the sides of the bearing faces shall show a similar bearing stiffness as the one presented here.

5. Conclusions

This research presents the load characteristic of a hydrostatic bearing using MR structures by means of an experimental setup, a numerical model and an analytical model. The research demonstrates that a local magnet together with a magnetorheological fluid generates similar effects as a local decrease in fluid film height. Similar but not identical since the resistance scales different compared to a change in fluid film height and applied pressure.

The three different models give characteristics that are in the same order of magnitude which means that they are useful in the design of a hydrostatic bearing lubricated with magnetorheological fluids. The analytical model is the coarsest but has as advantage that it is very quick to calculate. The numerical model is more precise but suffer from the fact that the computation is very demanding. The main reason for the inaccuracy of the analytical model are the coarse assumptions. The inaccuracy of the computation model is the result of an inaccurate material model. Furthermore, interesting to note is that the theory is also applicable for any other lubricant that behaves as a Bingham plastic.

Acknowledgement

The Dutch TKI maritime funding program has supported this research.

Appendix A. Supplementary data

Supplementary data to this article can be found online at <https://doi.org/10.1016/j.cap.2019.09.004>.

References

- [1] S.S. Perry, W.T. Tysoe, Frontiers of fundamental tribological research, *Tribol. Lett.* 19 (3) (2005) 151–161.
- [2] N.K. Myshkin, I.G. Goryacheva, Tribology: trends in the half-century development, *J. Frict. Wear* 37 (6) (2016) 513–516.
- [3] K. Holmberg, A. Erdemir, Influence of tribology on global energy consumption, costs and emissions, *Friction* 5 (3) (2017) 263–284.
- [4] S.G.E. Lampaert, J.W. Spronck, R.A.J. van Ostayen, Load and stiffness of a planar ferrofluid pocket bearing, *Proc. Inst. Mech. Eng. J. J. Eng. Tribol.* 232 (1) (2017) 14–25.
- [5] S.G.E. Lampaert, B.J. Fellingner, J.W. Spronck, R.A.J. van Ostayen, In-plane friction behaviour of a ferrofluid bearing, *Precis. Eng.* 54 (2018) 163–170.
- [6] M. Holmes, D. Trumper, Magnetic/fluid-bearing stage for atomic-scale motion control (the angstrom stage), *Precis. Eng.* 18 (1) (1996) 38–49.
- [7] W. Ochonski, Sliding bearings lubricated with magnetic fluids, *Ind. Lubr. Tribol.* 59 (6) (2007) 252–265.
- [8] H. Urreta, Z. Leicht, A. Sanchez, A. Agirre, P. Kuzhir, G. Magnac, Hydrodynamic bearing lubricated with magnetic fluids, *J. Intell. Mater. Syst. Struct.* 21 (15) (2010) 1491–1499.
- [9] X. Wang, H. Li, G. Meng, Rotordynamic coefficients of a controllable magnetorheological fluid lubricated floating ring bearing, *Tribol. Int.* 114 (April) (2017) 1–14.
- [10] J. Hesselbach, C. Abel-Keilhack, Active hydrostatic bearing with magnetorheological fluid, *Proc. Eighth Int. Conf. New Actuators*, 2002, pp. 343–346.
- [11] J. Hesselbach, C. Abel-Keilhack, Active hydrostatic bearing with magnetorheological fluid, *J. Appl. Phys.* 93 (10) (2003) 8441–8443.
- [12] J.M. Guldbakke, C. Abel-Keilhack, J. Hesselbach, Magnetofluidic bearings and dampers J.M. Colloidal Magnetic Fluids: Basics, Development and Application of Ferrofluids, 2009.
- [13] D. Brousseau, E.F. Borra, M. Rochette, D.B. Landry, Linearization of the response of a 91-actuator magnetic liquid deformable mirror, *Opt. Express* 18 (8) (2010) 8239–8250.
- [14] D.A. Bompos, P.G. Nikolakopoulos, Rotordynamic analysis of a shaft using magnetorheological and nanomagnetorheological fluid journal bearings, *Tribol. Trans.* 59 (1) (2016) 108–118.
- [15] D.A. Bompos, Tribological Design of Nano/Magnetorheological Fluid Journal Bearings, (2015).
- [16] D.A. Bompos, P.G. Nikolakopoulos, CFD simulation of magnetorheological fluid journal bearings, *Simul. Model. Pract. Theory* 19 (4) (2011) 1035–1060.
- [17] N. Vaz, et al., Experimental investigation of frictional force in a hydrodynamic journal bearing lubricated with magnetorheological fluid, *J. Mech. Eng. Autom.* 7 (5) (2017) 131–134.
- [18] A. Bouzidane, M. Thomas, An electrorheological hydrostatic journal bearing for controlling rotor vibration, *Comput. Struct.* 86 (3–5) (2008) 463–472.
- [19] O.-O. Christidi-Loumpasefski, I. Tzifas, P.G. Nikolakopoulos, C.A. Papadopoulos, Dynamic analysis of rotor – bearing systems lubricated with electrorheological fluids, *Proc. Inst. Mech. Eng. - Part K J. Multi-body Dyn.* 0 (0) (2017) 1–16.
- [20] J.S. Basavaraja, S.C. Sharma, S.C. Jain, A study of misaligned electrorheological fluid lubricated hole-entry hybrid journal bearing, *Tribol. Int.* 43 (5–6) (2010) 1059–1064.
- [21] S.C. Sharma, C.B. Khatri, Electro-rheological fluid lubricated textured multi-lobe hole-entry hybrid journal bearing system, *J. Intell. Mater. Syst. Struct.* 29 (8) (2018) 1600–1619.
- [22] S.G.E. Lampaert, R.A.J. van Ostayen, Virtual textured hybrid bearings, 44th Leeds-Lyon Symposium on Tribology, 2017, p. 84.
- [23] S.G.E. Lampaert, R.A.J. Van Ostayen, Hydrostatic bearing with MR texturing, *Book of Abstracts 16th German Ferrofluid Workshop*, 2017, pp. 94–95.
- [24] S.G.E. Lampaert, R.A.J. van Ostayen, Predicting the behaviour of magnetorheological textured bearings, *The 18th Nordic Symposium on Tribology – NORDTRIB 2018*, 2018.
- [25] S.G.E. Lampaert, R.A.J. van Ostayen, Load and stiffness of a hydrostatic bearing lubricated with a Bingham plastic fluid, *J. Intell. Mater. Syst. Struct.* (2019), <https://doi.org/10.1177/1045389X19873426>.
- [26] S.G.E. Lampaert, R.A.J. van Ostayen, Lubricated Sliding Bearing with Adjustment of the Properties of the Lubricant in Certain Parts of the Bearing Gap, WO2018212657, 2018.
- [27] M. Ashtiani, S.H. Hashemabadi, A. Ghaffari, A review on the magnetorheological fluid preparation and stabilization, *J. Magn. Magn. Mater.* 374 (2015) 711–715.
- [28] S.R. Gorodkin, R.O. James, W.I. Kordonski, Magnetic properties of carbonyl iron particles in magnetorheological fluids, *J. Phys. Conf. Ser.* 149 (2009) 012051.
- [29] V.A. Markel, Introduction to the Maxwell garnett approximation: tutorial, *J. Opt. Soc. Am. A* 33 (7) (2016) 1244.
- [30] A.C. Becnel, S. Sherman, W. Hu, N.M. Wereley, Nondimensional scaling of magnetorheological rotary shear mode devices using the Mason number, *J. Magn. Magn. Mater.* 380 (2015) 90–97.
- [31] K. Danas, S.V. Kankalana, N. Triantafyllidis, Experiments and modeling of iron-particle-filled magnetorheological elastomers, *J. Mech. Phys. Solids* 60 (1) (2012) 120–138.
- [32] D. Szabo, M. Zrinyi, Nonhomogeneous, non-linear deformation of polymer gels swollen with magneto-rheological suspensions, *Int. J. Mod. Phys. B* 16 (17–18) (2002) 2616–2621.
- [33] M. Chand, A. Shankar, Noorjahan, K. Jain, R.P. Pant, Improved properties of bi-dispersed magnetorheological fluids, *RSC Adv.* 4 (96) (2014) 53960–53966.
- [34] A. Ghaffari, S.H. Hashemabadi, M. Ashtiani, A Review on the Simulation and Modeling of Magnetorheological Fluids vol. 26, (2015), pp. 881–904 8.
- [35] J.L. Arias, V. Gallardo, F. Linares-Moliner, A.V. Delgado, Preparation and characterization of carbonyl iron/poly(butylcyanoacrylate) core/shell nanoparticles, *J. Colloid Interface Sci.* 299 (2) (2006) 599–607.
- [36] A. J. F. Bombard, I. Joeke, and M. Knobel, “Magnetic Susceptibility and Magnetic Hysteresis Loop of Some Carbonyl Iron Powders Used in Magnetorheological Fluids,” pp. 1–6.
- [37] M.A. Abshinova, S.M. Matitsine, L. Liu, C.R. Deng, L.B. Kong, High microwave magnetic permeability of composites with submicron iron flakes, *J. Phys. Conf. Ser.* 266 (1) (2011) 6–11.
- [38] M.T. López-López, J. de Vicente, G. Bossis, F. González-Caballero, J.D.G. Durán, Preparation of stable magnetorheological fluids based on extremely bimodal iron–magnetite suspensions, *J. Mater. Res.* 20 (04) (2005) 874–881.
- [39] P. Kim, J.I. Lee, J. Seok, Analysis of a viscoplastic flow with field-dependent yield stress and wall slip boundary conditions for a magnetorheological (MR) fluid, *J. Nonnewton. Fluid Mech.* 204 (2014) 72–86.
- [40] T.C. Papanastasiou, Flows of materials with yield, *J. Rheol. (N. Y. N. Y.)* 31 (5) (1987) 385–404.
- [41] D.N. Smyrniotis, J.A. Tsamopoulos, Squeeze flow of Bingham plastics, *J. Nonnewton. Fluid Mech.* 100 (1–3) (2001) 165–190.
- [42] P. Coussot, Yield stress fluid flows: a review of experimental data, *J. Nonnewton. Fluid Mech.* 211 (2014) 31–49.
- [43] M. Dinkgreve, J. Paredes, M.M. Denn, D. Bonn, “On different ways of measuring ‘the’ yield stress, *J. Nonnewton. Fluid Mech.* 238 (2016) 233–241.
- [44] J.C. Lambropoulos, C. Miao, S.D. Jacobs, Magnetic field effects on shear and normal stresses in magnetorheological finishing, *Opt. Express* 18 (19) (2010) 19713–23.
- [45] H.M. Laun, C. Kormann, N. Willenbacher, Rheometry on magnetorheological (MR) fluids, *Rheol. Acta* 35 (5) (1996) 417–432.
- [46] M. Zubieta, S. Eceolaza, M.J. Elejabarrieta, M.M. Bou-Ali, Magnetorheological fluids: characterization and modeling of magnetization, *Smart Mater. Struct.* 18 (9) (2009).
- [47] G.W. Stachowiak, A.W. Batchelor, *Engineering Tribology*, fourth ed., Elsevier Inc., 2014.
- [48] R. Van Ostayen, “The Hydro-Support: an Elasto-Hydrostatic Thrust Bearing with Mixed Lubrication, (2002).
- [49] H. Wang, C. Bi, J. Kan, C. Gao, W. Xiao, The mechanical property of magnetorheological fluid under compression, elongation, and shearing, *J. Intell. Mater. Syst. Struct.* 22 (8) (2011) 811–816.
- [50] P. Kuzhir, et al., Magnetorheological effect in the magnetic field oriented along the vorticity, *J. Rheol. (N. Y. N. Y.)* 58 (6) (2014) 1829–1853.
- [51] E. Dohmen, N. Modler, M. Gude, Anisotropic characterization of magnetorheological materials, *J. Magn. Magn. Mater.* 431 (2017) 107–109.
- [52] E. Dohmen, D. Borin, A. Zubarev, Magnetic field angle dependent hysteresis of a magnetorheological suspension, *J. Magn. Magn. Mater.* 443 (2017) 275–280.
- [53] P. Kuzhir, G. Bossis, V. Bashtovoi, O. Volkova, Effect of the orientation of the magnetic field on the flow of magnetorheological fluid. II. Cylindrical channel, *J. Rheol. (N. Y. N. Y.)* 47 (6) (2003) 1385.
- [54] P. Kuzhir, G. Bossis, V. Bashtovoi, Effect of the orientation of the magnetic field on the flow of a magnetorheological fluid. I. Plane channel, *J. Rheol. (N. Y. N. Y.)* 47 (6) (2003) 1373–1384.
- [55] J. Takimoto, H. Takeda, Y. Masubuchi, K. Koyama, Stress rectification in MR fluids under tilted magnetic field, *Int. J. Mod. Phys. B* 13 (14, 15 & 16) (1999) 2028–2035.
- [56] H.E. Hornig, C. Hong, S.Y. Yang, H.C. Yang, Novel properties and applications in magnetic fluids, *J. Phys. Chem. Solids* 62 (2001) 1749–1764.
- [57] C.-Y. Hong, Field-induced structural anisotropy in magnetic fluids, *J. Appl. Phys.* 85 (8) (1999) 5962–5964.

Rheological textures in bearing systems with parallel surfaces Presentation title in french (titre 1)

Maarten C. de Graaf ^a, Ron A.J. van Ostayen ^a and Stefan G.E. Lampaert ^a

a Delft University of Technology, Mekelweg 2, 2628 CD Delft, the Netherlands

Keywords: Magnetorheology, Hydrodynamic bearing, Tribology, Numerical simulation, Magnetic
Mots clés : Five keywords by order of importance, in French (keywords list).

Hydrodynamic bearings have superior wear behaviour but still in general the lifetime of this concept is not infinite. Wear of this bearing concept is generally caused by poor lubrication during high loading conditions or low speeds. This wear gets especially troublesome when surface textures are used to improve lubrication that can get worn away completely. The concept discussed in this work is that of creating the behaviour of surfaces textures with the use of a magnetorheological (MR) fluid. The fluid together with a local magnetic field can locally create solid like behaviour of the lubricant resulting in a so-called virtual surface texture that is not sensitive to wear.

This work presents several numerical simulations using different 2D fluid models incorporating an MR fluid. A configuration of a Rayleigh step using MR fluid shows an antisymmetric pressure distribution. This indicates pressurization of the fluid which can result in a load carrying capacity. This demonstrates that it is possible to create virtual surface textures using solely an MR fluid and a local magnetic field.

Text of the abstract in French (abstract) Texte du résumé (abstract) Texte du résumé (abstract) Texte du résumé (abstract)

1 Introduction

A hydrodynamic bearing is a type of fluid bearing in which the load is supported by a thin layer of rapidly moving pressurized liquid between the bearing surfaces [1]. Hydrodynamic bearings use the squeeze film principle or surface textures to pressurize the fluid (a changing fluid film height). At lower speeds hydrodynamic bearings have high wear and short life. This high wear especially occurs during starts and stops where the speed is not sufficient to maintain the thin fluid film.

Surface textures can be used to pressurize the fluid in hydrodynamic bearings. In [2] the friction characteristic of a journal bearing with dimpled bushings is investigated. These dimples contribute to the load carrying capacity and improve the frictional performance of journal bearings. In [3]-[5] textured thrust bearings are demonstrated. It is shown that the presence of the textures can provide better lubrication efficiency through both a reduction of friction and an increase in load carrying capacity. Also there are hydrodynamic bearings that utilize grooves textured in the bearing faces in order to obtain a load carrying capacity [6, 7]. Nevertheless, at lower speeds, starts, and stops these surface textures do wear down and the contribution to the bearing performance is lost. Therefore a surface texture is desired that is not sensitive to wear.

In the work of [8] a bearing is proposed where the resistance is increased locally by using an MR fluid and a local magnetic field. Here the resistance is modified locally in the lubricating film, however at a certain location in the lubricating film, the magnetic field is uniform across the full film gap. This concept cannot be used for textured hydrodynamic bearings, because for this a varying resistance over the bearing gap is required.

The magnetic properties of a magnetic fluid are obtained when particles that have magnetic properties are suspended in a carrier fluid. The magnetic particle material often used for an MR fluid is carbonyl iron since this has a saturation magnetization equal to 2.1 tesla, the highest value of known elements

[9]. MR fluids can appear as a liquid but can also act solid, depending on the strength of the magnetic field applied to it. This solid phase is due to the attractive dipolar forces between the particles that have been magnetized by the applied magnetic field. The strength of the solid phase is caused by the formation of certain structures by the particles, such as chain-like agglomerates (Fig. 1) [10]. The particles of MR fluids are normally around the size of micrometers [11]. The aggregation process for an MR fluid is more intense in presents of a field. That is why their flow behaviour can be controlled [12].

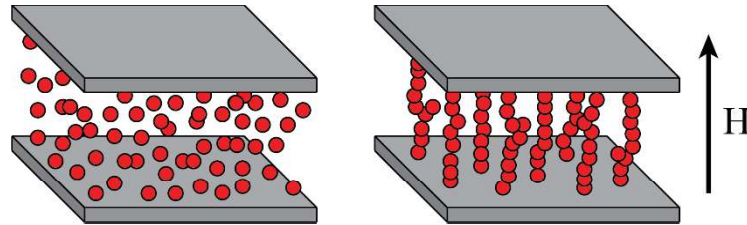


Fig 1 – Formation of chain-like agglomerates in an MR fluid when subjected to a magnetic field.

In [14] a new concept of hydrostatic bearings is presented that is lubricated with an MR fluid. A constant gap size for alternating payloads is achieved due to the fact that when an MR fluid is exposed to an external magnetic field the rheological properties change. In [15] a test bench has been developed to demonstrate that magnetic fluids can be used to develop active journal bearings. In [16] experiments are done with a constructed MR fluid film bearing. The dynamic properties of this bearing are evaluated both in its active and its inactive state. What the former concepts all have in common is that the magnetic field is constant and applied globally and not locally.

Numerical simulations can be used to predict the performance of MR fluid based applications. Literature reports several works in which a numerical simulation is used for modelling an MR fluid. In [17] and [18] only the magnetic field is considered for an MR fluid brake and clutch. In [19] and [20] the flow of the MR fluid is also considered but only at microscopic level. In [21] a higher level model coupled with magnetic simulation is presented which successfully describes MR fluids behaviour in flow mode. Considering textured hydrodynamic bearings, using an MR fluid in this application can be beneficial regarding wear and controllability of these surface textures. For textured hydrodynamic fluid bearings using an MR fluid a model regarding shear mode is required. In this sense it is desired to create a model which can describe MR fluids at a higher level and in shear mode.

For a textured hydrodynamic bearing one surface is moving tangentially relative to the other which results in a shear flow (Fig. 2). In the situation that the fluid has a constant yield stress across the full height of the channel, either no flow or a complete Newtonian flow happens. However, in order to create a solid part at the bottom of the channel, the yield stress at the bottom has to be higher than at the top of the channel. This varying yield stress cannot be obtained with a constant magnetic field. Now, a gradient in magnetic field is required, which results in a decreasing yield stress over the channel height.

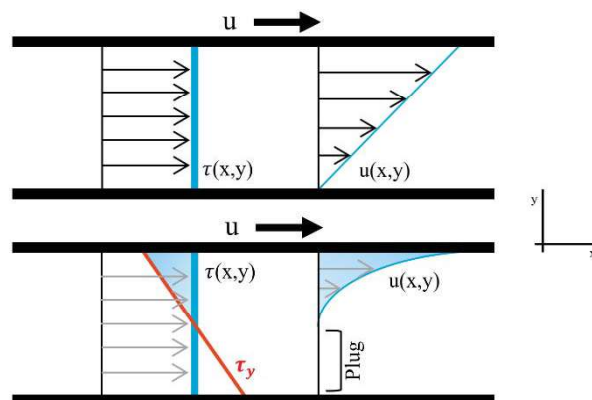


Fig 2 - Shear mode for a Newtonian fluid (top) and an MR fluid (bottom) between two parallel surfaces where one surface is moving relative to the other surface.

A solid part at the bottom for the full length of the channel does not show a change in pressure distribution over the length of the channel. To obtain a pressure distribution, only locally the channel

must behave as a solid while the other part of the channel behaves as a fluid (Fig. 3). This creates a difference in fluid transport along the length of the channel resulting in a changing pressure over the length of the bearing. In a bearing this pressurization of the fluid results in a load carrying capacity [13].

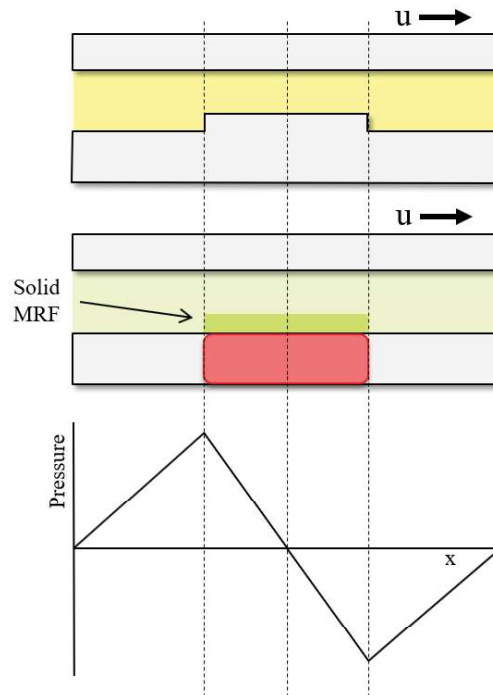


Fig 3 - The step geometry (top graph) leads to a saw tooth pressure profile (lower graph). The combination of a magnetic field and MRF (middle graph) also produces a similar geometry and therefore pressure.

This paper demonstrates that these surface textures can be created with an MR fluid with a local magnetic field. This is done with several numerical simulations using different 2D fluid models. At the end using a local magnetic field a configuration of a step geometry using MR fluid is created. Over this step an antisymmetric pressure distribution is obtained that indicates pressurization of the MR fluid. This step consists of the magnetic particles in the MR fluid and these do not wear down and do not leave the system.

2 Method

In order to create virtual surface textures with an MR fluid, a non-Newtonian fluid model which is able to describe the behaviour of an MR fluid has to be validated. Therefore first a fluid model regarding the flow mode is made. This is followed by a model which can describe an MR fluid in shear mode. Finally a self-created magnetic field is applied locally in order to obtain a virtual surface texture which is able to pressurize the fluid.

2.1 Fluid model

A model that is used to describe these non-Newtonian fluids is the Bingham model (Eq. 1 and 2) [22].

$$\tau = \tau_y + \eta\dot{\gamma}, \quad |\tau| > \tau_y \quad (1)$$

$$\dot{\gamma} = 0, \quad |\tau| \leq \tau_y \quad (2)$$

Here τ is the shear stress, τ_y is the yield stress, η is the viscosity, and $\dot{\gamma}$ is the shear rate. Compared to the Newtonian model, it is seen that the shear stress now depends on the yield stress of the fluid. For an MR fluid this yield stress is caused by a magnetic field, and with a change in magnetic field this yield stress changes (Fig. 4). This yield stress causes the solid phase of the MR fluid. The moment this yield stress is exceeded, the MR fluid starts to flow just like a Newtonian fluid.

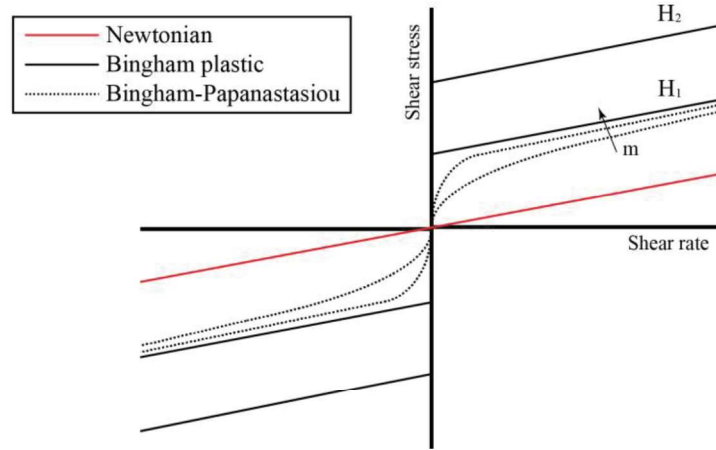


Fig 4 - Different models where the shear stress versus the shear rate is shown. Here $H_2 > H_1$ and m is the regularization parameter.

To simulate this behaviour a numerical simulation is made in COMSOL Multiphysics [23] where the Bingham-Papanastasiou model is implemented [24]. The Bingham-Papanastasiou model proposes an exponential regularization for the Bingham model (Eq. 3).

$$\tau = \tau_y(1 - e^{-m|\dot{\gamma}|}) + \eta_0\dot{\gamma} \quad (3)$$

$$\eta = \frac{\tau_y}{\dot{\gamma}}(1 - e^{-m|\dot{\gamma}|}) + \eta_0 \quad (4)$$

Here η_0 represents the viscosity when no magnetic field is applied, and m is the regularization parameter. The value of m controls the exponential growth of the shear stress. The higher the value, the faster the shear stress grows (Fig. 4). When there is no magnetic field present, the yield stress in the fluid is equal to 0 and then the apparent viscosity (Eq. 4) is equal to the viscosity when no magnetic field is applied, $\eta = \eta_0$.

2.2 Flow mode with a constant yield stress

To validate the model used, first a pure pressure driven flow (Poiseuille flow) is modelled using an MR fluid for different yield stresses. For this the parameters in [21] are considered. The dimensions used for this model are normalized (Table 1). Here the height of the channel is taken equal to 1, and the ratios between parameters used in [21] are used for further parameterization. The simulation for the flow mode evaluates the MR fluid for different yield stresses, which correspond to a certain constant magnetic field.

Parameters	
Channel ($l \times h$) [$L_{\text{norm}} \times h$]	10×1
Regularization parameter [$m_{\text{norm}} \times h$]	1250
Viscosity [η_{norm}]	0.28
Pressure drop [$\Delta p_{\text{norm}} \times (1/h)$]	60
Yield stress [$\tau_y \times (1/h)$]	0, 1, 2, 13/5, 3

Tab 1 - Normalized parameters from [21] used for simulating the MR fluid in flow mode.

2.3 Shear mode with a varying magnetic field

Pure shear flow for both a Newtonian fluid and MR fluid are seen in figure 2, this mode is also referred to as Couette flow. In order to create a solid part at the bottom of the channel, a varying yield stress is used. In the model a linear decrease in yield stress over the channel height is applied. For the model normalized parameters are used (Table 2). To simulate the shear mode the MR fluid is evaluated for different velocities of the moving surface.

Parameters	
Channel ($l \times h$) [$L_{\text{norm}} \times h$]	10×1
Regularization parameter [$m_{\text{norm}} \times h$]	10^4
Viscosity [η_{norm}]	1

Yield stress bottom [$\tau_y \times (1/h)$]	1
Yield stress top [$\tau_y \times (1/h)$]	0
Surface velocity [u_{norm}]	1/100, 3/20, 3/10, 3/4, 2

Tab 2 - Normalized parameters used for simulating an MR fluid in shear mode.

2.4 Step bearing configuration

Local solidification in the MR fluid is created with a local magnetic field. To realize this, an array of magnets and metal blocks is used. Using different parameters (Table 3) an environment is simulated representing a bearing consisting of 4 layers (Fig. 5). The MR fluid used is MRF140CG provided by Lord Corporation [25].

Parameters	
Channel (l x h) [$L_{norm} \times h$]	15 x 1
Ferromagnetic layer (l x h) [$L_{norm} \times h$]	15 x 1
Magnets (l x h) [$L_{norm} \times h$]	5/6 x 5/6
Ferromagnetic blocks (l x h) [$L_{norm} \times h$]	1/2 x 5/6
Regularization parameter [$m_{norm} \times h$]	10 ⁴
Viscosity [η_{norm}]	1
Surface velocity [u_{norm}]	1/100, 3/20, 3/10, 3/4, 2

Tab 3 - Normalized parameters used for simulating the MR fluid MRF140CG

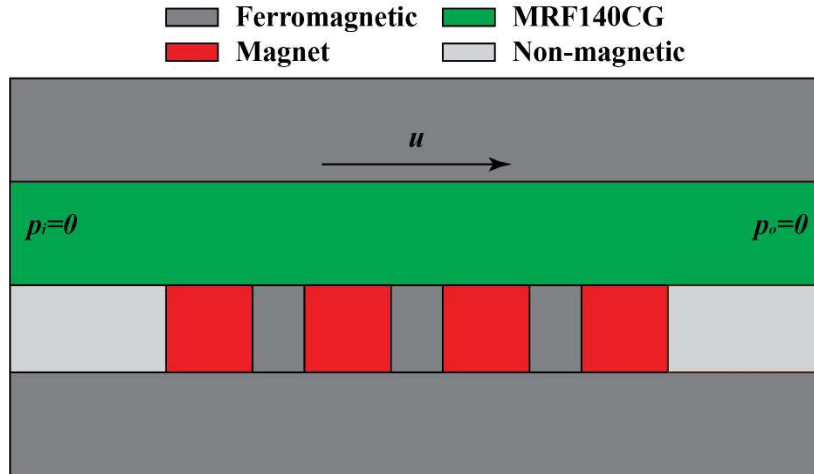


Fig 5 - An environment representing a bearing consisting of 4 layers: 2 layers of metal, a layer containing square magnets and metal blocks, and a layer of MR fluid. Here the top metal surface represents the moving shaft and the bottom two layers the fixed bearing surface.

The magnetic field that is created is related to the flow of the MR fluid. This means a relation has to be found between the magnetic field strength and the yield stress of the MR fluid which can be implemented into COMSOL. In [26]-[31] different models and approaches are presented to obtain the yield stress depending on the magnetic field. For the purpose of this model the relation between yield stress and magnetic field strength for MRF140CG is used. Implementing this and coupling the fluid and magnetic analysis, the behavior of the MR fluid is obtained. To simulate the shear mode the MR fluid is evaluated for different velocities of the moving surface.

Using this magnetic field, local solid zones are formed, located where the shear stress is lower than the local yield stress. These local solid zones act as a virtual surface texture, and influence the flow of the fluid and thus increase the pressure. To see if obtaining a load capacity from this is a possibility with an MR fluid, an antisymmetric pressure distribution over the surface textures has to be obtained (Fig. 3). The surface textures created have a step geometry. This step geometry is represented by the solid part in the MR fluid and can be created by a locally applied magnetic field.

3 Results and discussion

3.1 Flow mode with a constant magnetic field

The results for the velocity profiles for pressure driven flow (Poiseuille flow) are seen in figure 6. A parabolic velocity is observed for no yield stress applied, and is becoming flatter for increasing yield stress. No yield stress corresponds to the behaviour of a Newtonian fluid. The situations where a yield stress is applied correspond to the behaviour of an MR fluid subjected to a certain magnetic field. This also applies to results for the apparent viscosity, shear stress, and shear rate seen in figure 7, 8, and 9 respectively.

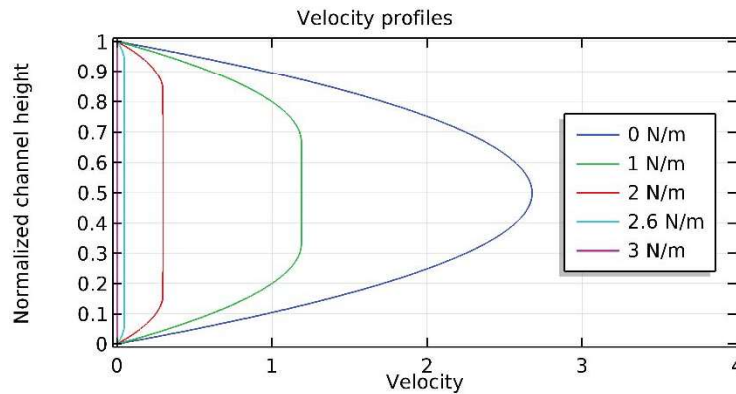


Fig 6 - The velocity profiles for a Poiseuille flow of the MR fluid for different yield stresses.

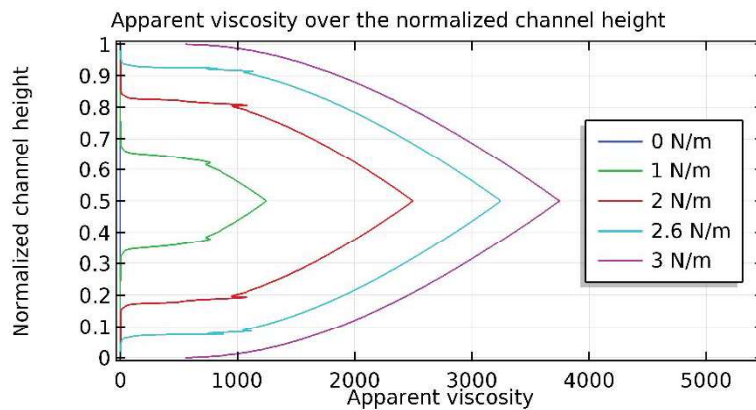


Fig 7 - The apparent viscosity for a Poiseuille flow of the MR fluid for different yield stresses.

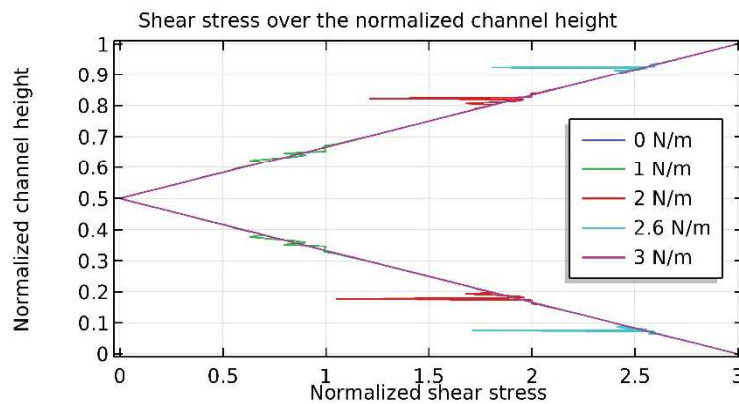


Fig 8 - The absolute normalized shear stress for a Poiseuille flow in the MR fluid for different yield stresses.

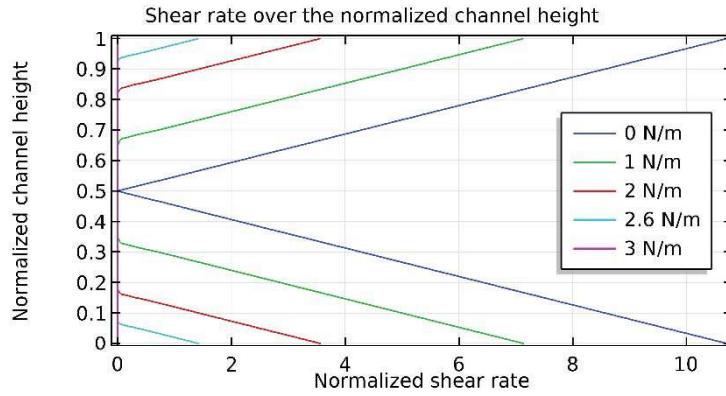


Fig 9 - The normalized shear rate for a Poiseuille flow in the MR fluid for different yield stresses.

The results are as expected and correspond to the results in [21]. For no yield stress, the apparent viscosity stays constant and the shear rate goes linearly to zero in the middle all according to the Newtonian model. For the MR fluid where a yield stress is applied different behaviour is observed. In the regions, the yield stress exceeds the shear stress, the velocity is constant, the apparent viscosity increases, and the shear rate is equal to zero. In these regions, the MR fluid can be seen as one solid moving through the channel. No change is seen in the shear stress, which is expected, only some irregularities are seen at some points. These irregularities happen at the point where the shear stress is equal to the yield stress applied in the different situations. This position is the boundary between fluid and solid.

3.2 Shear mode with a varying magnetic field

For shear mode the MR fluid is subjected to a varying yield stress in order to obtain the solid phase. In figure 10 the results for the velocity profiles are seen for different velocities of the moving wall using a linear decrease in yield stress over the channel height. The results for the apparent viscosity, shear stress, and shear rate are seen in figure 11, 12 and 13 respectively.

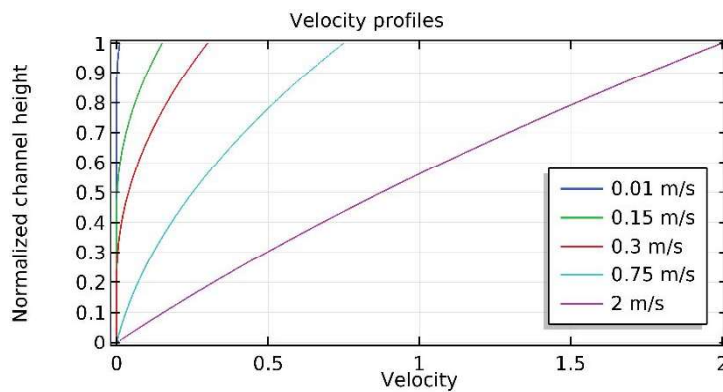


Fig 10 - The velocity profiles of the MR fluid for different velocities of the moving wall.

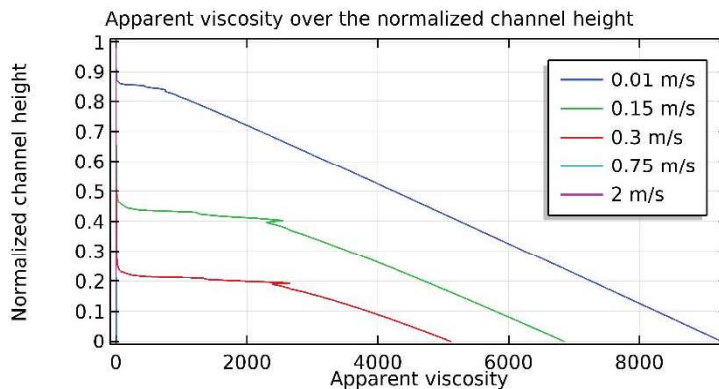


Fig 11 - The apparent viscosity of the MR fluid for different velocities of the moving wall.

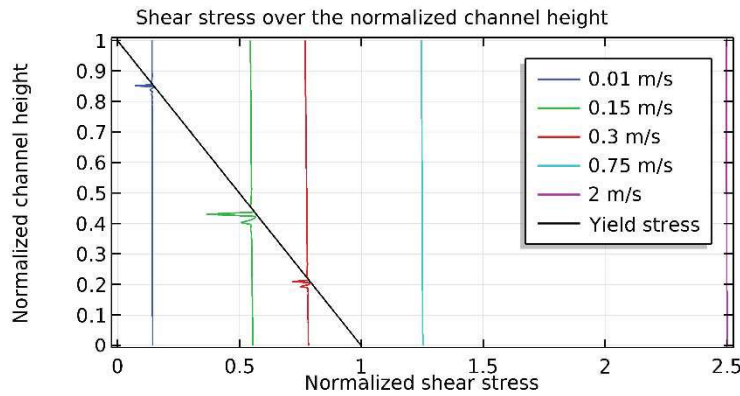


Fig 12 - The normalized shear stress in the MR fluid for velocities of the moving wall. Also the yield stress in the fluid is plotted here, this one is the same for every velocity

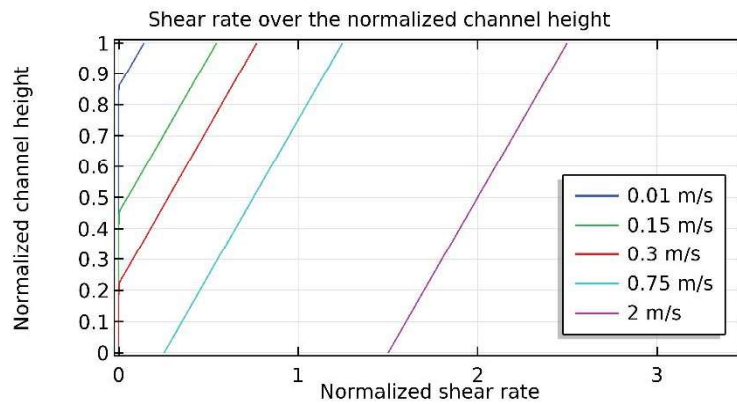


Fig 13 - The normalized shear rate in the MR fluid for different velocities of the moving wall.

The applied yield stress has a large impact on the velocity of the fluid, the apparent viscosity and the shear rate. At the region, the yield stress exceeds the shear stress the velocity of the MR fluid is zero, the apparent viscosity is high, and the shear rate is approaching zero. This indicates that in this region, the MR fluid appears solid and a virtual surface texture is created over the whole length of the channel. At a higher velocity, the impact of the yield stress is less and the size of the virtual surface textures decrease. This is because for higher velocities the shear stress in the fluid is greater. The regions where the yield stress is dominant over the shear stress are becoming smaller and more fluid starts to flow. At one moment, the shear stress exceeds the yield stress completely in the MR fluid and no solid phase is present. Still the effect of the yield stress is seen in the velocity profile. At the bottom of the channel, the liquid is still more viscous than at the top where it approaches the viscosity of the MR fluid where a lower yield stress is applied. This more viscous liquid results in larger resistance to flow and therefore no linear velocity profile is obtained.

3.3 Step bearing configuration

The result for the magnetic field strength of the created array is seen in figure 14. For this array a quite evenly spread magnetic field strength is obtained. Using the metal blocks in between the magnets, the magnetic field is deflected and a high magnetic field is obtained at the bottom of the channel. Due to this local magnetic field a local solid part, a virtual surface texture, is created in the middle of the length of the channel (Fig. 15). In figure 16 to 19 the results for the velocity profile, apparent viscosity, shear stress, and shear rate respectively are seen. Everything is obtained at the middle of the length of the channel.

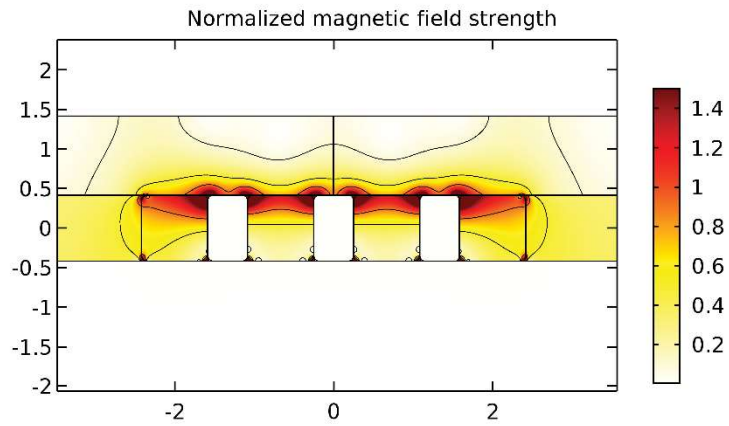


Fig 14 - Simulated array of magnets and metal blocks.

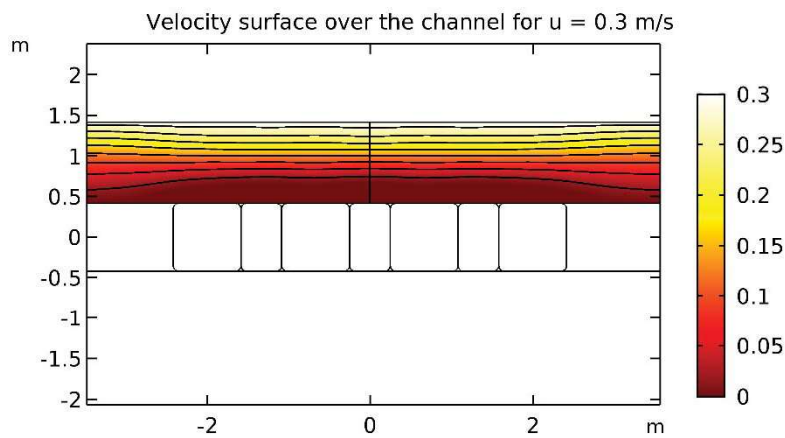


Fig 15 - Solid part created in the middle of the length of the channel at a velocity for the moving wall of 0.3.

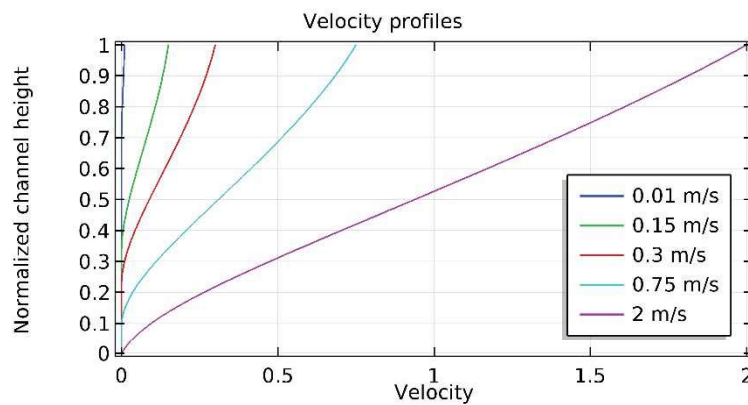


Fig 16 - The velocity profiles of the MR fluid with a solid part in the middle of the length of the channel for different velocities of the moving wall.

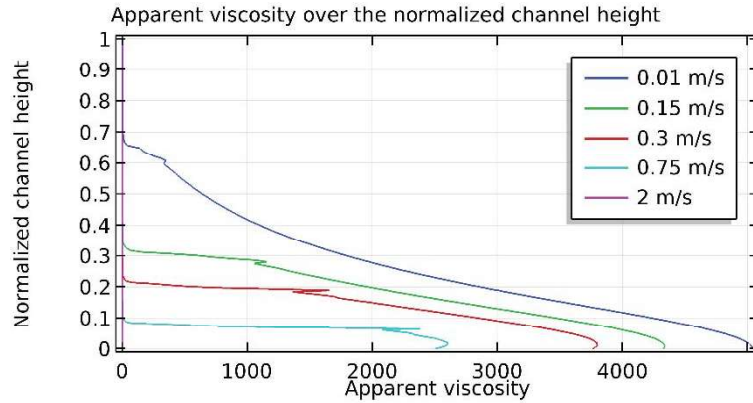


Fig 17 - The apparent viscosity in the MR fluid with a solid part in the middle of the length of the channel for different velocities of the moving wall.

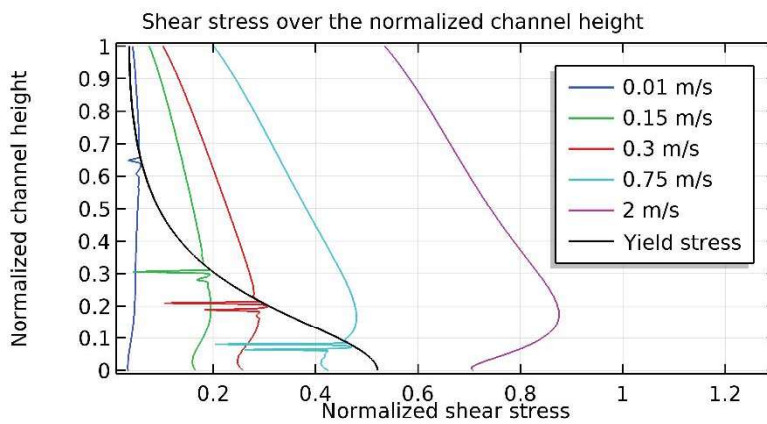


Fig 18 - The normalized shear stress in the MR fluid with a solid part in the middle of the length of the channel for different velocities of the moving wall.

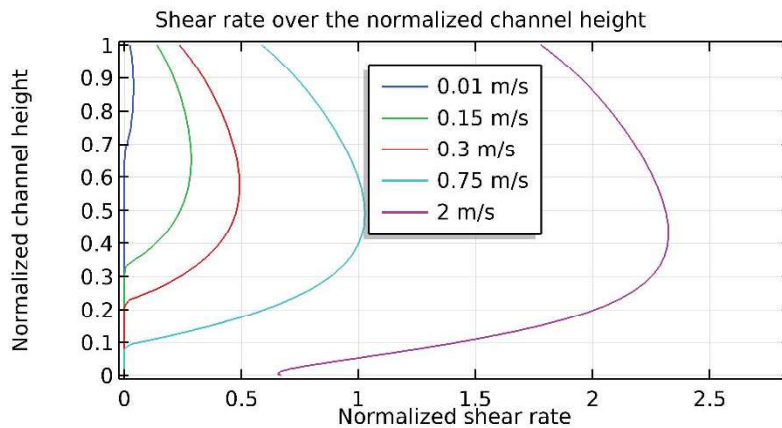


Fig 19 - The normalized shear rate in the MR fluid with a solid part in the middle of the length of the channel for different velocities of the moving wall.

The relation between the different results for a solid part in the middle of the length of the channel (figure 16 to 19) is the same as for the results discussed for where the solid part is present over the length of the whole channel (figure 10 to 13). Although these relations are still there, compared to the earlier results, the velocity starts to increase less at the top of the channel, the shear stress is not constant anymore, and the shear rate does not increase linearly because of the not linear yield stress. Here the physics of a pressure driven flow and shear flow are now combined. Due to the step, the fluid is pressurized which causes a shear stress due to a pressure driven flow which is added to the constant shear stress due to shear flow. This should result in a linear decrease in shear stress over the channel height. This trend is seen in with some irregularities (Fig. 18). At the edges of the created array the

magnetic field strength is higher (Fig. 14). Here the resistance to flow is higher than at middle of the length of the solid part. This is what causes the irregularities observed. This is also affecting the shape of velocity profile and the shear rate.

The result for the pressure distribution over this virtual surface texture is seen in figure 20. The pressure distribution obtained indicates that there is the possibility to create a load carrying capacity. Even when the shear stress in the MR fluid exceeds the yield stress (Fig. 18), and no solid part is present, a pressure distribution is observed (Fig. 20). This is because the magnetic field still influences the viscosity of the MR fluid. Instead of a solid part at the bottom in the middle of the length of the channel, a more viscous fluid than in rest of the channel is observed. This means that at the bottom the fluid flows with more resistance than at the top which causes the observed pressure distribution. So even for this situation it is possible to obtain a load carrying capacity.

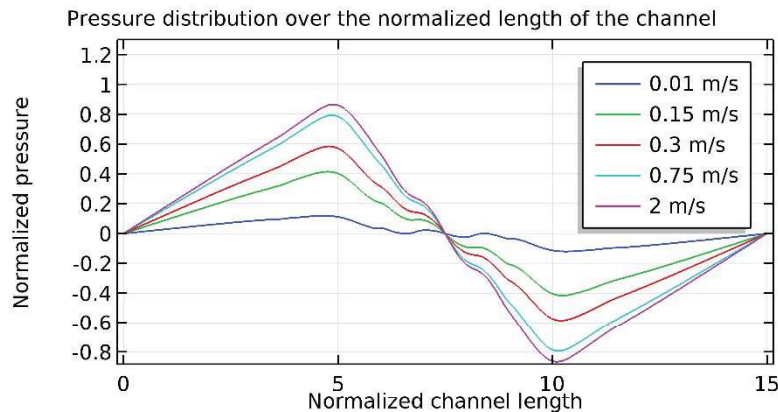


Fig 20 - The normalized pressure distribution in the MR fluid with a solid part in the middle of the length of the channel for different velocities of the moving wall.

4 Conclusion

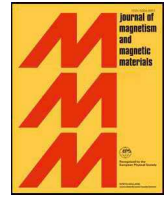
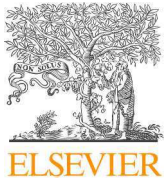
A magnetic field that is constant across the film height cannot be used to create a solid part in shear mode. Therefore a magnetic field that varies across the film height needs to be applied. For a fluid that is depending on a magnetic field a solid part is created at the bottom over the whole length of the channel, where the yield stress is the highest. As a result to an increase in velocity, this solid part decreases in size.

A virtual surface texture is obtained by applying a magnetic field that varies across the film height locally at the middle of the length of the channel. Due to this surface texture a pressure distribution is obtained which indicates that creating a load carrying capacity is possible using an MR fluid. It is interesting to note that for where the shear stress exceeds the yield stress and no solid part is observed, still a pressure distribution is obtained. This indicates that also a load carrying capacity can be obtained if no solid part is present. This is due to the more viscous MR fluid at the location of the previous solid part resulting in more resistance to flow.

5 References

- [1] Rowe WB. (2012) Hydrostatic, Aerostatic and Hybrid Bearing Design. Butterworth-Heinemann.
- [2] Lu X & Khonsari MM. (2007) An Experimental Investigation of Dimple Effect on the Stribeck Curve of Journal Bearings. Tribology Letters, 27(2), 169-176.
- [3] Etsion I, Halperin G, Brizmer V & Kligerman Y. (2004) Experimental Investigation of Laser Surface Textured Parallel Thrust Bearings. Tribology Letters, 17(2), 295-300.
- [4] Qiu Y & Khonsari MM. (2011) Experimental investigation of tribological performance of laser textured stainless steel rings. Tribology International, 44(5), 635-644.
- [5] Henry Y, Bouyer J & Fillon M. (2015) An experimental analysis of the hydrodynamic contribution of textured thrust bearings during steady-state operation: A comparison with the untextured parallel surface configuration. Proceedings of the Institution of Mechanical Engineers, Part J: Journal of Engineering Tribology, 229(4), 362-375.
- [6] Muijderland EA. (1965) Spiral Groove Bearings. Industrial Lubrication and Tribology, 17(1), 12-17.

- [7] Wong CW, Zhang X, Jacobson SA & Epstein AH. (2004) A Self-Acting Gas Thrust Bearing for High-Speed Microrotors. *Journal of Microelectromechanical Systems*, 13(2), 158-164.
- [8] Lampaert SGE & van Ostayen RAJ. (2017) Virtual Textured Hybrid Bearings. 44th Leeds-Lyon Symposium on Tribology.
- [9] Aslam M, Xiong-Liang Y & Zhong-Chao D. (2006) Review of mag-netorheological (MR) fluids and its applications in vibration control. *Journal of Marine Science and Application*, 5(3), 17-29.
- [10] Odenbach S. (2002) Ferrofluid. *Magnetically Controllable Fluids and Their Applications*. Springer Berlin Heidelberg.
- [11] Genc S & Derin B. (2014) Synthesis and rheology of ferrofluids: A review. *Current Opinion in Chemical Engineering*, 3, 118-124.
- [12] Kim IG, Song KH, Park BO, Choi BI & Choi HJ. (2011) Nano-sized Fe soft-magnetic particle and its magnetorheology. *Colloid and Polymer Science*, 289(1), 79-83.
- [13] Hamilton DB, Walowit JA & Allen CM. (1966) A theory of lubrication by micro irregularities. *Journal of Basic Engineering*, 8, 177-185.
- [14] Hesselbach J & Abel-Keilhack C. (2003) Active hydrostatic bearing with magnetorheological fluid. *Journal of Applied Physics*, 93(10), 8441-8443.
- [15] Urreta H, Leicht Z, Sanchez A, Agirre A, Kuzhir P & Magnac G. (2010) Hydrodynamic Bearing Lubricated with Magnetic Fluids. *Journal of Intelligent Material Systems and Structures*, 21(15), 1491-1499.
- [16] Bompos D & Nikolakopoulos P. (2016) Experimental and Analytical Investigations of Dynamic Characteristics of Magnetorheological and Nanomagnetorheological Fluid Film Journal Bearing. *Journal of Vibration and Acoustics, Transactions of the ASME*, 138(3), 1-7.
- [17] Senkal D & Gurocak H. (2009) Compact MR-brake with serpentine flux path for haptics applications. Third Joint EuroHaptics conference and Symposium on Haptic Interfaces for Virtual Environment and Teleoperator Systems, 91-96.
- [18] Xu X & Zeng C. (2010) Design of a Magneto-rheological Fluid Clutch Based on Electromagnetic Finite Element Analysis. 2nd International Conference on Computer Engineering and Technology, 5.
- [19] Climent E, Maxey MR & Karniadakis GE. (2004) Dynamics of Self-Assembled Chaining in Magnetorheological Fluids. *Langmuir*, 20, 507-513.
- [20] Pappas Y & Klingenberg DJ. (2006) Simulations of magnetorheological suspensions in Poiseuille flow. *Rheologica Acta*, 45(5), 621-629.
- [21] Daniel G, Yoan C, Zoltan P & Yves P. (2014) Bingham-papanastasiou and approximate parallel models comparison for the design of magnetorheological valves. IEEE/ASME International Conference on Advanced Intelligent Mechatronics, AIM, 168-173.
- [22] Walters K. (1989) *An Introduction to Rheology*. Elsevier Science Publishers, first ed.
- [23] COMSOL Multiphysics, available at <https://www.comsol.com/>.
- [24] Papanastasiou TC. (1987) Flows of Materials with Yield. *Journal of Rheology*, 31(5), 385-404.
- [25] Lord Corporation; available at <https://www.lord.com/>.
- [26] Ginder JM & Davis LC. (1994) Shear stresses in magnetorheological fluids: Role of magnetic saturation. *Applied Physics Letters*, 65, 3410-3412.
- [27] Genc S & Phule PP. (2002) Rheological properties of magnetorheological fluids. *Smart Materials & Structures*, 11(1), 140-146.
- [28] Bossis G, Lacis S, Meunier A & Volkova O. (2002) Magnetorheological fluids. *Journal of Magnetism and Magnetic Materials*, 252, 224-228.
- [29] Chen S, Huang J, Shu H, Sun T & Jian K. (2013) Analysis and testing of chain characteristics and rheological properties for magnetorheological fluid. *Advances in Materials Science and Engineering*, 2013, 1-7.
- [30] Guo CW, Chen F, Meng QR & Dong ZX. (2014) Yield shear stress model of magnetorheological fluids based on exponential distribution. *Journal of Magnetism and Magnetic Materials*, 360, 174-177.
- [31] Sherman SG, Becnel AC & Wereley NM. (2015) Relating Mason number to Bingham number in magnetorheological fluids. *Journal of Magnetism and Magnetic Materials*, 380, 98-104.



Research articles

Rheological texture in a journal bearing with magnetorheological fluids

Stefan G.E. Lampaert^{a,*}, Federico Quinci^b, Ron A.J. van Ostayen^a^a Delft University of Technology, Mekelweg 2, 2628 CD Delft, the Netherlands^b Bifrost Research and Development B.V., Molenvliet 34, 3961 MV Wijk bij Duurstede, the Netherlands

ARTICLE INFO

Keywords:

Magnetic fluid
Bingham plastic
Numerical modelling
Magnetism
Rheology
Fluid mechanics

ABSTRACT

This paper discusses a new type of hybrid journal bearing in which a magnetorheological fluid is used in combination with local magnetic fields, such that the hydrodynamic and hydrostatic working regimes are not compromised. This demonstrates the potential of using the concept of rheological texture in bearings. The performance of this new type of bearing is assessed via Finite Element Modelling (FEM) in which the behaviour of the fluid film is described by the ideal Bingham plastic fluid model. Both the yield stress and the viscosity increase as a function of the magnetic field.

1. Introduction

Bearing systems have been under a huge development for the last half century at least [1,2]. The presentation of the so-called “Jost Report” in 1966 gave recognition to the huge impact that bearings hold in our society [3]. For example, Holmberg & Erdemir estimated that about 23% (119EJ) of the world’s total energy is lost in tribological contacts [4].

Although decades of research and development have passed after the “Jost Report”, little conceptual development in bearing design has occurred.

Some effort has been made in the field of tribotronics to seek for new bearing concepts, where the potential is investigated of adding control systems to the bearing [5,6]. Likewise, new bearing concepts based on magnetism that use either ferrofluids [7–10] or magnetorheological fluids [11–20] have been explored. In a similar fashion, electrorheological fluids are investigated for a possible use in bearing systems [21–24]. The current work focuses on the use of magnetorheological fluid in journal bearings.

Hydrodynamic journal bearings are used pervasively in all types of machine design due to their cost-effective, superior friction and wear properties [25]. The bearing system consists of a cylindrical shaft inside a cylindrical bush, where the gap between the two is filled with lubricant. This geometry allows the shaft and housing to be able to freely rotate with respect to each other (Fig. 1a). The rotation, together with the converging wedge caused by eccentricity, creates a high-pressure region counteracting the eccentric position. The shaft is floating into this lubricating layer that guarantees a low wear and friction. The main drawback of this bearing configuration is that at low speeds the load

carrying capacity of the lubricating film might be incapable to sustain the load, thus leading the two surfaces into physical contact. This causes excessive friction and wear that may lead to system failure eventually.

One efficient way to overcome this drawback is to use a hydrostatic journal bearing instead (Fig. 1b). This concept uses a high-pressure lubricant supply which is supplied into large surface area recesses to make sure that the shaft floats in the lubricating film during high loads for both low and high speeds. However, the drawback of this design is that the high-pressure hydraulic supply is sensitive to failure, which fact moves the problem to another component in the system. The failure of the pump causes excessive wear in the bearing as it operates very poorly in the hydrodynamic regime due to the surface texture.

The ideal bearing combines the low friction and wear at high speeds with the high load capacity at low speeds. The type of bearing that meets these requirements is the hybrid journal bearing (Fig. 1c). In detail, this concept combines the smooth bearing surface of a hydrodynamic bearing with the high pressure supply of a hydrostatic bearing. In this way, it achieves sufficiently low wear and sufficiently high load capacity for the complete range of speeds and loading conditions. When the pump fails, the hybrid journal bearing reverts to a hydrodynamic journal bearing. The drawback of this concept is that the hydrostatic load capacity is limited due to the absence of surface recesses.

The three concepts in Fig. 1a, b and c share the fact that a modification in the geometry of the bearing surface causes changes in the bearing performance. Specifically, a physical change in the surface texture leads to a change in the film height, which in turn modifies locally the lubricant flow resistance. Controlling this local resistance is key to improve the performance of the bearing [26,27].

* Corresponding author.

E-mail address: S.G.E.Lampaert@tudelft.nl (S.G.E. Lampaert).<https://doi.org/10.1016/j.jmmm.2019.166218>

Received 29 July 2019; Received in revised form 13 November 2019; Accepted 26 November 2019

Available online 29 November 2019

0304-8853/ © 2019 The Authors. Published by Elsevier B.V. This is an open access article under the CC BY license

(http://creativecommons.org/licenses/by/4.0/).

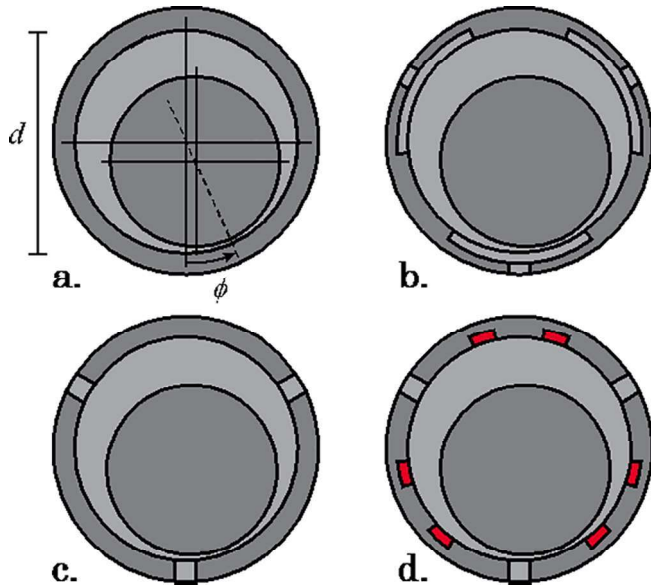


Fig. 1. a: Hydrodynamic journal bearing, b: hydrostatic journal bearing, c: hybrid journal bearing, d: hybrid journal bearing with rheological texture.

A possible approach to manipulate the flow resistance, other than changing the geometry, is to locally vary the rheological properties of the lubricant. This fluid manipulation is addressed as rheological texture and it can be carried out by using a magnetorheological fluid whose rheological properties change in response to a local variation of the magnetic field [28,29]. Based on the rheological texture, multiple new bearing configurations can be conceived that all have unique performance [30].

This paper demonstrates the potential of using the concept of rheological texture in journal bearings. The work discusses a new type of hybrid journal bearing in which a magnetorheological fluid is used in combination with local magnetic fields so as the hydrodynamic and hydrostatic working regimes are not compromised (Fig. 1d). In addition, the work discusses a herringbone bearing that uses the rheological texture in a v-shaped pattern. The performance is assessed in a FEM platform (COMSOL Multiphysics® 5.4) in which the ideal Bingham plastic fluid model is used to predict the behaviour of the fluid film. Both the yield stress and the viscosity increase as a function of the magnetic field.

2. Method

This study makes use of different journal bearing configurations as showcases to present the effect of including rheological textures in a bearing device. This work considers hydrostatic journal bearings with rheological texture, hybrid journal bearings with rheological texture and hydrodynamic journal bearings with the rheological texture in a herringbone-like v shape. Figs. 1–3 show both conventional hydrodynamic as well as hydrostatic journal bearing configurations considered in this investigation. In addition, a hydrodynamic bearing with a herringbone rheological textures is shown in Fig. 4.

For a fair comparison, the different configurations are tested against a conventional journal bearing. The lubricant in the bearing is modelled as a Bingham plastic and its flow is modelled using the Reynolds equations resulting from the standard thin film fluid flow assumptions. Tables 1 and 2 specify the different parameters used by the different bearing configurations.

The fluid film height h for all bearing configurations is described in relation (Eq. (1)). The eccentricity value e is the relative amount that the shaft is eccentric with respect to the housing. Its value is zero when the shaft is exactly in the middle and one when the shaft is touching the

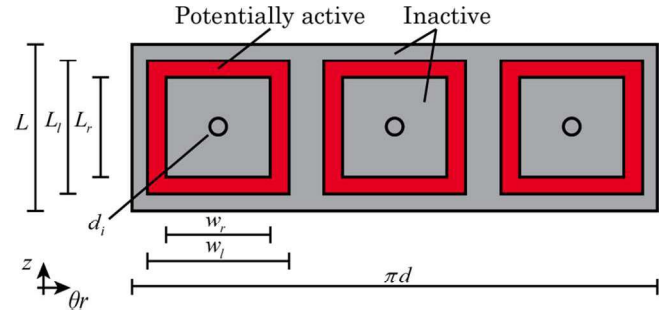


Fig. 2. Unfolded hybrid journal bearing (Fig. 1d) with rheological texture and three pads.

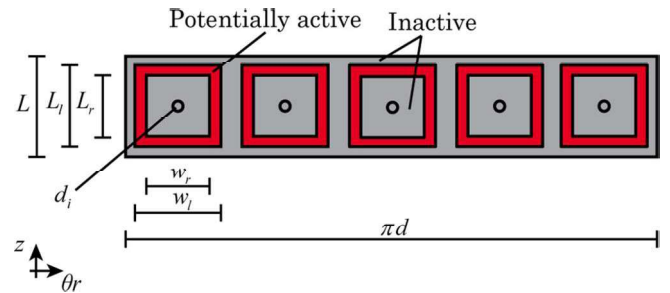


Fig. 3. Unfolded hybrid journal bearing (Fig. 1d) with rheological texture and five pads.

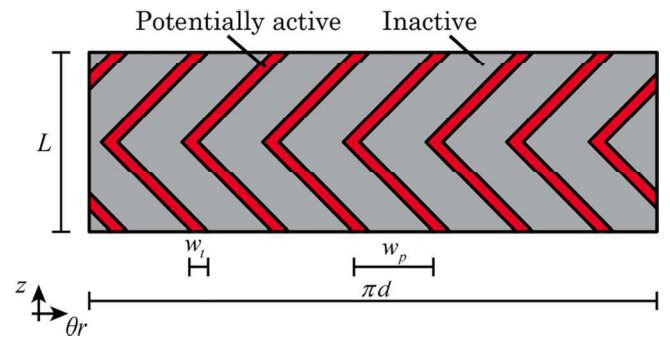


Fig. 4. Unfolded version of the hydrodynamic journal bearing with rheological textures in the shape of a herringbone.

Table 1
General model parameters used.

Variable	Symbol	Value
Bearing diameter	d	0.2[m]
Viscosity	η_g	0.05[Pa·s]
Clearance	c	$d/500$
Eccentricity	e	0.7
Speed	v	100[rpm]

Table 2
Model parameters for the bearing configurations presented in Figs. 2 and 3.

Inlet diameter	d_i	$L\Delta/n$
Land width factor	Δ	0.8
Land length	L_l	$L(1 - \Delta)$
Recess length	L_r	$L(1 - 2\Delta)$
Land width	w_l	$\pi d/n(1 - \Delta)$
Recess width	w_r	$\pi d/n(1 - 2\Delta)$
Restrictor value	R	$10^4 \text{m}^4/\text{N}^2 \text{s}$
Location of minimum film height	ϕ	$-\pi/12$

Table 3
Model parameters for the bearing configurations presented in Figs. 2 and 3.

	Non-Activated	Activated
Hydrodynamic	$p_s = 0\text{Pa}\eta_a = \eta_g\tau_0 = 0$ (Fig. 5a)	$p_s = 0\text{Pa}\eta_a = 20\eta_g\tau_0 = 500\text{Pa}$ (Fig. 5c)
Hybrid	$p_s = 10^6\text{Pa}\eta_a = \eta_g\tau_0 = 0$ (Fig. 5b)	$p_s = 10^6\text{Pa}\eta_a = 20\eta_g\tau_0 = 500\text{Pa}$ (Fig. 5d)

housing. The variable θ presents the angular coordinate in the bearing and the variable ϕ presents the angular offset where the film height has its minimum.

$$h = c(1 - \text{ecos}(\theta + \phi)) \quad (1)$$

The numerical model solves for the pressure in the lubricating film that leads to a load capacity F_r by taking the vector sum of the load capacity in x-direction F_x and y-direction F_y in relations (Eqs. (2)–(4)). The resulting load capacity is one of the output variables of the computation.

$$F_x = \iint_S p \sin(\theta) dA \quad (2)$$

$$F_y = \iint_S p \cos(\theta) dA \quad (3)$$

$$F_r = \sqrt{F_x^2 + F_y^2} \quad (4)$$

The friction force of the bearing is expressed by relation (Eq. (5)). The parameter τ_x is the amount of stress that is locally present to achieve the desired relative motion of the two surfaces. The friction coefficient f in (Eq. (6)) is calculated as the ratio between the load capacity F_r in (Eq. (4)) and the friction force of the bearing F_f in (Eq. (5)). To include the effects of cavitation, all negatives pressures are assumed to be zero.

$$F_f = \iint_S -\tau_{\theta r} - \frac{h}{2} r \frac{\partial p}{\partial \theta} dA \quad (5)$$

$$f = \frac{F_r}{F_f} \quad (6)$$

2.1. Rheological model

The Bingham plastic fluid model presented in (Eq. (7)) accommodates for a proper representation of the rheological behaviour of the magnetorheological fluid by presenting the stress in the material τ as a function of the shear rate $\dot{\gamma}$. The use of a magnetic field affects both the yield stress $\tau_0(H)$ as well as the viscosity of the fluid $\eta(H)$. The values are based on typical values from literature [29].

$$|\vec{\tau}| = \tau_0(H) + \eta(H)|\dot{\gamma}| \quad (7)$$

2.2. Thin film model

The flow in-between the two bearing surfaces is described by a mathematical model developed by the authors and published in [31]. The model derives a modified Reynolds equation that uses the exact Bingham plastic material model to simulate the thin film flow. The novelty is that in this way, there is no need for either a regularization technique [32] or an approximated thin film theory [33–35]. Since the method is not an approximation, the solution is more accurate and the simulation “running time” is considerably shortened due to the reduced degrees of freedom of the simulation.

2.3. Hybrid bearing

Figs. 2 and 3 illustrate an unfolded version of different bearing configurations to demonstrate the behaviour of a hybrid bearing with

rheological texture. The figures show three and five squares respectively over which the fluid can be activated to create a rheological texture. Note that the viscosity is increased and the limiting yield stress is active at these locations.

In practice, this effect can be associated to the application of a magnetic field that locally increases the effective viscosity of the magnetorheological fluid.

The fluid behaves as a Newtonian fluid everywhere else, that is, the yield stress of the fluid is zero since there is no magnetic field. The circles located in the middle of the bearing (Figs. 1 and 3) serve as high-pressure lubricant supply to make a hydrostatic bearing. An orifice restrictor controls the amount of lubricant supplied to the bearing. The relation presented in (Eq. (8)) represents the behaviour of the restrictor in this study. The variable R presents the restrictor value and the parameter p_r presents the recess pressure.

$$Q = R\sqrt{p_s - p_r} \quad (8)$$

The behaviour of a conventional hydrodynamic bearing is obtained when both rheological texture and supply pressure are switched off.

A conventional hybrid bearing is attained by only applying the feeding pressure without local activation of the fluid. The condition in which the fluid is locally activated and the supply pressure is not applied generates a hydrodynamic bearing with rheological texture. On the other hand, by locally activating the fluid and applying the supply pressure generates a hybrid bearing configuration with rheological texture.

Tables 1 to 3 list the values of the different parameters used to generate the results presented in this paper. These are typical values of bearings in this size category. The fluid properties are typical for magnetorheological fluids available on the market (silicon oil with ~70w% iron particles).

2.4. Herringbone

Fig. 4 presents the unfolded geometry of the herringbone journal bearing configuration which is presented here to demonstrate the effect of applying rheological texture for hydrodynamic lubrication exclusively. The figure shows seven v-shaped areas where the lubricant can be activated to create a rheological texture. Table 4 shows the parameters specific to this simulation, while Table 1 presents all other relevant parameters.

3. Results & discussion

3.1. Hybrid bearing

Fig. 5a to d illustrate the pressure distributions for the four different

Table 4
Model parameters for the herringbone bearing presented in Fig. 4.

Variable	Symbol	Value
Land width factor	Δ	0.9
Bearing length	L	d
Location of minimum film height	ϕ	0
Texture width	w_t	$L\Delta$
Texture pitch	w_p	$\pi d/7$

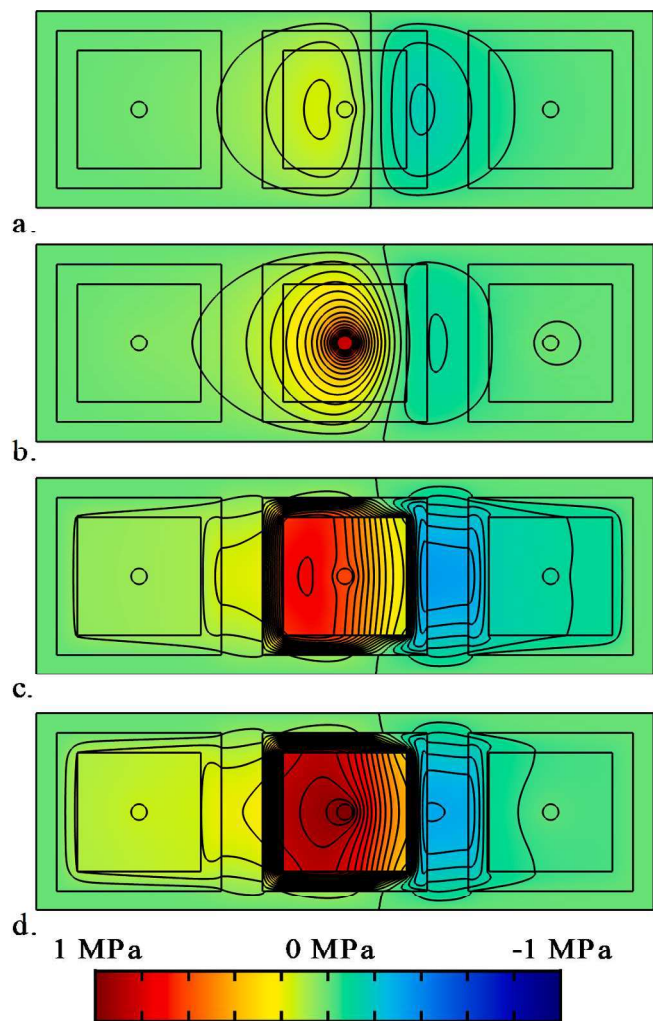


Fig. 5. a. Pressure distribution of a. conventional hydrodynamic bearing with non-activated regions b. conventional hybrid bearing with non-activated regions c. hydrodynamic bearing with activated regions d. hybrid bearing with Rheological textures.

configurations considered in this work. Note that these pressure distributions are presented on the unfolded geometries of the journal bearing configurations presented in Fig. 1. Table 3 presents the corresponding parameter values for these four different situations. Note that the results use a zero pressure reference, which means that in practice cavitation will occur when the pressure is negative. Since the focus of this work is on the resulting pressure distribution due to rheological textures, only a basic cavitation model is included that assumes all negative pressures to be equal to zero.

Fig. 5a displays the pressure distribution of a conventional journal bearing. There is a high-pressure region in the converging wedge and a low-pressure region in the diverging wedge. The central pressure supply shows a slight change in the pressure distribution due to a local change in distance between the bearing faces.

Fig. 5b shows the pressure distribution of a conventional hybrid journal bearing. A high-pressure region exists near the high-pressure supply at the converging part of the bearing. A low-pressure field exists at the diverging wedge of the bearing. Note that the pressure supply increases the both high-pressure and low-pressure fields more than is the case for the conventional hydrodynamic bearing. This causes less cavitation in the converging wedge.

Fig. 5c shows the pressure distribution of a hydrodynamic bearing with rheological texture. The figure shows a high-pressure field at the converging part of the bearing and a low-pressure field at the diverging

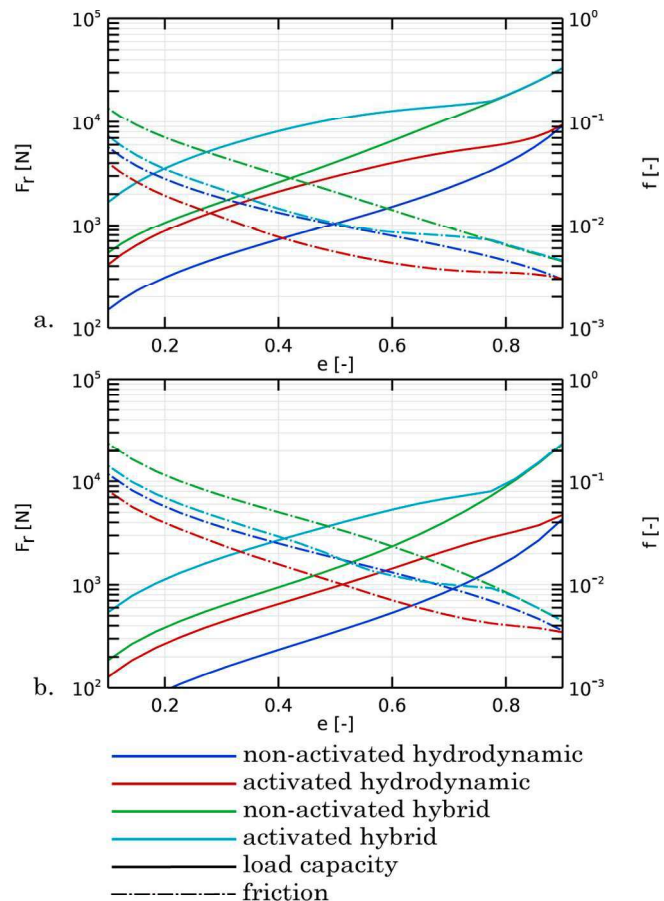


Fig. 6. a. Bearing load capacity and friction coefficient as a function of the eccentricity for the 3-pad bearing. b. Bearing load capacity and friction coefficient as a function of the eccentricity for the 5-pad bearing.

part of the bearing. By comparing this pressure distribution with the one in Fig. 5a for the conventional hydrodynamic bearing, it is clear that the rheological texture definitely affects the pressure distribution. The figure indicates first that the magnitude of the pressure is greater than that shown by the conventional hydrodynamic bearing, and secondly that the rheological texture causes a high pressure region within the activated square annulus. In addition, the area with cavitation presents now a low-pressure field located in-between the two square annuli.

Fig. 5d shows again a high-pressure field within the activated square annulus at the converging wedge. The annulus creates an even higher-pressure field due to the high-pressure supply. This behaviour is very similar to the conventional hydrostatic bearing where a high-pressure field is present in the recess of the bearing. The area within the square annulus acts as a recess area and the square annulus itself acts as a pad area of a hydrostatic bearing. Again, the area in-between the two right square annuli has a low-pressure field.

Fig. 6a and b show the load capacity and friction coefficient as a function of the eccentricity for both 3-pad and 5-pad bearing respectively. The dark blue line and the green line stand for the conventional hydrodynamic journal bearing and the hybrid journal bearing respectively. The conventional hybrid journal bearing has a higher load capacity and lower friction coefficient at low eccentricity ratios but this difference becomes smaller for large eccentricity ratios. This effect is explained by the fact that the hydrostatic effect has only a small influence at low eccentricity due to the limited supply pressure. These results are in good accordance with other studies in literature [25,31,32,36].

The green line and the cyan line represent the hydrodynamic

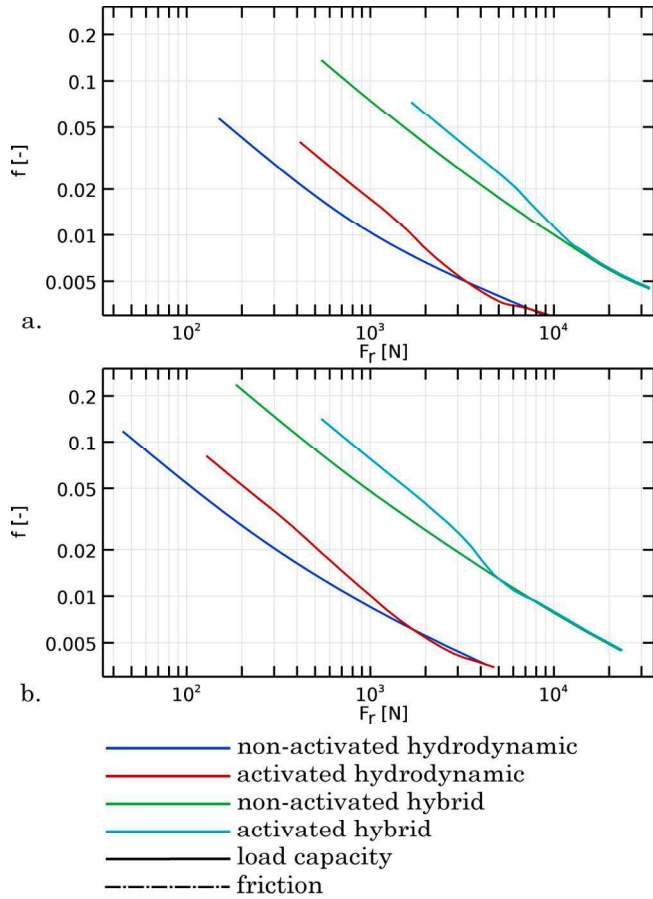


Fig. 7. Friction coefficient as a function of the load capacity for the same data as Fig. 6. Figure a presents the 3-pad bearing and figure b presents the 5-pad bearing.

journal bearing and hybrid journal bearing respectively both with rheological texture. Results show with clarity that the load capacity of the configurations with rheological texture significantly increases compared to the non-activated configurations at all eccentricity values. Also interesting to note here is that the stiffness remains roughly the same after applying the rheological texture. These results also make evident the fact that the friction coefficient generally increases when rheological texture is applied for a certain eccentricity ratio.

The results for the 3-pad bearing and 5-pad bearing are similar in shape. The load capacity and friction coefficient are higher for the 3-pad configuration than for the 5-pad configuration for a given eccentricity value. This means that making the bearing shorter does not necessarily produce a positive effect for the friction coefficient in this particular situation, although the negative effect is almost negligible.

Fig. 7a and b show the friction coefficient as a function of the load capacity by using the same set of data in Fig. 6. The figure illustrates whether a certain bearing configuration has a lower friction coefficient for a certain loading condition. Once more, it is evident that the friction coefficient generally increases when rheological texture is applied. Hybrid bearing configurations have a higher friction coefficient at low loading conditions but a slightly lower friction coefficient at high loading conditions compared to purely hydrostatic bearing configurations. The 3-pad and 5-pad bearing configuration present a similar trend.

Fig. 8a and b show the load capacity and friction coefficient as a function of the speed for the 3-pad and 5-pad configuration respectively. The green and dark blue line stand for the hydrodynamic journal bearing configurations with and without rheological texture respectively. The results demonstrate that the rheological texture causes the

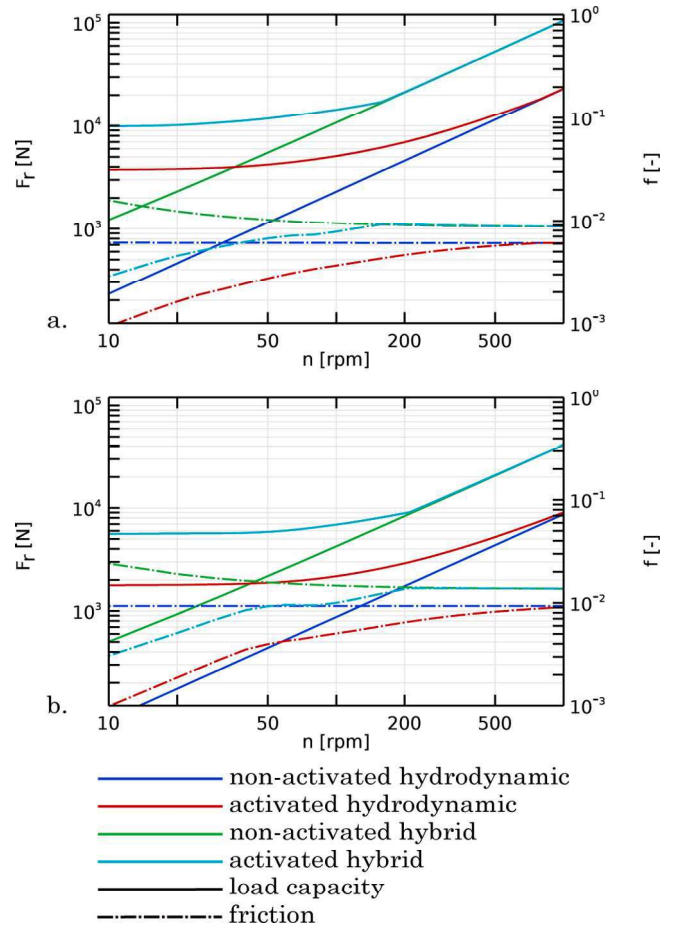


Fig. 8. Bearing load capacity and friction coefficient as a function of the speed of a. 3-pad bearing configuration and b. the 5-pad bearing configuration.

load capacity and friction coefficient to shift towards higher values. Note that the conventional hydrodynamic journal bearing exhibits a constant friction coefficient with increasing speed, while the corresponding hydrodynamic journal bearing with rheological texture shows an increase in friction coefficient at lower speeds instead. This outcome can be attributed to the behaviour of the lubricant, which is modelled as a Bingham material at the location of the rheological textures. The yield stress of the lubricant has a large effect at low speeds but only a small effect at high speeds in this specific circumstance.

The light blue and red line symbolize the hybrid journal bearing configurations with and without rheological texture respectively. Again, these results demonstrate that the rheological texture causes the load capacity as well as the friction coefficient to shift towards higher values. Hybrid bearing configurations work predominantly in hydrostatic regime at low speeds and predominantly in hydrodynamic regime at high speed, as expected.

In general, results reveal that load capacity increases significantly by applying the rheological texture for both the hydrostatic and the hydrodynamic regimes. This indicates that the method increases the specific load capacity (load per area) of the bearing. However, the price to pay for the local activation of the lubricant seems to be an increase in friction coefficient (load capacity per friction).

The hybrid journal bearing with rheological texture shows a very similar behaviour to that of a conventional hydrostatic bearing with physical texture. When the high pressure lubricant supply in this type of bearing is turned off, the presence of the physical texture causes an insufficient build-up of hydrodynamic pressure in the lubricant film, thus easily leading the two bearing surfaces into contact for already a minimal load, with unwanted side effects like wear.

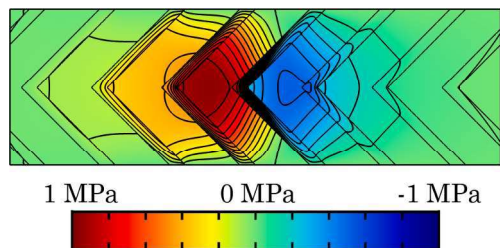


Fig. 9. Pressure profile of the herringbone bearing.

On the contrary, this condition would not cause severe damage in the hybrid bearing with rheological texture since it will just continue to operate in the hydrodynamic regime.

In the standard design of a hydrostatic bearing using geometric texture the hydrodynamic pressure build-up is compromised. Surface texture needed for a proper hydrostatic operation reduce the hydrodynamic operation. The use of rheological texture avoids this downside.

3.2. Herringbone

Fig. 9 shows the pressure distribution of the hydrodynamic bearing configuration with a rheological texture in the shape of a herringbone. As in Figs. 5,9 shows that the application of the rheological texture significantly changes the pressure distribution in the journal bearing. The texture causes the magnitude in the high-pressure field to increase and in the low-pressure side to decrease.

Fig. 10 shows both load and friction of the herringbone bearing as a function of the rotational speed. The dark blue line again represents the standard untextured hydrodynamic bearing identical to the hydrodynamic bearing configuration in Fig. 8. The green line represents the situation in which the rheological texture only has an increase in viscosity while the red line represents the situation where the rheological texture has an increase in both viscosity and yield stress. The inclusion of the yield stress causes higher load capacity as well as higher friction coefficient at low speeds but not much of a difference in case of high speeds. From this, it is assumed that the effect of the yield stress is in general negligible at higher speeds.

The cyan coloured lines represent the load capacity and friction coefficient of a purely hydrodynamic bearing with an increased viscosity compared to the situation of the standard hydrodynamic bearing. In this case, the viscosity is equal to the average viscosity of the

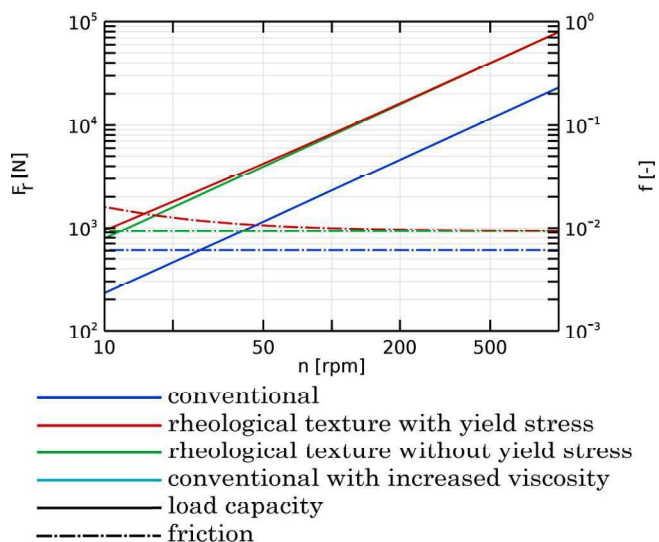


Fig. 10. Load and friction of the herringbone bearing as a function of the rotational speed. Note that the dark and light blue dash-dot line coincide.

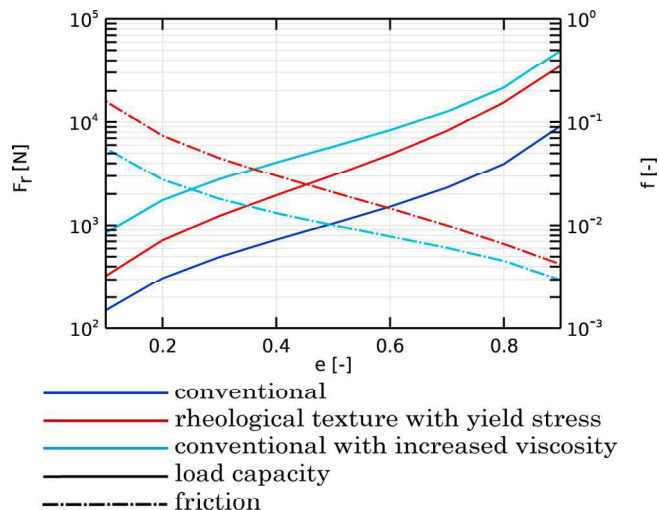


Fig. 11. Load and friction of the herringbone bearing as a function of eccentricity.

hydrodynamic bearing with no yield stress applied (green line). By averaging the viscosity, the resulting friction force of the two concepts is equal. This leads to a fair comparison between using rheological texture and increasing the viscosity in a uniform way. The results in Fig. 10 demonstrate that the rheological texture does not result in a lower friction coefficient, meaning that it does not create more load capacity per unit friction of the bearing. In other words, the use of rheological texture increases the load capacity of the bearing but not as efficiently as changing the viscosity uniformly. Note that this conclusion is only valid for this specific herringbone bearing configuration.

Fig. 11 presents the load and friction of the herringbone bearing as a function of the eccentricity. The dark blue line indicates the situation of the conventional hydrodynamic bearing, while the red line indicates the case of a hydrodynamic bearing with rheological texture (including yield stress). The cyan line represents the conventional hydrodynamic bearing configuration with a uniformly increased viscosity such that the average viscosity is equal to the average viscosity of the bearing configuration with rheological texture. The figure supports the statement that the load capacity and friction coefficient of the configuration with rheological texture scales in a similar way as the configuration without rheological texture. In addition, the assertion stating that the application of the rheological texture increases the load capacity of the bearing but not as efficiently as changing the viscosity uniformly still holds.

Fig. 12 shows the load and friction of the herringbone bearing as a function of the viscosity at the location of the rheological texture for a

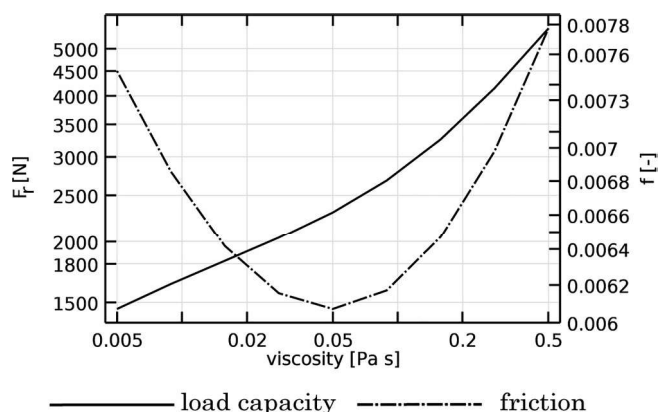


Fig. 12. Load and friction of the herringbone bearing as a function of the viscosity at the rheological textures. Note that the viscosity of the bulk is 0.05Pas.

rotational speed of 100 rpm. In this calculation, the yield stress is assumed to be zero everywhere in order to provide an easier comparison between the conventional bearing configuration and the bearing configuration with rheological texture. The results in Fig. 10 allow us to neglect the yield stress since it has only a minor effect on the load capacity and friction coefficient.

Fig. 12 shows an increase in load capacity for an increase in viscosity at the location of the rheological texture. This can be explained by the fact that the average viscosity of the lubricant within bearing gap increases. The friction force shows a minimum in friction at the point where the viscosity of the rheological texture is the same as the viscosity of the bulk. From this evidence, it seems that the use of the rheological texture in this bearing configuration always leads to an increase in friction coefficient.

Additional advantage of this concept is that the local viscous behaviour can be controlled, and thus the behaviour of the bearing can be modified during operation.

In general, the results presented in this work clearly demonstrate the power of the method to model the behaviour of a Bingham plastic in a lubricating film, as previously published by the authors in [31].

A possible and interesting next step in this research would be a shape optimization study of rheological textures that might increase the bearing performance. With the results herein presented, a fair comparison can be made between optimized rheological textures and optimized physical textures.

4. Conclusion

The work has shown that bearing performance can be enhanced by using rheological textures. This principle adds an extra parameter in the design of a bearing that can be used to boost the performance. The potential of this concept is illustrated by comparing different bearing designs. Generally, the results show an increase in specific load capacity but also an increase in friction coefficient.

A new hybrid journal bearing configuration using the rheological texture is proposed where both hydrostatic and hydrodynamic working regimes are not compromised.

Declaration of Competing Interest

The authors declare that they have no known competing financial interests or personal relationships that could have appeared to influence the work reported in this paper.

Acknowledgment

This research has been supported by the Dutch TKI maritime funding program.

Appendix A. Supplementary data

Supplementary data to this article can be found online at <https://doi.org/10.1016/j.jmmm.2019.166218>.

References

- [1] S.S. Perry, W.T. Tysoe, Frontiers of fundamental tribological research, *Tribol. Lett.* 19 (2005) 151–161, <https://doi.org/10.1007/s11249-005-6142-8>.
- [2] N.K. Myshkin, I.G. Goryacheva, Tribology: trends in the half-century development, *J. Frict. Wear.* 37 (2016) 513–516, <https://doi.org/10.3103/S106836661606009X>.
- [3] P. Jost, Lubrication (Tribology) – A report on the present position and industry's needs, 1966.
- [4] K. Holmberg, A. Erdemir, Influence of tribology on global energy consumption, costs and emissions, *Friction* 5 (2017) 263–284, <https://doi.org/10.1007/s40544-017-0183-5>.
- [5] S. Glavatskih, E. Höglund, Tribotronics-towards active tribology, *Tribol. Int.* 41 (2008) 934–939, <https://doi.org/10.1016/j.triboint.2007.03.001>.

- [6] Y. Liu, S. Niu, Z.L. Wang, Theory of tribotronics, *Adv. Electron. Mater.* 1 (2015) 1500124–1500134, <https://doi.org/10.1002/aelm.201500124>.
- [7] S.G.E. Lampaert, J.W. Spronck, R.A.J. van Ostayen, Load and stiffness of a planar ferrofluid pocket bearing, *Proc. Inst. Mech. Eng. Part J J. Eng. Tribol.* 232 (2017) 14–25, <https://doi.org/10.1177/1350650117739200>.
- [8] S.G.E. Lampaert, B.J. Fellinger, J.W. Spronck, R.A.J. van Ostayen, In-plane friction behaviour of a ferrofluid bearing, *Precis. Eng.* 54 (2018) 163–170, <https://doi.org/10.1016/j.precisioneng.2018.05.013>.
- [9] M. Holmes, D. Trumper, Magnetic/fluid-bearing stage for atomic-scale motion control (the angstrom stage), *Precis. Eng.* 18 (1996) 38–49, [https://doi.org/10.1016/0141-6359\(95\)00038-0](https://doi.org/10.1016/0141-6359(95)00038-0).
- [10] W. Ochonski, Sliding bearings lubricated with magnetic fluids, *Ind. Lubr. Tribol.* 59 (2007) 252–265, <https://doi.org/10.1108/00368790710820856>.
- [11] H. Urreta, Z. Leicht, A. Sanchez, A. Agirre, P. Kuzhir, G. Magnac, Hydrodynamic bearing lubricated with magnetic fluids, *J. Intell. Mater. Syst. Struct.* 21 (2010) 1491–1499, <https://doi.org/10.1177/1045389X09356007>.
- [12] X. Wang, H. Li, G. Meng, Rotordynamic coefficients of a controllable magnetorheological fluid lubricated floating ring bearing, *Tribol. Int.* 114 (2017) 1–14, <https://doi.org/10.1016/j.triboint.2017.04.002>.
- [13] J. Hesselbach, C. Abel-Keilhack, Active hydrostatic bearing with magnetorheological fluid, *Proc. Eighth Int. Conf. New Actuators* (2002) 343–346, <https://doi.org/10.1063/1.1555850>.
- [14] J. Hesselbach, C. Abel-Keilhack, Active hydrostatic bearing with magnetorheological fluid, *J. Appl. Phys.* 93 (2003) 8441–8443, <https://doi.org/10.1063/1.1555850>.
- [15] J.M. Guldbakke, C. Abel-Keilhack, J. Hesselbach, Magnetofluidic Bearings and Dampers J.M., in: *Colloid. Magn. Fluids Basics, Dev. Appl. Ferrofluids*, 2009.
- [16] D. Brousseau, E.F. Borra, M. Rochette, D.B. Landry, Linearization of the response of a 91-actuator magnetic liquid deformable mirror, *Opt. Express* 18 (2010) 8239–8250, <https://doi.org/10.1364/OE.18.008239>.
- [17] D.A. Bompos, P.G. Nikolakopoulos, Rotordynamic analysis of a shaft using magnetorheological and nanomagnetorheological fluid journal bearings, *Tribol. Trans.* 59 (2016) 108–118, <https://doi.org/10.1080/10402004.2015.1050137>.
- [18] D.A. Bompos, Tribological Design of Nano/Magnetorheological Fluid Journal Bearings, 2015.
- [19] D.A. Bompos, P.G. Nikolakopoulos, CFD simulation of magnetorheological fluid journal bearings, *Simul. Model. Pract. Theory.* 19 (2011) 1035–1060, <https://doi.org/10.1016/j.simpat.2011.01.001>.
- [20] N. Vaz, K.G. Binu, P. Serrao, M.P. Hemanth, J. Jacob, N. Roy, E. Dias, Experimental investigation of frictional force in a hydrodynamic journal bearing lubricated with magnetorheological fluid, *J. Mech. Eng. Autom.* 7 (2017) 131–134, <https://doi.org/10.5923/j.jmea.20170705.01>.
- [21] A. Bouzidane, M. Thomas, An electrorheological hydrostatic journal bearing for controlling rotor vibration, *Comput. Struct.* 86 (2008) 463–472, <https://doi.org/10.1016/j.compstruc.2007.02.006>.
- [22] O.-O. Christidi-Loumpasefski, I. Tzifas, P.G. Nikolakopoulos, C.A. Papadopoulos, Dynamic analysis of rotor – bearing systems lubricated with electrorheological fluids, *Proc. Inst. Mech. Eng. Part K J. Multi-Body Dyn.* (2017) 1–16, <https://doi.org/10.1177/1464419317725932>.
- [23] J.S. Basavaraja, S.C. Sharma, S.C. Jain, A study of misaligned electrorheological fluid lubricated hole-entry hybrid journal bearing, *Tribol. Int.* 43 (2010) 1059–1064, <https://doi.org/10.1016/j.triboint.2009.12.052>.
- [24] S.C. Sharma, C.B. Khatri, Electro-rheological fluid lubricated textured multi-lobe hole-entry hybrid journal bearing system, *J. Intell. Mater. Syst. Struct.* 29 (2018) 1600–1619, <https://doi.org/10.1177/1045389X17742731>.
- [25] G.W. Stachowiak, A.W. Batchelor, *Engineering Tribology*, fourth ed., Elsevier Inc., 2014.
- [26] A. Singh, S.S. Waydande, A review paper on performance analysis of hydrodynamic journal bearing with various types of lubricant for pressure distribution and cavitation, *Int. J. Adv. Eng. Res. Dev.* 4 (2017) 347–354.
- [27] L. Lentini, M. Moradi, F. Colombo, A historical review of gas lubrication: from Reynolds to active compensations, *Tribol. Ind.* 40 (2018) 165–182, <https://doi.org/10.24874/ti.2018.40.02.01>.
- [28] S.G.E. Lampaert, R.A.J. van Ostayen, Load and stiffness of a hydrostatic bearing lubricated with a bingham plastic fluid, *J. Intell. Mater. Syst. Struct.* (2019).
- [29] S.G.E. Lampaert, R.A.J. Van Ostayen, Experimental results on a hydrostatic bearing lubricated with a magnetorheological fluid, *Curr. Appl. Phys.* (2019) in review.
- [30] S.G.E. Lampaert, R.A.J. van Ostayen, Lubricated Sliding Bearing With Adjustment Of The Properties Of The Lubricant In Certain Parts Of The Bearing Gap, WO2018212657, 2018.
- [31] S.G.E. Lampaert, R.A.J. van Ostayen, A lubrication theory for bingham plastics, *Tribol. Int.* (2020) in review.
- [32] C. Dorier, J. Tichy, Behavior of a Bingham-like viscous fluid in lubrication flows, *J. Nonnewton Fluid Mech.* 45 (1992) 291–310, [https://doi.org/10.1016/0377-0257\(92\)80065-6](https://doi.org/10.1016/0377-0257(92)80065-6).
- [33] S.H.K. Wada, Hayashi, Haga, Behavior of a Bingham solid in hydrodynamic lubrication (Part 1, General Theory) *Bull. JSME.* 16 (92) (1973) 422–431.
- [34] S. Wada, H. Hayashi, K. Haga, Behavior of a Bingham solid in hydrodynamic lubrication (Part 2, Application to Step Bearing), *Bull. JSME.* 16 (1973) 432–440, <https://doi.org/10.1299/jsme1958.16.422>.
- [35] S. Wada, H. Hayashi, K. Haga, Behavior of a bingham solid in hydrodynamic lubrication (part 3, application to journal bearing), *Bull. JSME* (1974) 1182.
- [36] J.A. Tichy, Hydrodynamic lubrication theory for the Bingham plastic flow model, *J. Rheol.* 35 (4) (1991) 477–496, <https://doi.org/10.1122/1.550231>.

Lubrication Theory for Bingham Plastics

Stefan G. E. Lampaert, Ron A. J. van Ostayen

June 19, 2019

Abstract

A lot of lubricants that are used in bearing systems have a rheological behaviour that is reasonably modelled with the Bingham plastic material model. Literature presents basically three different methods to model a 2D flow behaviour of this lubricating film. The first method is to use the full 3D (Navier-)Stokes relations together with a CFD simulation to model the flow in the full 3D extend of the lubricating film. The second method is to use an approximated thin film model. The third method is to use a regularization technique that approximates the Bingham model by taking away the discontinuity. This overview demonstrates that an exact lubrication theory (no additional assumptions required to deal with non-linearity due to the yield stress) that is applicable to a 2D lubricating film does not exist yet. Therefore, this paper presents an exact lubrication theory for a Bingham plastic fluid. The theory is said to be exact in the sense that it requires no additional assumptions than the ones already used in the Generalized Reynolds Equation. Simulations on both infinite and finite journal bearings show that the results of the present method are in good accordance with literature, demonstrating the validity of the method.

1 Introduction

In many bearing systems lubricants are used of which the rheological behaviour is reasonably modelled with the Bingham plastic material model, which combines a solid behaviour at shear stress values below a critical yield stress, and with a constant viscosity flow above that yield stress. Some frequently used applications are for example the grease in roller bearings or low speed journal bearings. Some less frequent applications are for example magnetorheological and electrorheological bearing systems. The rheological properties of these fluids are a function of magnetic and electric field. This makes it possible to make an active bearing by controlling the rheological properties of the lubricant in the bearing [1, 2, 3, 4]. A proper design of these bearing systems is only possible when a proper method is used to predict the behaviour of a certain design. This has been shown to be troublesome due to the discontinuity in the Bingham plastic material model caused by the yield stress.

The work of Wada et al. [5] presents an approximated lubrication theory for Bingham plastics in 2D lubricating films. The method is said to be an approximation in the sense that it requires some additional assumptions to accommodate for the non-linearities caused by the Bingham material model. The theory was validated for the case of a step bearing by Wada et al. [6] and a journal bearing also by Wada et al. [7]. The method seems to provide a good approximation.

The method of Wada et al. was later successfully implemented by for example Christidi-Loumpasefski et al. [8] and Nikolakopoulos together with Papadopoulos [9]. In [8] the calculations are limited to situations where no plug flow occurs, significantly reducing the numerical complexity.

The work of Tichy [10] presents an exact lubrication theory for Bingham plastic fluids applicable to 1D lubricating films. This method can be said to be exact since it does not use any additional assumptions to accommodate for the non-linearities due to the yield stress. The method of Tichy [10] was later successfully implemented by for example Urreta et al. [11] and Forte et al. [12].

The work of Dorier and Tichy [13] presents a regularization strategy for lubrication theory for Bingham plastics applicable to 2D lubricating films. The method approximates the Bingham plastic model by using a model that is similar to the Bingham-Papanastasiou model [14]. This approximation converges to the conventional Bingham model for an increasing value of a regularization parameter but gets more computational demanding when it does so. The method has the added benefit that it removes the necessity of tracking the location of the plug in the film as is the case in the work of Tichy [10] and Wada et al. [5].

The method of Dorier and Tichy [13] was later successfully implemented by for example Sharma and Khatri [15], Jang and Khonsari [16] and Khlifi et al. [17].

The work of Gertzos et al. [18] presents a CFD method to model the behaviour of a Bingham Plastic in a lubricating film. It uses the Bingham-Papanastasiou model to approximate the Bingham behaviour while still maintaining a continuous material. The method of Gertzos et al. [18] was later successfully implemented by Peng and Zhu [19, 20]. The authors furthermore extend the method with a cavitation algorithm and a varying yield stress over the lubricating film.

The work of Bompos et al. [21, 22] and Kim et al. [23] demonstrates the use of a bi-viscous material model implemented in a CFD model to mimic the behaviour of the Bingham plastic material in a lubricating film. This model uses a relatively high viscosity to model the solid phase behaviour and a relatively low viscosity to model the fluid phase behaviour.

Literature demonstrates that there are basically three methods to model a 2D lubricating film. The first method is to use the full 3D (Navier-)Stokes relations together with a CFD simulation to model the flow in the full 3D extend of the lubricating film. The second method is to use the approximated thin film model presented by Wada et al. [5]. The third method is to use the regularization technique used by Dorier and Tichy [13]. An additional fourth method exists when modelling only a 1D lubricating film. The work of Tichy [10] presents an exact lubrication theory that is applicable to a 1D lubricating film. This overview demonstrates that an exact lubrication theory (no additional assumptions required to deal with non-linearity due to the yield stress) that is applicable to a 2D lubricating film does not exist yet.

Therefore, this paper presents an exact lubrication theory for a Bingham plastic fluid. The theory is said to be exact in the sense that it requires no additional assumptions than the ones already used in the Generalized Reynolds Equation [24]. The method is tested against other results presented in literature. Simulations on both infinite and finite journal bearings are performed.

2 Method

The method consists of two parts. The first part derives the lubrication theory for a Bingham Plastic. The second part discusses the numerical method used to solve the set of equations derived in the first part. Data from literature (Wada et al. [7], Tichy [10] and Gertzos et al. [18]) is used to compare the modelling results of both finite and infinite journal bearings. The data is gathered from these sources with the use of a data extraction utility [25].

2.1 Lubrication theory for Bingham plastics

2.1.1 Bingham material model

A Bingham plastic is a material model where the material behaves as a solid when the shear stress in the material $|\vec{\tau}|$ is below a given yield stress τ_0 and where the material shows viscous flow when the stress in the material is above that yield stress. Relation (1) describes this behaviour of the material with η describing the viscosity and $\dot{\gamma}$ the shear rate.

$$|\vec{\tau}| = \tau_0 + \eta|\dot{\gamma}| \quad (1)$$

Relation (2) describes the shear rate that occurs in response to an applied shear stress. The relation demonstrates that the material is solid below the yield stress and that the material flows above the yield stress.

$$|\dot{\gamma}| = \begin{cases} \frac{|\vec{\tau}| - \tau_0}{\eta} & \text{if } |\vec{\tau}| > \tau_0 \\ 0 & \text{if } |\vec{\tau}| \leq \tau_0 \end{cases} \quad (2)$$

For convenience later on in the derivation, at this stage we derive relation (3) that projects the shear rate in the proper direction with the use of a flow factor f . Relation (4) describes this flow factor which for all values of the shear stress and yield stress has a value between 0 and 1.

$$\vec{\dot{\gamma}} = f \frac{\vec{\tau}}{\eta} \quad (3)$$

$$f = \begin{cases} \frac{|\vec{\tau}| - \tau_0}{|\vec{\tau}|} & \text{if } |\vec{\tau}| \geq \tau_0 \\ 0 & \text{if } |\vec{\tau}| < \tau_0 \end{cases} \quad (4)$$

2.1.2 Stress distribution

The theory considers only lubricating films, and therefore only considers low Reynolds number flows where the film height is small compared to the film width and length. The Cauchy momentum equation is thus reduced to the form presented in relation (5), where p stands for the local film pressure and z presents the z -coordinate in the film (see also figure 1).

$$\frac{\partial \vec{\tau}}{\partial z} = \nabla p \quad (5)$$

Integrating relation (5) over the film height results in relation (6) that describes the stress in function of the film height and the stress $\vec{\tau}_c$ at $z = 0$. Figure 1 presents a graphical representation of this stress distribution in the x -direction.

$$\vec{\tau} = z \nabla p + \vec{\tau}_c \quad (6)$$

The magnitude of the shear stress vector is given by (7). Figure 2 presents a graphical representation of the shear stress magnitude $|\vec{\tau}|$. The blue part of the graph presents the amount of stress that causes flow since it is this is the only part above the yield stress. The green part presents the part of the shear stress that does not cause flow since it is below the yield stress. The red part presents the amount of additional shear stress that is required in order to cause flow.

$$|\vec{\tau}|^2 = z^2 |\nabla p|^2 + 2z \nabla p \cdot \vec{\tau}_c + |\vec{\tau}_c|^2 \quad (7)$$

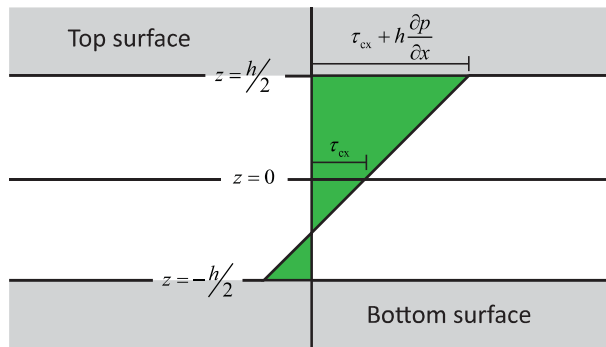


Figure 1: Stress components in x-direction

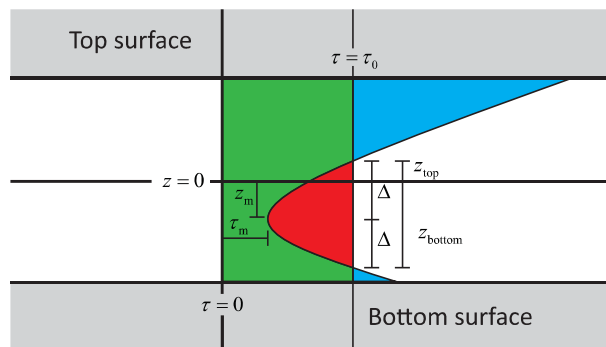


Figure 2: Magnitude of stress

2.1.3 Plug analysis

In-between the two surfaces, depending on the shear stress distribution, part of the material behaves as a solid and part as a fluid. Due to the nature of the shear stress distribution there are two possible transition points (z_{bottom} and z_{top}) where the lubricant changes from solid to fluid. The lubricant behaves as a solid in-between these two transition points and as a fluid outside these two transition points. In order to locate these points, first the z -coordinate of the minimum shear stress z_m and the corresponding minimum stress value τ_m are derived from (7) and presented in respectively relation (8) and (9).

$$z_m = -\frac{\nabla p \cdot \vec{e}_a}{|\nabla p|^2} \quad (8)$$

$$|\vec{\tau}_m|^2 = |\vec{\tau}_c|^2 - \frac{(\nabla p \cdot \vec{e}_c)^2}{|\nabla p|^2} \quad (9)$$

Rewriting relation (7) with the use of relation (8) and (9) leads to relation (10).

$$|\vec{\tau}|^2 = |\vec{\tau}_m|^2 + (z - z_m)^2 |\nabla p|^2 \quad (10)$$

Solving relation (10) for z when the stress is equal to the yield stress τ_0 , leads to relation (11). The parameter Δ presents the distance from the point of minimum stress z_m to the point where the stress is equal to the yield stress, see figure 2 for a graphical representation of this.

$$\Delta = |z - z_m| = \begin{cases} \left(\frac{\tau_0^2 - |\vec{\tau}_m|^2}{|\nabla \rho|^2} \right)^{\frac{1}{2}} & \text{if } |\vec{\tau}_m| < \tau_0 \\ 0 & \text{if } |\vec{\tau}_m| \geq \tau_0 \end{cases} \quad (11)$$

Relation (11) now finally leads to a relation of the two transition points z_{bottom} and z_{top} respectively presented by relation (12) and (13). The locations of these transition points describe the topology of the flow. The following situations are possible:

- Both values have the same value: No plug appears,
- Both values have different values and are inside the film: A plug is floating in-between the two surfaces,
- Both values have different values and one of the values is inside the film: A plug is present and sticking to one of the surfaces,
- Both values are outside and on the same of the film: No plug appears,
- Both values are outside the film and on different sides of the film: The material is completely solid in-between the two surfaces.

$$z_{\text{bottom}} = \min \left(\left\{ \frac{h}{2}, \max \left(\left\{ -\frac{h}{2}, z_m - \Delta \right\} \right) \right\} \right) \quad (12)$$

$$z_{\text{top}} = \min \left(\left\{ \frac{h}{2}, \max \left(\left\{ -\frac{h}{2}, z_m + \Delta \right\} \right) \right\} \right) \quad (13)$$

The max function in relation (12) and (13) makes sure that the value is not smaller than $-\frac{h}{2}$ and the min function makes sure that the value is not larger than $\frac{h}{2}$.

2.1.4 Flow field

Relation (14) describes the lubricant velocity across the film height by integrating relation (3) over the height of the channel. Figure 3 gives a graphical representation of a typical fluid profile. The green and blue parts represent respectively the lubricant above and below the plug that behave as a fluid. The red part represents the plug that behaves as a solid.

$$\vec{u} = \int_{-h/2}^z \frac{f}{\eta} \vec{\tau} dz + \vec{u}_a = \frac{1}{\eta} \int_{-h/2}^z f z dz \nabla \rho + \frac{1}{\eta} \int_{-h/2}^z f dz \vec{\tau}_c + \vec{u}_a \quad (14)$$

For convenience we define the flow factor integrals (15) such that the velocity difference between the two surfaces is described with relation (16)

$$F_n = \int_{-h/2}^{h/2} f z^n dz \quad (15)$$

$$\vec{u}_b - \vec{u}_a = \frac{F_1}{\eta} \nabla \rho + \frac{F_0}{\eta} \vec{\tau}_a \quad (16)$$

Now relation (17) describes the stress at $z = 0$.

$$\vec{\tau}_c = \eta \frac{\vec{u}_b - \vec{u}_a}{F_0} - \frac{F_1}{F_0} \nabla \rho \quad (17)$$

Substituting relation (17) into relation (14) results in relation (18) that describes the flow velocity over the height over the channel in function of the surface velocities.

$$\begin{aligned} \vec{u} &= \frac{1}{\eta} \int_{-h/2}^z f \vec{\tau} dz + \vec{u}_a = \frac{1}{\eta} \int_{-h/2}^z f z dz \nabla p + \frac{1}{\eta} \int_{-h/2}^z f dz \left(\frac{\vec{u}_b - \vec{u}_a}{F_0} \eta - \frac{F_1}{F_0} \nabla p \right) + \vec{u}_a \\ &= \frac{1}{\eta} \nabla p \int_{-h/2}^z f \left(z - \frac{F_1}{F_0} \right) dz + \vec{u}_a \left(1 - \frac{1}{F_0} \int_{-h/2}^z f dz \right) + \vec{u}_b \frac{1}{F_0} \int_{-h/2}^z f dz \quad (18) \end{aligned}$$

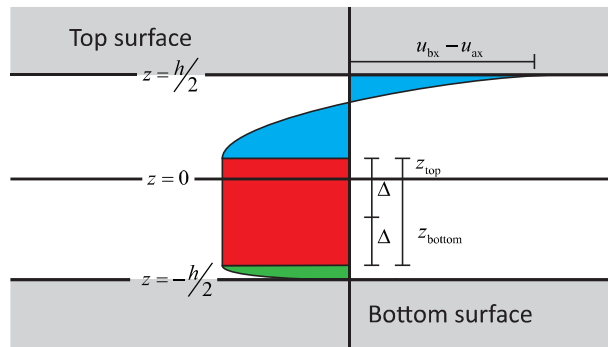


Figure 3: Velocity of the lubricant in x-direction

2.1.5 Flow rate

Integrating relation (14) across the height of the channel results in relation (19) that describes the flow rate through the system.

$$\vec{q} = \int_{-h/2}^{h/2} \vec{u} dz = \frac{1}{\eta} \nabla p \int_{-h/2}^{h/2} \int_{-h/2}^z f z dz dz + \frac{1}{\eta} \vec{\tau}_c \int_{-h/2}^{h/2} \int_{-h/2}^z f dz dz + \int_{-h/2}^{h/2} \vec{u}_a dz \quad (19)$$

Relation (20) uses integration by parts to simplify relation (19).

$$\begin{aligned} \vec{q} &= \frac{1}{\eta} \nabla p \left[\left[z \int_{-h/2}^z f z dz \right]_{-h/2}^{h/2} - \int_{-h/2}^{h/2} f z^2 dz \right] + \frac{1}{\eta} \vec{\tau}_c \left[\left[z \int_{-h/2}^z f dz \right]_{-h/2}^{h/2} - \int_{-h/2}^{h/2} f z dz \right] + \vec{u}_a h \\ &= -\frac{1}{\eta} \nabla p \left(F_2 - \frac{h F_1}{2} \right) + \frac{1}{\eta} \vec{\tau}_c \left(\frac{h F_0}{2} - F_1 \right) + \vec{u}_a h \quad (20) \end{aligned}$$

Relation (21) presents an alternative form of relation (20) by substituting relation (17) into relation (20).

$$\begin{aligned} \vec{q} &= -\frac{1}{\eta} \nabla p \left(F_2 - \frac{h F_1}{2} \right) + \frac{1}{\eta} \left(\eta \frac{\vec{u}_b - \vec{u}_a}{F_0} - \frac{F_1}{F_0} \nabla p \right) \left(\frac{h F_0}{2} - F_1 \right) + \vec{u}_a h \\ &= -\frac{1}{\eta} \nabla p \left(F_2 - \frac{h F_1}{2} \right) + \frac{1}{\eta} \left(\eta h \frac{\vec{u}_b - \vec{u}_a}{2} - \eta \frac{\vec{u}_b - \vec{u}_a}{F_0} F_1 - \frac{F_1}{2} \nabla p + \frac{F_1^2}{F_0} \nabla p \right) + \vec{u}_a h \\ &= -\frac{1}{\eta} \left(F_2 - \frac{F_1^2}{F_0} \right) \nabla p + \left(\frac{h}{2} + \frac{F_1}{F_0} \right) \vec{u}_a + \left(\frac{h}{2} - \frac{F_1}{F_0} \right) \vec{u}_b \quad (21) \end{aligned}$$

Both relation (20) and (21) describe the flow rate through the system and can as such be used to solve for the one remaining unknown, the film pressure p , using conservation of mass. However, this does require a solution for the flow factor integrals F_n which is described in the next section.

2.1.6 Flow factor integrals

Goal of this section is to get rid of the integral in the flow factor integrals F_n defined in relation (15). Eliminating these integrals removes the necessity to do a numerical integration step as is needed in the regularization method used by Tichy [10]. To achieve this, relation (15) is first rewritten to relation (22).

$$F_n = \int_{-h/2}^{h/2} f z^n dz = \int_{-h/2}^{h/2} \frac{|\vec{r}| - \tau_0}{|\vec{r}|} z^n dz = \int_{-h/2}^{h/2} z^n dz - \tau_0 \int_{-h/2}^{h/2} \frac{1}{|\vec{r}|} z^n dz \quad (22)$$

Note that relation (22) only applies at the location where there is no plug and thus (23):

$$\begin{aligned} F_n &= \int_{-h/2}^{z_{\text{bottom}}} z^n dz + \int_{z_{\text{top}}}^{h/2} z^n dz - \tau_0 \left(\int_{-h/2}^{z_{\text{bottom}}} \frac{1}{|\vec{r}|} z^n dz + \int_{z_{\text{top}}}^{h/2} \frac{1}{|\vec{r}|} z^n dz \right) \\ &= [\mathcal{F}_n(-\frac{h}{2}, z_{\text{bottom}}) + \mathcal{F}_n(z_{\text{top}}, \frac{h}{2})] - \tau_0 [\mathcal{G}_n(-\frac{h}{2}, z_{\text{bottom}}) + \mathcal{G}_n(z_{\text{top}}, \frac{h}{2})] \end{aligned} \quad (23)$$

where:

$$\mathcal{F}_n(a, b) = \int_a^b z^n dz = \frac{b^{n+1} - a^{n+1}}{n+1} \quad (24)$$

and:

$$\mathcal{G}_n(a, b) = \int_a^b \frac{z^n dz}{|\vec{r}|} = \int_a^b \frac{z^n dz}{\sqrt{|\vec{r}_m|^2 + (z - z_m)^2 |\nabla p|^2}} = \int_{a-z_m}^{b-z_m} \frac{(Z + z_m)^n dZ}{\sqrt{|\vec{r}_m|^2 + Z^2 |\nabla p|^2}} \quad (25)$$

or, after introducing the notation short-cuts:

$$A = a - z_m, \quad B = b - z_m, \quad a = |\vec{r}_m|, \quad b = z_m, \quad c = |\nabla p| \quad (26)$$

this integral is equal to:

$$\int_A^B \frac{(Z + b)^n}{\sqrt{a^2 + (cZ)^2}} dZ = \sum_{k=0}^n \binom{n}{k} b^{n-k} \int_A^B \frac{Z^k}{\sqrt{a^2 + (cZ)^2}} dZ = \sum_{k=0}^n \binom{n}{k} b^{n-k} H_k \quad (27)$$

where the integrals can be determined analytically:

$$H_0 = \frac{1}{c} \left(\operatorname{arsinh} \left(\frac{cB}{a} \right) - \operatorname{arsinh} \left(\frac{cA}{a} \right) \right) \quad (28)$$

$$H_1 = \frac{1}{c^2} \left(\sqrt{a^2 + (cB)^2} - \sqrt{a^2 + (cA)^2} \right) \quad (29)$$

$$H_2 = \frac{1}{2c^2} \left(B\sqrt{a^2 + (cB)^2} - A\sqrt{a^2 + (cA)^2} - a^2 H_0 \right) \quad (30)$$

2.2 Numerical model

The system of differential equations that describe the behaviour of a Bingham plastic in a lubrication film are solved using the commercial package COMSOL Multiphysics[®] 5.4.

The lubricating film in a journal bearing with one axial supply line is considered. The supply line is located at the top of the bearing with a supply pressure equal to ambient pressure. The film

is cut open at the top and folded open to obtain a 2D model. The height of the film is described by relation (31) where c is radial clearance, e the eccentricity and θ the radial bearing position. The pressure is constrained at all four sides to zero by using a Dirichlet boundary condition.

$$h = c(1 + e \cos \theta) \quad (31)$$

The model uses a triangular mesh with a maximum element size of 5% of the bearing length. The elements use a Lagrange shape function and are of a quadratic order for the PDE and of a quartic order for the weak contribution.

Two solver strategies are tested within this work:

Strategy A uses relation (20) to solve the system as a partial differential equation for the pressure p while implementing relation (16) as a weak contribution to force the correct surface velocities.

Strategy B uses relation (21) to solve the system as a partial differential equation for the pressure p . The values of F_0 , F_1 and F_2 are updated every iteration based on the current pressure distribution. The processes can be summarized with the following solver sequence:

0. Initial guess: $F_0 = h$, $F_1 = 0$, $F_2 = h^2/12$
1. Calculate p
2. Calculate F_0 , F_1 , F_2
3. Back to [1.], iterate, until convergence criteria are met

Both solver strategies use a parametric solver to guarantee convergence of the non-linear system. The solver starts with a zero yield stress and iterates towards the desired yield stress. The step size is generated automatically by the software package. The solver is assumed converged when a relative tolerance smaller than $1e-6$ is achieved. Computation is performed on a Intel Xeon CPU E5-1620 V3 @ 3.50 GHz with 32GB of Ram.

3 Results

Figure 4 show the normalized pressure distribution $p^* = \frac{h_0^2 p}{\eta u L}$ in a finite journal bearing for a Newtonian fluid for different eccentricities e . The figure shows both the results published by Wada et al. [7], Gertzos et al. [18] and the present work. Figure 5 show the pressure distribution in a infinite journal bearing both for a Newtonian fluid and for a Bingham plastic fluid, where the normalized yield stress is given by relation $T_0 = \frac{\tau_0 c}{u \eta}$. The figure shows the results of Tichy [10] compared to the current study.

Figure 6 and 7 present the pressure distribution in a finite journal bearing lubricated with a Bingham plastic for different values of T_0 and different bearing eccentricities. The figure shows both the work published by Wada et al. [7], Gertzos et al. [18] and the present work of this paper.

Figure 8 and figure 9 present the plug configuration derived with the method presented in this paper for a normalized yield stress of $T_0 = 0.8$ and an eccentricity of $e = 0.9$. The green surface presents the locations where there is no plug present, the height of the plug represents the value of z_m . The blue and red surfaces present respectively the bottom (z_{bottom}) and top (z_{top}) of the plug.

The models typically solve within a minute for one bearing configuration. The solution process tends to be relatively slow for large plug configurations and relatively quick for no or small plug configurations. No significant difference between method A and method B concerning speed or accuracy were found during this research.

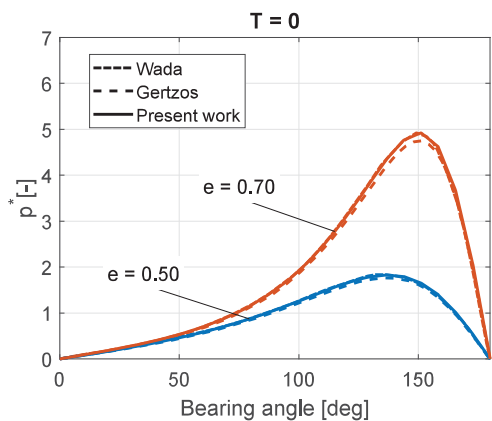


Figure 4: Pressure distribution for a Newtonian fluid in a finite journal bearing

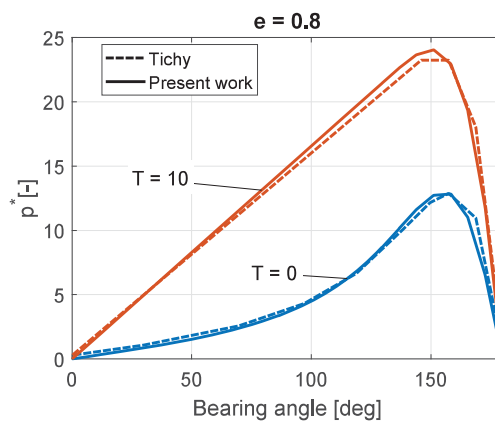


Figure 5: Pressure distribution in an infinite journal bearing for a Newtonian fluid and a Bingham plastic fluid

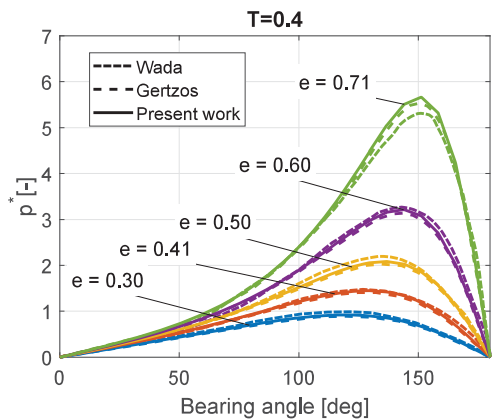


Figure 6: Pressure distribution for a finite journal bearing for the case $T_0 = 0.4$

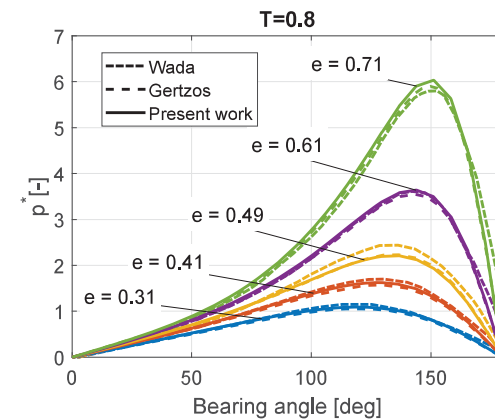


Figure 7: Pressure distribution for a finite journal bearing for the case $T_0 = 0.8$

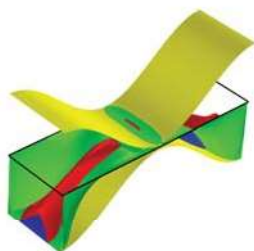


Figure 8: Plug configuration

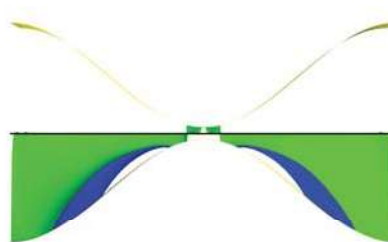


Figure 9: Plug configuration side view

4 Discussion

Figure 4 shows that the method of Wada et al. [5] corresponds exactly with the method presented in this work. This good fit is expected since the two methods use exactly the same assumptions for modelling the Newtonian condition; the two methods are fundamentally the same. The figure shows furthermore a slight offset between the method of Gertzos et al. [18] and the method presented in this paper. This might be explained by the fact that a full 3D CFD simulation is compared with a 2D thin film approximation.

Figure 5 shows that the method of Tichy [10] is in good accordance with the method presented in this paper. Extracting the data from the original journal paper most probably caused the slight offset between the two lines. It must be noted here that this analysis is only an infinite journal bearing analysis. This means that the shape of the fluid profile is more basic and there is no cross-coupling between the flow in x - and y - direction.

Figure 6 and 7 show a fair fit between the methods of Wada et al. [7], Gertzos et al. [18] and the one presented in this paper. The slight offset between the CFD analyses of Gertzos et al. [18] and the present method is also there for the Bingham plastic fluid. Interesting to note is that the pressure profile obtained using the present method always seems to exceed the pressure profile compared to [18].

The difference is again most probably caused by the nature of the simulation, one is full turbulent 3D CFD while the other is a laminar thin film approximation.

The perfect fit between the method of Wada et al. [7] and the one introduced in this paper is not there any more for a Bingham plastic fluid. This is most probably due to the extra assumptions made during the derivation of the method of Wada et al. [7]; the two methods are therefore not fundamentally the same any more. Since the method in the present work uses less assumptions, it might be considered more accurate. All three lines are in good accordance with the measurements performed in the work of Wada et al. [7].

Figure 8 and 9 demonstrate that the resulting pressure field and plug configuration have a smooth and symmetrical solution. Note that cavitation is not included in this model.

The speed of the present method is expected to be comparable to that of the method published by Wada et al. [5], both methods are of a similar form and most probably require a similar solver strategy. The present method is expected to be substantially faster than the method of Dorier and Tichy [13] since it does not require an numerical integration step in the solver sequence to get the proper viscous behaviour. The present method is also expected to be significantly faster than the method of Gertzos et al. [18] as this is a full 3D turbulent CFD calculation whereas the method proposed in this paper uses a thin film assumption and obtains a solution for a laminar pressure distribution in 2D, resulting in a huge reduction in degrees of freedom.

5 Conclusion

This paper presents an efficient numerical simulation method to describe the pressure in a lubrication film for Bingham plastic fluids. The derivation uses the 'exact' Bingham plastic fluid rheology model in combination with only the assumptions already required for the general Reynolds Equation. Therefore this makes the method accurate since it does not require to approximate the Bingham model or to use a regularization method. Also, the method is computationally highly efficient since no regularization technique is needed. Comparing the results with results found in literature demonstrates that all results are in good agreement.

References

- [1] Nathaniel Moles. *Actively controllabe hydrodynamic journal bearing design using magnetorheological fluids*. PhD thesis, The University of Akron, 2015. URL <http://ebooks.cambridge.org/ref/id/CB09781107415324A009>.
- [2] Xiaohu Wang, Hongguang Li, and Guang Meng. Rotordynamic coefficients of a controllable magnetorheological fluid lubricated floating ring bearing. *Tribology International*, 114(April):1–14, 2017. ISSN 0301679X. doi: 10.1016/j.triboint.2017.04.002. URL <http://dx.doi.org/10.1016/j.triboint.2017.04.002>.
- [3] Neil Vaz, K G Binu, Pruthivi Serrao, M P Hemanth, Jeffin Jacob, Nirmal Roy, and Eric Dias. Experimental Investigation of Frictional Force in a Hydrodynamic Journal Bearing Lubricated with Magnetorheological Fluid. *Journal of Mechanical Engineering and Automation*, 7(5):131–134, 2017. doi: 10.5923/j.jmea.20170705.01.
- [4] Stefan G.E. Lampaert and Ron A.J. van Ostayen. Load and Stiffness of a Hydrostatic Bearing Lubricated with a Bingham Plastic Fluid. *Journal of Intelligent Material Systems and Structures*, 2019.
- [5] Sanae Wada, Hirotsugu Hayahsi, and Kenji Haga. Behavior of a Bingham solid in hydrodynamic lubrication (Part 2, Application to Step Bearing). *Bulletin of the JSME*, 16(92):432–440, 1973. doi: <https://doi.org/10.1299/jsme1958.16.422>.
- [6] Sanae Wada, H Hayashi, and K Haga. Behavior of a Bingham solid in hydrodynamic lubrication (Part 1, General Theory). *Bulletin of the JSME*, 16(92):422–431, 1973. URL <http://www.hindawi.com/journals/ijrm/2004/546845/abs/%5Cnhttp://scholar.google.com/scholar?hl->
- [7] Sanae Wada, Hirotsugu Hayahsi, and Kenji Haga. Behavior of a Bingham Solid in Hydrodynamic Lubrication (Part 3, Application to Journal Bearing). *Bulletin of the JSME*, (September): 1182, 1974.
- [8] Olga-Orsalia Christidi-Loumpasefski, Ioannis Tzifas, Pantelis G Nikolakopoulos, and Chris A Papadopoulos. Dynamic analysis of rotor – bearing systems lubricated with electrorheological fluids. *Proceedings of the Institution of Mechanical Engineers, Part K: Journal of Multi-body Dynamics*, 0(0):1–16, 2017. doi: <https://doi.org/10.1177/1464419317725932>.
- [9] P.G. Nikolakopoulos and C.a. Papadopoulos. Controllable Misaligned Journal Bearings, Lubricated with Smart Fluids. *Journal of Intelligent Material Systems and Structures*, 8(2):125–137, 1997. doi: <https://doi.org/10.1177/1045389X9700800203>.
- [10] John a. Tichy. Hydrodynamic lubrication theory for the Bingham plastic flow model. *Journal of Rheology*, 35(4):477, 1991. ISSN 01486055. doi: 10.1122/1.550231. URL <http://sor.scitation.org/doi/10.1122/1.550231>.
- [11] H. Urreta, Z. Leicht, A. Sanchez, A. Agirre, P. Kuzhir, and G. Magnac. Hydrodynamic Bearing Lubricated with Magnetic Fluids. *Journal of Intelligent Material Systems and Structures*, 21(15):1491–1499, 2010. ISSN 1045-389X. doi: 10.1177/1045389X09356007. URL <http://jim.sagepub.com/cgi/doi/10.1177/1045389X09356007>.
- [12] P. Forte, M. Paternò, and E. Rustighi. A magnetorheological fluid damper for rotor applications. *International Journal of Rotating Machinery*, 10(3): 175–182, 2004. ISSN 1023-621X. doi: 10.1080/10236210490426253. URL <http://dx.doi.org/doi:10.1155/S1023621X04000181>.

- [13] Christopher Dorier and John Tichy. Behavior of a bingham-like viscous fluid in lubrication flows. *Journal of Non-Newtonian Fluid Mechanics*, 45(3):291–310, 1992. ISSN 03770257. doi: 10.1016/0377-0257(92)80065-6.
- [14] Tasos C. Papanastasiou. Flows of Materials with Yield. *Journal of Rheology*, 31(5):385–404, 1987. ISSN 0148-6055. doi: 10.1122/1.549926. URL <http://sor.scitation.org/doi/10.1122/1.549926>.
- [15] Satish C. Sharma and Chandra B. Khatri. Electro-rheological fluid lubricated textured multi-lobe hole-entry hybrid journal bearing system. *Journal of Intelligent Material Systems and Structures*, 29(8):1600–1619, 2018. ISSN 15308138. doi: 10.1177/1045389X17742731.
- [16] J Y Jang and M M Khonsari. Performance Analysis of Grease- Lubricated Journal Bearings. 119(October), 1997.
- [17] M. El Khlifi, D. Souchet, M. Hajjam, and F. Bouyahia. Numerical Modeling of Non-Newtonian Fluids in Slider Bearings and Channel Thermohydrodynamic Flow. *Journal of Tribology*, 129(3):695, 2007. ISSN 07424787. doi: 10.1115/1.2736732.
- [18] K. P. Gertzog, P. G. Nikolakopoulos, and C. A. Papadopoulos. CFD analysis of journal bearing hydrodynamic lubrication by Bingham lubricant. *Tribology International*, 41(12):1190–1204, 2008. ISSN 0301679X. doi: 10.1016/j.triboint.2008.03.002.
- [19] J Peng and KQ Zhu. Hydrodynamic characteristics of ER journal bearings with external electric field imposed on the contractive part. *Journal of Intelligent Material Systems and Structures*, 16(June):493–499, 2005. ISSN 1045-389X. doi: 10.1177/1045389X05052312. URL <http://jim.sagepub.com/content/16/6/493.short>.
- [20] Jie Peng and Ke Qin Zhu. Effects of electric field on hydrodynamic characteristics of finite-length ER journal bearings. *Tribology International*, 39(6):533–540, 2006. ISSN 0301679X. doi: 10.1016/j.triboint.2005.03.017.
- [21] Dimitrios A. Bompos and Pantelis G. Nikolakopoulos. CFD simulation of magnetorheological fluid journal bearings. *Simulation Modelling Practice and Theory*, 19(4):1035–1060, 2011. ISSN 1569190X. doi: 10.1016/j.simpat.2011.01.001. URL <http://dx.doi.org/10.1016/j.simpat.2011.01.001>.
- [22] Dimitrios A. Bompos and Pantelis G. Nikolakopoulos. Rotordynamic Analysis of a Shaft Using Magnetorheological and Nanomagnetorheological Fluid Journal Bearings. *Tribology Transactions*, 59(1):108–118, 2016. ISSN 1547397X. doi: 10.1080/10402004.2015.1050137. URL <http://dx.doi.org/10.1080/10402004.2015.1050137>.
- [23] Pilkee Kim, Jeong In Lee, and Jongwon Seok. Analysis of a viscoplastic flow with field-dependent yield stress and wall slip boundary conditions for a magnetorheological (MR) fluid. *Journal of Non-Newtonian Fluid Mechanics*, 204:72–86, 2014. ISSN 03770257. doi: 10.1016/j.jnnfm.2013.12.005. URL <http://dx.doi.org/10.1016/j.jnnfm.2013.12.005>.
- [24] D. Dowson. A generalized Reynolds equation for fluid-film lubrication. *International Journal of Mechanical Sciences*, 4(2):159–170, 1962. ISSN 00207403. doi: 10.1016/S0020-7403(62)80038-1.
- [25] Webplotdigitizer. URL <https://automeris.io/WebPlotDigitizer/>.

A self-healing hydrodynamic thrust bearing using a magnetorheological fluid

M.C. de Graaf, R.A.J. van Ostayen, S.G.E. Lampaert

Delft University of Technology, Mekelweg 2, 2628 CD Delft, the Netherlands

Abstract

Fluid bearings do have several disadvantages which have to be overcome. Some fluid bearings require an external pump which is sensitive to failure, others have fixed surface textures which are sensitive to wear, especially during starting and stopping. By applying a magnetic field the viscosity of a magnetorheological (MR) fluid can be altered, up to the point it becoming a solid. Using an MR fluid in combination with a magnetic field, local and controllable surface textures can be created which are less sensitive to wear.

In this work a proof of concept for a hydrodynamic thrust bearing lubricated with an MR fluid is modeled and produced. For the models two mechanisms utilizing surface textures for pressure buildup in a lubricating film using MR fluids are studied. The first uses local viscosity variation resulting in so-called virtual surface textures. The second uses local sedimentation of magnetic particles in locations of higher magnetic field strengths resulting in physical surface textures. The experimental results correspond to the situation where the magnetic particles are completely sedimented. Here self-healing surface textures are created, over which the carrier fluid flows. The carrier fluid is pressurized by these textures which results into a load carrying capacity.

Keywords:

Magnetorheology, Hydrodynamic, Tribology, Numerical, simulation

1. Introduction

To minimize friction and prevent wear are the main reasons why lubricants are used in fluid bearings. In fluid bearings the load is supported by a thin film of fluid which is externally pressurized or which is pressurized by a rapid movement of the bearing faces. But these lubricated bearings encounter different problems [1]. Metal to metal contact cannot be avoided due to a not sufficient oil pressure and viscosity at certain working conditions or due to that the oil film thickness breaks when the variation of the load and vibration exceed the acceptable level [2, 3]. In addition, a decrease in viscosity and load carrying capacity is possible due to the temperature increase of the lubricant during operation. Smart fluids, like magnetic fluids, have the potential to improve the performance and overcome the drawbacks of fluid bearings [4, 5].

The magnetic properties of a magnetic fluid are obtained when particles that have magnetic properties are suspended in a carrier fluid. MR fluids are fluids that can have a liquid behavior but can also act solid, depending on the strength of the magnetic field applied to it. MR fluids becoming a solid is due to the attractive dipolar forces between the particles which have been magnetized by the applied magnetic field [6]. The strength of the solid phase is caused by the formation of certain structures, such as chain-like agglomerates. The aggregation process for an MR fluid

is more intense in presents of a field than for ferrofluids, another well known magnetic fluid [7]. Due to this more intense aggregation process the flow behavior can be controlled [8].

In [9] an MR fluid film bearing is constructed, which is capable of exciting the MR fluid. The purpose is to evaluate the dynamic properties of this bearing both in its active and its inactive state. In [10] a virtual textured hydrostatic bearing is proposed where the resistance is increased locally by using an MR fluid and a local magnetic field. In [5] it is seen that the critical pressures of the proposed thrust bearing using a magnetic fluid are larger than those of the normal lubricated bearing under high speeds. In [11] it is shown that the load capacity of a magnetic-fluid-based porous inclined slider bearing is found to be greater than the configuration using a conventional lubricant seen in [12]. The research in [13] elaborated on [11] considering a slider consisting of an inclined pad and a flat pad. It was seen that the magnetic fluid increases the load capacity, and does not alter the friction.

In [14]-[17] journal bearings lubricated with a ferrofluid are presented. There it is concluded that the bearing performance is modified significantly, like increase in stiffness and load capacity, but only only for certain conditions. Far from these conditions, an insignificant effect is obtained for the magnetic lubrication. In [18] it is investigated if magnetic fluids can

be used as active lubricants in a hydrodynamic journal bearing, here both a ferrofluid and an MR fluid are tested. It is seen that the rheological change of the ferrofluid is negligible for the purpose of a tunable lubricant. On the other hand, the MR fluid has good potential to be used as a tunable lubricant. In [19] an active hydrostatic bearing with MR fluid is presented. Here it is shown that the drawbacks (stiffness, response time and variation in bearing gap) of conventional hydrostatic bearings are overcome with the use of an MR fluid.

Ferrofluids already show potential to overcome the drawbacks of lubricated bearings, but seen is that the tunability is low and it only works for certain conditions. Therefore it is beneficial to look into MR fluids and their application to overcome the drawbacks of wear present in lubricated bearings. The MR fluid together with a local magnetic field can locally create solid like behavior of the lubricant resulting in surface textures that are not sensitive to wear.

In this paper three different designs of hydrodynamic thrust bearings lubricated with an MR fluid are considered. All of the designs are numerically modeled and experimentally measured. The designs are modeled for the case that the particles stay completely in suspension and for the case that the particles show complete sedimentation, resulting in virtual and physical surface texturing respectively. Comparing the results of the model with the results of the experiments demonstrates which situation is likely to occur.

2. Method

First the model for perfect mixture resulting in virtual surface texturing is discussed followed by the model for complete sedimentation resulting in physical surface texturing, at last the experimental set-up is discussed. The models and proof of concept consist of several layers. In figure 1 a top view configuration is seen of the layer containing the magnets. Here θ is the angle under which the magnets lie, r is the radius of the bearing, l is the length of the magnet, and b is the width of the magnet. In figure 2a the cross section at location A-A in figure 1 is seen for the model used for perfect mixture. In this figure every layer used in the model is shown. In figure 2b the cross section is seen for the model used for complete sedimentation. Here the MR fluid film now consists of steps created by the sedimented magnetic particles over which the carrier fluid flows. In this model only the fluid film containing the steps is considered. The proofs of concept only consist of the layers below the MR fluid in figure 2.

In the numerical simulations a vapor pressure equal to 1 atmosphere is used. Here the vapor pressure as relating to cavitation refers to the vapor pressure in equilibrium conditions. Without cavitation for $\theta = 0$, the

negative pressure and the positive pressure will cancel out. However, due to the release of gas entrained in oil, the negative pressure cannot be lower than vapor pressure. In most cases the vapor pressure is nearly ambient due to long time exposure to air [20]. For this reason the vapor pressure is taken equal to 1 atmosphere.

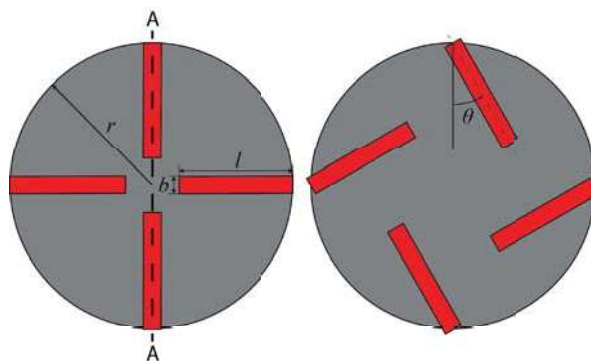


Figure 1: Configuration of the magnets used in the numerical simulations and proofs of concept.

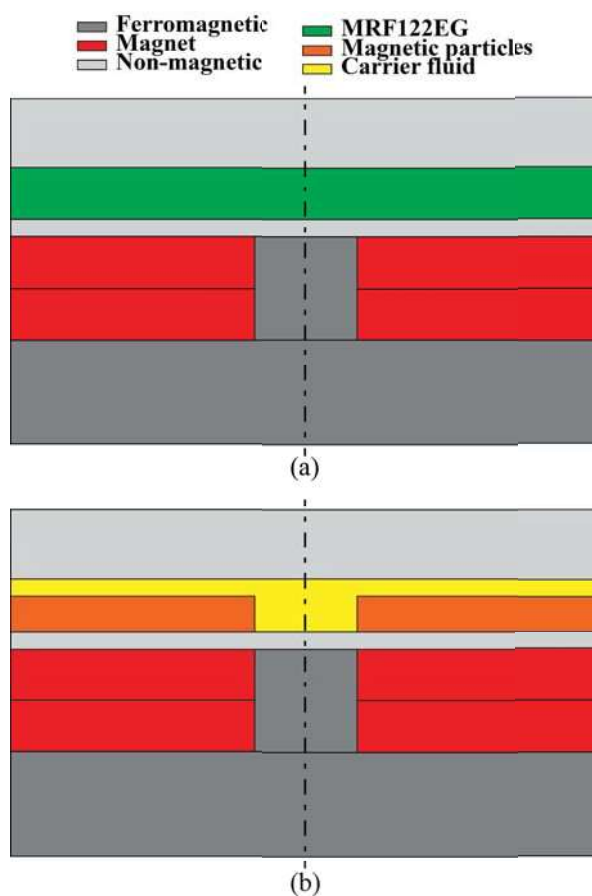


Figure 2: 2D section at location A-A in figure 1 of the geometry used in the numerical simulation. (a) Perfect mixture. (b) Complete sedimentation.

2.1. Model for perfect mixture

A three-dimensional numerical simulation in COMSOL Multiphysics [21] is made. This is done taken into consideration that on this model a proof of concept can be based. A model that is used to describe these non-Newtonian fluids is the Bingham model (Eq. 1 and 2) [22].

$$\tau = \tau_y + \eta\dot{\gamma}, \quad |\tau| > \tau_y \quad (1)$$

$$\dot{\gamma} = 0, \quad |\tau| \leq \tau_y \quad (2)$$

Here τ is the shear stress in the fluid and $\dot{\gamma}$ the shear rate. In the Bingham model the shear stress is dependent on the yield stress of the fluid. For an MR fluid this yield stress is depending on the magnetic field, the higher the magnetic field strength the higher the yield stress. Using a local magnetic field the viscosity and fluid pressure of the MR fluid can be controlled locally. To simulate this behavior the Bingham-Papanastasiou model [23] is implemented in the numerical simulation. The Bingham-Papanastasiou model proposes an exponential regularization for the Bingham model (Eq. 3 and 4).

$$\tau = \tau_y(1 - e^{-m|\dot{\gamma}|}) + \eta_0\dot{\gamma} \quad (3)$$

$$\eta = \frac{\tau_y}{\dot{\gamma}}(1 - e^{-m|\dot{\gamma}|}) + \eta_0 \quad (4)$$

Here η_0 represents the viscosity for no applied magnetic field, and m is the regularization parameter. The higher the value of m , the closer the Bingham-Papanastasiou model follows the Bingham plastic model. From this the apparent viscosity is obtained (Eq. 4).

The model for the perfect mixture is build up out of several layers representing a thrust bearing (Fig. 2a). Two layers of ferromagnetic material, one containing the magnets, a non-magnetic layer separating the magnets from the MR fluid, an MR fluid film which in reality is surrounded by air but is not shown in the figure, and a sliding top layer made of non-magnetic material. The MR fluid used is MRF122EG provided by Lord Corporation [24]. The parameters used in the model can be seen in table 1.

For this model a combined study regarding magnetism and fluid flow is used. The magnetic field is simulated for the whole domain. Given every part has its own magnetic properties, a certain magnetic field is formed. After simulating the magnetic field, the fluid flow of the MR fluid is simulated. This is done only for the domain where the MR fluid is present. Because the viscosity is depending on the local magnetic field, the results from the study regarding the magnetic field across the film height are obtained beforehand. The apparent viscosity (Eq. 4) is implemented in the simulation. Here it is seen that the yield stress depends

Table 1: Parameters used for simulating the perfectly mixed MR fluid.

Parameters	
Outer diameter bearing	30 [mm]
Ferromagnetic layer thickness	2 [mm]
Magnet (l x b x h)	7.5x1.1x1 [mm]
Remanent flux density of the magnet	1.28 [T]
Separation layer thickness	0.15 [mm]
MR fluid film height	0.2 [mm]
MR fluid film diameter	20 [mm]
Air surrounding MR fluid thickness	0.2 [mm]
Top layer thickness	2.2 [mm]
Viscosity MRF122EG	0.086 [Pa·s]
Regularization parameter	1
θ	0, 30, and 36 [degree]

on the magnetic field strength, which is obtained in the study for the magnetic field. The relation between the magnetic field strength and the yield stress for MRF122EG is used. The shear rate, obtained in the numerical simulation is a variable that is obtained during the study for the fluid flow. The viscosity η_0 and the regularization parameter m are known constants. The appropriateness of the chosen regularization parameter is checked with the results.

Bar magnets are used to create a magnetic field that decreases across the height of the fluid film. Due to the gradient in magnetic field strength, the effective viscosity of the fluid appears to be higher at the bottom. Near the magnets local surface textures are created that influences the tribological performance. This surface texture is used to pressurize the liquid and so a load carrying capacity is obtained.

2.2. Model for complete sedimentation

In an MR fluid where the magnetic particles are completely separated from the carrier fluid the magnetic particles cluster around the magnets. These agglomerates of magnetic particles represent physical steps, and these steps are simulated in a second model. An approximation for the dimensions of these steps is obtained in the previous model where a perfect mixture is assumed. It is assumed that for $\eta > 1000$ the fluid appears solid. Based on this the steps are represented using rectangular blocks with a certain length, width, and height equal to 7.5E-3 mm, 1.1E-3 mm, 1.8E-4 mm respectively. Using these dimensions the particles occupy 19% of the volume. This corresponds to the volume fraction of iron in MRF122EG. This rectangular block is used to approximate the behavior and see if it corresponds to the situation where the carrier fluid separates from the magnetic particles. These

steps are combined with a fluid that has the same viscosity as for the carrier fluid of MRF122EG. This is illustrated in figure 2b, a solid part representing the steps over which an oil flows. These steps pressurize the liquid and so a load carrying capacity is obtained.

In this model only the MR fluid film is simulated using the same angles and dimensions as in the model for perfect mixture. Now the particles are completely sedimented and in the fluid film now physical textures are present over which the carrier fluid flows. The sensitivity for the dimensions and viscosity is considered in this model. A change in value of 10% for the viscosity and dimensions of the step is implemented to obtain the parameter which has the most significant impact on the load capacity.

2.3. Experimental setup

Three proofs of concept seen in figure 3 are build up similar to the model. The Anton Paar rheometer MCR 302 (Fig. 4) is used for the experiments. This rheometer measures the normal force exerted on the parallel plate spindle used. The dimensions of the rheometer determine the diameter of the layer MR fluid, and also the maximum dimensions of the magnets which have to be placed under this layer MR fluid. The diameter of the spindle under which the MR fluid is captured is equal to 20 mm.



Figure 3: Proofs of concept used for the experiments. Here $\theta = 0$, $\theta = 30$, and $\theta = 36$.

The proof of concept consists of 2 layers of 2 mm thick steel, one of these layers containing 8 magnets, a layer of 0.15 mm thick glass that separates the MR fluid from the magnets, and several screws and bolts to hold it together. Both the layers of steel are made by laser cutting, where the bottom plate locks the prototype in the rheometer and the top plate contains the magnets. The magnets have a remanent flux density of 1.28 Tesla and the dimensions are 7.5x1.1x1 mm. Because the steel layer containing the magnets is 2 mm



Figure 4: The Anton Paar rheometer MCR 302 used for the experiments and one proof of concept placed in the rheometer.

thick, 2 magnets have to be stacked on top of each other resulting in the total of 8 magnets.

The measuring position, which is equal to the flying height, is set using the rheometer. The proof of concept is placed in the rheometer, then the zero-gap is set in order to determine the position with respect to the spindle. The rheometer lowers the spindle until first contact is made, this position is equal to a height of 0 mm. This is done without the presence of any liquid.

During operation of the rheometer, the MR fluid is captured between the glass and the spindle of the rheometer. During the experiments the revolutions per minute of the spindle is given as an input and the normal force acting on the spindle is given as an output. A total of 10 measurements are done using an interval of 10 milliseconds between data points, up to a total of 1000 data points. In the end the average of these 10 measurements is taken.

3. Results and discussion

In figure 5 the results for the numerical simulations can be seen. Here both the results for a perfect mixture and complete sedimentation of magnetic particles and carrier fluid are shown for θ equal to 0, 30, 36 degrees and a flying height equal to 200 μm . For perfect mixture the yield stress in the MR fluid is in the order of 10^5 . Using an exponential growth factor $m = 1$ the Bingham-Papanastasiou model follows the Bingham plastic model down to a shear rate $\dot{\gamma} = 10\text{s}^{-1}$. Shear rates lower than $\dot{\gamma} = 10\text{s}^{-1}$ are assumed to be of negligible influence to the solution. The shear rate in the simulation is in order of 10^3 , so this is a valid assumption.

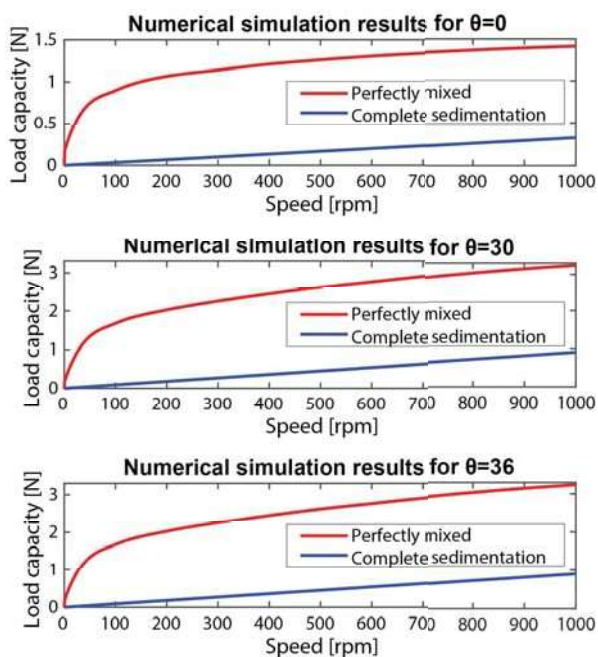


Figure 5: Results for the numerical simulations. Here the results for both perfect mixture and complete sedimentation are shown.

For perfect mixture an exponential decay (increasing form) in load capacity is seen for every configuration. This is due to a trade-off between saturation of the liquid (influencing the viscosity and the geometry of the bearing), and the load capacity due to the pressurization of the fluid for increasing velocity. At low speed the viscosity of the fluid appears higher and size of the textures are larger because of the lower stresses. The moment the velocity increases, the viscosity decreases and also the size of the textures decrease which results in a smaller increase in load capacity.

For complete sedimentation physical surface textures are implemented over which a fluid flows with a viscosity equal to the viscosity of the carrier fluid. This is used to approximate the behavior and see if it corresponds to the situation where the carrier fluid separates from the magnetic particles. Here a linear increase for the load capacity is observed. This is due to that now the geometry of the bearing is fixed and the viscosity is constant.

In figure 6 the experimental results together with the numerical results for complete sedimentation (Fig. 5) are seen for θ equal to 0, 30, 36 degrees and a flying height equal to $200 \mu\text{m}$. For the experimental results the average of 10 measurements is shown for an interval of 10 milliseconds between data points up to a total of 1000 data points. A boxplot is shown to indicate the sensitivity of the measurements.

At zero speed, already a normal force is obtained due to the magnetization of the MR fluid. The appli-

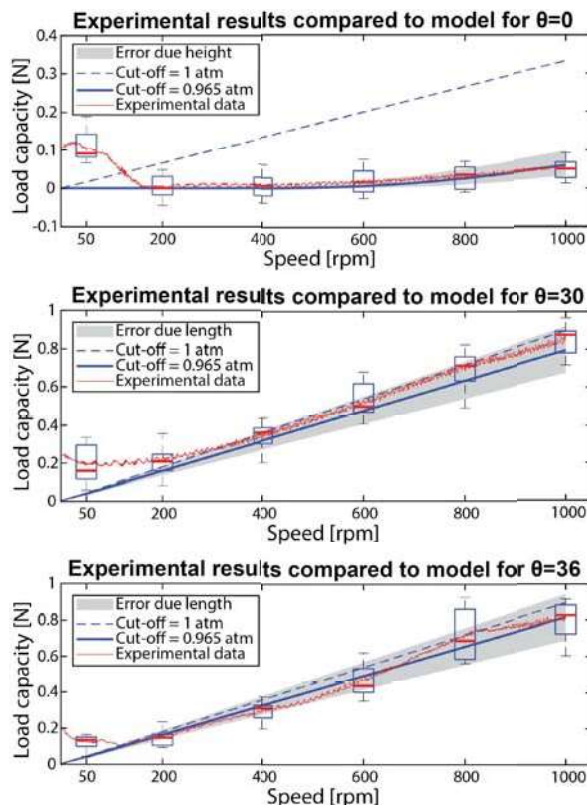


Figure 6: Comparison of the experimental results to numerical simulations for complete sedimentation.

cation of an external magnetic field increases the pressure inside the fluid after which the fluid is capable of carrying loads as already seen for ferrofluid bearings [25]–[28]. The local magnetic field has a strong effect on the fluid and pressurizes the liquid resulting in a load capacity at zero speed. Also the fluid shows viscoelastic behavior due to the higher viscosity of the fluid at zero speed. This viscoelastic behavior results in a stiffness depending on the magnetic field [29, 30] resulting in a load capacity. For an increase in velocity the fluid is sheared and the viscosity decreases and with it less elastic behavior is seen. The load capacity increases at the point pressurization of the liquid due to the rapid movement of the bearing faces overcomes these effects.

It is observed that the experiments where $\theta > 0$ show similar behavior as for a fixed geometry with a fluid flowing over it with a viscosity equal to 0.03. Knowing that the viscosity of the carrier fluid is equal to 0.03 it shows that there is the possibility that what is measured is actually the carrier fluid separated from the magnetic particles flowing over physical surface textures created by the magnetic particles itself. At first the vapor pressure is taken equal to the atmospheric pressure, but for θ equal to zero this shows different behavior. A lower vapor pressure significantly lowers the value of the load capacity for $\theta = 0$. This is

due to the pressure distribution which is antisymmetric for $\theta = 0$. For $\theta > 0$ the vapor pressure has a less significant impact, because here the positive pressurization is dominant. A lower vapor pressure is simulated which does correspond with the experimental data of $\theta = 0$. Seen is that this new vapor pressure which is close to 1 atm, still corresponds for θ equal to 30 and 36 degrees.

The impact of different parameters are considered, these parameters are the width, length, and height of the bearing, and also the viscosity of fluid flowing over the steps. The impact is investigated for a change of 10% for each parameter, and the influence on the load capacity of the parameter which has the most significant impact is obtained (Fig. 6). It is seen that for $\theta = 0$ the height of the step has the most significant impact, besides the vapor pressure. For θ equal to 30 and 36 the length of the step has to most significant impact. The change in load capacity due to the vapor pressure falls within these limits.

Observed is that the experimental results correspond to the situation where the magnetic particles are completely sedimented. This sedimentation is observed after doing the experiments (Fig. 7). Clearly the oil is separated and is laying on top of the magnetic particles, also oil is seen on the spindle. Already in literature this separation of the carrier fluid from the magnetic particles is observed. In [31] this phenomenon is discussed using two terms, Fluid Particle Separation (FPS) in combination with the clumping effect. It is discovered that the magnetic particles of the MR fluid are trapped in the forming chains of the magnetic field, the so called clumping effect [32, 33]. Here the carrier fluid can still flow freely separately. This effect occurs when for a longer period of time a high magnetic field is applied [34].



Figure 7: Oil seen on the spindle and laying on top of the magnetic particles after the experiments.

The FPS is linked to the clumping effect. Experiments done in [35, 36] showed separation of the carrier fluid. This is caused by the distribution in magnetic field, the pressure that is build up due to squeezing and changes in the chain structure of the magnetic particles. From this study, it is concluded that the fluid-particle separation phenomenon increased at low carrier fluid viscosity, low compression speed, and

high magnetic field intensity.

It can be stated that during the experiments the particles form self-healing physical surface textures. The agglomerated magnetic particles do not wear down and do not leave the system. Over these textures a fluid flows with a viscosity equal to the viscosity of the carrier fluid (Fig. 8). At the top the MR fluid is trapped between the bearing surfaces and no magnetic field is applied, so the magnetic particles are evenly spread over the volume. Then a magnetic field is applied to the MR fluid by adding permanent magnets indicated with red in the figure. Near these magnets the magnetic field strength is high and therefore agglomerates are formed around the magnets. When the velocity of the bearing is increased, some of the magnetic particles further away from the magnets are sheared off because here the magnetic field is not sufficient to hold them in place. The magnetic particles that are kept in place form steps that pressurize the fluid. These steps are self-healing, because magnetic particles are traded among these steps. A magnetic particle sheared of from the previous step, fills a gap in the following step and so the steps do not decay.

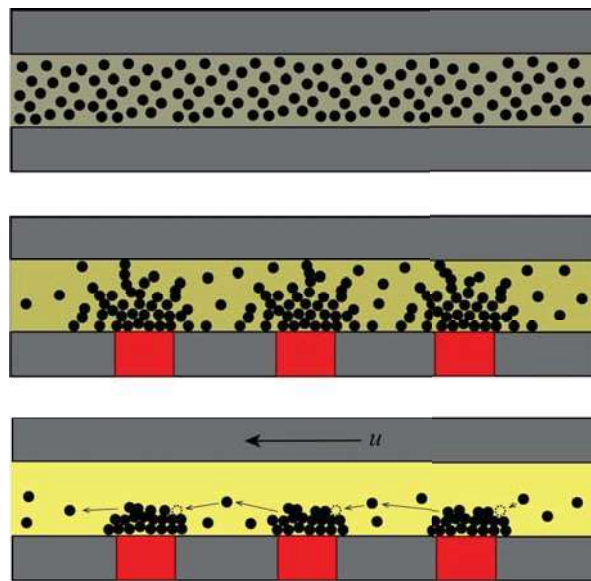


Figure 8: Illustration of the self-healing bearing.

4. Conclusion

It is concluded that a self-healing bearing is created. The surface textures consists of the magnetic particles over which the carrier fluid flows which is pressurized resulting in a load carrying capacity predicted with the numerical model for a complete sedimentation. Near the magnets the magnetic field strength is high and therefore agglomerates are formed around the magnets. During operation the magnetic particles are traded among the created textures. These textures

are self-healing, because the magnetic particles do not wear down and do not leave the system.

References

- [1] S.N. Bhole, N.D. Khaire, "Analytical and Experimental investigation of Magnetorheological Fluid in Hydrodynamic journal bearing," *International Engineering Research Journal*, pp. 271277.
- [2] A.M. Loeb, "Electric analog study of hydrostatic bearings," *Journal of the Franklin Institute*, vol. 263, no. 5, pp. 450452, 1957.
- [3] F.Y. Zeidan, B.S. Herbage, "Fluid Film Bearing Fundamentals and Failure Analysis," *Texas A&M University. Turbomachinery Laboratories*, pp. 161186, 1991.
- [4] P.G. Nikolakopoulos, C.A. Papadopoulos, "Controllable Misaligned Journal Bearings, Lubricated with Smart Fluids," *Journal of Intelligent Material Systems and Structures*, vol. 8, no. 2, pp. 125137, 1997.
- [5] K. Nagaya, S. Takeda, A. Sato, S. Ikai, H. Sekiguchi, N. Saito, "Thrust bearing using a magnetic fluid lubricant under magnetic fields," *Tribology International*, vol. 26, no. 1, pp. 1115, 1993.
- [6] S. Odenbach, *Ferrofluid. Magnetically Controllable Fluids and Their Applications*. Springer Berlin Heidelberg, 2002.
- [7] L. Vks, "Ferrofluids and Magnetorheological Fluids," *Advances in Science and Technology*, vol. 54, pp. 127136, 2008.
- [8] I.G. Kim, K.H. Song, B.O. Park, B.I. Choi, and H.J. Choi, "Nano-sized Fe soft-magnetic particle and its magnetorheology," *Colloid and Polymer Science*, vol.289, no. 1, pp. 79-83, 2011.
- [9] D. Bompos, P. Nikolakopoulos, "Experimental and Analytical Investigations of Dynamic Characteristics of Magnetorheological and Nanomagnetorheological Fluid Film Journal Bearing," *Journal of Vibration and Acoustics, Transactions of the ASME*, vol. 138, no. 3, pp. 1-7, 2016.
- [10] S.G.E. Lampaert and R.A.J. van Ostayen, "Virtual Textured Hybrid Bearings," *44th Leeds-Lyon Symposium on Tribology*, 2017.
- [11] V.K. Agrawal, "Magnetic-fluid-based porous inclined slider bearing," *Wear*, vol. 107, no. 2, pp. 133139, 1986.
- [12] J. Prakash, S.K. Vij, "Hydrodynamic Lubrication of a Porous Slider," *Journal of Mechanical Engineering Science*, vol. 15 no. 3, pp. 232234, 1973.
- [13] V.M. Bhat, G.M. Deheri, "Porous Composite Slider Bearing Lubricated with Magnetic Fluid," *Japanese Journal of Applied Physics*, vol.30 .no. 10, pp. 25132514, 1991.
- [14] D.C. Kuzma, "The Magnetohydrodynamic Journal Bearing," *Journal of Basic Engineering*, volume 85, no. 3, 1963.
- [15] C.Q. Chi, Z.S. Wang, P.Z. Zhao, "Research on a new type of ferrofluid-lubricated journal bearing," *Journal of Magnetism and Magnetic Materials*, vol 85 no. 13, 257260, 1990.
- [16] T.A. Osman, G.S. Nada, Z.S. Safar, "Static and dynamic characteristics of magnetized journal bearings lubricated with ferrofluid," *Tribology International*, vol. 34 no.6, pp. 369380, 2001.
- [17] N. Patel, D. Vakharia, G. Deheri, "A Study on the Performance of a Magnetic-Fluid-Based Hydrodynamic Short Journal Bearing," *ISRN Mechanical Engineering*, vol. 2012, 2012.
- [18] H. Urreta, Z. Leicht, A. Sanchez, A. Agirre, P. Kuzhir, and G. Magnac, "Hydrodynamic Bearing Lubricated with Magnetic Fluids," *Journal of Intelligent Material Systems and Structures*, vol. 21, no. 15, pp. 1491-1499, 2010.
- [19] J. Hesselbach and C. Abel-Keilhack, "Active hydrostatic bearing with magnetorheological fluid," *Journal of Applied Physics*, vol. 93, no. 10, pp. 8441-8443, 2003.
- [20] X. Lu, M.M. Khonsari, "An Experimental Investigation of Dimple Effect on the Stribeck Curve of Journal Bearings," *Tribology Letters*, vol. 27, no. 2, pp. 169176, 2007.
- [21] *COMSOL Multiphysics*, available at <https://www.comsol.com/>.
- [22] K. Walters, "An Introduction to Rheology," *Elsevier Science Publishers*, first ed., 1989
- [23] T.C. Papanastasiou, "Flows of Materials with Yield," *Journal of Rheology*, vol. 31, no. 5, pp. 385-404, 1987.
- [24] *Lord Corporation*. available at <https://www.lord.com/>.
- [25] S.G.E. Lampaert, "Planar Ferrofluid Bearings: Modelling and Design Principles," *DSPE Conference. 20160*, 2016.
- [26] S.G.E. Lampaert, J.W. Spronck, R.A.J. van Ostayen, "Load and stiffness of a planar ferrofluid pocket bearing," *Proceedings of the Institution of Mechanical Engineers, Part J: Journal of Engineering Tribology*, vol. 232 no. 1, pp. 1425, 2018.
- [27] S.G.E. Lampaert, B.J. Fellingner, J.W. Spronck, R.A.J. van Ostayen, "In-plane friction behaviour of a ferrofluid bearing," *Precision Engineering*, vol. 54, pp. 163170, 2018.
- [28] A.S.T. Boots, L.E. Krijgsman, B.J.M. de Ruiter, S.G.E. Lampaert, J.W. Spronck, "Increasing the load capacity of planar ferrofluid bearings by the addition of ferromagnetic material," *Tribology International*, vol. 129, pp. 4654, 2019.
- [29] Y. Xue, S. Changgeng, "The stiffness and damping properties of magnetorheological fluid-elastomer composites," *21st International Congress on Sound and Vibration 2014, ICSV 2014*, vol. 5, pp. 43774381, 2014.
- [30] J.S. Oh, S.B. Choi, "State of the art of medical devices featuring smart electro-rheological and magneto-rheological fluids," *Journal of King Saud University - Science*, vol. 29 no. 4, pp. 390400, 2017.
- [31] S.A. Wahid, I. Ismail, S. Aid, and M.S.A. Rahim, "Magneto-rheological defects and failures: A review," *In IOP Conference Series: Materials Science and Engineering*, vol. 114, 2016.
- [32] A. Farjoud, R. Cavey, M. Ahmadian, M. Craft, "Magneto-rheological fluid behavior in squeeze mode," *Smart Materials and Structures*, vol. 18, no. 9, 2009.
- [33] A. Farjoud, M. Craft, W. Burke, and M. Ahmadian, "Experimental Investigation of MR Squeeze Mounts," *Journal of Intelligent Material Systems and Structures*, vol. 22, no. 15, pp. 1645-1652, 2011.
- [34] K. Adjerid, "A Study on the Dynamic Characterization of a Tunable Magneto-Rheological Fluid-Elastic Mount in Squeeze Mode Vibration," Virginia Polytechnic Institute and State University, 2011.
- [35] I. Ismail, S.A. Mazlan, H. Zamzuri, A.G. Olabi, "FluidParticle Separation of Magnetorheological Fluid in Squeeze Mode," *Japanese Journal of Applied Physics*, vol. 51, 2012.
- [36] I. Ismail and S.N. Aqida, "Fluid-Particle Separation of Magnetorheological (MR) Fluid in MR Machining Application", *Key Engineering Materials*, vols. 611-612, pp. 746-755, 2014.

Capillary rheometer for magnetic fluids

S M Allebrandi, R A J van Ostayen and S G E Lampaert¹ 

Department of Precision and Microsystem Engineering, Technical University Delft, Mekelweg 2, 2628 CD Delft, The Netherlands

E-mail: S.G.E.Lampaert@tudelft.com (S G E Lampaert)

Received 17 May 2019, revised 5 August 2019

Accepted for publication 29 August 2019

Published 13 November 2019



CrossMark

Abstract

Magnetic fluids have been around since the 1940s. They come in different forms: magnetorheological fluids (MR fluids) and ferrofluids. MR fluids characterise themselves by having a large change in viscosity under the influence of a magnetic field. Ferrofluids have a significantly smaller change in viscosity, however ferrofluids are colloidal suspensions. After their discovery many applications followed, such as the MR clutch, magnetic damper and bearing applications, in which the fluids are subjected to ultra high shear rates. Little information is available on what happens to the rheological properties under these conditions. In general, the characteristics determined at lower shear rates are extrapolated and used to design new devices. Magnetic fluids have potential in the high tech and high precision applications and their properties need to be known in particular at shear rates around 10^6 s^{-1} . Commercially available magnetorheometers are not able to measure these fluids at ultra high shear rates and are limited to 10^5 s^{-1} . Therefore a new magnetorheometer is required to measure ultra high shear rates. In this paper the physical limitations of current measuring principles are analysed and a concept is designed for ultra high shear rate rheometry in combination with a magnetic field. A prototype is fabricated and the techniques used are described. The prototype is tested and compared to a state of the art commercial rheometer. The test results of the prototype rheometer for magnetic fluids show its capability to measure fluids to a range of 10^4 s^{-1} – $1.16 \times 10^6 \text{ s}^{-1}$ and the capability to measure the magnetorheological effect of magnetic fluids.

Keywords: ferrofluid, magnetorheological fluid, high shear, micromechanical, microfluidics, viscometer, rheology

(Some figures may appear in colour only in the online journal)

1. Introduction


Magnetic fluids come in different forms with different properties. Commonly they are known as magnetorheological fluids (MR fluids) and ferrofluids. In the 1940s Jacob Rabinow created the first MR fluid. These MR fluids alter their rheological properties (viscosity) significantly under the influence of a magnetic field. The first use of ferrofluids is credited to Papell while working for NASA in 1963 [1]. Ferrofluids have significantly less change in their viscosity, however, are the first magnetic fluids that are colloidal suspensions [2–4]. Due

to their unique characteristics these magnetic fluids quickly found their applications. In 1948 Rabinow patented the first application of a MR fluid, the MR clutch [5]. Soon after he patented the MR force transmitter [6]. Later on came applications such as magneto rheological damper [7], MR brake [8] and many more [9, 10].

Ferrofluids found applications in bearing applications [11, 12], dynamic sealing applications [13] and more [14].

In these systems the fluid flows at high speed. For example fluid bearings typically have a thin film ($10 \mu\text{m}$) and rotate at high speed (10 m s^{-1}). Little knowledge is available about what happens to the fluid characteristics at these speeds. Prior research has reached shear rates up to 10^5 s^{-1} [15–18].

Commercial rheometers are not designed to measure at high shear rates (above 10^4 s^{-1}) but to measure a large range of fluids and rheological behaviour. These devices are mostly

 Original content from this work may be used under the terms of the [Creative Commons Attribution 3.0 licence](https://creativecommons.org/licenses/by/3.0/). Any further distribution of this work must maintain attribution to the author(s) and the title of the work, journal citation and DOI.

¹ Author to whom any correspondence should be addressed.

Table 1. List of symbols.

Symbol	Description	Unit	Symbol	Description	Unit
β	Viscosity temperature sensitivity	$\Delta\eta \text{ K}^{-1}$	L_m	Measuring length	m
$\dot{\gamma}$	Shear rate	s^{-1}	L_{cc}	Cylinder length	m
$\dot{\gamma}_{app}$	Apparent shear rate	s^{-1}	L_{ex}	Exit length	m
η	Viscosity	Pa s	L_{cap}	Channel length capillary	m
ρ	Density	kg m^{-3}	L_{sl}	Channel length slit	m
τ	Shear stress	Pa	M	Torque	N m
σ	Surface tension	N m^{-1}	Na	Nahme number	
ω	Angular velocity	rad s^{-1}	P	Pressure	Pa
d	Time delay	s	P_h	Sensor pressure high	Pa
d_h	Hydraulic diameter	m	P_l	Sensor pressure low	Pa
h_{pp}	Gap height parallel plate	m	P_{in}	Inlet pressure	Pa
h_{sl}	Gap height slit	m	Q	Flow rate	$\text{m}^3 \text{ s}^{-1}$
k	Thermal conductivity	$\text{W K}^{-1} \text{ m}^{-1}$	R_{cap}	Capillary radius	m
r	Radial distance	m	R_{in}	Inner radius	m
$t_{response}$	Response time	s	R_{out}	Outer radius	m
v	Velocity	m s^{-1}	R_{pp}	Radius parallel plate	m
v_s	Slip velocity	m s^{-1}	\tilde{R}	Radial Reynolds number	
w	Channel width	m	Re	Reynolds number	
D	Characteristic linear dimension	m	Ta	Taylor number	
L	Channel length	m	V	Fluid velocity	m s^{-1}
L_e	Entrance length	m			

parallel plate or cone plate devices and have a modular design where inserts can be added to extend the functionality of the rheometer. However, they are limited in shear rate. Existing commercial equipment reaches 10^5 s^{-1} [19, 20]. There are rheometers available reaching shear rates up to 10^7 s^{-1} . These are capillary rheometers [21, 22], tapered bearing simulation (TBS) [23], or concentric cylinder rheometers [24]. However, these lack the ability to apply a magnetic field. Therefore, there is a need for a new apparatus which is capable of reaching shear rates in the range of bearings and damper and is able to apply a magnetic field.

This paper focusses on the design of a rheometer capable of measuring magnetic fluids to a shear rate of 10^6 s^{-1} under the influence of a homogeneous magnetic field of 1 T. In order to develop the most promising magneto-rheological rheometer for high shear rates, the first part of the paper describes a comprehensive comparison between relevant rheometer types. This comparison is an original contribution to the field of rheometry in general. The second part of the paper describes the design, construction, and testing of the new high shear rate, magnetorheometer. This part in particular is a new contribution to the field of magnetorheometry. A list of the symbols used in this paper can be found in table 1.

2. Theory

The physical principles used in rheometers are determined and the theoretical working ranges set out. There are four main principles for measuring at high shear rates.

1. Parallel plate
2. Concentric cylinder

3. Round capillary
4. Slit capillary

The geometrical definition of these rheometer are given in figure 1 and will be used throughout the paper. The cone plate is left out as it has a similar but smaller measuring range as the parallel plate and is less suited for measuring high shear rates.

The goal of the measuring device is to determine the rheological properties of a fluid. The viscosity is determined by applying a velocity and measuring the force or torque required or vice versa. These are converted through a model into the viscosity. The model assumes the following conditions for the measurement.

1. Unidirectional shear
2. Laminar flow
3. Wall adherence
4. Isothermal flow
5. Incompressible flow

Once the assumptions are untrue, errors enter the measurement. Each model assumption is discussed and its limitation derived.

2.1. Unidirectional shear

Unidirectional shear means that no secondary flows are present. At high shear rates the measured fluid is moving at high speed. As long as the viscous force is dominant over the centrifugal force the flow is unidirectional. However, once this is no longer true, the fluid starts moving outwards and unwanted flows occur. This inertial effect is present in all rotational devices, although there is a difference in how the rheometers counteract this inertial effect and thus what

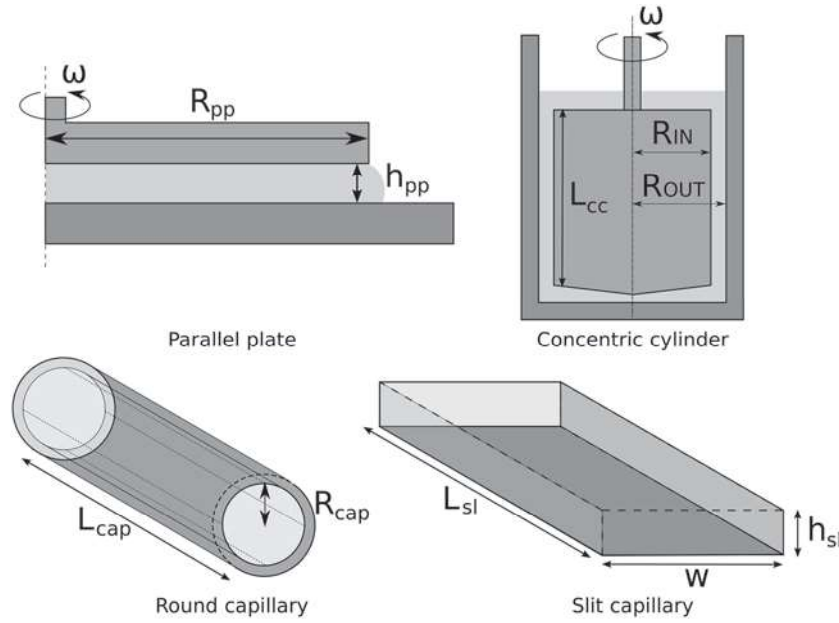


Figure 1. Geometrical definitions.

range they can measure before the effect dominates the measurement.

2.1.1. Parallel plate. In the case of these rotary measurement methods the flow towards the outside is the first occurring secondary flow. At one plate the fluid will flow from inside to outside and at the other reversed. The secondary flow is initially laminar but can become turbulent. A dimensionless number can be formed describing the onset of secondary flows [25], according to the following analysis. The secondary flow is characterised by the forces acting on a unit volume. The forces acting on this unit can be evaluated in a steady state in the radial direction. The dimensionless number \tilde{R} is created to give the ratio of these forces, equations (1) and (2). Geometrical definitions for parallel plate from figure 1 are used. The \tilde{R} number is the Reynolds number in the radial direction.

$$\tilde{R} = \frac{\rho\omega^2 r}{\left(\frac{\tau}{h}\right)} \quad (1)$$

$$\text{Plate plate : } \tilde{R} = \frac{\rho\omega^2 r}{\left(\frac{\eta\omega r}{h_{pp}^2}\right)} = \frac{\rho\omega h_{pp}^2}{\eta} \quad (2)$$

When the critical \tilde{R} number is exceeded, secondary flows will occur which results in a higher measured viscosity. In particular non-Newtonian fluids will show complex behaviour as the increased shear stress will alter the viscosity. The critical value of the \tilde{R} number for cone-plate and parallel plate is 6 according to [25].

At the edges of parallel plate measuring geometry, the forces on the unit volume are different. As these devices have open edges the centrifugal force is countered by the surface tension. There is the possibility that the centrifugal force overcomes the surface tension. This phenomenon, known as radial migration, limits the range of the rheometer, equation (3) [26]. The balance between the surface tension and the inertial forces results in a

critical shear rate. This critical shear rate is fluid dependent and strongly dependent on the gap height. The equation for the critical shear rate can be found in equation (4) [26]. Geometrical definitions for parallel plate from figure 1 are used.

$$\frac{3}{20}\rho(\omega^2 R_{pp}^2) > \frac{\sigma}{h_{pp}} \quad (3)$$

$$\dot{\gamma}_{app,c} = \left(\frac{\omega R_{pp}}{h_{pp}}\right)_c = \sqrt{\frac{20\sigma}{3\rho h_{pp}^3}} \quad (4)$$

The result of radial migration can be seen as a drop in measured torque. As there is less fluid, the shear stress is reduced. Repeating the measurement will result in lower torques measured due to the loss of fluid and thus a lower viscosity is measured.

2.1.2. Concentric cylinder. As with the parallel plate rheometers, the concentric cylinder is influenced by the centrifugal forces in the fluid. However, due to the fluid being held inside by the outside cylinder, the fluid cannot be flung out. A rising pressure gradient occurs between the inner and outer cylinder. This balance is not stable and when the rotational speed exceeds a certain point, secondary flows occur. This phenomenon was first studied by Geoffrey Ingram Taylor in 1923. Through dimensionless analysis a quantification of the relation between viscous forces and the inertial forces was described. He found the critical Taylor number at which Taylor vortices occur. The Taylor number is defined in equation (5) [27, 28]. Geometrical definition from figure 1 for concentric cylinder are used.

$$Ta = \rho^2 \dot{\gamma}^2 \frac{(R_{out} - R_{in})^5}{R_{in} \eta^2} \quad (5)$$

When increasing the angular velocity even further, different Taylor vortices occur. The Taylor vortices are initially

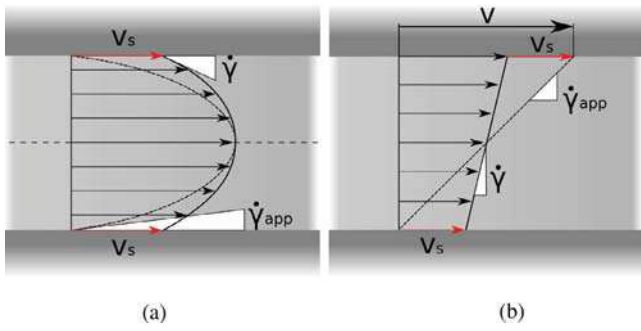


Figure 2. Effect of wall slip on the flow profile. In red the slip velocity. (a) Wall slip pressure driven flow. (b) Wall slip Couette flow.

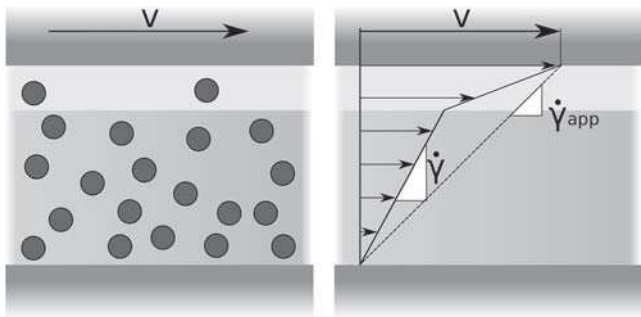


Figure 3. Wall depletion in suspensions.

laminar flows. The increased shearing in the fluid results in a higher torque measured and thus higher viscosities measured. For non-Newtonian fluids the extra shear affects the viscosity in the fluid. The critical Taylor number that defines the first occurrence of the vortices is 1700 [28].

2.2. Laminar flow

Laminar flow is required to generate a well-defined flow profile. The flow profile is used to determine the shear rate in the fluid. As the speed of the fluid increases, the laminar flow transitions into turbulent flow. Turbulence occurs due to layers of fluid moving at different speeds. Turbulence has been studied for many types of pipe flow. The capillary devices are pipe flows and therefore are limited to the onset of turbulence which can be expressed by a critical dimensionless Reynolds number. The Reynolds number is used to quantify the balance between inertia forces and the viscous forces. The Reynolds number is defined in equation (6).

$$Re = \frac{\rho VD}{\eta} \tag{6}$$

For the capillary devices the Reynolds number is transformed in different shape specific equations, equations (7) and (8). Geometrical definition from figure 1 for round capillary and slit capillary were used respectively. Turbulence creates extra shear stress in the fluid and chaotic flow. This increases the friction and results in higher viscosities measured. The critical Reynolds number defines the limit of the laminar flow.

Table 2. Table showing the Nahme–Griffith number for different types of rheometers [30], geometrical definitions from figure 1.

Rheometer	Nahme–Griffith
	$Na =$
Parallel plate	$\frac{\eta \beta h_{pp}^2 \dot{\gamma}^2}{k}$
Concentric cylinder	$\frac{\eta \beta (R_{out} - R_{in})^2 \dot{\gamma}^2}{k}$
Slit capillary	$\frac{\eta \beta h_{sl}^2 \dot{\gamma}^2}{k}$
Round capillary	$\frac{\eta \beta R_{cap}^2 \dot{\gamma}^2}{4k}$

Table 3. Equations defining the max–minimum viscosity at a given shear rate due to the sensor and max–minimum shear rate due to actuation limitations. Geometrical definitions from figure 1.

Rheometer	Limit due to sensing	Limit due to actuation
	$\eta =$	$\dot{\gamma} =$
Parallel plate	$\frac{2M}{\dot{\gamma} \pi R_{pp}^3}$	$\frac{\omega R_{pp}}{h_{pp}}$
Concentric cylinder	$\frac{M}{\dot{\gamma} \pi R_{in}^2 L_{cc}}$	$\frac{\omega (R_{in} + R_{out})}{2(R_{out} - R_{in})}$
Slit capillary	$\frac{wh_{sl}}{2\dot{\gamma} (w + h_{sl})} \frac{\Delta P}{L_{sl}}$	$\frac{6Q}{wh_{sl}^2}$
Round capillary	$\frac{R_{cap}}{2\dot{\gamma}} \frac{\Delta P}{L_{cap}}$	$\frac{4Q}{\pi R_{cap}^3}$

$$\text{Round capillary : } Re = \frac{\rho \dot{\gamma} R_{cap}^2}{2\eta} \tag{7}$$

$$\text{Rectangular capillary : } Re = \frac{2\rho \dot{\gamma} wh_{sl}^2}{6\eta (w + h_{sl})} \tag{8}$$

Turbulence occurs in the rotational devices as well, although it forms after the instabilities discussed in the previous section. The Reynolds number is proportional to the speed of the fluid. This means turbulence starts occurring at the edges of the rotational devices.

2.3. Wall adherence

A key assumption is the zero wall slip condition. This condition states that fluid in contact with a wall does not move along the wall. In reality, this is not always true. When the cohesion forces are stronger than the adhesion forces the fluid is pulled along the walls. When wall slip occurs the flow profile is changed, figure 2. The true shear rate is lower than the apparent shear rate the model assumes. Therefore the viscosity is underestimated.

Depending on the fluid and for example the wall material, slip can occur. Slip can also be caused by other factors such as wall depletion, i.e. larger particles are pushed out of the boundary layer. The smaller particles then form a lubricating layer along the walls. The shearing is then mostly limited to the boundary layers, figure 3.

Corrections for wall slip have been developed since 1931 by Mooney. The Mooney analysis is applicable to all the analysed devices [29].

Table 4. Variables in de measurement systems, geometrical definitions from figure 1.

Device	Variable
Parallel plate	h_{pp}
	R_{pp}
Concentric cylinder	R_{in}
	R_{out}
	L_{cc}
Slit capillary	h_{sl}
	w
	L_{sl}
Round capillary	R_{cap}
	L_{cap}

The slip will not be taken into account in the determination of the measuring range as it is fluid and material dependent. Furthermore, current rheometers do not correct for wall slip.

2.4. Isothermal flow

In general, the viscosity of a fluid is strongly temperature dependent. Most rheometers are temperature controlled to either measure or negate this temperature dependence. As the shear rates increase at constant forcing more energy is put into the fluid. All of this energy is converted into heat. This heat is dissipated through the fluid and eventually transferred to the outside world or absorbed by the fluid increasing the fluid temperature. As the viscosity of a fluid is temperature dependent this heating of the fluid must be avoided. When the temperature starts influencing the viscosity the momentum equation of the Navier–Stokes equation becomes coupled to the energy equation making the prediction of the fluid flow complicated. An indicator for the significance of the heating of the fluid is given by the dimensionless Nahme–Griffith number [30]. This number is the ratio between heat generation inside the fluid over the dissipation of the heat. As long as more heat is dissipated than generated due to viscous friction the effect is negligible. The Nahme–Griffith number is closely related to the Brinkman number which is used to quantify the effect a certain temperature change has on the viscosity. The formulas for the Nahme–Griffith number of the different rheometers types can be found in table 2.

When viscous heating is present, the viscosity is locally lowered. The measured viscosity is therefore reduced. In literature, a Nahme number of 1 is seen as the limit [31].

2.5. Incompressible flow

The compressibility of the fluid flow has an effect on the measurement of the viscosity. The model assumes the viscosity is not a function of the pressure. Most fluids can be considered incompressible. In reality, the pressure does influence the viscosity, however, this effect is limited. The pressure dependence of the viscosity for water at different temperatures is presented in [32] and is $-2.4 \mu\text{Pa s MPa}^{-1}$ to $-0.25 \mu\text{Pa s MPa}^{-1}$ for a temperature range of $0 \text{ }^\circ\text{C}$ – $25 \text{ }^\circ\text{C}$.

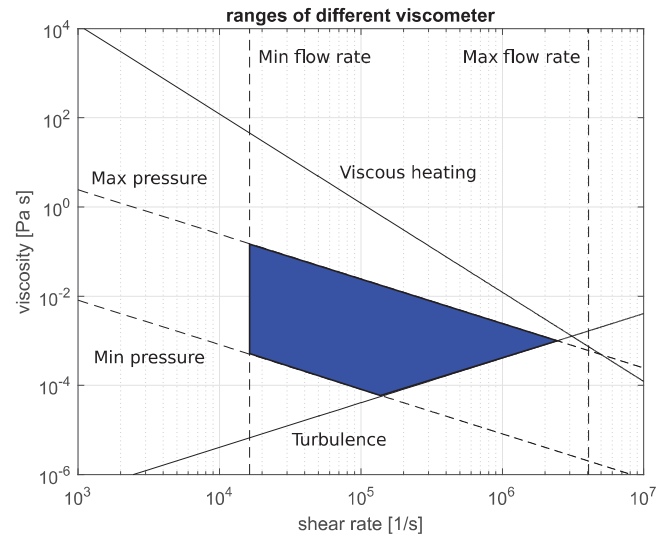


Figure 4. Example of the measuring range for a slit rheometer.

For lubricating oils the pressure dependence of the viscosity is larger, but it may still be neglected at the low pressure levels expected in the rheometers discussed in this study. The capillary rheometers will be more influenced by this assumption as they introduce a pressure difference to function, although, this effect is still negligible.

2.6. Pressure/speed limits

The system requires sensors and actuation. These have their limitations. These sensor maximum and minimum can be translated into a maximum and minimum viscosity at a given shear rate. These limitations create operation boundaries. Similarly, the actuation will have a limit defining a maximum and minimum attainable shear rate. Table 3 presents the equations used to find the limits of the analysed devices. By inserting the measuring range of the sensor in to the formula a maximum and minimum measurable viscosity is calculated for a given shear rate. By inserting the actuation range of the actuator in to the formula a maximum and minimum attainable shear rate is calculated.

2.7. Comparison

Taking into account all the discussed limitations in the previous sections, the working area of the measurement principles can be predicted. This gives the ability to determine the working range of different rheometer types. The free geometrical variables are listed in table 4.

The goal of the analysis is to compare the working principles to make a choice for the best design in a specific case. Therefore, the measuring methods have to be linked together. A way to do this is to match a characteristic dimension. In this case the characteristic length should be related to the shearing of the fluid. A re-occurring parameter in table 4 is the gap height. By linking the height of the gap, a link is made between the devices on the space where the shearing takes place.

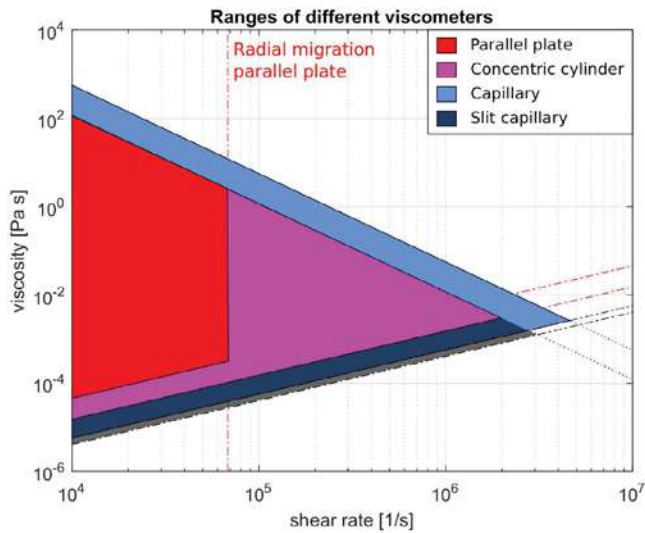


Figure 5. Theoretical ranges of the measurement principles for a gap of 35 μm.

Table 5. Requirements.

Shear rate	10 ⁶	s ⁻¹
Magnetic field density	1	T
Repeatability	2	%
Accuracy	2	%

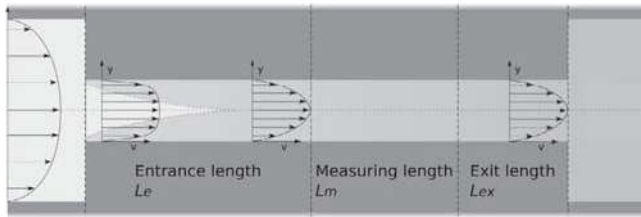


Figure 6. Channel design.

The gap heights of the parallel plate, concentric cylinder and the slit capillary can be matched. This leaves the round capillary. The round capillary can be matched with the slit capillary through the hydraulic diameter, equation (9).

$$d_h = \frac{4 \times \text{Cross sectional area}}{\text{Wetted perimeter}} = \frac{2wh_{sl}}{w + h_{sl}}. \quad (9)$$

As an example the measuring range is calculated for a slit rheometer measuring kerosene, figure 4, with measuring length: 1 mm, gap height: 50 μm, width: 0.5 mm, maximum pressure: 4 MPa, minimum pressure: 10 kPa, maximum flow rate: 25 ml min⁻¹ and minimum flow rate: 100 μl min⁻¹.

In figure 4 the different limitations discussed in previous sections are put together to define the theoretical measuring range. Turbulence from section 2.2. Viscous heating from section 2.4. The maximum/minimum pressure and shear rate from section 2.6. Depending on the geometrical dimensions chosen the theoretical measuring range can be determined.

The limits of each measuring principle as defined in section 2 have been applied and the measuring ranges defined for a common characteristic of 35 μm as defined in section 2.7.

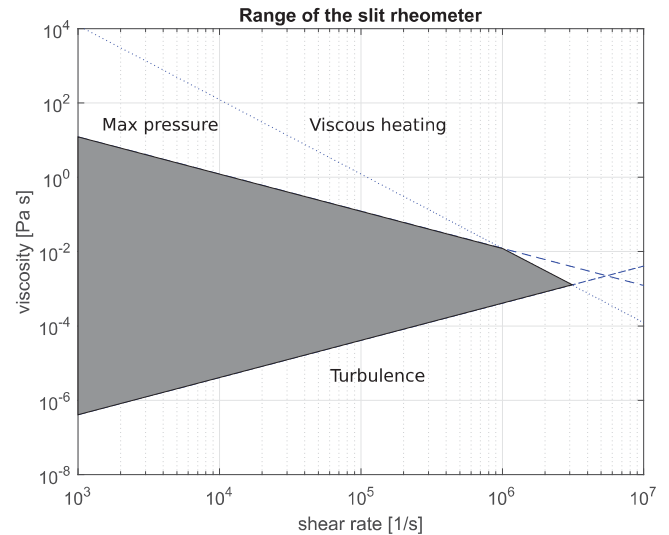


Figure 7. Working range of designed rheometer.

Table 6. Final pressures at different locations of the channel.

Parameter		Value (MPa)
Inlet pressure	P_{in}	4
Sensor pressure high	P_h	0.90
Sensor pressure low	P_l	0.15

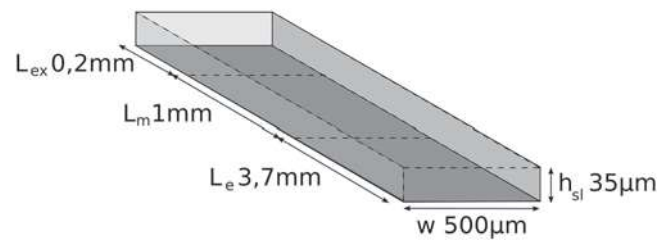


Figure 8. Final dimensions of the channel.

An overlay of the theoretical ranges can be found in figure 5. The fluid properties of kerosene are used in the measuring ranges.

From figure 5 we can see that the capillary devices have a slight advantage in measurement range. Moreover, both capillary devices are less influenced by viscous heating. The Nahme–Griffith number describes the viscous heating at a specific shear rate. Pressure driven flows have a varying shear rate over their gap, where the shear rate is highest at the edges. For concentric cylinder devices the shear rate is nearly constant over the gap. When this shear rate is high enough to cause viscous heating, the entire fluid is heating up. Additionally, the capillary devices continuously introduce new fluid to the system whereas the rotational devices reuse the fluid which could already have been affected by viscous heating. Thus intensifying the heating of the fluid. Lastly, capillary devices have an advantage in the application of a homogeneous magnetic field due to the linear shape.

The capillary concept, therefore, best fulfils the requirements. Within this group, the slit capillary concept is chosen due to the fact that producing rectangular microchannels is more cost effective and can be done more consistently.

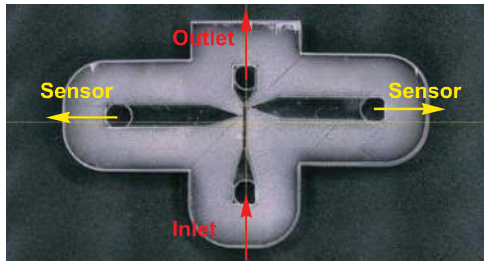


Figure 9. Design assembled slit.

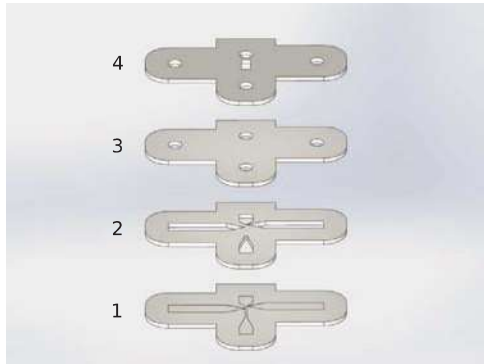


Figure 10. Exploded view of chip design in layers.

3. Design of measuring geometry

Firstly, the current commercially available and research magnetorheometers are analysed. Secondly, the non-magnetorheometers are analysed for their characteristics in order to determine the requirements for a new rheometer. The requirements can be found in table 5. These requirements are set as a target for the new design.

A slit capillary consists of three parts: the entrance length, the measuring length and the exit length, figure 6.

The entrance length is needed to create a fully developed flow and should be sufficient for the lowest viscosity fluid targeted. The transition to turbulent flow on macro scale is seen as a Reynolds number of 2300. In literature the transition phase for microfluidics is however still disputed. The consensus is that it does not start before a Reynolds number of 1000 [33]. To accommodate the fluid entering and stabilising, an entrance length is determined by equation (10) [34].

$$\frac{L_e}{d_h} \approx \frac{0.63}{1 + 0.035\text{Re}_{\max}} + 0.044\text{Re}_{\max}. \quad (10)$$

The measuring length is 1 mm as this creates a measurable pressure drop for low viscosity fluids while not requiring an excessive feed pressure for higher viscosity fluids. The exit length is 0.2mm. Increasing the exit length increases the required inlet pressure. However, by extending the exit length the magnetic fluid can be drained more easily from the channel.

Lastly, the gap height needs to be determined. A lower gap height results in higher shear rates, lower viscous heating and an increase in the required inlet pressure. The goal is to measure rheological properties magnetic fluids. This means the gap height must be large enough to allow the magnetic particles through and form chains to create the magnetorheological effect.

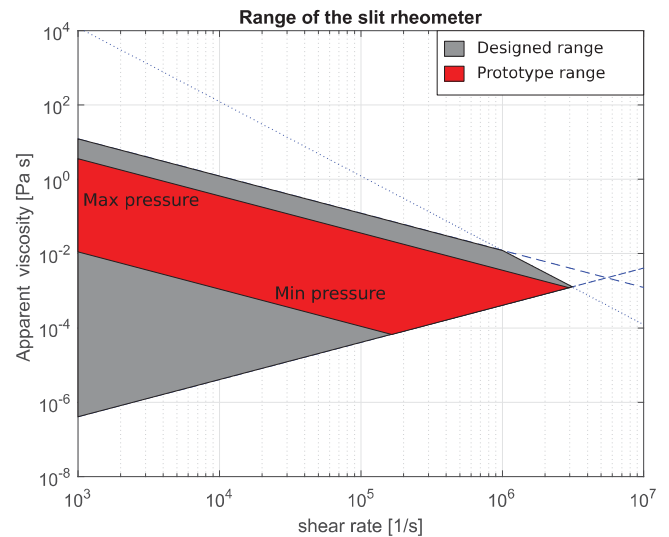


Figure 11. Prototype working range limited due to used syringe pump pressure limits.

The particle size for MR fluids are around 1 μm , therefore a lower limit of 20 μm is set to allow for chains of more than 10 particles to form [35].

Through an iterative process of weighing the pressures required to drive the fluid and the heat generation, a gap height of 35 μm was chosen. This results in the following measuring range for kerosene, figure 7.

The maximum shear stress to be measured is tuned to have a Nahme–Griffith number of 1 at 10^6 s^{-1} which results in a pressure at the entrance of the channel of 4MPa, equation (11) [30]. The parameter values can be found in table 6 and figure 8.

$$\frac{\Delta P}{\Delta L} = \tau \frac{2(w + h_{sl})}{wh_{sl}}. \quad (11)$$

The width of the channel has a lower limit. Edge effects of the side walls are negligible when the width is at least 10 times the gap height [36, 37]. The width of the channel has limited effect on the range but determine the flow rate. By tuning the width of the channel, the flow rate is adjusted to combine it with the flow rate of the pump, equation (12).

$$Q = \frac{wh_{sl}^2 \dot{\gamma}}{6}. \quad (12)$$

The magnetic core was designed to apply a homogeneous and uniform field over the microchannel. The choice was made to use a symmetric design to create this homogeneous field. The field has to be concentrated on the small area of the channel. The size on the pole piece was made four times as large as the channel dimensions. A 3D simulation of the magnetic field showed negligible variation of the field density over the microchannel. The coil geometry was determined using the magnetic reluctance [38]. The final parameters used can be found in table 6 and figure 8. The design of the core is presented in figure 18.

The simplest design would be to have the pressure sensors directly next to the channel, however, due to the magnetic core which surrounds the channel, there is limited space.



Figure 12. Silicon master.

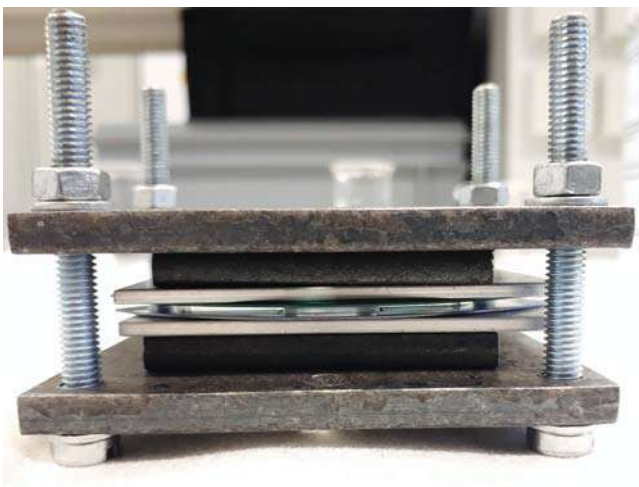


Figure 13. Assembled press.

Therefore, sensor channels are created, figure 9. The sensor channels have to be much wider than the channel in order not to create significant pressure drop to the pressure sensors.

The final design can be seen in figure 10 with the layers numbered. This results in a multi layered design where in the second layer the sensor channels are cut out. The third layer seals the sensor channels and allows for connectors to be mounted. A fourth layer is added to create more connecting length for the connectors and make them more robust.

To show the functioning of the designed rheometer, a prototype is manufactured. This prototype uses a syringe pump with a maximum pressure of .67MPa and a maximum flow rate of $25.99 \text{ ml min}^{-1}$. This limits the measuring range. The range can be seen in figure 11.

The range in figure 11 is limited by the syringe pump used, however, does reach the desired high shear rates.

4. Fabrication

For the fabrication of the entire device 3 subsystems have to be built. Firstly, the microchannel itself. Secondly, the magnetic system and finally the external systems such as data acquisition and the pump.

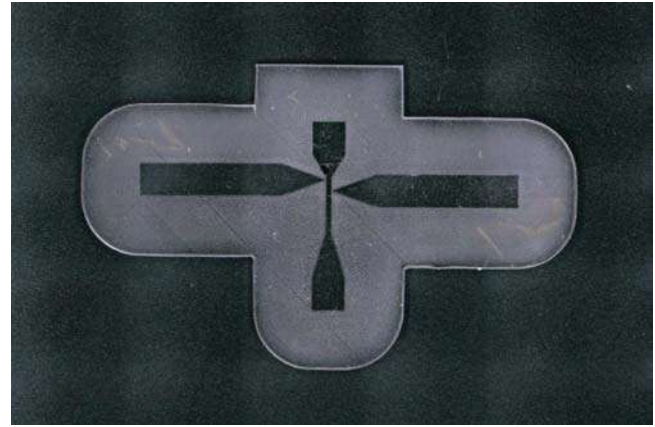


Figure 14. Embossed PMMA.

4.1. Microchannel fabrication

The fabrication of the micro device is complicated. Most micro devices are made through a chemical etching process, however, this is expensive and time consuming. In microfluidics, hot embossing techniques have been developed for quick prototyping [39]. Hot embossing uses a master design to press features into a plastic substrate. This process has been chosen in order to make devices in a cost effective manner. The substrate material chosen is Poly(MethylMethAcrylate), (PMMA). PMMA was chosen as it is a cheap material, has a high stiffness, is transparent and easily moulded [40]. The fabrication process for the chip consists of five steps.

1. Master production
2. Hot embossing
3. Flattening
4. Bonding
5. Final assembly

4.1.1. Master production. A laser etching machine is chosen to etch the master design in silicon. The laser is a Spectra Physics Q-switched Talon laser 355-15 with maximum output of 15W at 50kHz repetition frequency and with 13W at 100kHz. The maximum frequency is 500kHz with a pulse width of 35 ns. Different laser patterns and rotations have been tested to optimize the height differences created by the laser path. The best result was obtained by laser etching the silicon with a $5 \mu\text{m}$ line spacing in a net pattern. The etch is repeated once with a 45° rotation of the net etching pattern. A firing rate of 20kHz with a laser speed of 20 m s^{-1} was used [41]. The produced master is cleaned in Isopropanol with an ultrasonic cleaner for half an hour, then spincoated with an anti stiction monolayer, EVGNIL ASL for releasing the PMMA after the embossing process, figure 12.

4.1.2. Embossing. The master is placed in a mechanical press and covered with a piece of 1 mm thick PMMA cut into the shape of the chip design. The PMMA is covered with a silicon wafer to improve the surface roughness of the counter surface.

The assembly is clamped between two sheets of aluminium and two cast steel plates and tightened by four bolts, figure 13. The bolts are hand tightened and the assembly placed in an

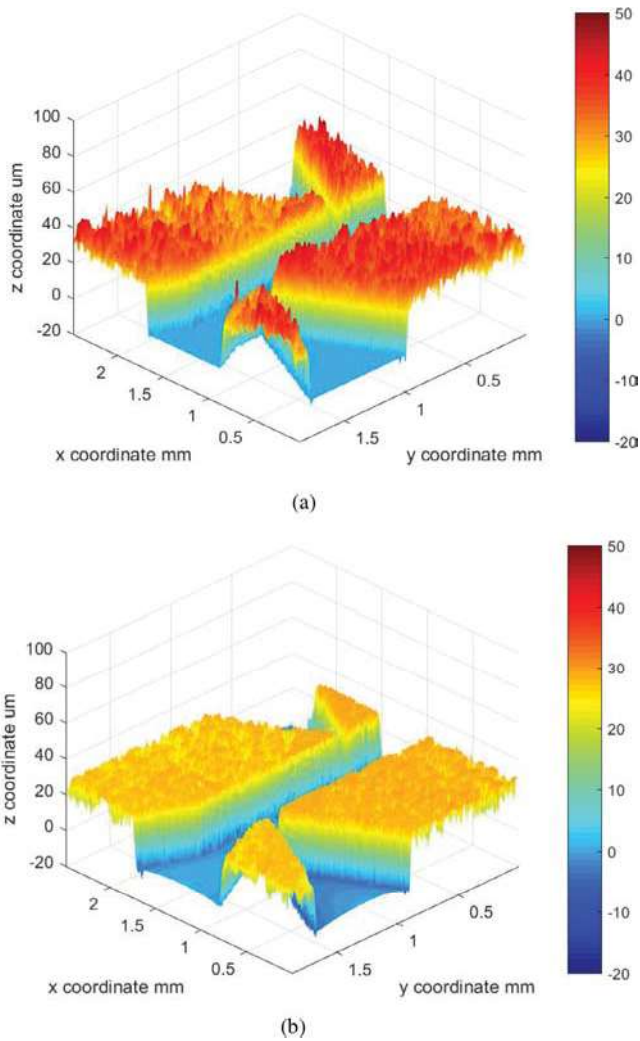


Figure 15. White light interferometry images of PMMA surface before (a) and after (b) the flattening process. (a) Before flattening. (b) After flattening.

oven preheated to 145 °C for 20 min. The bolts are then tightened with a torque wrench to an overall pressure of 0.9 MPa. The assembly is left in the oven for 20 min, then slowly cooled to 110 °C in about 20 min. The pressure is removed and the press is disassembled. The master is separated from the PMMA and left to cool to room temperature. The temperature and pressure are sketched in figure 17 as the solid lines. The embossing procedure is taken from [42] and adapted through trial and error to get the best results for the used equipment. The embossed PMMA can be seen in figure 14.

4.1.3. Flattening. The uneven surface on the PMMA, due to the laser etched surface, is subjected to flattening stages. As a result of these steps, the bonding is improved and a sealed microchannel is obtained. The PMMA is put in between two layers of silicon and assembled in the press. A pressure of 0.57 MPa is applied. The assembly is put in a preheated oven at 110 °C for 55 min and then cooled under pressure to room temperature. The improvement of the bonding surface can be seen in figure 15. The flattening process does have an effect on



Figure 16. The assembled chip.

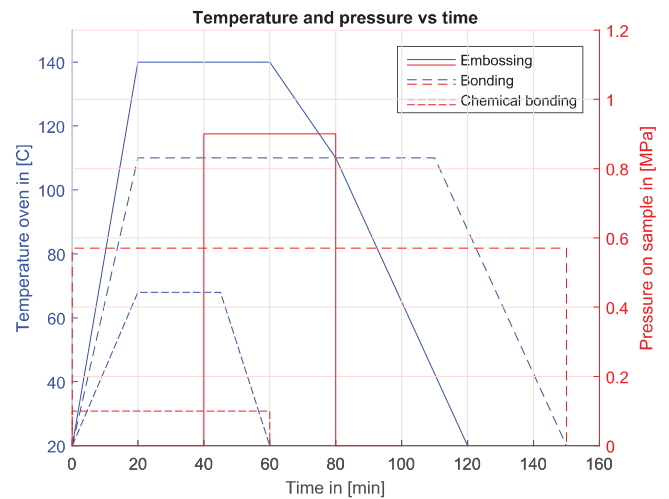


Figure 17. Embossing, bonding and chemical bonding process parameters. Temperature in the oven and pressure on PMMA against time.

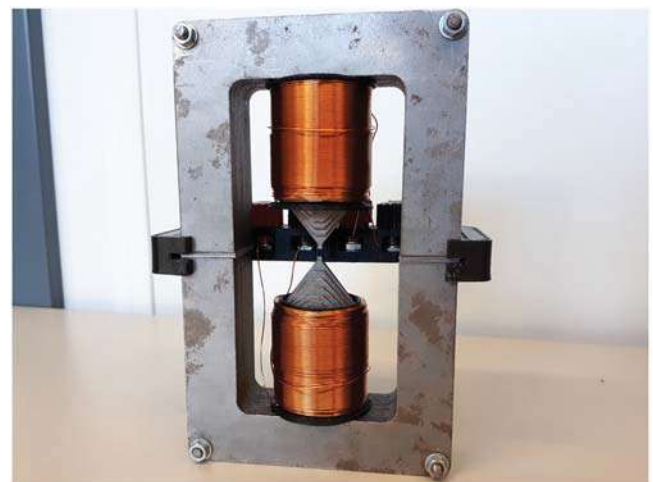


Figure 18. Fabricated core.

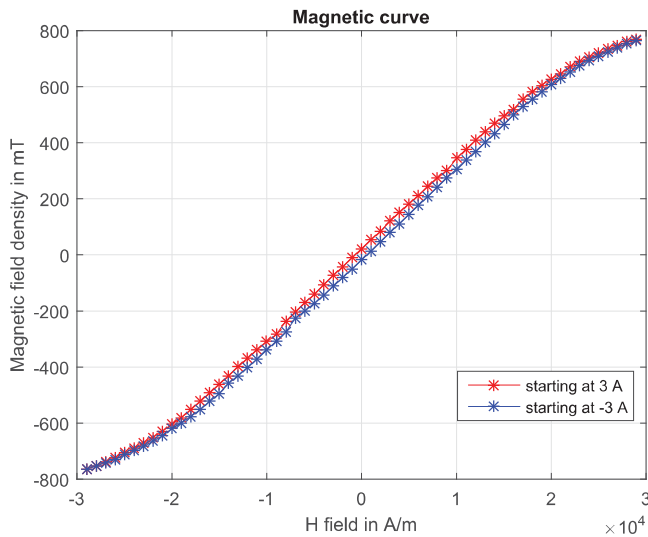


Figure 19. Magnetic field strength curve at microchannel in air.

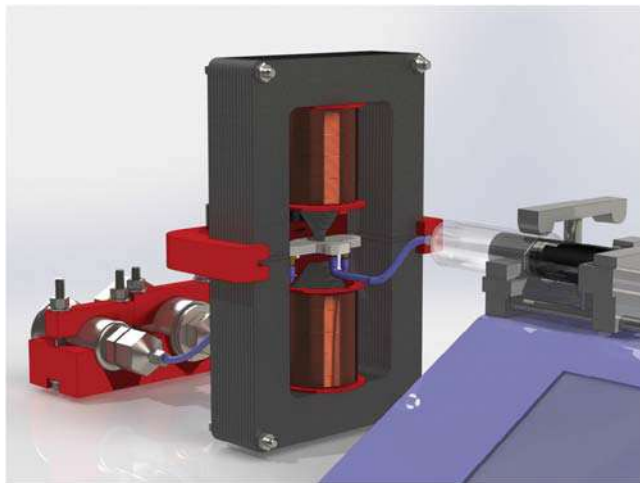


Figure 20. Test setup.

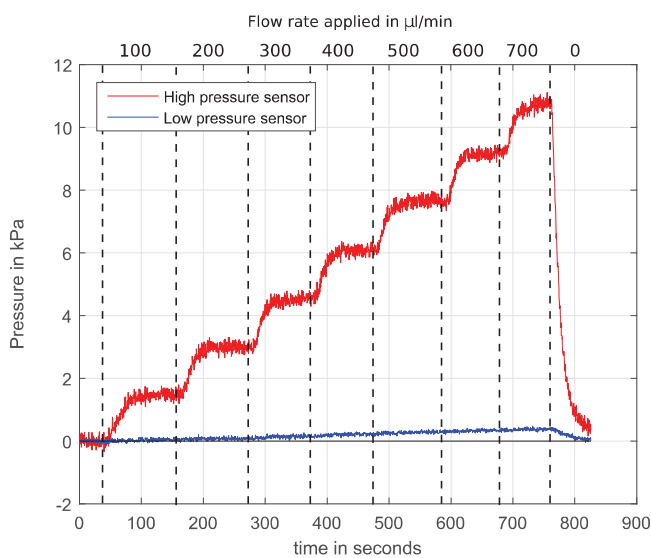


Figure 21. Typical measurement of pressure against time at different flow rates with deionized water.

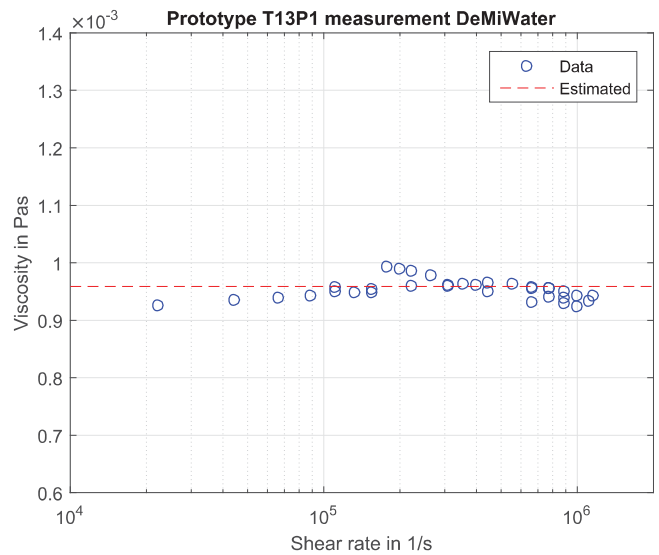


Figure 22. Viscosity of deionized water at high shear rates.

the channel geometry. Due to the temperature and pressure the channel swells slightly.

4.1.4. Bonding. The bonding step is similar to the embossing step but requires a lower temperature to inhibit deformation of the geometry. Layers 2, 3 and 4, figure 10, are aligned and assembled in the press. For a smooth counter surface, silicon wafers are placed on either side. The press is tightened to 0.57MPa and placed in an oven preheated to 110 °C. The assembly is left in the oven for 90 min and then slowly cooled to room temperature. The pressure is removed and the press is disassembled.

The bond of the embossed PMMA to the bonded layers 2–4, figure 10, is done chemically [43]. A solution of 70% Isopropanol is distributed on top of the embossed PMMA. The remaining layers placed on top. The assembly is pressed together and the excess solution is removed. While under slight pressure the layers are aligned using alignment tools. The press is hand tightened and placed in a preheated oven of 68 °C. The press is left for 15 min. The press is removed and slowly cooled to room temperature. Once cooled the pressure is removed. The temperature and pressure are sketched in figure 17 as the striped lines and dotted lines as thermal bonding and chemical bonding respectively. The final assembled chip can be seen in figure 16.

4.2. Magnetic system

A magnetic core has been designed to apply the 1 T field on the microchannel. The core has been fabricated from St37 steel. The core has been designed as a layered design to be able to laser cut and assemble the core. The coils have a diameter of 30 mm and are wrapped with 400 windings of 0.55 mm diameter magnetic copper wire. The gap is 3 mm to allow for the microchannel to be placed in between. The fabricated core can be seen in figure 18.

The magnetic behaviour has been characterised at the location of the microchannel using a Gauss meter. The current has

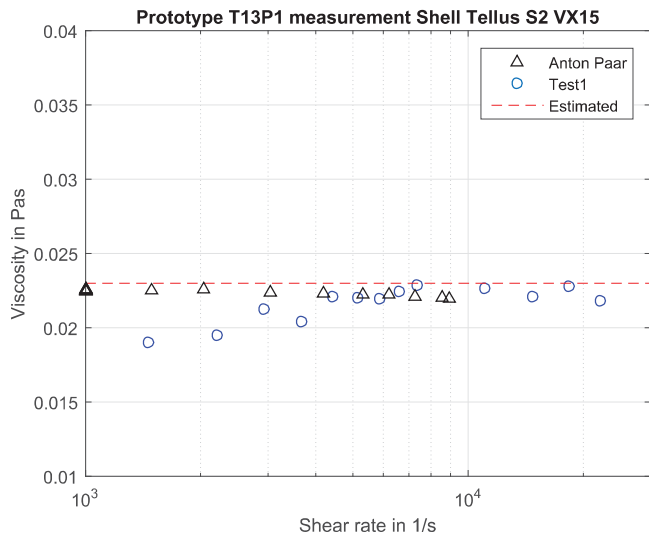


Figure 23. Viscosity of Shell Tellus S2 VX15 at high shear rates.

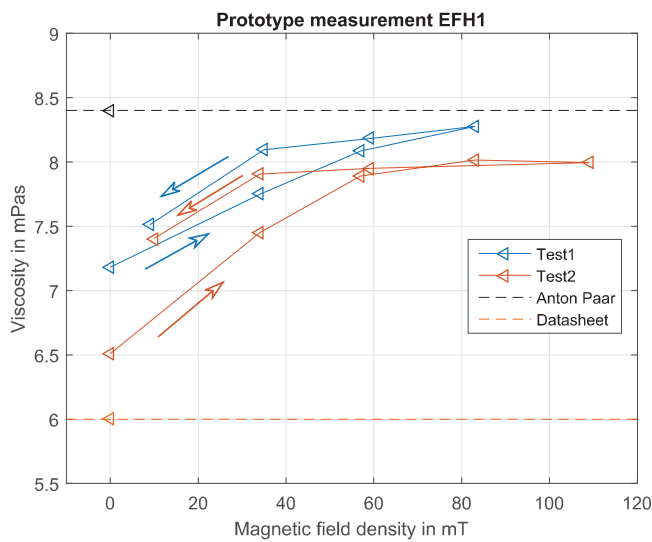


Figure 24. Viscosity of magnetic fluid with different magnetic fields at a constant shear rate.

been varied from -3 A to 3 A whilst measuring the magnetic field density, figure 19.

4.3. Final assembly

The PMMA assembly needs to be connected to the supply pump and sensors. The connectors are adapted Festo straight barbed 3 mm connectors. One side is filed down to 3 mm diameter. The connections are glued in place with Bison plastic epoxy. The Festo piping connects the PMMA to the pressure sensors and the syringe pump. The test setup can be seen in figure 20.

4.4. Sensors and data acquisition

The pump being used is a Kd Scientific Legato 111 double syringe programmable infusion and withdrawal pump. The syringe used is a 10 ml plastic Terumo syringe. The pump has a maximum flow rate with this syringe of $25.99 \text{ ml min}^{-1}$ which is sufficient to reach shear rates over 10^6 s^{-1} .

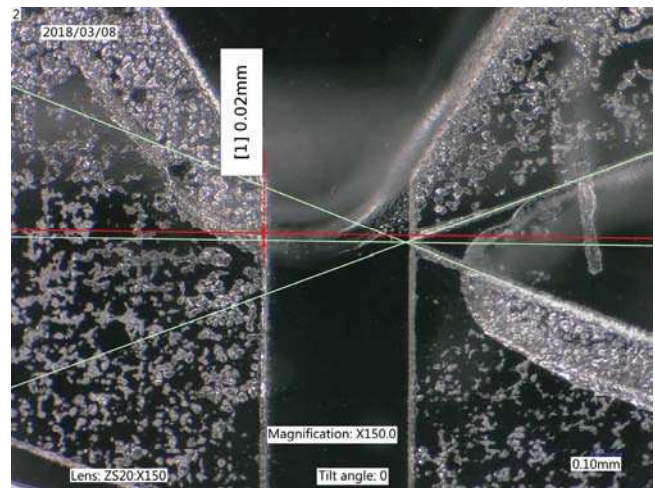


Figure 25. Misalignment influencing the measured low pressure.

5. Measurement procedure

Figure 21 shows a typical measurement. The measurement is started in steady state with zero flow. By taking 100 samples a zero measurement for the sensors is made. After these, a starting flow rate is applied. Once the measured pressure has reached a steady state the flow rate is increased. This process is repeated until the syringe is empty. As the flow is stopped the pressures quickly return to their zero value.

The measured pressures and flow rates are converted into shear stresses and shear rates through the geometrical model, equations (11) and (12), respectively.

6. Results

6.1. Preliminary test

The seal of the microchannel is tested through two simple tests. Firstly the chip is submerged in water for a leak test. Air is pressed into the channel through a syringe. The air bubbles appearing show the flow of air and the leakages.

In the second test water is pressed into the chip with a syringe. The meniscus moving through the chip can be perceived, showing that the fluid does not flow in between the layers.

6.2. Results

The results are plotted in figures 22–24.

6.2.1. Deionized water. The resulting viscosities at different shear rates are compared to the viscosity of deionized water at $21.8 \text{ }^\circ\text{C}$, 0.96 mPa s [44]. The maximum shear rate measured was $1.16 \times 10^6 \text{ s}^{-1}$. Higher shear rates were not measured as the pump engine stalled.

The chip was cleaned and filled with Shell Tellus S2 VX15. The resulting viscosities can be seen in figure 23. The expected viscosity is taken from the data sheet provided by Shell. The expected viscosity is 23 mPa s . The measurements from the Anton Paar rheometer have been added.

Lastly, Ferrotec EFH1 has been measured to show the magnetorheological effect. The relation between magnetic

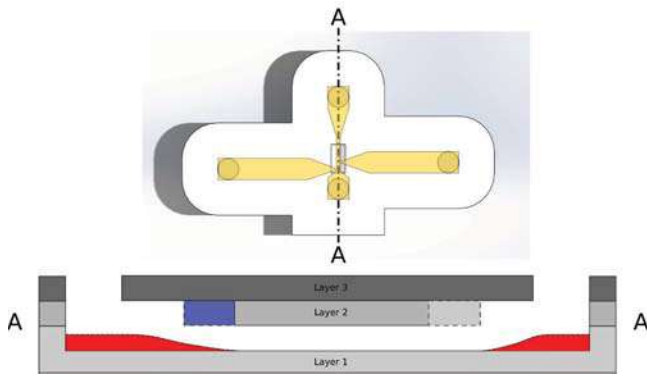


Figure 26. Entrance restriction, channel swelling in red, misalignment in blue.

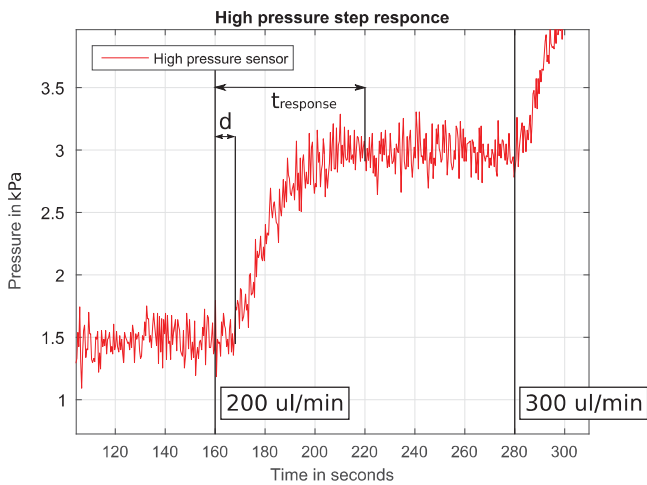


Figure 27. High pressure response to flow rate step increase.

field and the current steps was measured to be able to translate the current into magnetic field density. In figure 24 the flow rate was kept constant over the entire measurement, $1.8 \times 10^4 \text{ s}^{-1}$. The current was increased in steps and then reduced. The resulting pressure rise translates into an increase in viscosity, showing the magnetorheological effect. The resistance to flow has increased due to the magnetic field.

7. Discussion

Firstly, a measuring principle was determined. After a comprehensive comparison of pertinent rheometer concepts, the slit capillary rheometer was selected as the most promising concept. It was chosen because of its high measuring range compared to other rheometer types, the simple application of the magnetic field and its low viscous heating effects. This concept was further developed into a detailed design for a prototype. Fabrication techniques were found and used to build the prototype. The resulting prototype succeeded in measuring deionized water, figure 22, Shell Tellus S2 VX15 oil, figure 23, and Ferrotec EFH1 and showed the magnetorheological effect, figure 24.



Figure 28. Deformation of the syringe due to high pressure in the system.

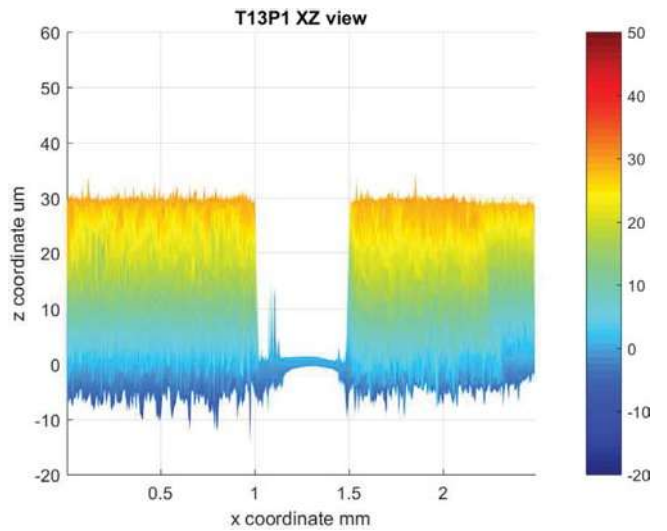


Figure 29. XZ view of T13P1 showing the channel swell.

7.1. Low pressure sensor

In the prototype a misalignment was introduced, effectively reducing the exit length of the slit. The misalignment is created during the chemical bonding of layers 1 and 2, figure 10. A closer look at the misalignment is given in figure 25. The exit length was dimensioned to be 0.2mm but is measured to be 0.02mm. This results in reduced pressures measured at the sensors. This brings the measured signal at the low pressure sensor in the noise range. The misalignment can be prevented by adding alignment features to the design. The results in this paper have been corrected for this error by using the actual exit length, not the designed exit length.

7.2. Experimental setup

7.2.1. Maximum shear rate. The maximum shear rate measured is $1.16 \times 10^6 \text{ s}^{-1}$, figure 22. No higher shear rates were measured as the syringe pump motor stalled. This means the

maximum pump pressure was applied to the chip. The expected pressure at the entrance for the maximum shear rate measured is 0.44 MPa, whereas the maximum pressure produced by the pump is 0.67 MPa. This means this pressure is lost between the pump and the sensors. Further analysis revealed that this is caused by a restriction in the channel entrance. The restriction has two sources: the channel swelling in the flattening stage and the misalignment between layers 1 and 2, figure 10.

As layer two is closer to the swelling of the channel (blue in figure 26), the entrance becomes much smaller than designed and causes an increased pressure drop. The swelling of the channel could be prevented by removing the flattening stage, section 4.1.3. This means improving the master such that the bonding surfaces are smooth. The swelling at the entrances does not affect the accuracy of the measurement but restricts the maximum shear rate reached with the maximum pressure of the syringe pump.

72.2. Response time. As a step in the applied flow rate is initiated, a delay (d) is noticed in the pressure response. After this delay the pressure rises steadily and stabilises to a pressure, figure 27. The delay is primarily caused by air bubbles in the syringe. The air in the syringe is compressed as the pressure increases, reducing the applied flow rate temporarily. After this initial delay the measured pressure increases, although not instantly as the incompressibility assumption would suggest. The slow response, (t_{response}), is caused by the type of pressure sensors used. The sensors have a membrane which deforms due to the applied pressure. The deformation is measured and converted into a pressure. Due to the incompressibility, the deformation of the membrane means an increase in the volume in the sensor channel. This volume has to be filled with fluid from the measuring channel to increase the measured pressure. The limited access to the measuring channel creates a flow restriction which causes the slow response of the measured pressure.

The delay can be prevented by draining the air bubbles from the system before measuring. The pressure response can be accelerated by having smaller measuring membranes in the sensors or increasing the stiffness of the membrane. This reduces the volume flow required for the pressure to increase. A further improvement would be to reduce the restriction to the measuring channel.

72.3. Blockages. Some measurements failed due to blockages in the microchannel. It is critical to keep the system clean as the microchannel is a mere 30 μm in height. This issue was encountered with the first measurement using magnetic fluids. Due to the misalignment and swelling of the channels the effective gap was reduced significantly at the entrance. The entrance became blocked by the particles bridging across the channel [45]. The blockage increased the pressure drastically at the entrance causing a leak of the chip. The entrance geometry can be improved to reduce the formation of particle bridges. The tapered entrance strengthens the bridges that are formed. Therefore a sharp entrance is preferred.

72.4. Syringe. Due to the high flow rates required and the restriction in the flow path, the maximum force is applied to the syringe. After the high shear measurements it was perceived that the syringe had deformed due to the applied force. The fixation of the syringe pump is not able to hold the syringe in place, figure 28.

This results in a slightly lower flow rate being applied to the chip which means lower pressures are being measured. During the data processing this results in lower viscosity due to the flow rate used in calculation is higher than in reality. The deformation can be prevented by using stainless steel syringes, creating a custom fixation for the syringe pump or using a different pumping concept.

72.5. Sensor zeroing. Before each measurement the pressures at zero flow rate were measured. The data is corrected during the data processing for the non-zero pressure at zero flow. The non-zero values are due to the gravitational force of the fluid in the connection tubes to the sensors and the offset of the sensors. However, due to the restriction in the sensor channels and surface tension of the measured fluid, the pressure did not always reach the true zero pressure value. The sensor channels were able to keep an over or under pressure. Once the flow was initiated the flow would correct itself.

72.6. Gap height. The gap height is only known before the chemical bonding. As the channel swells about 2 μm , the exact gap height is slightly varying over the channel, figure 29. The gap height is therefore slightly altered to fit the deionized water measurements. The alterations are less than 2 μm . Once the parameter is set it is not altered for any other measurement.

73. Discussion measurements

The highest deviation for the water measurement after geometrical corrections is less than 8% for deionized water and Shell Tellus VX15 oil. The maximum shear rate measured is $1.16 \times 10^6 \text{ s}^{-1}$. The measurements with Ferrotec EFH1 show the device is able to measure the magnetorheological effect. This means that this prototype can be expanded into the measuring of larger particle magnetic fluids at high shear rates. To be able to perform these measurements some improvements will be necessary. Currently the system is not strong enough to withstand the pressures involved with measuring MR fluids at high shear rates as the viscosity of MR fluids are higher.

8. Conclusions

From the physics based analysis of the measuring principles, it follows that capillary devices have an advantage in measuring magnetic fluids as they can reach higher shear rates while at the same time simplifying the application of a magnetic field. The measurement has a maximum deviation of 8% compared to the true viscosity. The viscosity is measured to a shear rate range of 10^4 s^{-1} – $1.16 \times 10^6 \text{ s}^{-1}$.

The measurement on the magnetic fluid clearly show the influence of the magnetic field on the rheology of the fluid. More experiments should be performed with the designed rheometer on magnetic fluids to fully capture the potential of the device.

The final conclusion of this paper is that we can say that we have successfully designed and built a prototype of an ultra high shear rheometer capable of measuring magnetic fluids and a range of 10^4 s^{-1} – 10^6 s^{-1} .

ORCID iDs

S G E Lampaert  <https://orcid.org/0000-0002-8268-1457>

References

- Papell S S 1965 Low viscosity magnetic fluid obtained by the colloidal suspension of magnetic particles
- McTague J P 1969 Magnetoviscosity of magnetic colloids *J. Chem. Phys.* **51** 133
- Odenbach S 2004 Recent progress in magnetic fluid research *J. Phys.: Condens. Matter* **16** R1135–50
- Odenbach S 2000 Magnetoviscous effects in ferrofluids *Appl. Rheol.* **10** 178–84
- Rabinow J 1948 The magnetic clutch *AIEE Trans.* **67** 1308–15
- Jacob R 1951 Magnetic fluid torque and force transmitting device *US Patent* 2,575,360
- Carlson J D and Chrzan M J 1994 Magnetorheological fluid dampers *US Patent* 5,277,281
- Huang J, Zhang J Q, Yang Y and Wei Y Q 2002 Analysis and design of a cylindrical magneto-rheological fluid brake *J. Mater. Process. Technol.* **129** 559–62
- Baranwal D and Deshmukh T S 2012 MR-Fluid technology and its application—a review *Int. J. Emerg. Technol. Adv. Eng.* **2** 563–9
- Wang J and Meng G 2005 Magnetorheological fluid devices: principles, characteristics and applications in mechanical engineering *Proc. Inst. Mech. Eng. L* **215** 165–74
- Lampaert S G E 2015 Planar ferrofluid bearings modelling and design principles *Master's Thesis* Technical University Delft
- Bompos D A 2015 Tribological design of nano/magnetorheological fluid journal bearings *PhD Thesis* University of Patras
- Ochoński W 1989 Dynamic sealing with magnetic fluids *Wear* **130** 261–8
- Raj K and Chorney A F 1998 Ferrofluid technology—an overview *Indian J. Eng. Mater. Sci.* **5** 372–89
- Wang X and Gordaninejad F 2006 Study of magnetorheological fluids at high shear rates *Rheol. Acta* **45** 899–908
- Goncalves F 2005 Characterizing the behavior of magnetorheological fluids at high velocities and high shear rates *PhD Thesis* Virginia Polytechnic Institute and State University
- Becnel A, Hu W and Wereley N 2012 Measurement of magnetorheological fluid properties at shear rates of up to 25 000 s⁻¹ *IEEE Trans. Magn.* **48** 3525–8
- Hezaveh A N I and Fazlali H 2011 Synthesis, rheological properties and magnetoviscous effect of fe2o3/paraffin ferrofluid *J. Taiwan Inst. Chem. Eng.* **43** 159–64
- Paar A 2016 Application specific accessories for additional parameter setting
- TA Instruments 2014 Discovery hybrid rheometers temperature systems and accessories
- ACA Systems OY 2014 *ACA V Runnability Analyzers for Coating Colors and Pigment Slurries* (Finland: ACA systems OY)
- RheoSense 2019 The Ideal Viscometric Characterization Platform *hts-VROC Viscometer, High Temperature High Shear Viscosity* (RheoSense)
- TannasCo TBS 2100 2019 *E-F, HTHS Tapered Bearing Simulator Viscometer* (Tannas Co)
- PCS Instruments 2016 *Ultra Shear Viscometer* (London: PCS Instruments)
- Dewey C F 1984 Secondary flow and turbulence in a cone-and-plate device *J. Fluid Mech.* **138** 379–404
- Connelly R W and Greener J 1985 High shear viscometry with a rotational parallel disk device *J. Rheol.* **29** 209–26
- Watanabe K, Sumio S and Ogata S 2006 Formation of Taylor vortex flow of polymer solutions *J. Fluids Eng.* **128** 95
- White F M 2011 *Fluid Mechanics* 7th edn (New York: McGraw-Hill)
- Kalyon D M 2005 Apparent slip and viscoplasticity of concentrated suspensions *J. Rheol.* **49** 621–40
- Macosko C W 1994 *Rheology, Principles Measurements and Applications* (New York: Wiley)
- Costa A, Melnik O and Vedeneva E 2007 Thermal effects during magma ascent in conduits *J. Geophys. Res.* **112** 1–16
- Schmelzer J W P, Zanotto E D and Fokin V M 2005 Pressure dependence of viscosity *J. Chem. Phys.* **122** 074511
- Obot N T 2002 Toward a better understanding of friction and heat/mass transfer in microchannels a literature review *Technology* **3954** 155–73
- Chen R Y 1973 Flow in the entrance region at low Reynolds numbers *ASME J. Fluids Eng.* **1** 153–8
- Whiteley F W X and Gordaninejad J 2010 Behavior of magneto-rheological fluids in microchannels *Electro-Rheological Fluids and Magneto-Rheological Suspensions* (Singapore : World Scientific) pp 523–9
- Baird D G and Collias D I 2014 *Polymer Processing and Design* 2nd edn (New York: Wiley)
- Xing D, Yan C, Wang C and Sun L 2013 A theoretical analysis about the effect of aspect ratio on single-phase laminar flow in rectangular ducts *Prog. Nucl. Energy* **65** 1–7
- Balakrishnan A, Joines W T and Wilson T G 1997 Air-gap reluctance and inductance calculations for magnetic circuits using a Schwarz–Christoffel transformation *IEEE Trans. Power Electron.* **12** 654–63
- Esch M B, Kapur S, Irizarry G and Genova V 2003 Influence of master fabrication techniques on the characteristics of embossed microfluidic channels *Lab Chip* **3** 121
- Worgull M 2009 Chapter 3—Molding materials for hot embossing *Hot Embossing (Micro and Nano Technologies)* (Boston, MA: William Andrew Publishing) pp 57–112
- Jia B 2017 Evaluation of fast prototyping method of laser micromachining by thermal damage *Master's Thesis* Technical University Delft
- Shamsi A, Amiri A, Heydari P, Hajghasem H, Mohtashamifard M and Esfandiari M 2014 Low cost method for hot embossing of microstructures on PMMA by SU-8 masters *Microsyst. Technol.* **20** 1925–31
- Bamshad A, Nikfarjam A and Khaleghi H 2016 A new simple and fast thermally-solvent assisted method to bond PMMA to PMMA in micro-fluidics devices *J. Micromech. Microeng.* **26** 065017
- Anton Paar 2018 Viscosity of Water <https://wiki.anton-paar.com/en/water/>
- Sendekie Z B and Bacchin P 2016 Colloidal jamming dynamics in microchannel bottlenecks *Langmuir* **32** 1478–88